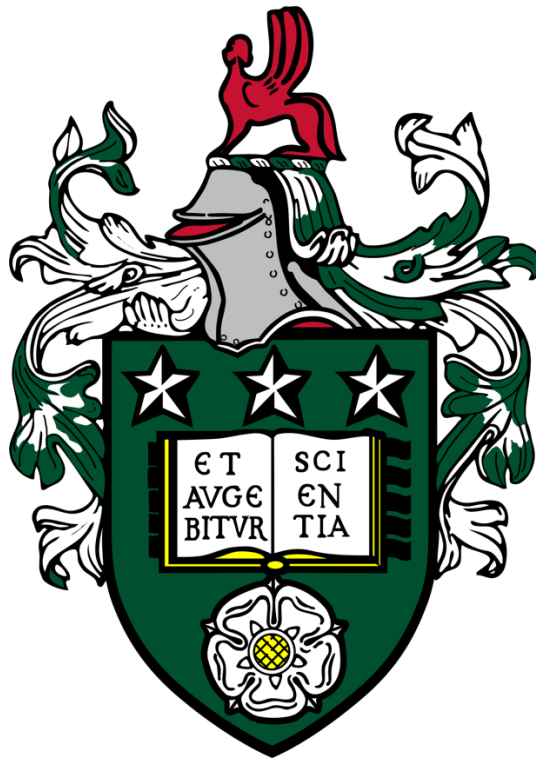


The impact of faults on fluid flow in microbial and hydrothermal carbonates



Dorothy Leigh Drayton

Submitted in accordance with the requirements for the degree of
Doctor of Philosophy

The University of Leeds
School of Earth and Environment

Submitted November 2022
Revised January 2023

The candidate confirms that the work submitted is his/her own and that appropriate credit has been given where reference has been made to the work of others.

This copy has been supplied on the understanding that it is copyright material and that no quotation from the thesis may be published without proper acknowledgement.

The right of Dorothy Leigh Drayton to be identified as Author of this work has been asserted by her in accordance with the Copyright, Designs and Patents Act 1988.

© 2022 The University of Leeds and Dorothy Leigh Drayton

Acknowledgements

First and foremost, I would like to thank my supervisor Professor Quentin Fisher for guidance throughout my PhD studies, offering valuable feedback, entertainment on many a fieldtrip and always being an email away regardless of where in the world he is. I would also like to thank Dr Sam Allshorn and Dr Carlos Grattoni for teaching me the ways of the petrophysical lab, helping me fix the things I break and questing whether travertines are real rocks; John Martin who patiently taught me how run the triaxial test rigs (multiple times) and was always happy to help on the many times I needed to change/fix/adapt my test setup; and Harry Wyn Williams who guided me through the long process of making thin sections. Additional thanks to the National Environmental Research Council and the Carbonate Fault Rock Research Group for funding the project.

Finally, I would not have got through the last few years without having such great friends. Particular thanks goes to SBC for all vibes, and fun Leeds times; to Portakabin Party for listening when I complain about anything and everything; to my office pals in 7.131 for making the PhD liveable providing the needed distractions of coffee trips, gossip, and pointless discussions; and to Delia for the escape rooms, the hype and providing access to Bobs. Lastly, a huge thank you to my family who knew not to ask how the PhD was going and to Tim who has kept me sane and got me through all the stress, panic, and e-scooter accidents.

Abstract

Faulting may provide conduits or baffles in subsurface hydraulic systems. Despite substantial research characterising faults, heterogeneities within carbonates means that there are no current empirical relationships which can be used as a predictive tool in fault zone characterisation. This is especially true for non-marine carbonates which include a range of complex microbial and hydrothermal facies. Despite substantial interest surrounding oil-bearing non-marine carbonates of the South Atlantic pre-salt, data to provide analogues for deformation within non-marine carbonates remains scarce. This thesis aims to improve understanding of the controls on fault formation and resultant fluid-flow impacts within non-marine carbonates. This is carried out through the integration of fieldwork, petrophysical analysis, geomechanical experimentation and optical, and CT scan microstructural analysis, with existing work on carbonate faults. Faulted, non-marine carbonate exposures are limited due to the under-representation of ancient non-marine carbonates due to alteration and poor preservation. However, observations show that shallow deformation varies greatly within different non-marine carbonate deposits and is dependent on the stress, lithology and rock strength as a product of diagenesis. The Ballik travertine (Turkey) hosts hybrid dilational faulting at low stresses which can act as fluid conduits. This contrasts the Crato Formation (NE Brazil) where poorly cemented, fine-grained laminated limestone results in semi-brittle deformation. Triaxial mechanical tests and ultra-sonic velocity measurements, show that depending on principal stress relationships, fault heterogeneity can be related to the primary depositional fabrics. Confining pressures typical of 200 – 1500 m burial depth likely produce deformation within travertines dominated by initial brittle deformation, localised in moderate porosity, micrite-dominated facies resulting in enhanced permeability. Permeability reduction may then occur in more mature fault zones from progressive microcracking and brecciation processes. Conversely, shrub travertine facies deform by compactional processes resulting in localised reductions in grain-size and porosity, impeding permeability. The study provides quantitative data to be integrated into future global datasets on non-marine carbonate rock properties and demonstrates the potential for conceptual models for characterising uncertainty in the prediction of deformation and subsurface fluid flow.

Table of contents

1. Introduction.....	1
1.1 Project rationale	1
1.2 Aims and objectives	2
1.3 Thesis outline.....	5
2. The impact of faults on fluid flow in non-marine carbonates: a review	7
2.1 Microbial and hydrothermal carbonates	7
2.1.1 Non-marine carbonate host rocks	7
2.2 Carbonate hosted faults.....	15
2.2.1 The brittle-ductile transition in carbonate rocks	17
2.2.2 Rock physics: elastic and acoustic properties of carbonates	21
2.2.3 Carbonate fault rocks.....	23
2.2.4 Fault rock characterisation.....	26
2.3 Summary of key knowledge gaps	40
3. Methodological overview	42
3.1 Introduction.....	42
3.2 Field observations and sampling	43
3.3 Sample preparation	43
3.4 Helium porosity measurements	44
3.5 Permeability measurement.....	45
3.5.1 Core plug permeability.....	45
3.5.2 Probe permeability	46
3.5.3 Klinkenberg correction.....	48
3.6 Triaxial testing and velocity measurement	49
3.6.1 Triaxial rig set up	49
3.6.2 Multistage triaxial test procedure.....	51
3.7 CT scanning and image analysis workflow	54
3.8 Microstructural analysis.....	54
3.8.1 Undeformed samples.....	54
3.8.2 Deformed core plugs.....	54
4. Characterisation of deformation features in non-marine carbonates from field observations.....	55
4.1 Introduction.....	55
4.1.1 Background	57
4.2 Methodology	68

4.2.1	Field investigation	68
4.2.2	Microstructural analysis	69
4.2.3	Petrophysical analysis	69
4.3	Results	69
4.3.1	Microbialites	69
4.3.2	Travertines	77
4.4	Discussion	103
4.4.1	The presence of deformation within non-marine carbonates	103
4.4.2	Structural styles	105
4.4.3	Permeability impacts of shallow deformation features	112
4.5	Conclusions	116
5.	<i>Influence of rock fabric on the mechanical behaviour of travertine</i>	117
5.1	Introduction	117
5.2	Mechanical failure within carbonates	117
5.3	Materials and methodology	119
5.3.1	Travertine	119
5.3.2	Sample collection and preparation	122
5.3.3	Petrophysical analysis	122
5.3.4	Triaxial multiphase mechanical testing	122
5.3.5	CT scan imaging and macro-porosity modelling	123
5.3.6	Optical microscopy	123
5.4	Results	123
5.4.1	Porosity	123
5.4.2	Permeability heterogeneity	125
5.5	Mechanical properties of travertine	130
5.5.1	Stress-strain response to failure	130
5.5.2	Critical stresses and yield envelopes	134
5.5.3	Velocity analysis	138
5.5.4	Failure plane orientation	140
5.6	Structural analysis of failure in travertine	141
5.6.1	Macro-porosity evolution	141
5.6.2	Microstructure	145
5.7	Discussion	148
5.7.1	Deformation mechanisms within travertine	148
5.7.2	The control of travertine heterogeneity on failure	153
5.7.3	Possible impacts of failure within travertine on fluid flow	155
5.8	Summary	156
6.	<i>Discussion</i>	158
6.1	Introduction	158
6.2	What are the structural characteristics of faults within non-marine carbonates?	159
6.2.1	Faulting within laminated limestones	160

6.2.2	Dilational faulting within travertines	160
6.2.3	Fault- and fracture-related karst systems within travertine	162
6.2.4	Comparison of field observations and mechanical failure	163
6.3	What is the impact of deformation within non-marine carbonates on fluid flow in the subsurface?	165
6.3.1	Small-scale faults within laminated limestones	165
6.3.2	Dilation vs compaction in travertine	167
6.4	Can host rock characteristics be used to predict the style of deformation and permeability in space and time within non-marine carbonates?	168
6.4.1	Combined depositional and deformation models for non-marine carbonates	168
6.4.2	Implications for reservoir characterisation in South Atlantic Pre-Salt basins	172
6.4.3	Crato Formation as a pre-salt reservoir analogue	173
6.4.4	Travertines as a pre-salt reservoir analogue	173
6.4.5	Faults within sag stage sequences	179
7.	Conclusions and Further Work	181
7.1	Aims and objective.....	181
7.2	Key findings	181
7.2.1	Structural characteristics of faults within non-marine carbonates.....	181
7.2.2	Impact of deformation in non-marine carbonate on permeability.....	182
7.2.3	Using host rock characteristics to predict deformation style and permeability within non-marine carbonates	183
7.3	Future work	183
	Appendix 1: Crato Formation core plug data.....	207
	Appendix 2: Travertine core plug petrophysical data	208
	Appendix 3: P-Q Critical stresses	212
	Appendix 3: Stress-strain curves	215

Table of tables

Table 2-1. Principle categories of benthic microbial carbonate deposits (adapted from Riding, 2012).....	9
Table 4-1. Non-marine carbonate formations studied in this thesis with latitude and longitude coordinates.	58
Table 4-2. Information of different non-marine carbonates investigated in this study.	59
Table 4-3. Porosity and permeability results from the small-scale faults within the Nova Olinda Member, Araripe Basin, Brazil.	76
Table 4-4. Overview of different structural features observed in visited non-marine carbonate outcrops for this study. Ages and depositional and tectonic settings detailed in Table 4-2.	104
Table 5-1. Overview of travertine facies found within tested travertine cores.	120
Table 5-2. Description of facies identified in Figure 5-4 with associated pore type and typical abundance.	125
Table 5-3. Summary of distribution properties for porosity measurements of samples from Italy and Turkey used in poro-perm anisotropy analyses.	128
Table 5-4. R ² values for linear and logarithmic regression lines for Peloidal Micrite and Shrub facies samples at different core-plug angles. Data in raft facies is omitted due to a limited number of samples for best fit curves.	129
Table 5-5. Overview of travertine samples tested under triaxial conditions. Φ : porosity pre-deformation (%); k: Permeability pre-deformation; C ₀ : cohesion (MPa); μ : internal friction coefficient; C [*] : transition from compaction to dilation during triaxial test; SEC: Localised shear enhanced compaction; LC: Localised compaction; BD: Brittle deformation.	131
Table 5-6. Overview of modelled macro-porosity volumes of RT8 (Rapalano Terme, Italy).	143

Table of figures

Figure 2-1. Triangular diagram showing the three processes governing microbial carbonate formation (from Riding, 2021).	8
Figure 2-2. Lacustrine carbonate facies model of the Green River Formation, Utah. (From Sarg et al., 2013)	9
Figure 2-3. Summary of travertine morphologies. Formation models adapted and compiled from Pentecost & Viles (1994), Guo & Riding (1998), Pedley (2009) and Chafetz & Folk (1984).	12
Figure 2-4. A process-cantered framework for understanding non-marine carbonate early diagenesis by De Boever et al. (2017). Corners of the triangle represent groups of processes with illustrating examples and the length axis of the prism represents time. Arrows illustrate the evolving environmental context, including climate, dominant fluids and the presence and degradation of organic matter (De Boever et al., 2017).....	14
Figure 2-5. Schematic diagram illustrating the difference between a juxtaposition and fault rock type seal (after Yielding et al., 2010).	15
Figure 2-6. Schematic illustration of fault permeability structures (Modified from Caine et al., 1996).....	17
Figure 2-7. Stress-strain curves related to different deformation modes at low temperatures (edited from Wang et al., 2020). B) Simplified yield curve of a rock where low pressures are associated with localised dilatant behaviour and high-pressure side is associated with distributed compaction. The critical state point defines the transition between dilation to compaction (edited from Bedford et al., 2018). P^* is the hydrostatic yield point and marks the onset of grain crushing and pore collapse. C) Generally, yield curve envelopes are found to decrease in size with increasing porosity (edited from Bedford et al., 2018.....	19
Figure 2-8. Pore collapse pressures for carbonate rocks and tuffs presented by Baud et al. (2012).	20
Figure 2-9. Two conceptual models of failure micromechanisms (from Vajdova et al., 2004). A) Conceptual model of plastic pore collapse modelled from Curran & Carrol (1979). Dark grey zone represents the initiation of plastic deformation while the remaining volume (light-grey) experiences elastic deformation. B) Wing crack model Dilatancy and brittle faulting.....	21
Figure 2-10. Carbonate velocity-porosity data (measured at 8 MPa effective pressure) defined by pore type (from Eberli et al., 2003)	22

Figure 2-11. Schematic models illustrating fault core (FC) and damage zone (DZ) definitions. Models modified from Billi et al. (2003); Solum and Huisman (2017) and Mitchel and Faulkner (2009).	24
Figure 2-12. Graph from Micarelli et al. (2006) illustrating the relationship of damage zone width with displacement in high-porosity carbonate hosted faults in the Hyblean Plateau, Sicily.	26
Figure 2-13. Comparison of fault classification schemes from A) Sibson (1977), B) Killick (2003), C) & D) Woodcock & Mort (2008). Portions of classification scheme of interest to this study (for brittle faulting in the upper crust) are highlighted in blue.	28
Figure 2-14. Graph of porosity and permeability of calcite and dolomite host rocks and their respective fault rocks (from Michie et al., 2020).	30
Figure 2-15. Poro-perm plots from Michie et al. (2020) comparing host rock and fault rock data for high porosity (> 10%) carbonates. Data illustrates general trend of decreasing porosity and permeability of fault rocks compared to their host rocks.....	34
Figure 2-16. A) Outcrop examples of a dilation fault zone within a carbonate from the Jebel Hafeet region (U.A.E.) Ca: Carbonate; Cl: Clayey carbonate; b: fault cavities with inclusion of Cl material; c: empty fault zone cavity. B) Example of opening mode fracture with layered clastic infill with different zones labelled. Zone A: Wall rock; Zone B: Rim of precipitated calcite; Zone C: centre of fracture filled with stratified sediments. C and D) Large fissures with rotated wall rock blocks. From Gent et al. (2010).	35
Figure 2-17. Summary figure of work from Van Noten et al. (2019). A) illustrates location of the Turkish Ballik travertine with B) illustrating location of quarry outcrops and mapped faults. C) Example of faulting in area with D) figure of slickenlines from hangingwall of the fault and E) evidence of multiple phases of faulting shown by different generations of fault breccia and travertine mineralisation. F) Example of larger displacement fault. G) Example of complex fault with several deformation and infill phases.	36
Figure 2-18. Staircase fracture within laminated travertine (Acquasanta Terme, Italy) illustrating ramp and lamination parallel fracture segments (from Maggi et al. 2015).	38
Figure 2-19. A-C) CT images with interpretation of the fault core and damage zone of experimentally sheared travertine from Giwelli et al. (2016a). D) Graph illustrating relationship between dynamic transmissibility and shear displacement (Giwelli et al., 2016a).	39
Figure 2-20. Permeability relationship with mean effective stress during triaxial testing on a) damage zone analogue samples and b) fault core analogue samples (from Delle Piane et al., 2016).....	40
Figure 3-1. Workflow of methods used within this study.....	42
Figure 3-2. Schematic of orientated core plugs and thin sections taken from samples collected. A) Orientated cores taken from undeformed travertine blocks. B) Example of core plug	

orientations taken from faulted laminated limestone samples. Small blocks for thin sections were taken across faults in plan view and x-section.44

Figure 3-3. Schematic of steady state probe permeameter (API, 1998). B) Probe permeameter set up to take permeability measurements along transects of a travertine slab. C) Example of probe placement on measured samples.47

Figure 3-4. Example of Klinkenberg plot from measured permeability data.48

Figure 3-5. Triaxial test set up for measurement of 1.5-inch samples (From Kaminskaite, 2019) A) Overall rig set up. B) schematic of Hoek-type cell used. Platens were adapted to included ultrasonic transmitters and receivers (from McPhee et al., 2015).49

Figure 3-6. MTS triaxial test equipment set up used for 1-inch samples. A) Loaded sample set up of MTS rig. B) Confining pressure system to load and drain MTS triaxial cell with oil. C) Inner triaxial cell.53

Figure 4-1. Overview of microbial carbonate localities investigated in this study.57

Figure 4-2. Non-marine carbonate examples. A) Bioherm, Hot Springs Formation, Idaho (USA). B) Caddisfly microbial mound, Green River Formation, Wyoming (USA). C) Stromatolite, Green River Formation, Utah (USA). D) Cyanobacterial carbonate mounds, Perachora Peninsula, Greece. E) Saturnia Hot Springs, Italy. F) Saturnia travertine hot springs, Italy. G-H) San Giovanni Fissure Ridge, Italy.62

Figure 4-3. A) Regional Geology of the Araripe Basin, Brazil. B) Local Geology of Nova Olinda. Quarry locations indicate laminated limestone exposures. C) Lithostratigraphy of the Araripe Basin. (Modified after Catto et al., 2016)70

Figure 4-4. Field example and corresponding schematics of small-scale faulting in the Nova Olinda member from the Crato Formation.73

Figure 4-5. A/B) Hand specimen and schematic of faulted laminated carbonates from the Crato Formation. C) SEM image of faulted segment. D-E) Photomicrographs of fault planes taken from specimen.74

Figure 4-6. A/B) Hand specimen and schematic of faulted segment from the laminated carbonates of the Crato Formation. C-K) SEM and photomicrographs of faulted segments.75

Figure 4-7. A) Graph illustrating permeability reductions between the host rock and across small scale faulting within the Nova Olinda Member (Araripe Basin, Brazil). C) Plot of porosity and permeability of all samples from the Nova Olinda Member.77

Figure 4-8. Regional geology of the Tivoli travertines, Italy and Ballık travertines, Turkey (edited from Faccenna et al. (2008)). A) Regional Geology of the Acque Albule Basin. B) Tivoli travertine quarried outcrops (edited from Billi et al. 2016). C) Regional geology of the Denizli Horst Graben System (DGHS). (edited from Özkul et al. (2013)). Location of DGHS (study

area) marked on inset of Turkey. D) Quarried outcrops of the Ballık travertine body with studies locations indicated (edited from Van Noten et al. (2019))......78

Figure 4-9. Karst features observed in Italian Travertines. A) Example of cavern in a travertine block, Acquasanta Terme. B) Karst cavity, Poggi Quarry, Tivoli. C) Karst collapse feature (Poggi Quarry, Tivoli). D/E) Karst with grey clastic sediment infill and localised cavities (Poggi Quarry, Tivoli). F) Narrow karst collapse feature (Poggi Quarry, Tivoli).81

Figure 4-10. Karst features observed in the Ballık travertines, Turkey. A) Elongated, bedding parallel karst cavity. B) Karst with clastic sediment infill and travertine blocks. C) Bedded sediment fill in a karst structure with inclusion of travertine host rock clasts. D) Complex karst structure with transitions between sediment infill, vugs and travertine breccia. E) Elongated karst structure with bedded clastic sediments cross-cut by fractures,82

Figure 4-11. Examples of stair-step mode 1 fractures in travertine. A) Complex, highly connected stair-step fractures in a strongly bedded travertine body related to karst collapse feature (Poggi Quarry, Italy). B) Stair-step fracture, (Kömürçuoğlu Quarry, Turkey). C) Mode 1 fractures in a massive travertine block with interbedded clastic sediment layer (Çakmaklar Quarry, Turkey).85

Figure 4-12. Mode 1 fracture with sediment infill in the Ballık travertines (Kömürçuoğlu Quarry, Turkey). A) N dipping fracture filled with conglomerate and terrigenous sediment from overlying sequence. Infilled fracture is cut by near vertical S dipping fractures which cut through the whole sequence and remain unfilled. B) unfilled and conglomerate filled fracture. Filled fracture has heterogenous fracture walls (increases up to 1 m width at bottom of section) which has refractured along the left fracture boundary and propagates through the conglomerate layer.86

Figure 4-13. Examples of dilational fractures in the Ballık travertines (Kömürçuoğlu Quarry, Turkey). A) Fracture with poorly consolidated centre and locally preserved well cemented infill conglomerate along fracture walls. B) Close-up image of conglomerate infill in fracture from A. 3 different types of conglomerate can be observed: a light brown, matrix-supported conglomerate with travertine and light brown sedimentary clasts; a dark brown matrix-supported conglomerate with clasts of light brown fine-grained sedimentary rocks, calcite clasts and conglomerate clasts (these have relatively smaller clast sizes); and a conglomerate with variable texture (dominantly clast supported) which has a higher proportion of clasts. C) inset from B. White arrow shows black manganese alteration in clasts consisting of calcite. Yellow arrow highlights clasts coated by calcite. D) Dilational fracture with open central cavity with heterogeneous conglomerate infill locally preserved on fracture walls. E) Conglomerate infill from fracture illustrated in D. Distinct sub-horizontal layers of conglomerates and fine-grained light to dark brown terrigenous sediments can be seen. F) Hand specimen taken from fracture in D composed of a travertine clast bounding a brown matrix supported conglomerate infill material. White arrow illustrates example of mm-scale calcite veins that commonly cross-cut secondary fracture infill.87

Figure 4-14. Dilation fracture observed in the Ballık travertine (Kömürçuoğlu Quarry, Turkey). A) Lower portion of fracture characterised by open cavities with collapsed travertine infill.

Fracture walls preserve fracture parallel calcite veins, travertine layers and light brown fine grained sedimentary fracture infill material. B) Inset from A illustrating irregular, relatively smooth edge of fracture wall and interfingering of fine grained light brown sediment, possible inferring widening of the fracture width by dissolution. C) Focus of fracture wall from A illustrating vertical to sub horizontal mm-cm layers of calcite, fine-grained terrigenous sediments, and conglomerates. D) Close up of black travertine shrubs (Mn or Fe rich) along fracture wall which are coated with a 2cm vein of banded calcite. E) Hand specimen taken from fracture composed of a fine-grained matrix supported conglomerate. Matrix is especially prone to Mn or Fe alteration. F) Hand specimen of fracture wall showing Mn/Fe rich black travertine shrubs surrounded by calcite. mm-scale undulose layers of dark brown/black fine-grained sediments interbedded with fine-grained light brown sediments is observed parallel to the calcite vein.88

Figure 4-15. Map of Kömürçuoğlu Quarry, Turkey with fault observed normal faults mapped and plotted onto the inset stereonet.90

Figure 4-16. Small scale (<0.5 m apparent throw) dip-slip faulting observed in Turkey. A) Near vertical apparent reverse fault observed in Çakmaklar quarry. B) ~ 20 cm throw dilational normal fault observed in the Kömürçuoğlu Quarry, Turkey. C) Normal faulting in travertine interbedded with conglomerate layer (Kömürçuoğlu Quarry, Turkey).94

Figure 4-17. Dilational normal fault observed in the Kömürçuoğlu Quarry, Turkey. A) Overview of fault illustrating heterogeneous fault wall geometries and changing dip. Inner portion of fault is infilled with loose friable material composed of travertine clasts and clay rich sediment. B) Fault parallel layers of well cemented conglomerates with varying textures and matrix and clast composition locally preserved along fault walls. C) Detailed image of fault parallel bands of conglomerates with thin layers of calcite between some different conglomerates. D) Hand specimen from conglomerate bands (location in B) shows distinct bands of conglomerates and calcite veins. Manganese alteration of the calcite matrix and fine-grained sedimentary clasts is pervasive. E-F) Hand specimen taken from fault wall illustrating fault parallel banded undulose calcite vein. Millimetre layer of dark manganese rich layer formed either through alteration of calcite layer or deposited as a microbially induced crust.95

Figure 4-18. Dilational normal faults observed in the Kömürçuoğlu Quarry (Turkey) with throws between 1-3 m. A) Dilational normal fault with heterogeneous fault core thickness composed of unconsolidated, friable material. B) Normal fault with partially cemented fault core. C) Dilational normal fault with a poorly consolidated fault core composed of large travertine clasts and brown, clay rich mud.96

Figure 4-19. Large scale (>6 m displacement) normal fault observed in the Kömürçuoğlu Quarry, Turkey. A) Fault core is composed of poorly consolidated, friable material with large (up to 4 m) travertine host rock clasts in a brown oxidised mud matrix. B) Cemented calcite mineralisation and original 'breccia' along fault wall locally preserved. C) Mud rich cemented breccia locally observed in placed along the fault wall.99

Figure 4-20. WNW-SES trending strike slip fault observed in the Ballık travertine body (Braşaranlar Quarry, Turkey). A) Satellite view of the Braşaranlar quarry with fault outcrop

locations marked by red fault line. B) Slicken lines observed on primary slip plane of fault. C) Overview of eastern fault outcrop location illustrating undulose fault plane. D) Overview of second fault outcrop location illustrating multiple fault segments (detailed in Figure 4-22). 100

Figure 4-21. Detailed pictures of the strike slip fault observed in Braşaranlar Quarry from Figure 4-20. A) Photograph of west/east? segment from fault. B) Heterogeneous fault core of the strike slip fault with multiple segments. C) Heavily fractured fault parallel travertine and black Fe and Mn rich crusts. D) Detail of fault parallel travertine layers and chaotic poorly cemented material within fault core. D) Example of fault parallel travertine deposition bounding the fault core. 101

Figure 4-22. Relationship between fault throw and fault core thickness of the faults observed in Kömürçuoğlu Quarry (field measurements from the study) and the surrounding Ballık travertine body (from literature), Turkey. Data from literature is taken from Van Noten et al. (2019) and Özkul et al. (2013). 103

Figure 4-23. Diagram showing possible dilational fault evolution observed in the Ballık Travertines (Turkey). Stage 2 illustrates initial hybrid failure of the travertine, where interbeds of mechanically weaker units such as palaeosols result in changes in fault geometry. Stage 3 illustrates the widening of the fault and formation of a connected karst system through dissolution. Travertine deposition or calcite mineralisation may be deposited onto the fault walls. Stage 4 shows filling of the fault void by terrigenous material sourced from overlying strata and brecciated segments of wall rock. Stage 5 and 6 illustrates the reactivation of the fault through hybrid faulting resulting in new generation of fault infill. 111

Figure 4-24. Influence of dilational faulting on permeability anisotropy within travertines. A) Dilational faults act as conduits for fluid flow and provide a preferential vertical pathway for fluids as vertical permeability across travertine laminations is much lower than permeability parallel to travertine beds. B) Travertine deposition and calcite mineralisation is common along the fault walls of these faults. Continuous fault parallel travertine will result in a lateral permeability reduction in the fault core. The presence of vertical layers of travertine or additional mineralisation and veins may result in a reduced re-distribution of fluids from the inner fissure acting as a conduit to the surrounding fault rock. C) illustrates a fault where the central fissure is composed of infilled conglomeritic sediment. The permeability within the central part of the fault zone is controlled by the composition and diagenesis of the infill and may represent a permeability decrease compared to the host rock where sediments are clay rich and have undergone significant diagenesis. However, high porosity vertical layers of travertine can act as fluid pathways depending on the continuity D) illustrates a the most common type of dilational faults observed where the preservation of the older deposition within the fault fissure are locally preserved and so the sediment infill of the fault controls the overall hydraulic system along the fault. The central part of the fault is often also composed of different types of conglomerate infill providing further local permeability heterogeneity within the fault zone. 115

Figure 5-1. Studied travertine locations for mechanical analysis. 119

Figure 5-2. Hand specimen and photomicrograph examples of facies found within tested travertine samples. A-B) Clotted peloidal micrite/sparite facies from the Tivoli travertine body. B) illustrates peloidal micrite spheres surrounded by microsparite cement. C-D) Laminated micrite/microsparite with lens shaped porosity. D) illustrates prismatic sparite crystals coating laminations. E-F) Shrubs facies. E) shows layers of dendritic shrubs with alternating layers of shrub density. F) illustrates clotted peloidal dendritic micrite within a sparite cement. H-I) Coated bubble facies. I) illustrates spherical to semi-spherical bubble framework formed of clotted peloidal micrite. Micritic bubble framework is coated with equant to prismatic sparite. 121

Figure 5-3. A) Porosity distribution of travertine core plugs with percentages of each fraction labelled. B) Core plug examples from low porosity peloidal micrite to high porosity laminated micrite/microsparite with coated bubbles. 124

Figure 5-4. A) Travertine block composed of layers of Dendritic crusts (F1), micritic dendrite shrubs (F2), clotted peloidal micrite/microsparite (F3) and Coated bubbles (F4). Red arrow highlights shrub facies illustrated in photomicrograph E. White arrow highlights coated bubbles illustrated in photomicrograph C. B) Probe permeability results along three vertical transects. Each circle represents a Klinkenberg corrected measurement. D) Photomicrograph illustrating partially collapsed coated bubbles from A. D-E Photomicrographs showing clotted peloidal dendritic texture of shrub layers. 126

Figure 5-5. A-B) Permeability distribution of measured travertine core plugs. A) Permeability distribution categorised based on core orientation. B) Permeability distribution categorised based on predominant facies of cores of all sample orientations. C-D) Relationship of permeability with porosity categorised by facies and core orientation. 127

Figure 5-6. Representative multi-stage triaxial test data measured in travertines at 10, 20 and 30 MPa confining pressure. A) and B) present data from shrub facies (samples RT8 H2, RT8 A1 and RT8 P1). A) Axial stress and strain of raft facies illustrate increasing yield points with decreasing angle of bedding. Shrub samples show variable extents of strain hardening. B) Mean stress and volumetric strain data from shrub facies illustrate variable volumetric responses during failure with associated critical stress states. C' indicates the onset of dilatancy defined by a decrease in volumetric strain; C* indicates onset of shear enhanced compaction marked by an increase in volumetric strain; and C*' marks transition from shear enhanced compaction to dilatancy marked by switch from increasing volumetric strain to a decrease in volumetric strain. C) and D) present the typical stress-strain response in laminated and peloidal micrite/microsparite (samples AT27H2 and AT27P2). C) Axial stress-strain data illustrate typical curves ending in brittle failure. D) Volumetric strain changes with mean stress illustrating volumetric strain decreases with critical stress C' points. (Note greyed out lines represent loading and unloading phases between triaxial stages). (Sample information: Table 5-2). 132

Figure 5-7. Cohesion (A), internal friction (B) and UCS (C) data for tested travertine samples with different bedding orientations. 133

Figure 5-8. UCS data (derived from triaxial mechanical testing against porosity), characterised by facies type. Dashed line represents the linear, best fit trend line for all data points demonstrating a very weak/absent, likely non-significant correlation. 134

Figure 5-9. Critical stress states (C' , C^* , C^{**}) presented in P-Q space (P: Mean stress; Q: differential stress) with best fit polynomial curves representing partial yield curves for each facies tested. A) Partial yield curves of laminated micrite/microsparite samples. Yield curves for samples both orientated vertical and perpendicular to bedding fall within the dilational regime. Yield curve for vertically bedded travertines show higher critical stresses than those in horizontally bedded samples. B) Partial yield curves of peloidal micrite/microsparite samples. Yield curves for samples both orientated vertical and perpendicular to bedding fall within the dilational regime. Yield curve for vertically bedded travertines show higher critical stresses than those in horizontally bedded samples. C) Critical stress data from shrub facies. Vertically bedded travertine illustrates higher critical stresses with a transition to compaction at the highest stresses observed. Critical stresses in horizontally and dipping travertine show a substantial spread in data with high uncertainty in best fit curves ($R_2 = 0.34$ for 45° orientated samples: $R_2 = 0.47$ for samples 90° to bedding). C^{**} critical stress states illustrate the expansion and change in yield envelope. D) Illustrates all best fit yield envelopes..... 137

Figure 5-10. V_p (compressional wave velocity) measured on dry travertine samples at 10 MPa confining pressure. Data is categorised by travertine facies. A) V_p versus porosity shows no correlation. B) V_p and UCS show a weak positive correlation with an R^2 of 0.43. C) V_p and Density show little correlation. 138

Figure 5-11. Velocity data measured during triaxial testing of travertine. Symbols signify individual samples tested. A) V_p evolution with increasing differential stress. B) V_p/V_s (ratio of V_p and V_s) changes with axial strain. C) V_p changes with increasing axial strain. D) V_s changes with increasing axial strain. 140

Figure 5-12. CT scan images from deformed travertine samples illustrating the different angles of fracture formation. A) Cores with long-axis orientated horizontal bedding often show open mode fractures parallel to bedding resulting in near horizontal fractures. B) Core with long axis orientated at 45° to bedding where fracture forms along bedding. C) CT scans of cores with long-axis orientated parallel to bedding. Fractures are commonly observed to have dips ranging from 60° to 70° 142

Figure 5-13. 3D macro-porosity volumes derived from CT scan data for three samples of different orientations to bedding (parallel, perpendicular and 45°) before and after triaxial testing. Colours demark isolated, internally connected pore volumes determined using Avio3D. A-C) 3D macro-porosity volume pre- (A) and post deformation (B) with 2D CT scan (C) of failure plane in sample parallel to bedding. D-F) 3D macro-porosity volume pre- (D) and post deformation (E) with 2D CT scan (F) of failure plane in sample 45° to bedding. G-I) 3D Macro-porosity volume pre- (A) and post deformation (B) with 2D CT scan (C) of failure plane in sample perpendicular to bedding. Colours of pore volumes illustrate different connected pore segments. 143

Figure 5-14. Photomicrographs of deformed samples. All images are orientated so that the maximum principal stress is vertical. Label abbreviations: PC: pore collapse; F: fracture; MC: microfracture; PEF: pore emanating fracture; LC: localised compaction; LSC: localised shear compaction; ESF: enechelon shear fracture; MT: mechanical twinning; GC: grain crushing. Photomicrographs A to F are from samples interpreted to deform in the brittle regime. A) Pore collapse feature with through going fracture across bedding. Fracture has an irregular geometry. Minor micro-fractures are also present. B) Brittle fractures at multiple orientations. Fractures cut through bedding with stepping geometry and locally follow bedding parallel pores. C) Pore collapse structures are common within large pores > 0.5 mm wide. Mechanical twinning is also observed within sparite cements. D) Pore emanating fractures. Both low angle and tensile fractures are present. E) low angle fractures in horizontally bedded samples. Stepping of fractures across laminations/beds is common in laminated micrite/microsparite facies). F) Tensile fractures. G) Enechelon geometry fractures within a shear band with localised compaction. H) Localised compaction defined by grain crushing and packing. Tensile and shear fractures cross-cut areas of localised compaction. I) Low angle stepping fracture in horizontally bedded shrub samples. Grain crushing and packing is observed locally at bends in the fracture. J) Shear compaction band formed of multiple compaction strains. K) Conjugate shear enhanced compaction bands. L) Shear enhanced compaction band which has been partially fractured. M) Pore collapse with pore emanating fracture. N) High angle shear enhanced compaction band overprinted by throughgoing fracture. Multiple fractures and shear enhanced strands are observed to splay from the primary failure plane. O) complex zone of localised compaction bands and cross cutting fractures. 148

Figure 5-15. Comparison of critical stress data from peloidal and laminated micrite travertine samples deformed in this study compared to published carbonate data. Data for additional carbonates: Indiana limestone and Tavel Limestone: Vajdova et al. (2014); Solnhofen Limestone: Baud et al. (2000a)..... 149

Figure 5-16. Summary of deformation styles observed in differently orientated travertine cores. 152

Figure 5-17. Comparison of microstructure within deformed travertine samples. A) Photomicrograph from this study illustrating enhanced shear compaction bands with localised dilation. B) Sample photograph and C) SEM image from Delle Piani et al., 2016 of experimentally sheared travertine. SEM image from A (red inset identifies location) illustrates grain size reduction and fracturing..... 156

Figure 6-1. Comparison of dilational structures observed in the Ballık travertines (Turkey) with scale model presented by Gent et al., 2010. A) 10 cm offset normal fault with widening of fault core and brecciation of travertine and conglomerate layer. Similar structure observed in scale structure indicated by arrow. B) Dilational fracture with terrigenous infill and travertine clasts which show similarities to scale model where tensile fracturing is common at the near surface. C) ~ 7 m throw dilational fault which formed at the surface of the travertine body. D) scale model formed of hemihydrate and a sand layer (dark band) with horizontal elongation of 7% (Gent et al., 2010). Model illustrates tensile and hybrid failure mode in the top 10 mm and shear failure modes in the lower half of the model. 162

Figure 6-2. Schematic yield curves for travertine facies studied based on mechanical observations. Three example stress paths are mapped in dashed, black lines. A stress path equivalent of very shallow faulting at the near surface illustrates deformation within all travertine facies and orientation will fail on left side of P-Q yield curve. Stress path at confining stress of ~ 30 MPa will result in a variety of deformation styles depending on the facies type. Stress path at high confining pressures (i.e., large burial depth) will result in compactive deformation of all facies depending on differential stress. Dashed yield curves illustrate the expansion of yield curves after shear enhanced compaction. 164

Figure 6-3. Plot of inverse permeability contrast (fault rock permeability divided by host rock permeability) for different carbonate faults from Michie et al. (2020). Measurements from laminated limestones (classified as mudstones using Dunham classification) from the Crato Formation have been added to this global data base and show a permeability reduction. Note that data are from faults < 0.2 m throw and are therefore not representative of larger scale structures. 166

Figure 6-4. Conceptual model and outcrop photographs from Della Porta et al. (2016) with possible deformation model from mechanical observations with broadly equivalent stresses to 1.2 km burial depth from this study. A) Slope Apron depositional model of the Acquisanta Terme (Italy) travertine slope apron. B) Outcrop from the Cardi Quarry (Acquisanta Terme, Italy) illustrating variation of travertine sequence. Unit 2 is dominated by shrubs, and coated bubble travertines. Kinematic indicators illustrate the preferential orientation for formation of compactive deformation of high porosity layers (adapted from Della Porta et al., 2016). C) Field exposure of smooth slope travertines (composed of laminated micrite/microsparite, crystalline dendrites, and radial coated grain grainstone) with possible brittle deformation styles..... 170

Figure 6-5. Comparison of non-marine reservoir carbonate examples with similar facies of carbonates studied within this project. A) Laminated limestones. Ai) Planar laminates from the Barra Velha Formation (BVF) (Santas Basin, SE Brazil) (from Terra et al., 2010). Aii) Laminated limestone from the Crato Formation (Araripe Basin, NE Brazil). Aiii) Photomicrograph of laminated limestone from BVF (from He et al., 2022). Aiv) Photomicrograph of laminated limestone from the Crato formation displaying similar slightly dentate laminations. B) Microbial boundstones: Bi) Microbial boundstone from the BVF with microbial peloids (from Pietzsch et al., 2020). Bii) Photomicrograph of clotted dense micrite from Tivoli Travertine body (Italy) illustrating similar micritic texture. C) Shrubs: Ci) Hand specimen of shrub textures found within the BVF (after Wright & Tosca, 2016). Cii) Shrub textures observed in pre-salt lacustrine carbonates within the Kwanza Basin (after Saller et al., 2016). Ciii) Example of typical travertine shrub facies from Tivoli travertine body (Italy). Civ) Photomicrograph of dendritic shrub growth within travertines (Tivoli, Italy). Cv) Photomicrograph of shrubby calcite growth with microcrystalline bands and dolomite between growths (after Saller et al., 2016). Vi) hand specimen of shrub interval layer in travertine from Rapolana Terme (Italy). Vii) and Viii) Photomicrographs of crystal shrub growth from BVF (after Hosa et al., 2020). Shrubs within the BFV are characterised by fibrous calcitic crystal aggregates. 174

Figure 6-6. Poroperm plot comparing shrub facies within travertines (this study) and pre-salt shrub facies from the Campos and Santos basins (Herlinger et al., 2017; Basso et al., 2021).
 176

Figure 6-7. Comparison of porosity networks between crystal shrubs from the Berra Velha Formation (Santos Basin, offshore Brazil) and micritic shrubs in travertine (Rapalano Terme, Italy). A) CT volume of crystal shrubs from BVF with segmented pore model illustrating growth framework pores separated by low porosity layers. B) Low resolution CT scan images from shrub travertine facies with modelled macro pore network. High inter-dendrite porosity form large connected networks separated by low-porosity layers. C) model adapted from Basso et al. (2021) illustrating different in shrub morphologies between travertines and those found within pre-salt reservoirs. 178

Figure 6-8. Fracture examples in static and dynamic normalised acoustic borehole image logs from Berra Velha Formation (pre-salt lacustrine carbonates in the Santos Basin, SE Brazil) (after Wennberg et al., 2021). A) High amplitude (bright) fracture which could be deformation bands or veins. B) Low amplitude vuggy fractures. C) Minor fault with observed offset. D) Fault with un-known offset. 180

Chapter 1

1. Introduction

1.1 Project rationale

Faults and fractures have long been recognised as a controlling factor in the hydraulic system of rock formations which has implications for a range of industries including oil and gas production, nuclear waste disposal, CO₂ storage and geothermal energy. As such, significant research has been conducted to understand the conditions in which faults act as barriers, conduits or partial barriers to fluid flow (e.g., Yielding et al., 2010). However, this existing research has largely contributed to predicting and modelling the sealing behaviour of fault within siliciclastic rocks where established predictive tools (e.g. shale gauge ratio; Fisher & Knipe 1998) are widely used within the energy industry. Conversely, despite significant research characterising carbonate faults carried out in the past 10 years (e.g. Tondi et al., 2006; Billi, 2010; Molli et al., 2010; Rath et al., 2011; Michie, 2015; Haines et al., 2016; Delle Piane et al., 2017; Cooke et al., 2018, 2019; Ferraro et al., 2019; Kaminskaite et al., 2020; Michie et al., 2014, 2020, 2021), the complexity and heterogeneity associated with carbonates means that there are no current empirical relationships which can be used as a predictive tool in fault zone characterisation within carbonate fault rocks. As carbonate reservoirs are estimated to form 60% of the world's oil and 40% the worlds gas reserves (Burchette, 2012), greater understanding of the controls and impacts of faulting within carbonates is needed.

Particular interest in this research project is given to non-marine carbonate rocks, which include a range of complex highly heterogeneous lithologies including microbial and hydrothermal carbonates. Interest in these deposits has increased substantially since the discovery of extensive Early Cretaceous, non-marine carbonate, hydrocarbon reservoirs in the pre-salt stratigraphy of the South Atlantic rifted margins in 2006 (Bohacs et al., 2013; Bosence et al., 2015; Gallois et al., 2015; Ronchi & Cruciani, 2015; Wright & Rodriguez, 2018; Lima & De Ros, 2019; Gomes et al., 2020). Similar deposits are also potential reservoir intervals for shallow, low temperature geothermal opportunities (e.g., Aquasanta Terme, Italy – Madonna et al., 2005) as well as providing valuable stratigraphic archives of hydrology and palaeoclimate (Anzalone et al., 2007; Portman et al., 2005). However, the focus of existing

work relating to non-marine carbonates has largely focused on depositional processes (e.g., Chafetz & Folk 1984; Burne & Moore, 1987; Altunel & Hancock, 1996; Heimhofer et al., 2010; Wright, 2012; Capezzuoli et al., 2014; Catto et al., 2016; Della Porta et al., 2016), geobody architecture (e.g. Claes et al., 2015; Chafetz et al., 2018; HENCHIRI et al., 2017; Mancini et al., 2019) and petrophysical host rock characterisation (e.g. Osmond, 2000; Bohacs et al., 2013; Claes et al., 2017; da Rocha et al., 2019; Hosa et al., 2020; Basso et al., 2021 Rodríguez-Berriguete et al., 2022). As a result, the research presented in this thesis aims to document and assess fault zone characteristics within non-marine carbonates while working towards understanding the key controls on deformation mechanisms in these rocks.

1.2 Aims and objectives

The main aim of the research presented in this thesis is to provide a greater understanding of the key controls of fault formation within non-marine carbonates to assess the behaviour and implications of faulting and deformation on fluid flow in the sub surface. This aim is approached through the following three research questions:

1. What are the structural characteristics of faults and associated deformation structures within non-marine carbonates?

The substantial focus on depositional processes and architectures in non-marine carbonates (e.g., Wright, 2012) has not been matched with characterisation of their deformation structures. Despite the common association of faults with non-marine carbonates, either as providing accommodation for lacustrine deposition (Wright, 2012; Della Porta, 2015) or being important hydraulic conduits for carbonate-rich fluids responsible for their deposition (Altunel & Hancock, 1996; Hancock et al., 1999; Özkul et al., 2002; Brogi, 2004; Croci et al., 2016), relatively few studies have provided well-documented examples of deformation within non-marine carbonates (cf. Giwelli et al., 2016a,b; Delle Piane et al., 2016). As a result, characterisation of deformation within carbonate rocks has largely been focussed on marine platform carbonates (e.g., Bonson et al., 2007; Michie et al., 2014) which can differ substantially in their lithological (Burne & Moore, 1987; Riding, 2000; Della Porta, 2015), petrophysical (Mancini et al., 2004; Chidsey et al., 2015; Li et al., 2021; Basso et al., 2021), and mechanical properties (Soete et al., 2015; Giwelli et al., 2016a,b; Delle Piane et al., 2016; Rodríguez-Berriguete, 2020; De Boever et al., 2022) from non-marine carbonates. This thesis will investigate the structural characteristics of deformation within non-marine carbonates through the following objectives:

- i) A literature desk-study documenting known non-marine carbonate exposures and their tectonic setting to document likely deformed non-marine carbonates (*Chapters 3 and 4*).
- ii) Characterisation of exposed deformation structures within non-marine carbonate exposures identified through the literature desk study, at outcrop and microstructural scales (*Chapter 4*).
- iii) Geomechanical experiments (triaxial testing) of undeformed non-marine carbonate host rock to examine and quantify deformation mechanisms and mechanical properties for different, key non-marine facies types (*Chapter 5*).

2. What is the impact of deformation within non-marine carbonates on fluid flow in the subsurface?

The scarcity of deformed outcrop and experimental studies on deformation within non-marine carbonates means the relationship between deformed, and host-rock properties on the hydraulic network within non-marine carbonates has remained largely unexplored and hypothetical (Giwelli et al., 2016a,b; Delle Piane et al., 2016). This has generated a lack of data on a) the contrast of porosity and permeability between intact and deformed non-marine carbonates; b) the character of porosity and permeability within deformed and non-deformed non-marine carbonates; c) the timing of permeability-enhancing, and permeability-mitigating deformation within a typical burial history for non-marine carbonates. This thesis aims to provide quantitative data and qualitative observations to begin addressing this gap through the following objectives:

- i) Characterisation of exposed deformation structures with key indicators of palaeo-fluid flow events such as diagenetic alteration and cement precipitation (*Chapter 4*).
- ii) Petrophysical testing on deformed and undeformed outcrop samples, and lab-deformed samples from non-marine carbonates studied in the field (*Chapter 4 and Chapter 5*).
- iii) Geomechanical testing and quantification of deformation within lab-deformed samples under different confining pressures to characterise the timing of dilational and compactive deformation (*Chapter 5*).
- iv) Semi-quantitative characterisation of pre- and post-deformation pore networks using CT scanning (*Chapter 5*).

- v) Comparison between documented marine and non-marine carbonate deformation structures and mechanical properties (*Chapter 5, 6*).

3. Can non-marine carbonate host-rock characteristics be used to predict petrophysical characteristics of faults in space and time?

Well established relationships between host-rock and fault-rock lithological and mechanical properties (e.g., clay content, brittleness) exist for characterising faults within siliciclastic rocks (e.g., Fisher & Knipe, 1998). Within carbonates, establishing these relationships has been challenging but detailed characterisation of platform carbonate fault rocks indicate that variations of strength controlled by grain- versus micrite dominance of host-rock facies may govern the resultant fault zone architecture and likely petrophysical character (e.g., Michie et al., 2014). Recent studies (e.g., Cooke et al., 2019) document that the resultant host-rock porosity of certain carbonate facies may demonstrate relationships with fault permeability, but that this may be strongly stress dependent. Within non-marine carbonates however, the initial variability of host-rock facies is considerably different and is more strongly controlled by variations in mineral precipitation and microbial activity (e.g., Wright, 2012) than environmental controls on the proportion of bio-clast dominated deposition (e.g., Reijmer, 2021). This may be further complicated by relationships with active structures and remineralisation during and after deformation and deposition (e.g., Altunel & Hancock et al., 1996). This thesis aims to investigate the potential for empirical relationships between host-rock characteristics and the petrophysical character of faults within non-marine carbonates through the following objectives:

- i) Collection of host- and fault-rock porosity and permeability data from exposed non-marine carbonates to demonstrate the presence or absence of relationships with depositional facies (*Chapter 4, 5*)
- ii) Combine geomechanical and petrophysical characterisation to derive potential relationships between geomechanical properties and depositional fabrics (*Chapter 5*)
- iii) Comparison with documented empirical relationships for fault vs host rock permeability in other carbonates (*Chapter 4, 5, 6*).

1.3 Thesis outline

This thesis has been divided into 7 chapters which present and analyse results from work carried out to address the previously outlined:

Chapter 2: The impact of faults on fluid flow in non-marine carbonates: a review

Chapter 2 describes the general properties and depositional models of non-marine carbonates including the complex role of diagenesis during early deposition. A review of the brittle-ductile transitional and associated deformation mechanisms is also presented, providing background for an overview of the characterisation of fault zones within carbonates. Lastly an overview of the current understanding of non-marine carbonate fault rocks is provided with a summary of the key knowledge gaps that have been recognised after a review of existing literature.

Chapter 3: Methodology

Chapter 3 presents the research workflow, methodologies and equipment used during this project and details individual methods used in Chapter 4 and 5.

Chapter 4: Characterisation of deformation features in non-marine carbonates from field observations

Chapter 4 first presents work from an extensive desk study and field investigation to investigate the presence of and characterise deformation structures within microbial and hydrothermal carbonates. A discussion of results provides an assessment of the impact observed deformation may have on fluid flow.

Chapter 5: Influence of rock fabric on the mechanical behaviour of travertine

Chapter 5 presents work from an integrated analysis of porosity-permeability measurements, mechanical triaxial test data, CT scan macro-porosity modelling and microstructural observations to provide an understanding of deformation mechanisms typical for travertine.

Chapter 6: Discussion

Chapter 6 discusses results present in Chapter 4 and 5 with the aim of understanding the variety of structural deformation observed over a range of burial conditions. The key controls on deformation within non-marine carbonates are also discussed and compared to existing

carbonate geomechanical, petrophysical and fault rock models. Lastly, the implications of results and the applicability to reservoir analogues are discussed.

Chapter 7: Summary

Chapter 7 provides a summary and presents the overall conclusions of this thesis along with suggestions for future work.

Chapter 2

2. The impact of faults on fluid flow in non-marine carbonates: a review

2.1 Microbial and hydrothermal carbonates

Carbonates are generally characterised by their heterogeneity and complex microstructures due to the range of depositional environments and intricate diagenetic processes (Delle Piane et al., 2017). This is especially true for non-marine carbonates which are found to host a range of complex, poorly understood lithologies (such as microbial shrubs and mounds) which can experience very early, almost instantaneous diagenesis (De Boever et al., 2022). For example, the deposition and characterisation of unusual crystalline shrub carbonates found within the pre-salt Barra Velha Formation in the Santos Basin (NE Brazil), which are considered to have the best reservoir properties within the pre-salt stratigraphy, have a disputed depositional model (Basso et al., 2021, 2022). Understanding host textures and heterogeneity is essential to assess how intrinsic rock properties can be modified by deformation. As microbial carbonates are not found to be adequately defined by classic carbonate rock classification systems (e.g. Folk, 1962; Dunham, 1962) the following review of non-marine carbonates provides descriptions of rock type definitions used within this study.

2.1.1 Non-marine carbonate host rocks

2.1.1.1 Microbial carbonate depositional systems

Burne & Moore (1987) first introduced the term microbialite, defining them as *“organosedimentary deposits that have accreted as a result of a benthic microbial community trapping and binding detrital sediment and/or forming the locus of mineral precipitation”*. It is agreed that there are three main processes (Figure 2-1) involved in microbialite formation; *“trapping and binding of detrital sediment; biologically influenced precipitation and inorganic precipitation”* (Bosence et al., 2015); although it should be noted that varying terminology is used to describe different microbial carbonate types. A combination of one or more of these

processes control the formation of different types of microbialites (Riding, 2012) described in Table 2-1.

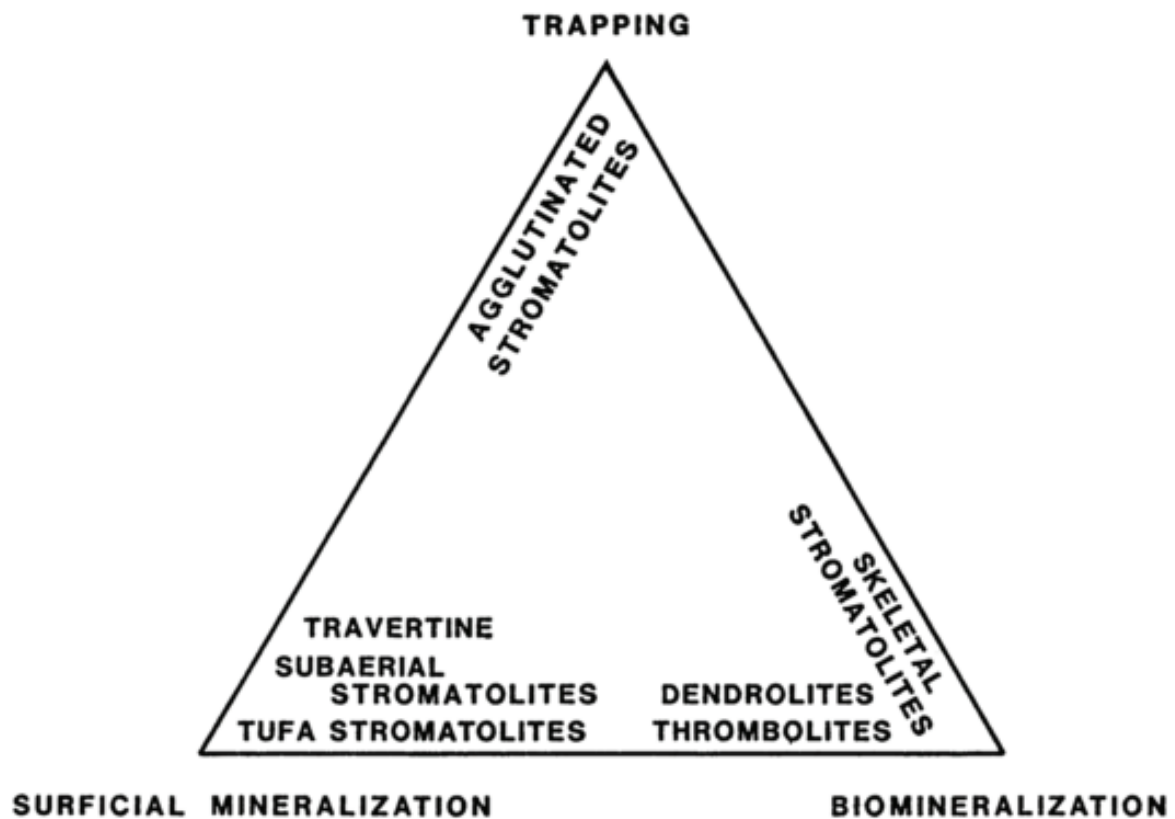


Figure 2-1. Triangular diagram showing the three processes governing microbial carbonate formation (from Riding, 2021).

Of specific interest to this study are microbial and hydrothermal carbonates formed in lacustrine environments. Within carbonate lake systems (Figure 2-2) small bioherms and stromatolites (Sarg et al., 2013) are associated with lake littoral facies and stromatolites/tufa bioherms are commonly associated with sublittoral facies (Platt & Wright, 1991). Such carbonates are promoted in an environment of calcium-rich waters, especially at outputs from springs or seeps, and where there is a reduced input of siliciclastic material (Gierlowski-Kordesch, 2009). They are found to form in a variety of tectonic environments where subsidence is greater than the rate sedimentation resulting in the establishment of stable lake basins (Platt and Wright, 1991).

Table 2-1. Principle categories of benthic microbial carbonate deposits (adapted from Riding, 2012).

Major Category	Variety	Formation
Stromatolite, laminated microbial deposit	Agglutinated stromatolite	Produced by trapping/binding of particulate sediment
	- Fine grained well laminated - Coarse grained crudely laminated	
	Tufa	Produced by precipitation of minerals on (rather than within) organic tissue
	Skeletal stromatolite	Produced by calcified in place organisms
	Subaerial stromatolite	Produced by mineralisation in a desiccating environment
Dendrolite		Macroscopically dendritic
Thrombolite		Macroscopically clotted
Travertine		Layered benthic microbial deposit with a dendritic microfabric
Cryptic microbial carbonate		Have micritic, clotted, peloidal or spiritic microfabrics but which lack distinctive macrofabrics

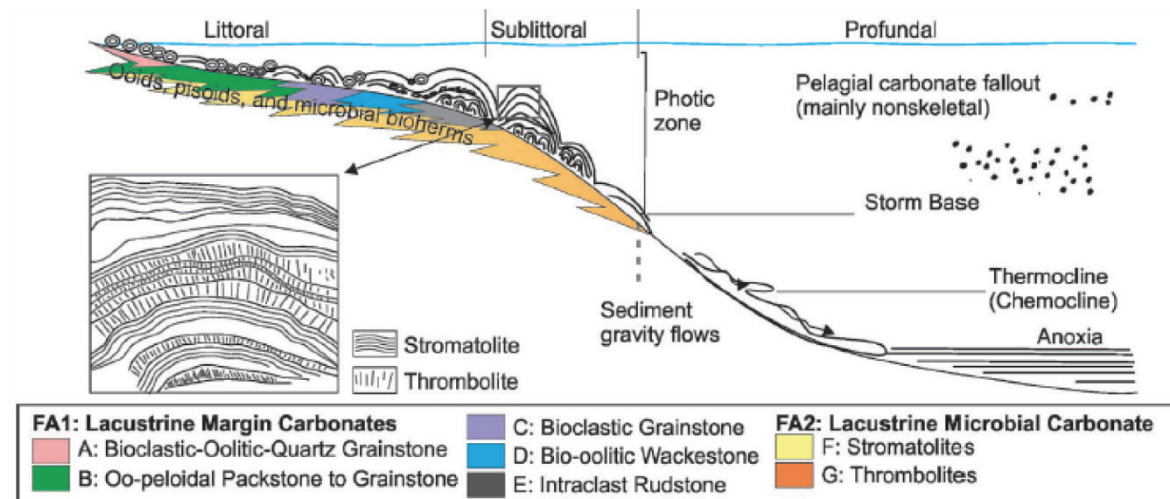


Figure 2-2. Lacustrine carbonate facies model of the Green River Formation, Utah. (From Sarg et al., 2013)

2.1.1.2 Travertine

The term travertine remains poorly defined within literature with some authors favouring its use for the description of deposits precipitated from Ca-rich hydrothermal fluids (Riding, 1991; Ford & Pedley, 1996; Pedley, 2009); while others use the term to describe both hydrothermal carbonates and cool water calcareous tufa (Chafetz & Folk 1984; Pentecost, 2005; Capezzuoli et al., 2014; Bosence et al., 2015; Maggi et al., 2015).

According to Pedley (2009), the term *travertine* should be used to describe continental carbonates formed from hot, supersaturated carbonate waters, resulting in laminated deposits with a dominantly inorganic crystalline fabric. Conversely, the term *tufa* should be used to describe continental carbonates that are poorly bedded, precipitated from waters at ambient temperature and are often characterised by abundant micro- and macro-biota. However, Capezzuoli et al. (2014) noted that the distinction between travertine and tufa using these lithological associations can be difficult, as thermal waters which have cooled distally from resurgence points will produce tufa-like facies.

An alternative definition of travertine is provided by Pentecost (2005) which, recognises two classes of travertine: thermogene (hot-water derived), where CO₂ results primarily from interaction of bedrock and CO₂-rich fluids, and meteogene (ambient temperature), where CO₂ originates from soils and epigeal atmospheres. This classification scheme, however, is difficult to apply to ancient deposits where detailed geochemical analysis is required (Pedley, 2009) suggesting that classification schemes based on water temperature and source are more useful only for modern deposits (Bosence et al., 2015). It can therefore be considered that travertines and calcareous tufa are end-members of a complex depositional spectrum dependant on tectonics, climate, geochemistry and biological activity (Golubić et al., 2008; Maggi et al., 2015).

Travertine morphology can be broadly classified into four groups (Figure 2-3):

1. **Depression depositional systems:** Largely horizontal travertine deposits (Guo & Riding, 1998) which are dominated by thinly bedded travertine that can form units several metres thick with a lateral extent of tens to hundreds of metres (Guo & Riding 1998; Pedley, 2009).
2. **Slope depositional system:** Include smooth, slope facies (Guo & Riding, 1998; Capazzuoli et al., 2014) and complex terrace deposits, both of which develop as lobate, plane-sheets away from thermal resurgence points (Ford & Pedley, 1996) and are

associated with localised cascades/waterfalls (Guo & Riding, 1998; Ford & Pedley, 1996). Travertine slope systems are controlled both by the underlying morphology and the deposition rate, where high deposition rates can rapidly bury and change the underlying morphology (Capezzuoli et al., 2014).

3. **Fissure ridge deposits:** Linear, elongated travertine mounds (De Filippis et al., 2012), characterised by a central fissure, generally filled by vertically laminated, banded travertine (Brogi et al., 2014). Ascending hot waters cause carbonate precipitation both within the fissure space (*banded* travertine) and on the flanks of the structures (*bedded* travertine) (De Filippis et al., 2012).
4. **Mound depositional systems:** Isolated thermal spring deposits such as towers, pinnacles and mounds which are generally point sourced with rapid deposition of travertine resulting in steep sided constructional morphologies (Capezzouli et al., 2014)

		MORPHOLOGY				FORMATION MODELS
		<i>Chafetz & Folk 1984</i>	<i>Pentecost & Viles 1994</i>	<i>Guo & Riding 1998</i>	<i>Pedley 2009</i>	
TRAVERTINE	Lake filled deposits	Fluvial Crusts Lucustrine Crusts	Shrub flat facies Marsh pool facies	Depression depositional system		
	Terraced mounds	Barrages	Terrace slope facies Smooth slope facies		Slope depositional system	
	Waterfall/Cascade deposits	Cascades	Waterfall facies			
	Fissure ridge	Fissure ridge	Fissure ridge	Fissure ridge		
	Sloping mounds, fans or cones	Spring mounds	Reed mound facies	Mound depositional system		

Figure 2-3. Summary of travertine morphologies. Formation models adapted and compiled from Pentecost & Viles (1994), Guo & Riding (1998), Pedley (2009) and Chafetz & Folk (1984).

2.1.1.3 Diagenesis of non-marine carbonates

Carbonate diagenesis is defined by Tucker and Bathurst (1990) as a group of physical, chemical and biological “*processes which affect carbonate sediments after deposition until the realms of incipient metamorphism of elevated temperatures and pressures*”. Diagenesis can have a significant impact on the chemical, mechanical and petrophysical properties of the carbonate rock mass (Armenteros, 2010, Flügel, 2010, Moore & Wade, 2013; De Boever et al., 2017, De Boever et al., 2022). These processes can also alter the depositional fabric, (micro)biological assemblage and geomechanical properties of a carbonate rock mass (Flügel 2010; De Boever et al., 2017). As such, diagenesis has significant implications for modelling reservoir properties of carbonates and carbonate fault rocks.

While carbonate diagenesis has been extensively documented and reviewed (Berner, 1980, Moore, 1989, Tucker & Wright, 1990, Tucker & Bathurst, 1990, Flügel, 2010, Moore & Wade, 2013), classification schemes of typical diagenetic processes have mainly been applied to marine settings where processes are linked to different diagenetic environments or the fluid type present (De Boever et al., 2022). However, these established approaches do not adequately depict the early stages of diagenesis within non-marine environments. Frisia et al. (2018) reviewed that the definition of early diagenesis by Berner (1980), where deposited sediments are subsequently “*exposed through time to an environment that has different physical and chemical characteristics with respect to the initial depositional setting*”, does not apply to non-marine carbonates such as microbialites, travertines and tufas. Instead, here, the formation and subsequent diagenesis usually occur in the same near-surface meteoric environment (Frisia et al., 2018). Within the near surface meteoric, vadose and phreatic zones (the setting of most non-marine carbonates) diagenetic processes have generally focused on the corrosive nature of fresh water and minor cementation of previously deposited and uplifted carbonate sediments (De Boever et al., 2017). This ignores the range of early diagenetic environments found in non-marine carbonates with varying fluid composition, temperature, and biology (De Boever et al., 2017) that can exhibit variable diagenetic effects (Armenteros, 2010). Recognising early diagenesis within these deposits is further complicated due to the difficulty in differentiating the primary from secondary features of non-marine carbonates (De Boever et al., 2022; Rodríguez-Berriguete, 2020). Ultimately, diagenesis in these environments can be considered contemporaneous to deposition and difficult to define the transition between primary deposition and start of diagenesis (Armenteros, 2010; De Boever et al., 2017), especially where some diagenetic processes in these settings can result in textures and microscopic fabrics that are considered primary in other settings (Frisia et al.,

2018). The complexity of different diagenetic processes in these environments has been summarised by De Boever et al. (2017) and proposes a process-centred framework to describe early diagenesis in non-marine carbonates (Figure 2-4).

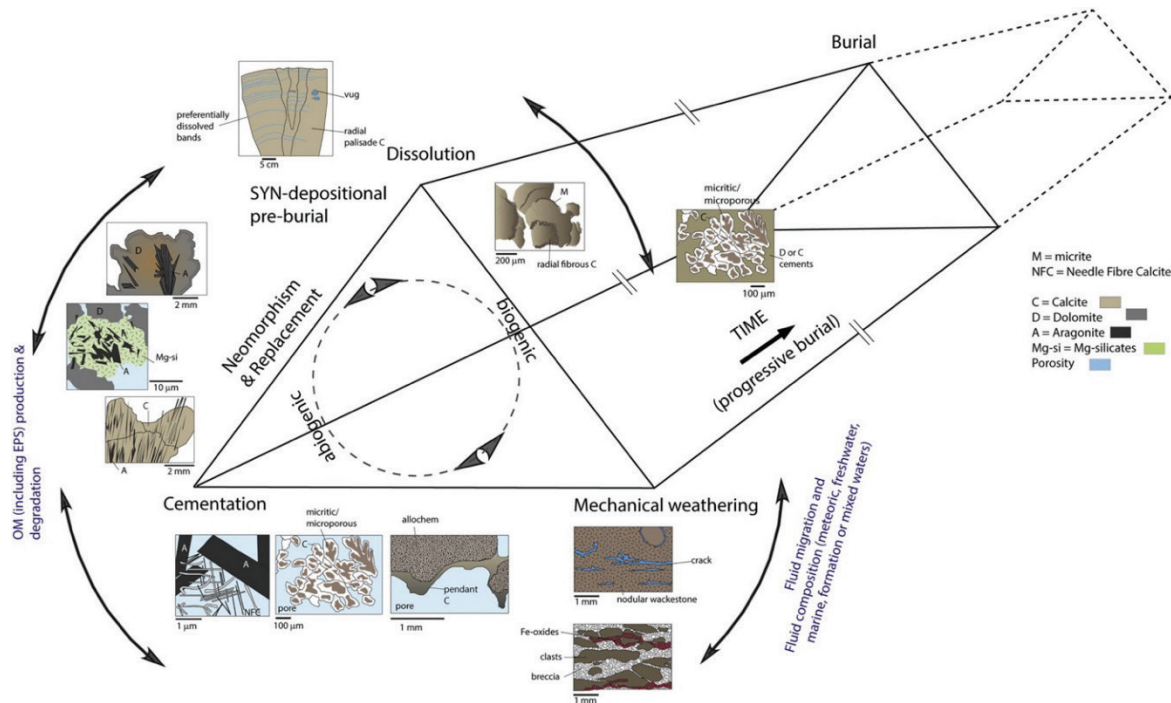


Figure 2-4. A process-centered framework for understanding non-marine carbonate early diagenesis by De Boever et al. (2017). Corners of the triangle represent groups of processes with illustrating examples and the length axis of the prism represents time. Arrows illustrate the evolving environmental context, including climate, dominant fluids and the presence and degradation of organic matter (De Boever et al., 2017).

Comparisons of recent and fossil spring deposits by Golubić et al. (2018) (Plitvice, Croatia and Rocchetta a Volturno, Italy) and De Boever et al. (2022) (Mammoth Hot Springs, Yellowstone, USA) illustrate that early diagenetic processes are generally constructive and result in an overall coarsening of the micro-fabric (with the exception of micritisation) and leads to homogenisation of complex and diverse primary microfabrics. These diagenetic processes can result in a reduced porosity compared to the primary porosity (De Boever et al. 2022) and can also significantly affect the pore geometry. The micro-fabric, porosity and pore structure are controlling factors of the elastic properties in carbonate sediments (Anselmetti & Eberli 1993, Eberli et al. 2003) and have therefore early diagenesis in non-marine carbonate has significant implications for mechanical properties of the rock (Török et al. 2010). For example, mechanical analysis of travertine, which is known for its rock strength and durability as a building stone, by Török et al. (2010) illustrates how travertines with relatively homogenous micro-fabric and lower porosity (2.4 – 5.6%) have a higher mechanical strength than less

homogenous laminated travertines with higher porosity (4.5 – 13%). Generally, the construction of self-supporting framework fabrics coupled with constructive early diagenesis processes results in very stable rock fabrics with high elastic properties during (Anselmetti & Eberli, 1993) very early stages of deposition.

2.2 Carbonate hosted faults

Faults can act as either barriers or conduits, or in some cases can be a combined barrier/conduit to fluid flow and the prediction of fault sealing behaviour is crucially important for modelling carbon capture and storage (CCS) and hydrocarbon traps (Fisher & Knipe, 1998; Jolley et al., 2010). For the petroleum industry in particular, capturing the complexity and heterogeneous nature of faults is essential for identifying structural traps, predicting hydrocarbon column heights (i.e., the height of hydrocarbons that can be supported by the fault) and the degree of reservoir compartmentalisation (Knipe et al., 1997; Jolley et al., 2010).

It is recognised that there are two fundamental sealing mechanisms for faults (Figure 2-5):

1. **Juxtaposition seals:** Whereby faulting has caused juxtaposition of high permeability rocks (for example, a high porosity sandstone) against low permeability, 'sealing', lithologies such as shales or evaporites.
2. **Fault rock seals:** Deformation processes during fault displacement and the faults subsequent evolution can result in the fault zone itself acting as a baffle to fluid flow.

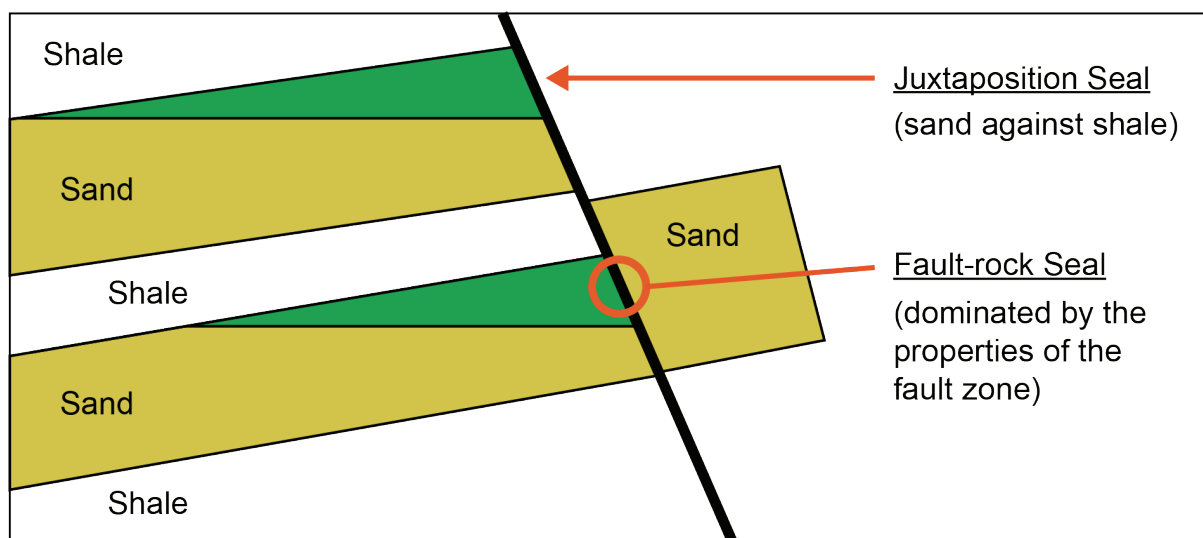


Figure 2-5. Schematic diagram illustrating the difference between a juxtaposition and fault rock type seal (after Yielding et al., 2010).

The fault seal type and the resulting seal effectiveness is dependent on a variety of factors, including fault throw, burial depth, host rock properties (porosity, pore size and type, permeability and lithology), and the trapped fluid type (it's buoyancy, viscosity and charge rate).

The sealing behaviour of faults within siliciclastic lithologies has been widely documented and discussed with robust predictive algorithms established (Knipe, 1992; Caine et al., 1996; Yielding et al., 1997; Knipe et al., 1997; Fisher & Knipe, 1998, 2001; Crawford et al, 2002; Yielding, 2015; Fisher et al., 2018). The abundance of data of siliciclastic fault rocks has resulted in the relatively simple classification of siliciclastic fault rocks (clay smears, phyllosilicates and deformation bands) based predominantly on the host rock clay content (Fisher & Knipe, 1998), and also burial history (and temperature), kinematics and mechanical properties. Additionally, the understanding in fault zone development, fault geometry and fault populations in these sequences has improved the accuracy of modelling siliciclastic fault seals in the subsurface (Pei et al., 2015).

Conversely, deformation including faulting within carbonates tends to be more complex than within siliciclastic rocks (Michie et al., 2018) due to the ductile and physio-chemical deformation processes (Delle Piane et al., 2017; Wu et al., 2020) associated with carbonates. Key parameters such as the protolith lithology, pressure and temperature, fault maturity and fluid-rock interactions influence deformation processes such as dynamic re-crystallisation or fluid assisted pressure solution (Delle Piane et al., 2017). As a result, complex faulted carbonates have been documented as having a range of sealing potentials, from barriers, where low porosity and low permeability fault cores can form (Michie and Haines, 2016), to conduits or dual conduit-seal characters (Figure 2-6) (Michie et al., 2018) with permeability that may allow across-fault fluid flow (Michie and Haines 2016).

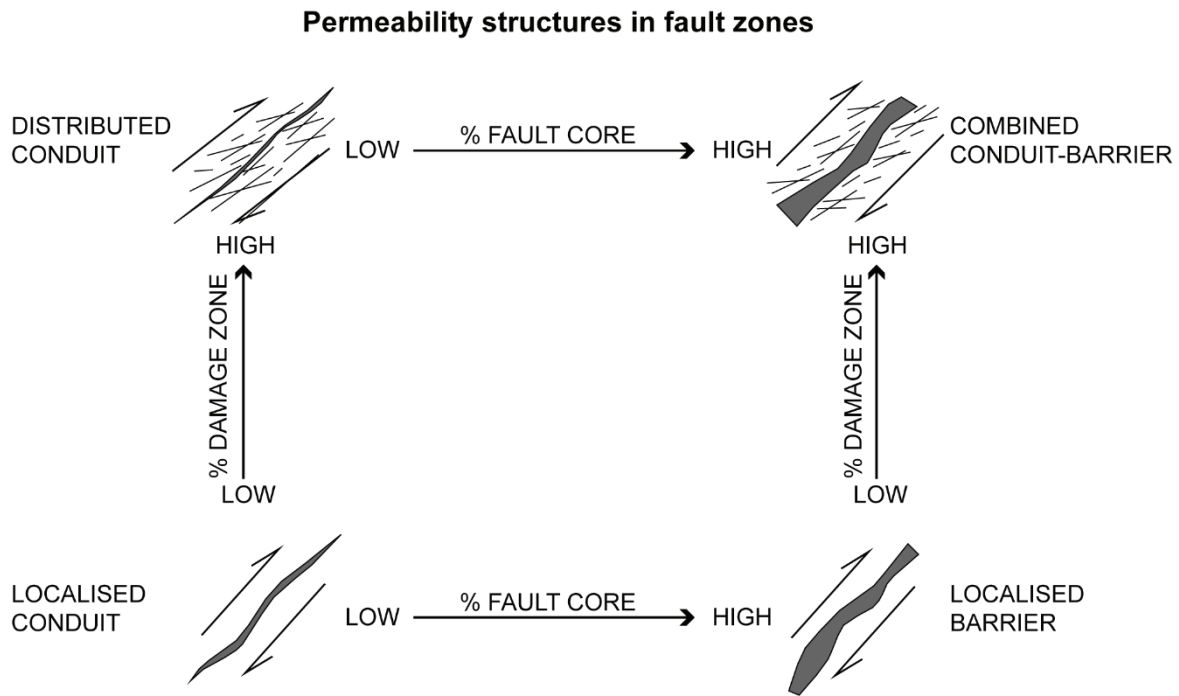


Figure 2-6. Schematic illustration of fault permeability structures (Modified from Caine et al., 1996).

2.2.1 The brittle-ductile transition in carbonate rocks

As rock deformation has fundamental implications for fluid flow, predicting the onset of inelastic strain and quantifying the type of deformation (compactional vs dilational) associated with different rock types can aid the prediction fault characterisation in the sub-surface. Under compression a rock under an applied load will initially have a linear elastic response. With increasing stress, the rock will transition from the elastic regime and accumulate permanent inelastic strain (the yield point) (Bedford et al., 2018). The inelastic behaviour observed in porous rocks when undergoing deformation is found to undergo a transition from brittle to ductile failure mechanisms with increasing pressures and temperatures (Heard, 1960; Mogi, 1966; Byerlee, 1968; Fredrich et al., 1989; Wong, 1990; Paterson & Wong 2005; Wong & Baud 2012; Zheng et al., 2016; Walton et al., 2017; Walton, 2021; Wang & Yang, 2022). Paterson & Wong (2005) provide a simple macroscopic distinction between brittle and ductile deformation where ductile behaviour is recognised in rocks capable of undergoing substantial permanent strain without macroscopic failure, while brittle behaviour is recognised by the presence of macroscopic failure. Macroscopic fracturing in the brittle field is associated with cataclastic processes involving micro-cracking and frictional sliding among grain fragments (Rutter, 1986; Wong & Baud, 2012) while inelastic ductile deformation is observed to be dominated by a range of processes including crystal plasticity, diffusion mass transfer and

cataclasis (Wong & Baud 2012; Ferraro et al., 2018; Zhao et al., 2018). This deformation can either be homogeneously distributed, leading to cataclastic flow, or localised in compaction bands (Walton, 2021).

The deformation behaviour of rocks can be recognised by the shape of stress-strain curves (Figure 2-7a) and generally, the stress-strain curve will evolve with increasing confining pressure for a given rock (Faulkner et al., 2008; Bedford et al., 2018; Wang et al., 2020). Brittle failure can be recognised by stress-strain curves which drop suddenly at, or just after yield while ductile behaviour is defined by a strain-hardening response in stress-strain curves (Figure 2-7). At intermediate confining pressures between pressures resulting in brittle and ductile behaviour, stress-strain curves tend to exhibit strain hardening with an eventual drop in stress (either sudden brittle failure or strain softening) (Faulkner et al., 2008; Bedford et al., 2018; Wang et al. 2020). Failure parameters (i.e. yield stresses and critical stresses such as onset of dilatancy, hydrostatic failure) can also be presented in terms of the mean pressure, $P ((\sigma_1 + \sigma_2 + \sigma_3)/3)$ and differential stress, $Q (\sigma_1 - \sigma_3)$ to determine the yield envelope for a given rock (Figure 2-7b). P-Q yield curves for a particular rock type can then be used to predict the stresses at which brittle or ductile inelastic deformation may occur (Bedford et al., 2018).

The mechanical behaviour and failure mode of porous rocks are generally found to be dependent on extrinsic variables such as confining/pore pressures, temperature, strain rate and pore fluid chemistry and intrinsic variables such as mineralogy, grain size and porosity (Baud et al., 2000; Klein et al., 2001; Chen et al., 2022). The brittle-ductile transition within carbonate rocks is somewhat distinct from deformation responses in silicate rocks due to the ability of calcite to initiate mechanical twinning and dislocation slip even at ambient, near-surface temperatures and pressures (Baud et al., 2000; Wong & Baud, 2012).

Under hydrostatic pressure, carbonate rocks are found to undergo pore collapse at a critical pressure, P^* , which is found to decrease significantly with increasing porosity from 3 to 15%, after which P^* still decreases but at a more gradual rate (Figure 2-8) (Baud et al., 2000/2017; Vajdova et al., 2004; Dautriat et al., 2011; Wong & Baud, 2012). Deformation experiments under triaxial conditions (vertical stress, $\sigma_1 >$ minimum horizontal stress, σ_3) of moderate porosity carbonates (3-18%) find that dilatancy and shear localisation occurs at low confining pressures (Vajdova et al., 2004; Wong & Baud, 2012). At high confining pressures, the onset of inelastic deformation is associated with shear-enhanced compaction and strain hardening followed by a switch to dilatancy which results in localised failure (Vajdova et al., 2004; Wong & Baud, 2012; Nicolas et al., 2016). The change from shear enhanced compaction to dilatancy

does not equate to a strict change in the deformation mechanisms but rather marks the change in the relative dominance in development of cracks over shear-enhanced compaction (Baud et al., 2000; Vajdova et al., 2004; Nicolas et al., 2016).

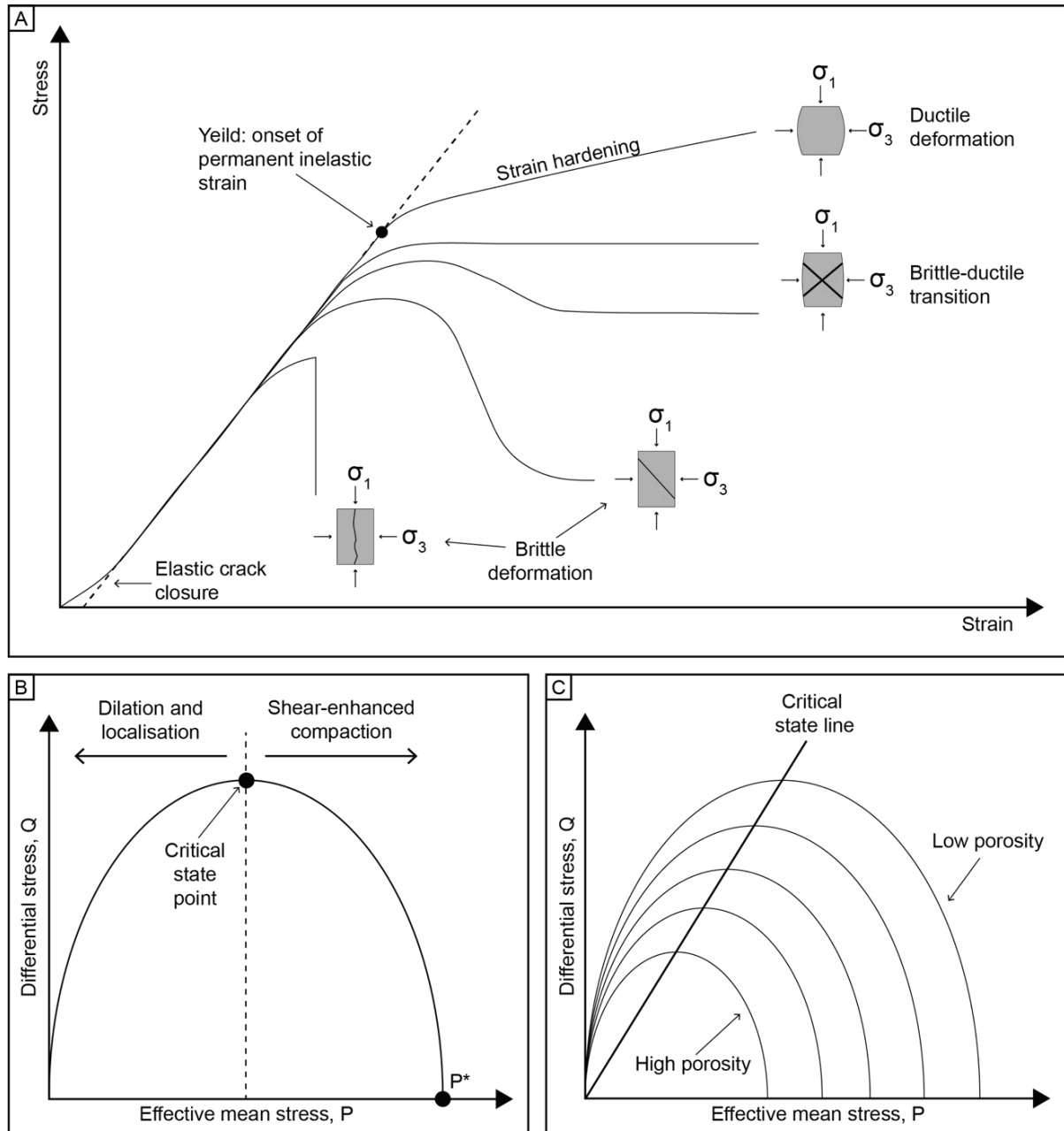


Figure 2-7. Stress-strain curves related to different deformation modes at low temperatures (edited from Wang et al., 2020). B) Simplified yield curve of a rock where low pressures are associated with localised dilatant behaviour and high-pressure side is associated with distributed compaction. The critical state point defines the transition between dilation to compaction (edited from Bedford et al., 2018). P^* is the hydrostatic yield point and marks the onset of grain crushing and pore collapse. C) Generally, yield curve envelopes are found to decrease in size with increasing porosity (edited from Bedford et al., 2018).

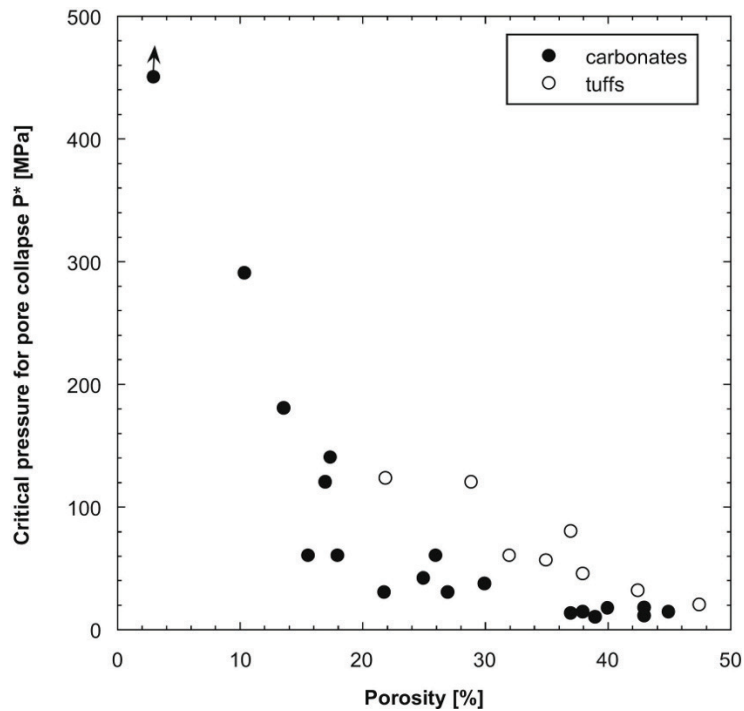


Figure 2-8. Pore collapse pressures for carbonate rocks and tuffs presented by Baud et al. (2012).

In the brittle failure regime, deformation is largely characterised by both intra- and inter-granular cracking which can be modelled using the sliding wing crack model (Figure 2-9b, Ashby & Sammis, 1990) where growth of wing cracks initiates from tensile stress concentration at the tips of pre-existing cracks undergoing frictional slip (Baud et al., 2000). Mechanical results from triaxial tests on multiple carbonate rock types have also shown that the Hertzian fracture model (pore collapse due to grain-scale brittle processes, Zhang et al., 1990) does not wholly apply to compaction deformation within limestones which have highly heterogeneous grain structures. The lack of coherency with a Hertzian fracture model is a result of Hertzian assumptions that grains have ideal elastic and fracture mechanics properties as well as uniform defect structure (Vajdova et al., 2004). Baud et al. (2000) argued that plastic collapse of pores characterised by Curran & Carroll (1979) (Figure 2-9a) is a more appropriate model of pore collapse where stress-induced compaction arises from the plastic collapse of isolated spherical pores. However, Vajdova et al. (2004) notes that neither of these two end-member models fully fit the mechanical response of limestones tested, suggesting that the deformation mode during shear enhanced compaction also includes cataclastic processes. On analysis of microstructure, Vajdova et al. (2004) found that within more porous limestones and chalk, mechanical twinning dominates, while dislocation slip is activated in more compact limestones. Consequently, the controlling deformation mechanisms appear to be controlled

by the host rock properties, which likely drives the variety and extent of carbonate fault rock types observed in nature (discussed in Section 2.2.4).

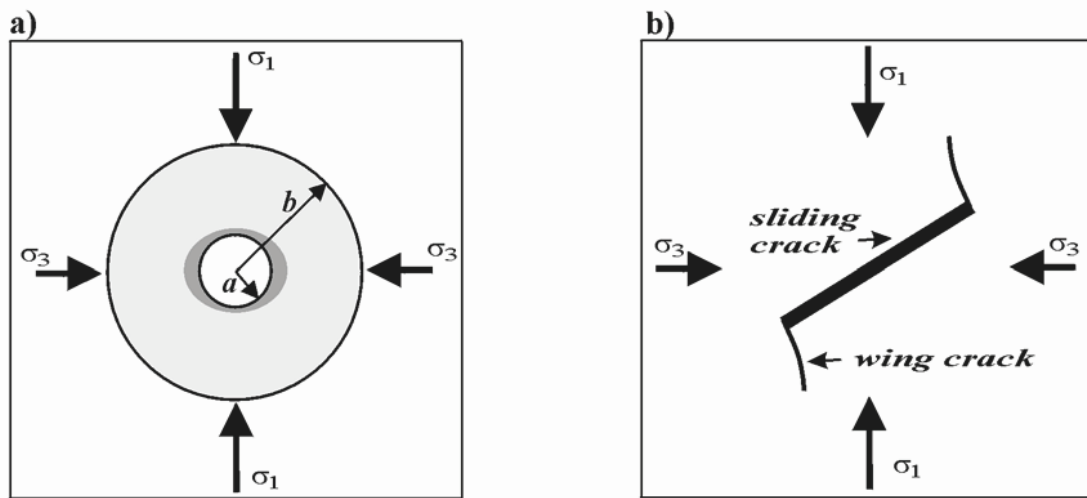


Figure 2-9. Two conceptual models of failure micromechanisms (from Vajdova et al., 2004). A) Conceptual model of plastic pore collapse modelled from Curran & Carroll (1979). Dark grey zone represents the initiation of plastic deformation while the remaining volume (light-grey) experiences elastic deformation. B) Wing crack model Dilatancy and brittle faulting

2.2.2 Rock physics: elastic and acoustic properties of carbonates

The relationship between the elastic properties and rock properties (such as porosity and density) has long been a key interpretive tool of borehole and seismic data. Therefore, the correlation of velocity with petrophysical parameters is essential for reliable interpretation of such geophysical data. However, unlike siliciclastic rocks, carbonates display little correlation between acoustic properties (compressional, V_p , and shear-wave, V_s , velocities) and porosity abundance (Anselmetti & Eberli 1993; Eberli et al., 2003; Lønøy et al., 2006; Fabricius et al., 2007; Sayers 2008; Neto et al., 2015). As such, using well-known porosity-velocity relationships, such as the Wyllie time-average (Wyllie et al., 1956), is often inaccurate in predicting porosity from velocity data or vice versa in carbonate rocks. Instead, the correlation between carbonates and acoustic properties has been found to be a complex interplay between pore volume and pore-type, and diagenetic fabrics (Anselmetti & Eberli 1993; Eberli et al., 2003; Baechle et al., 2008; Weger et al., 2009; Soete et al., 2015). Due to the variety of carbonate textures and pore types, velocity data is typically found to display a substantial range of values for a given porosity. For example, Eberli et al. (2003) show that carbonate rocks with porosity of 39% can have P-wave velocities between 2400 m/s and 5000 m/s

(Figure 2-10). Whilst a gross negative correlation between P-wave velocities and a broad range of porosities (0-60%) can be observed within this, the pore type plays an important control on elastic properties (Eberli et al., 2003), and understanding of carbonate heterogeneity can aid in prediction of pore-type/porosity velocity correlation.

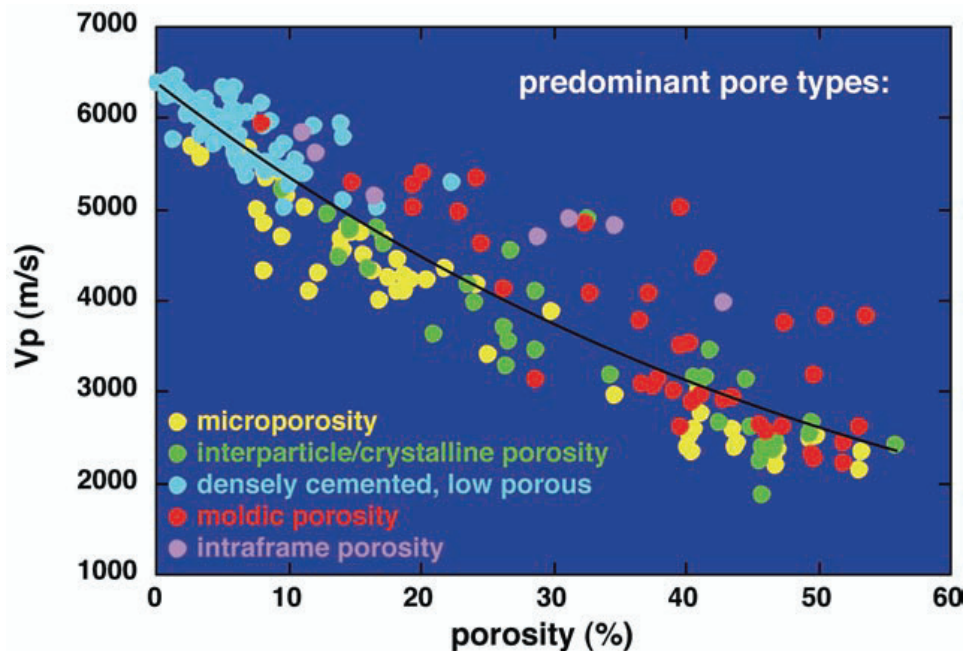


Figure 2-10. Carbonate velocity-porosity data (measured at 8 MPa effective pressure) defined by pore type (from Eberli et al., 2003)

As velocity is controlled by porosity and pore-type, mechanical compaction and strain localisation within rocks is likely to result in changes to elastic wave velocities. (Baud et al., 2017). Many experimental studies of the elastic wave velocities during inelastic deformation have focused on sandstone (e.g., Ayling et al., 1995; Fortin et al., 2005, 2007; Makhnenko & Labuz, 2016; Pijenburg et al., 2019; Li et al., 2021). These experimental studies generally demonstrate decreases in V_p and V_s are generally observed with the onset of inelastic compaction controlled by grain crushing processes forming new cracks. Recent mechanical experiments measuring changes in elastic wave velocities within limestones show a similar response in elastic wave velocities during brittle and semi-brittle deformation where dilatant micro-cracking deformation mechanisms dominate (Brantut et al., 2014; Nicolas et al., 2016). Baud et al. (2017) however, illustrates that inelastic deformation in high porosity limestone characterised by compaction begins with a substantial decrease in V_p due to microcracking before a subsequent increase in V_p due to porosity reduction. Brantut et al. (2018) also observed no change in V_p and V_s during hydrostatic compaction of porous limestones though found that elastic wave velocities decreased during unloading which is interpreted to reflect the increase of crack density. As detailed above, the evolution of elastic wave velocities is

largely restricted to marine-limestone carbonates with no known syn-deformational studies within non-marine carbonates.

2.2.3 Carbonate fault rocks

The variability of deformation processes that occur in carbonates means that fault zone architecture and related fault rocks are also highly variable (Delle Piane et al., 2017). In an analysis of different carbonate faults with a range of lithofacies, tectonic regime, burial depth and displacement by Michie et al. (2020) it was found that the host lithofacies texture and host porosity appear to be the primary control on the deformation style, fault rock type and therefore permeability. Therefore, categorisation of carbonate hosted faults generally falls into two broad categories based on the host lithology: i) low porosity carbonate (< 10 %) host rocks and ii) high porosity carbonate host rocks (> 10 %) (Delle Piane et al. 2017; Michie et al., 2020).

2.2.3.1 Fault zone architecture

It is evident that to understand the heterogeneous nature of faults and their effect on fluid flow, their formation and resulting structural architecture need to be understood. Faults in the shallow crust occur when stresses supersede the frictional strength of the rock, whereby the stresses are accommodated by the formation and interaction and growth of structural elements (Sibson, 1977; Fossen et al., 2010; Scholz, 2019). A range of different deformation and diagenetic mechanisms can be associated with this deformation including fracturing, brecciation, cataclasis, dissolution and precipitation (Sibson, 1994; Peacock et al., 1998; Agosta & Aydin, 2006; Mitchell and Faulkner, 2009). This deformation results in the formation of fault rocks (Sibson, 1977) which are specific to these mechanisms.

Generally, a fault zone is characterised by a fault core and a damage zone (Figure 2-11, Caine et al., 1996; Agosta and Aydin, 2006; Agosta et al., 2007; Mitchell and Faulkner, 2009; Giwelli et al., 2016a,b). The fault core is defined as a narrow zone which commonly forms between major slip surfaces (Agosta et al., 2007) and is generally characterised by deformation processes such as abrasion, particle rotation and crushing (Michie and Haines, 2016). The damage zone, which flanks the fault core, is characterised by a macroscopic fracture network which does not completely destroy the host rock fabric (Agosta et al., 2007). The permeability contrast between the fault core and damage zone (and also the host rock) is a primary control on the barrier-conduit characterisation of the fault zone (Caine et al., 1996).

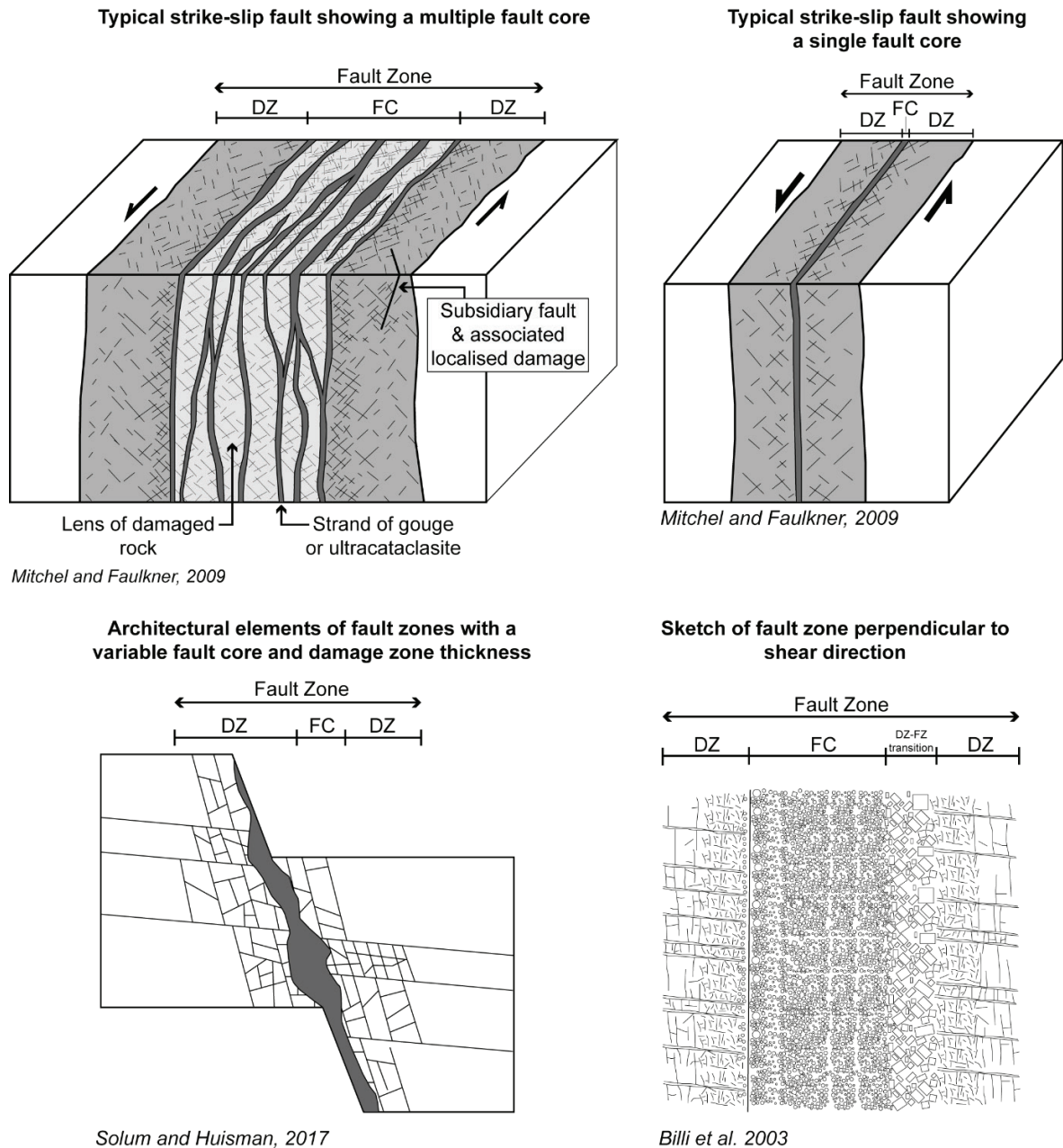


Figure 2-11. Schematic models illustrating fault core (FC) and damage zone (DZ) definitions. Models modified from Billi et al. (2003); Solum and Huisman (2017) and Mitchel and Faulkner (2009).

2.2.3.2 Fault core

The fault core defines the part of the fault zone which usually experiences localisation of strain (Chester et al., 2016) and therefore accommodates most of the fault's displacement (Caine et al., 1996; Billi et al., 2003; Childs et al., 2009). The fault core may include one or more slip surfaces with the inclusion of fault core lenses (Gabrielsen et al., 2017), fault gouge, breccias, cataclastic and geochemically altered zones (Sibson, 1994; Caine et al., 1996). Understanding the complexity of fault core structure and associated fault rocks is essential to analysing and

calculating a fault's hydrological characteristics. Despite this, according to generalised models the fault core is generally considered to be a low porosity, low permeability barrier to across fault fluid flow and/or a conduit to fluids parallel to the fault (Bastesen et al., 2009). However, it should be noted that across fault communication is likely to occur where highly permeable rocks are included within the fault zone, for example where lenses of fractured or permeable breccia fault rocks are present (e.g., Bastesen, et al., 2009). Ultimately, the structure and petrophysical properties of the fault core can be highly heterogenous and can also vary through time during periods reactivation or enhanced fluid pressure (Caine et al., 1996).

2.2.3.3 Damage zone

The damage zone bounds the fault zone and is characterised by subsidiary features such as secondary faults, veins and fractures and/or deformation bands (Caine et al., 1996; Bastesen, 2008; Haussegger et al., 2010; Agosta et al., 2007). The permeability of the damage zone is primarily dominated by the fracture network (Caine et al., 1996), which can have significantly different mechanical and hydraulic properties to the surrounding intact host rock (Ostermeijer et al., 2020). Highly fractured damage zones can be associated with higher permeabilities compared to that of the fault core and host rock (Caine et al., 1996; Agosta et al., 2007). Conversely, structures such as deformation bands, mm-scale tabular zones of localised but indiscrete strain, typically forming as a result of grain reorganisation, cataclasis, and/or dissolution processes can result in a lower permeability than that of the host rock (Rath et al., 2011; Rotevatn et al., 2017).

The presence of strongly fractured damage zones, in carbonate rocks particularly, can be affected by diagenesis during burial (cementation, dissolution), which can significantly affect their permeability (Haines et al., 2016; Wu et al., 2020). Therefore, highly fractured damage zones are thought to enhance significant diagenetic modifications during a fault's evolution (Wu et al., 2020). The fracture density and distribution within the damage zone is a key control on permeability (Kim et al. 2004; Molli et al., 2010; Mercuri et al., 2020). A common characteristic of damage zones is that the fracture density (and thus connectivity) decreases away from the fault core (Savage & Brodsky, 2001; Mercuri et al., 2020). The relationship between fault throw and damage zone thickness can therefore be a useful tool for predicting fracture network properties. Several studies (Micarelli et al 2006; Savage & Bordsky, 2011; Balsamo et al., 2019) have found that initial fault growth and damage zone widening is scalable until a critical throw past which the rate of damage zone widening decreases (Figure 2-12). For example, Savage & Brodsky (2011) found that faults with a total displacement of < 150 m have a damage zone that decays as the inverse of the distance from the fault.

Comparatively, faults with > 150 m total displacement show a much more gradual damage zone decay and a decrease in the rate of fault zone width with displacement. The break in scaling infers that the deformation mechanisms involved in forming the damage zone change as the fault zone matures (Savage & Borsky, 2011). This break in scaling has been attributed to the transition from a strain hardening to a strain softening behaviour caused by the development of subsidiary slip surfaces (Shipton & Cowie, 2003; Mercuri et al., 2020). These subsidiary faults nucleate when enough fractures coalesce into shear planes so this change does not require a change in physical processes between large and small faults (Savage & Borsky, 2011).

It should also be noted that faults within hard rocks, mudstones and carbonates can have very narrow or no damage zone at all (Shipton & Cowie, 2003). This is thought to occur where the fault zone is very weak resulting in localized deformation (Shipton & Cowie, 2003).

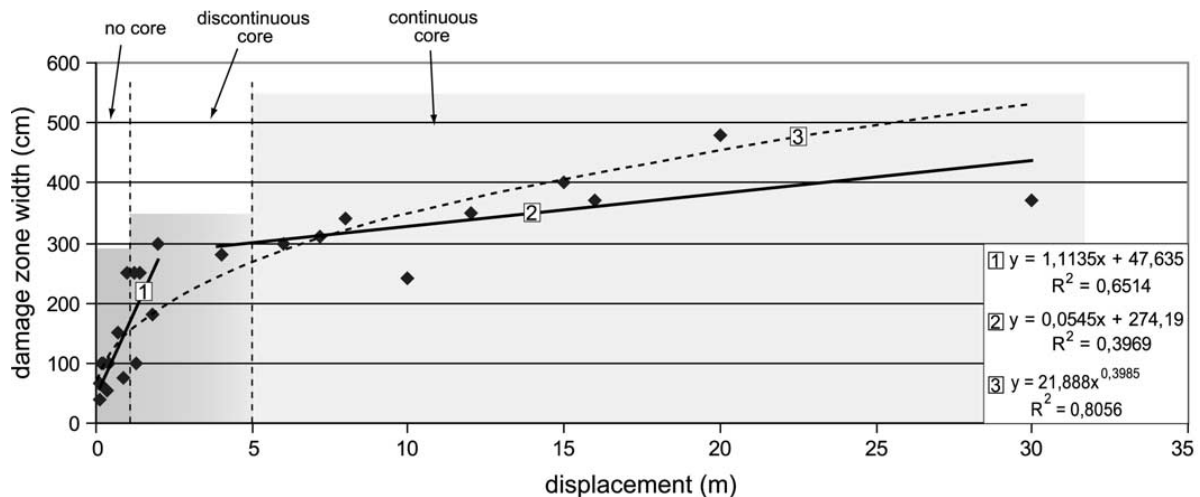


Figure 2-12. Graph from Micarelli et al. (2006) illustrating the relationship of damage zone width with displacement in high-porosity carbonate hosted faults in the Hyblean Plateau, Sicily.

2.2.4 Fault rock characterisation

Fault rocks are defined by Sibson (1977) as “a collective term for the distinctive rock types found in zones of shear dislocation at both high and low crustal levels, whose textures are thought to arise at least in part from the shearing process”. One or more different types of fault rocks, such as cataclasites, mylonites and indurated gouge, can be found within a single fault zone and can also vary along strike and dip of the fault (Higgins et al., 1971; Sibson et al., 1977; Caine et al., 1996; Chester et al., 2004; Woodcock & Mort, 2008).

Sibson (1977) created a widely used fault classification scheme which uses primary cohesion and presence of foliation to distinguish fault rock types (Figure 2-13a). Classification based on foliation and primary cohesion however can be flawed as cataclasis associated with brittle faulting can produce well-foliated fault gouge (Chester et al., 1986; Jefferies et al., 2006). A notable modification of this scheme was created by Killick et al. (2003) (Figure 2-13b), which does not recognise cohesive breccias as a fault rock category, suggesting that these rocks can be included as proto-cataclasites. However, it is generally accepted that fault breccia's can have primary cohesion (Sibson, 1977; Woodcock & Mort, 2008). Woodcock & Mort (2008) noted that the observed cohesion is difficult to distinguish between primary (i.e., cohesion at time of fault movement) and secondary (acquired through post-faulting processes) cohesion and as such should be omitted as a primary criterion from the fault rock classification scheme. They also highlight the importance of recognising and categorising different types of fault breccia due to their control on the hydraulic properties of fault rocks. Therefore, the Woodcock & Mort (2008) classification scheme defines breccias based on grain size rather than its lack of cohesion at time of faulting, whereby a fault breccia is defined as having "at least 30% of its volume being clasts larger than 2 mm in diameter" (Figure 2-13c-d). This definition means that fault breccia's can be cohesive, non-cohesive, foliated or not and may be of any composition (Woodcock & Mort 2008). This classification scheme further subdivides fault breccias using the terms crackle, mosaic and chaotic breccia according to how well clasts fit together (Woodcock & Mort 2008).

A) Sibson (1977) classification

	Random fabric		Foliated	
Incohesive	Fault breccia (>30% visible fragments)		?	
	Fault gouge (<30% visible fragments)		?	
Cohesive	Glass or devitrified glass	Pseudotachylite		?
		Crush breccia (fragments >5 mm) Fine crush breccia (fragments 1-5 mm) Crush microbreccia (fragments <1 mm)		0-10%
	Tectonic reduction in grain size dominates grain growth by recrystallisation	Protocataclasite	Protomylonite	10-15%
		Cataclasite	Mylonite	50-90%
		Ultracataclasite	Ultramylonite	90-100%
Grain growth pronounced	?	Blastomylonite		

B) Killick et al. (2003) classification

	Random fabric		Foliated		
Incohesive	Fault breccia (>30% visible fragments)		?		<70%
	Fault gouge (<30% visible fragments)		?		>70%
Cohesive	Glass or devitrified glass	Pseudotachylite			% MATRIX
		Protocataclasite	Protomylonite	0-50%	
	Cataclasite	Mylonite	50-90%		
	Ultracataclasite	Ultramylonite	90-100%		
	visible grain growth	?	Blastomylonite	>0-1-100%	

C) Woodcock & Mort (2008) classification

	Non-foliated		Foliated	
>30% large clasts >2 m	75-100% large clasts (>2 mm)	Fault breccia	Crackle breccia	
	60-70% large clasts (>2 mm)		Mosaic breccia	
	30-60% large clasts (>2 mm)		Chaotic breccia	
<30% large clasts >2 m	Incohesive	Fault gouge		
	Glass or devitrified glass	Pseudotachylite		
	0-50% matrix (<0.1 mm)	Protocataclasite	Protomylonite	
	50-90% matrix (<0.1 mm)	(Meso)cataclasite	(Meso)mylonite	
	90-100% matrix (<0.1 mm)	Ultracataclasite	Ultramylonite	
Pronounced grain growth		Blastomylonite		

D) Woodcock & Mort (2008) ternary diagrams

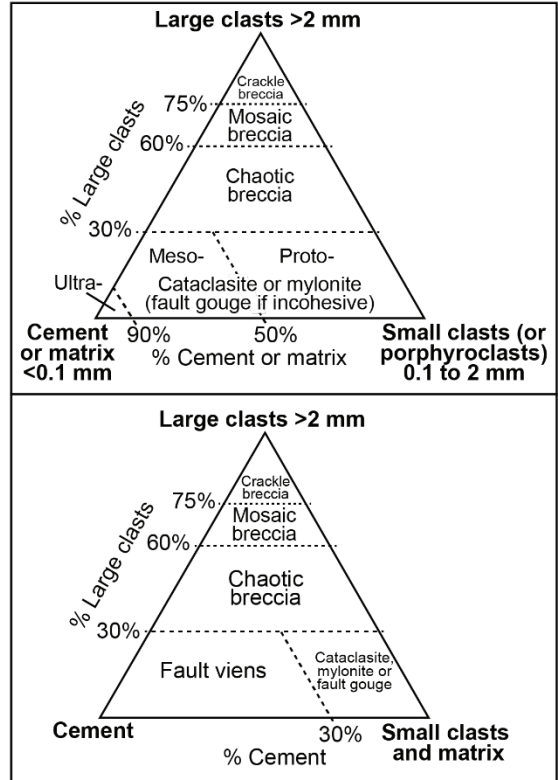


Figure 2-13. Comparison of fault classification schemes from A) Sibson (1977), B) Killick (2003), C) & D) Woodcock & Mort (2008). Portions of classification scheme of interest to this study (for brittle faulting in the upper crust) are highlighted in blue.

2.2.4.1 Low porosity carbonate fault rocks

Faults within low porosity (< 10%) carbonates are generally found to be characterised by dispersed brittle processes (fracturing, veining, brecciation) (Molli et al., 2010; Bussolotto et al 2015; Michie 2015; Haines et al., 2016; Delle Piane et al., 2017; Cooke et al., 2018). The fault zone of low porosity carbonates is generally modelled to have a highly fragmented fault core of tens of cm to metres thick surrounded by an intense damage zone consisting of large fracture networks and fault rock lenses (Michie 2015; Haines et al., 2016; Delle Piane et al., 2017; Cooke et al., 2018). However, highly segmented fault zones lacking a well-defined fault core and evident shear strain can also be found in low porosity, crystalline, host rock carbonates (Schröckenfuchs et al., 2015; Delle Piane et al., 2017) where domains of cataclastic, comminuted rocks are organised in networks of minor faults and fractures forming from in-situ shattering/pulverisation mechanisms (Schröckenfuchs et al., 2015). These types of fault zones are typically found within dolomite host rocks inferring that deformation processes and the resulting fault architecture are also partially controlled by the carbonate lithology (Schröckenfuchs et al., 2015; Bauer et al., 2016; Delle Piane et al., 2017; Kaminskaite et al., 2020).

Work by Bauer et al. (2016) (Hochschwab massif, Austria) and Kaminskaite et al. (2020) (San Vito lo Capo, Sicily) illustrate the architectural difference of fault zones hosted in low porosity limestones and dolostones. Fault zones in dolostones are observed to have distributed brittle deformation across wide fault zones with multiple heterogeneous cataclastic shear bands. Conversely, fault zones in the limestones are observed to be laterally distinct with a single fault core where strain is localised. Kaminskaite et al. (2020) infers that this contrasting behaviour of deformation is controlled by mineralogy, where dolostone is stronger and therefore more brittle than calcite. Therefore, deformation in dolomite results in early intense fragmentation and disintegration over a wide zone of deformation, whereas calcite, which has higher solubility and plasticity, can accommodate more strain prior to faulting leading to strain localisation. Ferraro et al. (2019) also illustrates the contrasting structural diagenesis of dolostone and calcite fault rocks from extensional faults in the central-southern Apennines, Italy. Here, physical compaction dominated diagenesis of dolomite-rich fault rocks is observed, whilst chemical compaction with dissolution is associated with calcite-rich fault rocks. It was also observed that cementation of calcite rich fault rocks is widespread in the fault core while it is virtually absent in dolomite rich fault rocks. Ferraro et al. (2019) theorises that this is due to the chemical stability of dolomite whereby dissolution only typically occurs at burial depths > 1.5 km. Further work by Ferraro et al. (2020) shows that in the cemented limestone fault

rocks within the fault core permeability and porosity significantly decrease compared to the outer fault core where cementation is not present.

Petrophysical impacts of faults in low porosity carbonates

The porosity and permeability of faults in low porosity carbonates are generally found to increase from the host rock towards the fault zone in the damage zone, controlled by the connectivity and anisotropy of fracture networks and/or breccia zones (Bauer et al., 2016; Delle Piane et al., 2017; Michie et al., 2020). Fault zones hosted in limestones, which have a typical fault zone of a single fault core and surrounding fractured damage zone, are likely to form anisotropic hydraulic systems whereby the cataclastic fault rocks in the fault core act as a baffle to fluid flow, while the damage zone acts a fractured, fault parallel conduit for fluid (Agosta et al., 2007; Billi, 2010; Kaminskaite et al., 2020; Michie et al., 2020). As shown by Ferraro et al. (2020), diagenesis plays an important role in the hydrodynamic properties of the fault zone, where cementation will cause a decrease in permeability of remaining porosity, and is especially common in calcite-rich fault rocks within the fault core. However, in a synthesis of fault rock petrophysical data (Figure 2-14) by Michie et al. (2020), there is significant overlap of poro-perm data for both limestone and dolomite fault rocks. Both show an increase in porosity and permeability compared to host rock values with dolomite fault rocks only having a slightly higher fault rock permeability.

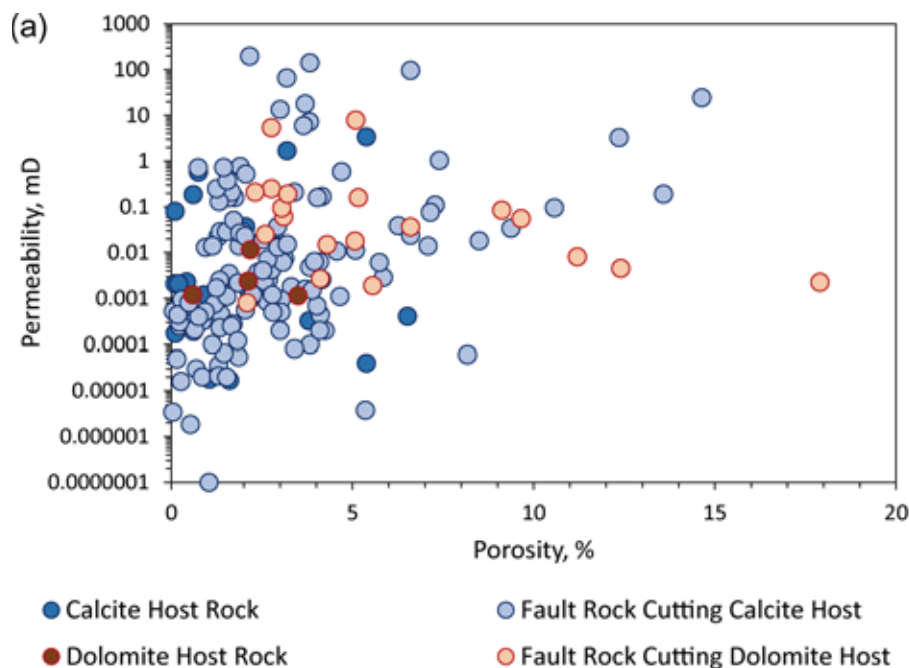


Figure 2-14. Graph of porosity and permeability of calcite and dolomite host rocks and their respective fault rocks (from Michie et al., 2020).

2.2.4.2 High porosity carbonate faults

Low displacement faults (< 2 cm) within high porosity (>10%) carbonate host rocks are commonly associated with deformation band formation (Tondi et al., 2006, Rath et al., 2011; Cilona et al., 2012; Rotevatn et al., 2014; Kaminskaite et al., 2019, Michie et al., 2020). Strain in these host rocks is commonly accommodated by dilation, compaction or shear enhanced compaction resulting in deformation band formation (Tondi et al., 2006; Cilona et al., 2012; Cooke et al., 2018) and can often occur in clusters creating a deformation band network. Cilona et al. (2012) describes 4 stages of deformation within porous limestones:

1. Compaction and strain localisation into narrow bands accommodated by pore collapse, grain rotation and sliding.
2. Formation of pressure solution seams within compacted bands as a result of pressure solution of grain contacts resulting in grain size reduction.
3. Subsequent shearing of pressure solution seams.
4. Cataclasis development localised along sheared pressure solution seams.

Varied formation conditions (temperature and pressures), host lithology (e.g. cementation and peloidal content) and maturity of deformation leads to variation of deformation band type (Rotevatn et al., 2014; Kaminskaite et al., 2019). For example, the presence of soft micrite peloids results in compaction band formation controlled by plastic smearing and grain size reduction of the peloids with minor occurrences of grain crushing and pressure solution (Antonelli et al., 2014). Rath et al. (2011) also found that diagenesis influences the deformation mechanisms in deformation bands. Deformation bands in uncemented high porosity carbonates (from the Eisenstadt-Sopron Basin, Austria/Hungary) are dominated by grain rotation, translation and porosity reduction mechanisms while a later generation of deformation bands through cemented host rock are dominated by cataclasis (Rath et al., 2011).

Faults with higher throws than deformation bands in high porosity carbonates are comparatively less well documented. However, extensive work has been carried out analysing high porosity (> 10%) carbonate hosted faults in Oligo-Miocene platform carbonates in Malta (Bonson et al., 2007; Michie 2015; Michie et al., 2014, 2018; 2021; Haines et al., 2016; Michie & Haines 2016; Dimmen et al., 2017, 2020; Cooke et al., 2018, 2019; Cooke et al., 2019; Nixon et al., 2020) which provides key trends for deformation mechanisms associated with different lithofacies and characterises their resulting fault rock development.

Faults within grain dominated carbonates such as those from Malta (i.e., grainstones and bioclastic packstones) are found to localise deformation and conform to general fault zone models: a single slip surface with a well-developed cataclastic veneer surrounding by a symmetrical damage zone characterised by a network of deformation bands (Michie, 2015; Cooke et al., 2018; Michie et al., 2020). Localisation of deformation in these rocks is thought to be related to the lithofacies fabric, whereby the coarser grains present results in a high strength rock mass (Michie et al., 2014; Michie et al., 2020). Deformation mechanisms during fault development are associated with grain scale cataclasis, granular flow and grain translation leading to formation of proto-cataclasites and cataclasites. This contrasts with cataclastic formation in low porosity carbonates, which is driven by brittle deformation processes, like fracturing (Michie, 2015; Cooke et al., 2018, 2019). Diagenesis also impacts fault zone properties of these rocks. Aggrading neomorphism (transformation of micrite to microspar) is common in the damage zone of grain dominated carbonates which results in a decrease in porosity and increasingly strong but brittle limestone. (Haines et al., 2016). This effect can introduce a tendency for increased fracturing following diagenesis (Haines et al., 2016).

Compared to high porosity carbonates, which are grain supported, those with high micrite content typically have lower strength due to fine particle sizes of micritic matrix. Increasing micrite content is seen to produce more dispersed deformation dominated by hydraulic breccias and disperse fracturing evolving into cataclasis (Michie et al., 2014; Michie et al., 2020). Similar deformation styles are observed in grain supported lithofacies with high algal content or within those that have been recrystallised (forming a low porosity host rock) (Michie et al., 2020). At low fault displacements (~10 m), fault zones in micritic carbonates typically lack continuous fault cores (< 10 m lateral continuity) and are observed to become more continuous and prevalent with increasing throw (Haines et al., 2016). However, whilst continuity of fault cores increases, they become increasingly heterogeneous through increasing incorporation of different lithofacies with greater throw (Michie, 2015, Michie et al., 2020). However, this highly heterogeneous fault core character is limited, and dependent on the scale and variability of host-rock layering, with higher displacement (> 100 m) faults showing a return to fairly homogenous fault rocks (Michie et al., 2018).

Petrophysical impacts of faults in high porosity carbonates

The above work based on carbonate hosted faults in Malta show that porosity is only an intrinsic control on deformation style and fault rock type in carbonates with minimal micritic

content. However, host rock porosity is important to understand the overall hydraulic system as it is the difference between the host-rock and fault rock permeability that controls whether a fault zone will act as barrier or conduit of fluid flow (Michie et al., 2020,2021). High porosity carbonates are, however, typically associated with deformation band formation, either in the damage zone of large-scale fault zones or as concentrated corridors of deformation band networks. Regardless of deformation band type (i.e. maturity and deformation mechanism), porosity and permeability is typically found to be lower than that of the host rock (Tondi et al., 2016, Kaminskaite et al., 2019, Michie et al., 2020,2021) and their presence can result in porosity and permeability reductions by 1 – 4 orders of magnitudes (Rath et al., 2011; Rotevatn et al., 2014). This reduction in permeability is much higher than values reported for non-cataclastic bands found within porous siliciclastic sandstones with similar burial depths (Rath et al., 2011; Rotevatn et al., 2014). Rath et al. (2011) hypothesises that this is due the ability of carbonates to accommodate strain through plastic deformation at shallow burial conditions. Deformation band assemblages in carbonates are therefore more likely to produce strong complex heterogeneous baffles to fluid flow in the sub-surface compared to siliciclastics.

In Michie et al. (2020), analysis of porosity and permeability of fault rocks in high porosity carbonates shows that even though *absolute* values for permeability and porosity of fault rocks increases with host rock porosity, fault rocks in high porosity carbonates generally show a decrease in poro-perm measurements *relative* to their host rock (Figure 2-15). This is consistent with observations by Cooke et al. (2019) where high porosity carbonate fault rocks achieve permeability contrasts with their host rock of around 4 order of magnitude.. However, this effect may be fairly localised given the lack of continuity and heterogeneity of cataclastic fault cores allowing for low displacement (< 10 m) faults such as those observed in micrite dominated carbonates to be prone to leakage (Michie & Haines, 2016; Cooke et al., 2019). At higher displacements however (> 100 m), increasingly homogenous fault cores are dominated by fewer fault rock types resulting in a fault core which is more likely to provide a barrier to fluid flow.

Diagenesis, as observed in grain dominated fault zones, will act to reduce the porosity and therefore the permeability of the damage zone, though subsequent formation of fracture networks through the sequence can act to increase permeability through this zone (Haines et al., 2016). Exposed examples of paleo-fluid indicators in micrite dominated carbonate fault zones, as discussed, illustrate how the damage zone can act as fluid conduits especially with enhanced fracture network connectivity (Dimmen et al., 2017, 2020).

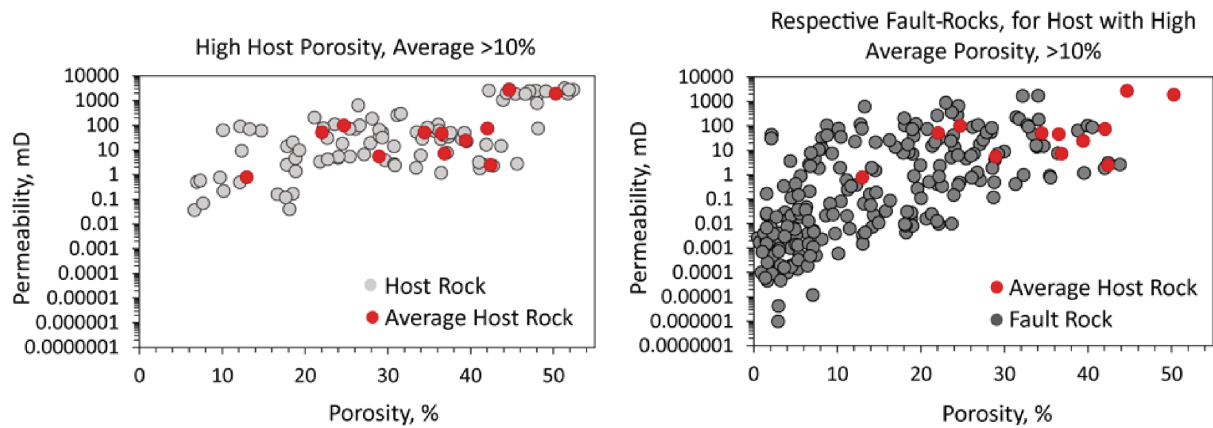


Figure 2-15. Poro-perm plots from Michie et al. (2020) comparing host rock and fault rock data for high porosity (> 10%) carbonates. Data illustrates general trend of decreasing porosity and permeability of fault rocks compared to their host rocks.

2.2.4.3 Dilational normal faults

Dilational features are predominantly associated with tensile, mode I deformation and formation of karst systems such as fault caves (formed as a result of dissolution) (Gent et al., 2010). These structures are particularly interesting within carbonates, which at shallow depths are strong relative to the mean effective stress which means they can sustain dilational features such as open fractures and cavities due to their cohesion and high tensile strength (Gent et al., 2010). Given their open nature (e.g., Gent et al., 2010) achieving measurements of hydraulic behaviour of dilation faults is limited to active flow monitoring from near-surface systems (e.g., from springs (Frery et al., 2015)). However examples of the impact of partly preserved or filled, dilational faults on the hydraulic behaviour of rock masses are largely unexplored.

Dilational faults are often associated with hybrid failure type in which the fault has components of both tensile and shear modes of failure, controlled by the mechanical stratigraphy of the sequence (Ferrill & Morris, 2003; Ferrill et al., 2011, 2012, 2017, 2020; Gent et al., 2010). However, it has been well documented, with examples in near surface basalts in NE Iceland, that dilatant fault zones can form purely by mode I tensile fracturing near the surface (Opheim & Gudmundsson, 1989; Gudmundsson 1994; Kettermann et al., 2019; Bramham et al., 2021).

There have been comparatively few dilational fault outcrop examples within carbonate sequences. Of note are the wide chaotic breccia zones within the Pembroke Limestone group in Wales which Woodcock et al. (2014) suggested are formed as a result of collapse into voids along dilational faults. Gent et al. (2010) also recognised evidence of dilational faulting in carbonates from the Jebel Hafeet anticline (UAE and Oman) where normal faults can be found

to have apertures of several decimetres (Figure 2-16). These dilational faults are seen to be filled with carbonate veins, crushed wall rock or sediments (Figure 2-16a-b). Fault infill is distinctly different from the host wall rock (Figure 2-16b) and can also show stratification which Gent et al. (2010) interpret as evidence of episodic sedimentation within the fault zone as a product of either gravitation or hydraulic transport.

Scaled model experiments using layered cohesive hemihydrate powder show that these dilatant faults evolve through linking of Mode I fractures in a shear zone and are associated with fragmentation and gravity driven breccia formation of the 'host' medium (Gent et al., 2010). Additional experiments by Kettermann and Urai (2015) illustrate the effect of overburden on the fault mode and how failure mode transition can change with depth. As with examples of faults in Iceland (Opheim & Gudmundsson, 1989; Gudmundsson 1994; Kettermann et al., 2019; Bramham et al., 2021), Kettermann and Urai (2015) observed that smaller overburden pressures (i.e. at or near the surface) leads to formation of dilatant fault zones whereas at depth with increasing overburden pressures the material fails in shear (Bramham et al., 2021).

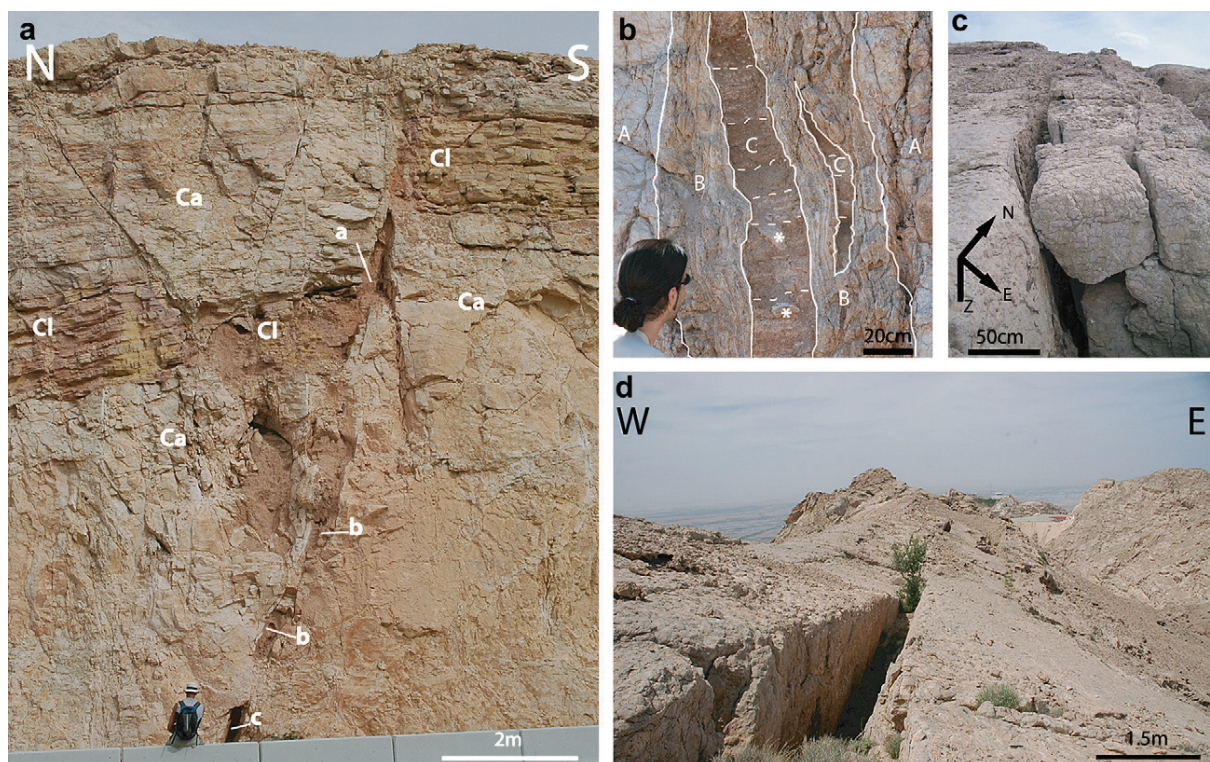


Figure 2-16. A) Outcrop examples of a dilation fault zone within a carbonate from the Jebel Hafeet region (U.A.E.) Ca: Carbonate; Cl: Clayey carbonate; b: fault cavities with inclusion of Cl material; c: empty fault zone cavity. B) Example of opening mode fracture with layered clastic infill with different zones labelled. Zone A: Wall rock; Zone B: Rim of precipitated calcite; Zone C: centre of fracture filled with stratified sediments. C and D) Large fissures with rotated wall rock blocks. From Gent et al. (2010).

2.2.4.4 Non-marine carbonate fault rocks

Comparatively little work has been carried out on deformation of continental or non-marine carbonate fault rocks compared to other carbonate types. This is especially true for travertine hosted faults where an apparent lack of suitable outcrop exposures of travertine deposits may mean most exposed travertines, being Pleistocene – Holocene in age have undergone little to no tectonic deformation.

Outcrop examples of deformed travertines

The tectonic reconstruction of the Ballık Travertine in SW Turkey (Figure 2-17a-b) by Van Noten et al. (2019), presents a detailed structural analysis of Early Pleistocene normal and strike slip faulting. Though this study is of recent (Pleistocene) surface deposits meaning that deformation is not directly analogous to reservoir conditions (under increased pressure and temperature), observations from this study are valuable to recognise deformation mechanisms within travertine and characterise structures which may be characteristic of these deposits before undergoing burial. It is also important to consider travertines as a signifier of enhanced fluid flow in some basins where complex fault-fracture networks have formed such as at graben intersections, such as those observed in the Denizli Basin (Van Noten et al., 2019). Deformation within the Denizli travertine deposits produces dilational faulting which display dissolution of the fault walls and infill by muddy and chaotic material (Figure 2-17c-f) (Van Noten et al., 2019). The open nature of these faults is likely due to the low normal stresses acting on the travertine body resulting in a hybrid failure style (Ferril et al., 2020). These faults also usually have several phases of fault parallel mineralisation and travertine deposition (Figure 2-17e-g); which is evidence of secondary fluid flow through the fault and fracture network (Van Noten et al., 2019). Deformation largely appears to be localised to the fault core with some diffuse fracturing forming the damage zone. Deformation is largely dilational and as such forms open pathways for fluid flow prior to infill, which results in the deposition of fault/fracture parallel travertine deposition (Figure 2-17e-g).

Figure 2-17. (Next page) Summary figure of work from Van Noten et al. (2019). A) illustrates location of the Turkish Ballık travertine with B) illustrating location of quarry outcrops and mapped faults. C) Example of faulting in area with D) figure of slickenlines from hangingwall of the fault and E) evidence of multiple phases of faulting shown by different generations of fault breccia and travertine mineralisation. F) Example of larger displacement fault. G) Example of complex fault with several deformation and infill phases.

Mechanical properties

Due to the heterogeneity of travertines, owing to their varied and changing depositional morphology, the mechanical properties of travertine host rocks may influence fracturing (as in the micrite versus non-micrite prone carbonates of Michie, 2015). However, with the exception of few limited studies, this remains largely unexplored within travertines and non-marine carbonates. Maggi et al. (2015) characterised staircase fractures within the Acquasanta Terme travertine deposits (Figure 2-18) to understand the control of lamination-related mechanical anisotropy following observations of a tendency to form staircase fractures. Maggi et al. (2015) proposed that the higher probability of intersections with mechanical layering for fractures within strongly laminated sequences likely meant lamination parallel fracture segments, and resulting staircase fractures, were a common deformation style within travertines.

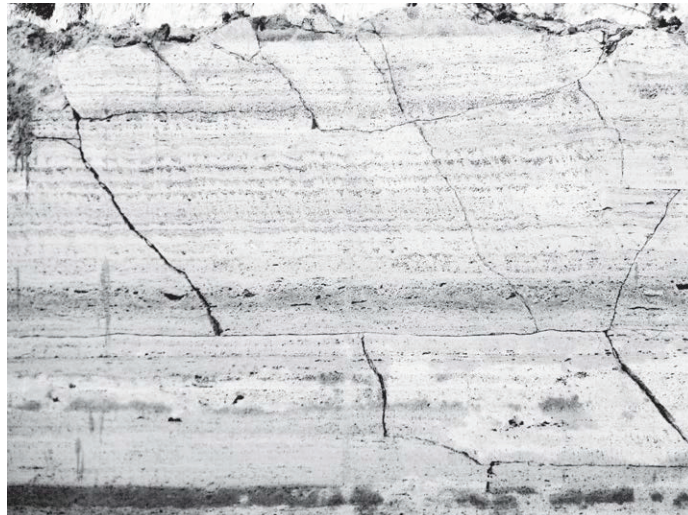


Figure 2-18. Staircase fracture within laminated travertine (Acquasanta Terme, Italy) illustrating ramp and lamination parallel fracture segments (from Maggi et al. 2015).

One of the few studies into continental carbonate fault rocks carried out by CSIRO as part of their fault reactivation in carbonates research projects focuses on experimental deformation of travertine samples taken from the Acquasanta Terme region of Italy (Giwelli et al., 2016a,b; Delle Piane et al., 2016; Kiewiet et al., 2020). Published work from Giwelli et al. (2016a,b), Delle Piane et al. (2016), Kiewiet et al. (2020) analyses results from direct shear experiments conducted on intact travertine blocks to understand the effect of shearing on fluid flow. Microstructural observations of faulting during initial shearing to 20mm displacements (Figure 2-19a-b) show that initial porosity and permeability reduction can be attributed to localised compaction and asperity shearing. This means that even at relatively low displacements this type of faulting has the potential to create a narrow but effective barriers to fluid flow. Further

displacement results in the development of continuous gouge along the fault core (Figure 2-19c) and further increases the faults capacity to act as a barrier to flow. As such, dynamic transmissibility is observed by Giwelli et al. (2016a,b) to decrease as total shear displacement increases (Figure 2-19d).

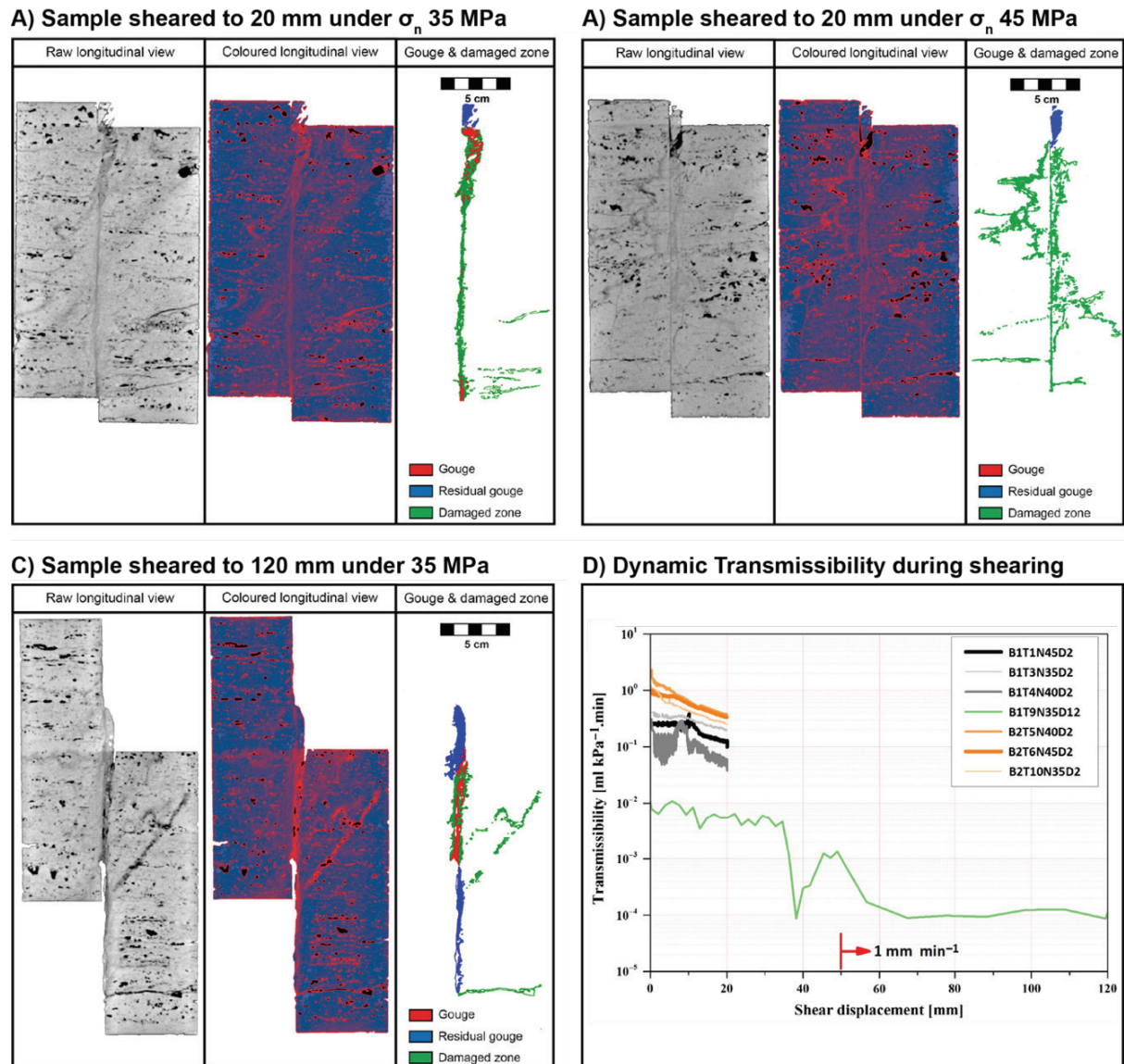


Figure 2-19 A-C) CT images with interpretation of the fault core and damage zone of experimentally sheared travertine from Giwelli et al. (2016a). D) Graph illustrating relationship between dynamic transmissibility and shear displacement (Giwelli et al., 2016a).

A further study of these rocks by Delle Piane et al. (2016) evaluated the behaviour of these fault rocks and their hydrodynamic properties during reactivation. Sheared blocks, classified as analogous to either the fault core (sheared to 120 mm with continuous gouge) or damage zone (sheared to 20 mm resulting in a fracture network) were cored and 'reactivated' during

triaxial testing. Results from Delle Piane et al. (2016) show that overall permeability for all samples decreased with increasing mean stress (Figure 2-20). The study further illustrates the different hydrodynamic response during reactivation, whereby the rate of permeability decrease in fault core analogue samples is much higher than that of the damage zone samples (Figure 2-20). Delle Piane et al. (2016) propose this is due to the different microstructural characterisation of the different samples. For example, it is inferred that the lower rate of permeability decrease in the damage zone samples is due to the network of Riedel shears and related open porosity created during shearing which creates effective across and along fault fluid pathways. Conversely, the higher rate of permeability decrease observed in fault core analogue samples are inferred to result from elastic closure of cracks during confinement and possibly related to pressure-induced closure of fracture bands (Delle Piane et al., 2016).

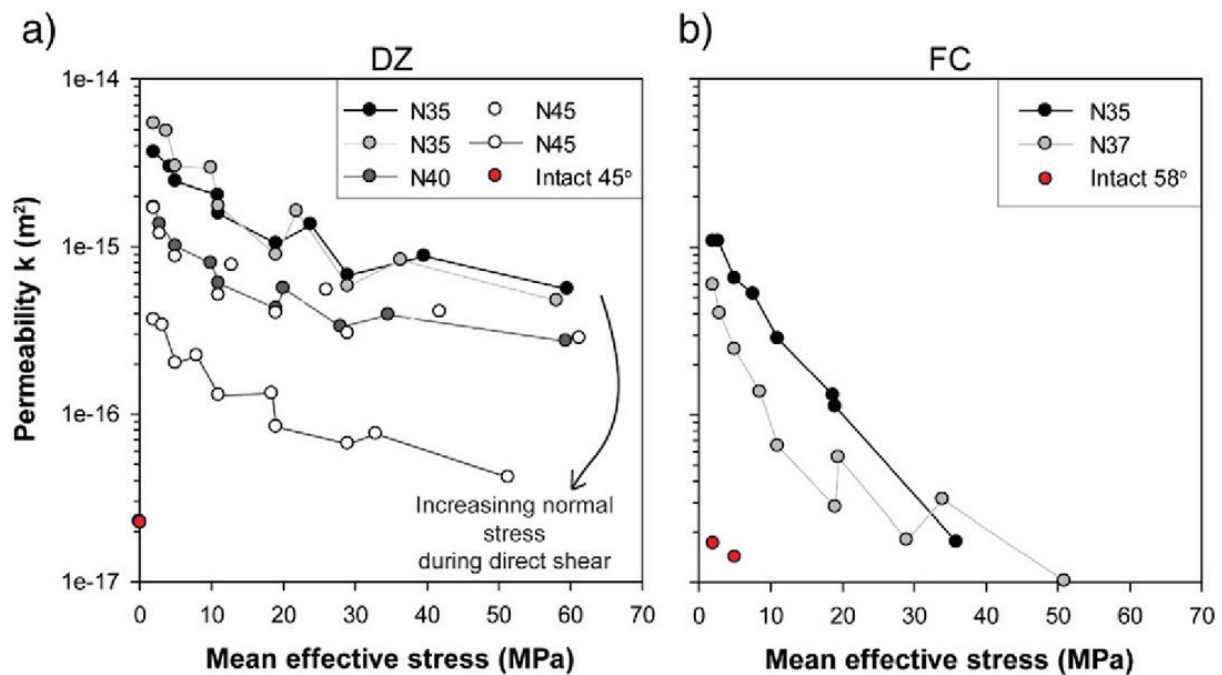


Figure 2-20. Permeability relationship with mean effective stress during triaxial testing on a) damage zone analogue samples and b) fault core analogue samples (from Delle Piane et al., 2016).

2.3 Summary of key knowledge gaps

A comprehensive review of literature has identified several key gaps in the understanding of deformation and fluid flow within non-marine fault rocks:

1. There is a comparative lack of structural studies on deformed non-marine carbonates and a lack of knowledge of whether this is a genuine reflection of atypical structural behaviour of non-marine carbonate or is due to the lack of representation of such deposits within the rock record.
2. There remains a relative lack of hard data of petrophysical properties within non-marine carbonates so the understanding of how these rocks fit within the wider carbonate framework is relatively unexplored.
3. There is limited experimental investigation into the mechanical response of microbial and hydrothermal carbonates to stresses typical of surface and shallow burial depths.
4. Deformation mechanisms within carbonate rocks are observed to be complex, variable and lack intrinsic, empirical relationships that can be used for the prediction of fault zone character and sealing behaviour.

Chapter 3

3. Methodological overview

3.1 Introduction

This study integrates field observations and structural analysis of faults within non-marine carbonates with experimental deformation of travertines to assess the nature of faulting within these deposits. This chapter outlines the methodology for different data collection and analysis workflows used throughout this study. Figure 3-1 illustrates the workflow carried out to integrate the following methods.

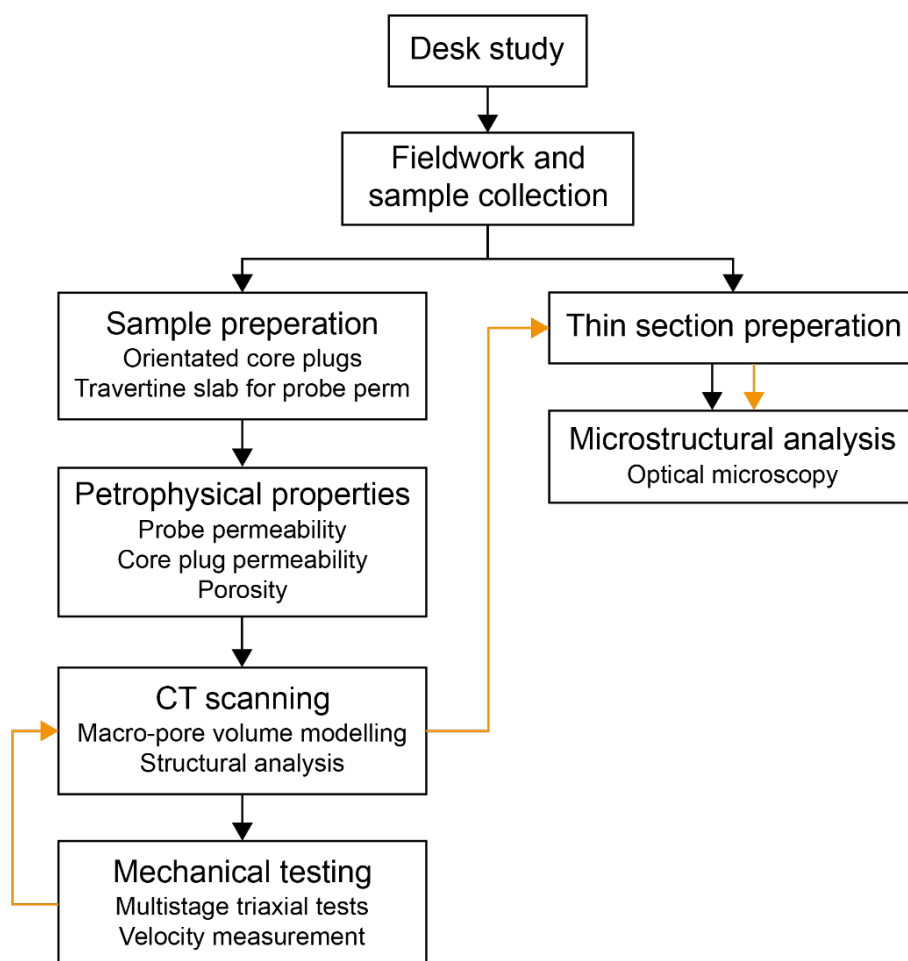


Figure 3-1. Workflow of methods used within this study.

3.2 Field observations and sampling

Fieldwork was carried out in a number of global locations to observe structures within non-marine carbonated (Chapter 4). Structural observations and measurements included:

1. Structural orientations of faults and fractures
2. Fault width and displacement. Displacement was measured from offset markers. Where offset markers could not be observed a minimum displacement was defined by the fault outcrop height.
3. Geological observations of the fault zone and host rock
4. Photography of studied outcrops

Where possible hand specimens were taken from fault zones and fractures for detailed descriptions and for thin sections where possible (in most cases fault rock material was too friable to preserve). Host rock samples (blocks up to 30x20x15) were also taken from travertine localities for petrophysical analysis and mechanical testing (Chapter 5).

3.3 Sample preparation

Three different orientations of core plugs were made from collected travertine sample blocks for mechanical testing and petrophysical analysis. If sample size allowed, core plugs were cored at 0° (parallel), 45° and 90° (perpendicular) to bedding (Figure 3-2a). Where sample blocks could not accommodate coring of all three orientation 0° and 90° orientations were prioritised. A combination of 1.5 and 1 inch diameter core plugs were made. Core plugs were cut to have a length to diameter ratio between 2.5-2:1. Samples ends were then ground flat to an accuracy of 0.02 mm using a diamond sintered grinding wheel to ensure the even distribution of stress on samples during mechanical testing. After plugs were cored, they were oven dried at 65° to remove internal residual water saturations until their weight remained constant for 2 days of measurements.

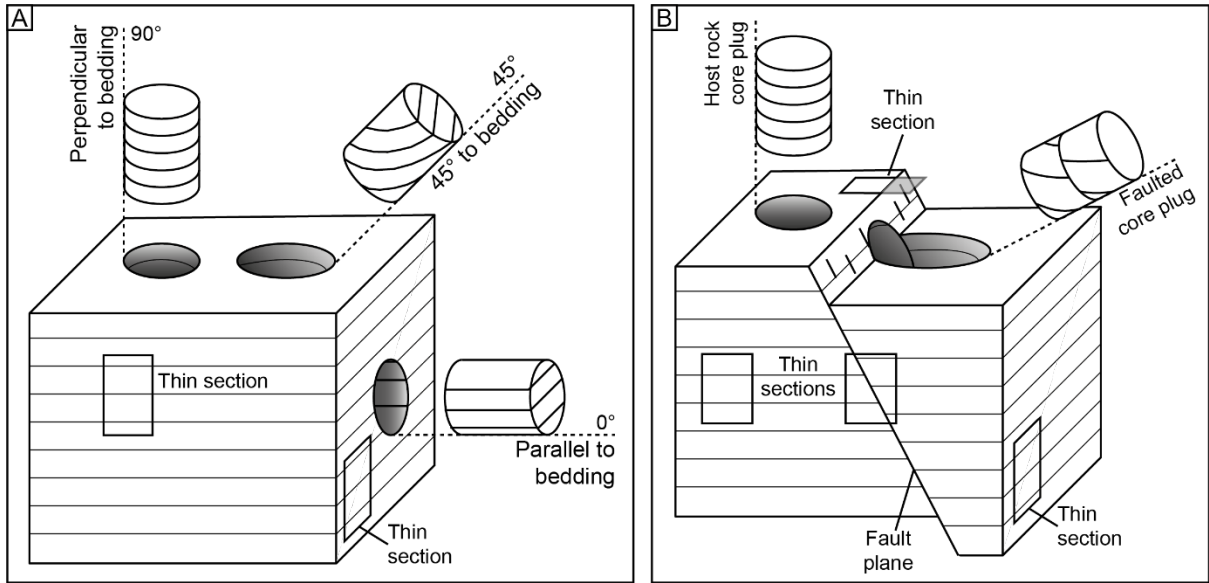


Figure 3-2. Schematic of orientated core plugs and thin sections taken from samples collected. A) Orientated cores taken from undeformed travertine blocks. B) Example of core plug orientations taken from faulted laminated limestone samples. Small blocks for thin sections were taken across faults in plan view and x-section.

In faulted samples (e.g. Crato Formation, Brazil) 1.5-inch diameter core plugs of variable lengths were cored perpendicular to fault planes to measure fault rock permeability (Figure 3-2b). Vertical core plugs were also taken in both the hanging wall and foot wall of faults. Core plugs ends were cut to make sample ends perpendicular to core plug axis. Samples were dried at 65° until sample weights remained unchanged.

3.4 Helium porosity measurements

Porosity of core plugs was calculated from measurement of the bulk volume (BV) and grain volume (GV) of individual core plugs using the following equation:

$$\phi = \left(\frac{BV - GV}{BV} \right) \times 100 \quad (3-1)$$

Bulk volume of core plugs is measured using a calliper to measure length and diameter. Grain volume was measured using the Boyle's Law double-cell method (API, 1998) using a double cell helium porosimeter. Boyles law states that at constant temperate, the volume of a given mass of ideal gas varies inversely with it's absolute pressure:

$$\frac{V_1}{V_2} = \frac{P_1}{P_2} \text{ or } P_1V_1 = P_2V_2 \quad (3-2)$$

The core plug of grain volume is placed into a chamber of known volume (V_2). Helium is then held in a reference chamber of known volume V_1 and pressure P_1 (15 Psi). The two chambers are then connected resulting in a pressure drop (P_2) as helium fills the sample chamber and pore space within the sample. This procedure is repeated three times for each sample and values are averaged to reduce errors. The grain volume of the core plug can then be calculated using Equation 3-2 which can then be used to calculate porosity using Equation 3-1.

3.5 Permeability measurement

3.5.1 Core plug permeability

Permeability (k) of core plugs was measured using a steady-state method in samples with permeabilities > 0.1 mD. Where samples could not be measured using a steady-state method, with permeability < 0.1 mD, they were measured using a pulse decay method. Both were measured using Helium gas with a CoreLab 200 PDP pulse decay permeameter adapted to also measure steady state measurements. Samples are measured under confining pressures of 1500 and 2500 Psi (10.3 and 17.2 MPa) to assess the stress dependency of permeability values. The Klinkenberg values presented in this thesis are measurements taken at 2000 Psi.

3.5.1.1 Pulse decay permeability measurement

The pulse decay method follows methodology outlined by Brace et al. (1968) which measures a pressure transient to calculate flow. The permeameter is composed of an upstream (V_1) and downstream (V_2) gas reservoir at either end of a high-pressure core holder. A differential pressure transducer and downstream pressure transducer were used to monitor pressures. The test procedure is carried out by saturating the sample to a set pore pressure after which the downstream valve is opened to initiate the pressure transient. Calculation of permeability, using the pressure transient, is then automated using methodology of Jones (1997).

3.5.1.2 Steady state permeability measurement

Steady state measurements are based on a modified form of Darcy's Law which accounts for gas compressibility and can be used to calculate permeability using the steady state method with the following equation (API, 1998):

$$k = \frac{2000\mu L Q P_{atm}}{A(P_1^2 - P_2^2)} \quad (3-3)$$

Where k = permeability (mD); μ = dynamic viscosity of the fluid (cP); L = length of core plug (cm); Q = flow rate at ambient conditions (cm³/s); P_{atm} = atmospheric pressure (atms) A = cross-sectional area of the sample (cm²); P_1 = upstream pressure (atms); P_2 = downstream pressure (atms).

The steady state test procedure measures gas at a known flow rate with pressure introduced at the upstream end of the samples. As gas flows through the sample the differential pressure decays. Once flow reaches an equilibrium, the flow rate and differential pressure can be used to calculate permeability using Equation 3-3.

3.5.2 Probe permeability

Probe permeability measurements were taken along three 15cm long transects with measurements spaced every 3 mm, on a flat surface of a travertine block (Figure 3-3) using a probe permeater. Probe permeability uses the steady state method where compressed air is injected into the sample via a probe which is sealed against the sample surface. To relate the equation for linear gas steady state flow (Equation 3-3) the geometric terms of the equation use a dimensionally consistent term (Sutherland et al., 1993):

$$k_{ap} = \frac{2000\mu Q P_{atm}}{(P_1^2 - P_2^2)G_0 a} \quad (3-4)$$

Where a = radius of the seal area and G_0 = is a geometric factor. G_0 is a function of the ratio between the outer radius, r_0 , of the probe seal to its inner radius, r_1 . The probe used had an outer diameter of 8 mm with a 2 mm probe seal diameter. Measurements were taken at several mean pore pressures to apply Klippenberg slip correction. These measurements were then mapped on to an image of the travertine slab to provide visualisation of permeability changes.

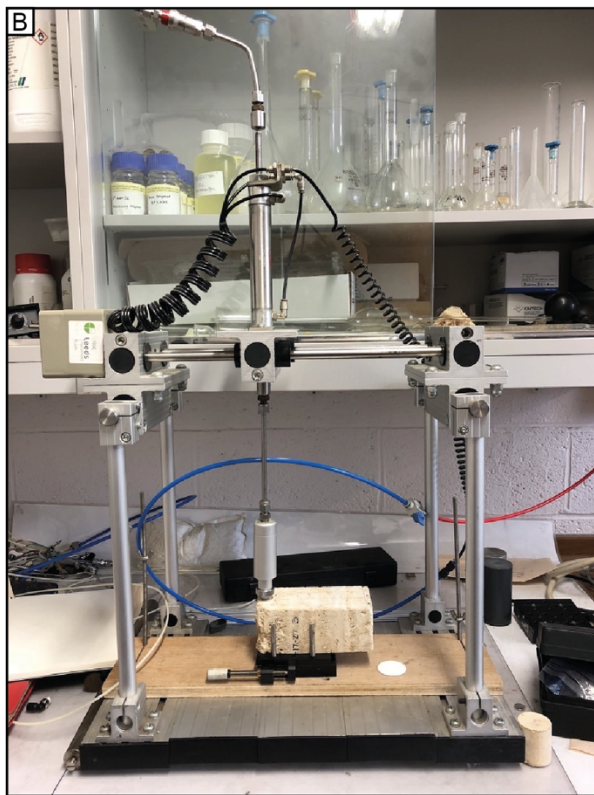
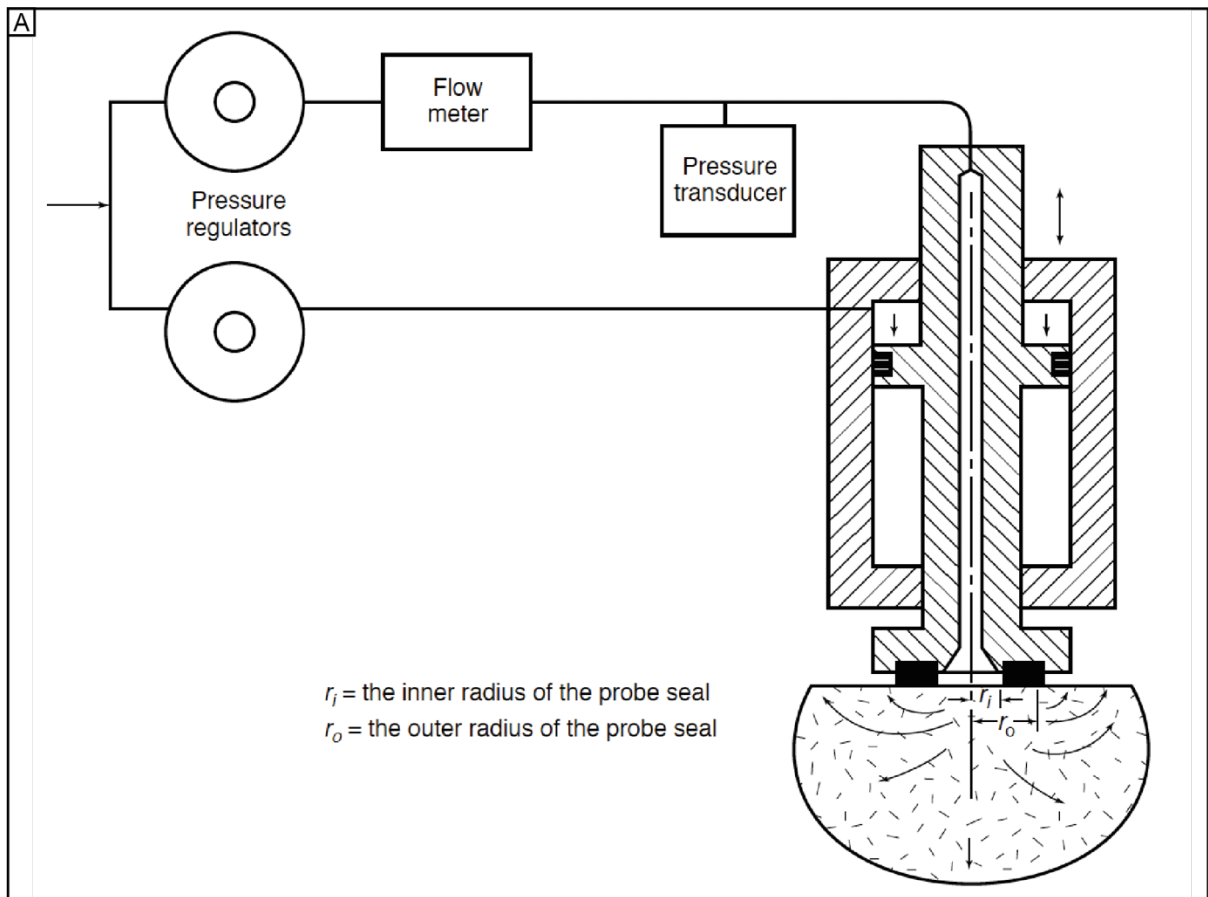


Figure 3-3. Schematic of steady state probe permeameter (API, 1998). B) Probe permeameter set up to take permeability measurements along transects of a travertine slab. C) Example of probe placement on measured samples.

3.5.3 Klinkenberg correction

The use of gas to measure permeability means that flow is subject to gas slippage effects, where, unlike liquid flow, interaction between sample pore walls and gas molecules enable the gas to move in the direction of flow (McPhee et al., 2015). Gas slippage effects are accounted for using a Klinkenberg correction, applied to all measurements to derive the Klinkenberg permeability which is equivalent to the permeability of a non-reactive liquid (McPhee et al., 2015). Klinkenberg correction of each sample is derived through measuring gas permeability (for all permeability methods used) at multiple mean pressures (at least three) (McPhee et al., 2015). Gas permeability data for an individual sample is then plotted against the corresponding inverse mean pressure data (McPhee et a., 2015). Klinkenberg permeability can then be calculated using:

$$k_g = k_\infty \left(1 + \frac{b}{P_m} \right) \quad (3-5)$$

Where k_g is the measured gas permeability data (mD); k_∞ is the Klinkenberg permeability (mD); P_m is the mean pressure (psi); and b is a constant for the measure of slippage.

Using Equation 3-5 Klinkenberg permeability can be derived from linear regression analysis of gas permeability and inverse mean pressure values where k_∞ corresponds to the intercept for P_m^{-1} (Figure 3-4).

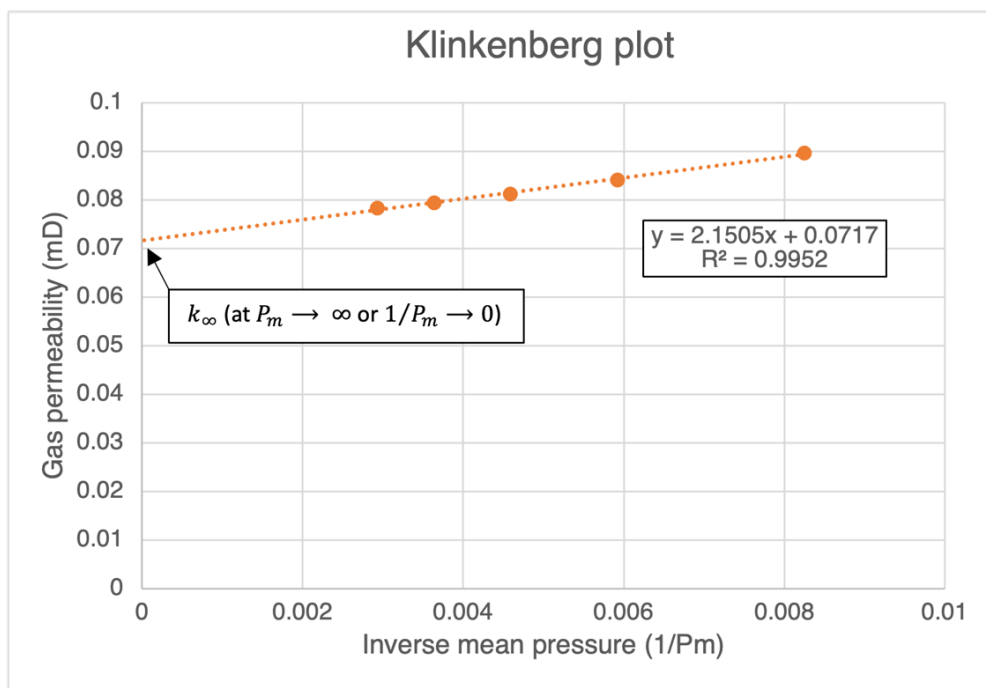


Figure 3-4. Example of Klinkenberg plot from measured permeability data.

3.6 Triaxial testing and velocity measurement

Multistage triaxial tests were carried out on dry core plugs of un-deformed travertine to determine the critical stresses of samples for analysis of failure mechanisms. Multistage tests (i.e. carrying out mechanical triaxial tests at multiple confining pressures on one sample) were used instead of carrying out single triaxial tests on multiple samples due to the high heterogeneity and limited sampling. Tests were also carried out on samples of variable bedding orientation at 0°, 45° and 90° from the direction of principle stress to assess the role of mechanical anisotropy.

3.6.1 Triaxial rig set up

3.6.1.1 1.5 inch samples with velocity measurement

1.5-inch samples were tested using a compression testing rig with a Hoek-type cell (Figure 3-5). Confining pressure was applied to the sample by a hydraulic pump via a rubber sleeve around the circumference of the rock cylinder. The confining stress applied radially defines the minimum stress σ_3 where $\sigma_3 = \sigma_2$.

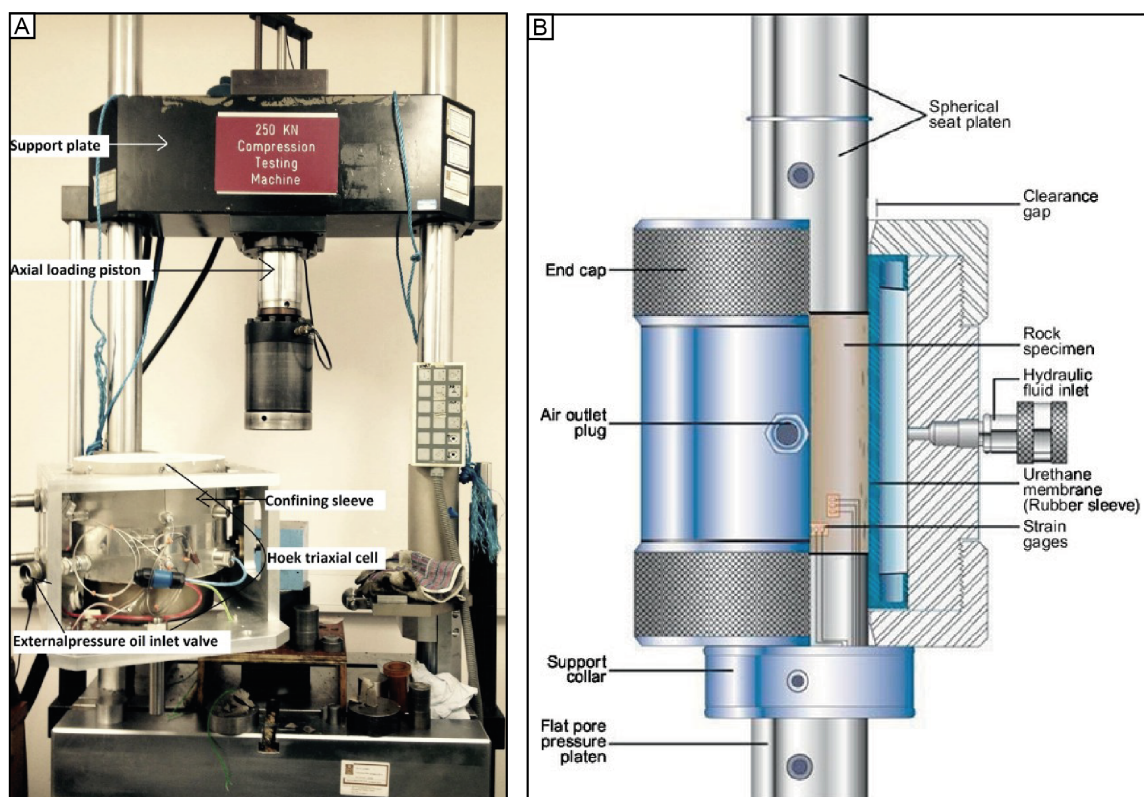


Figure 3-5. Triaxial test set up for measurement of 1.5-inch samples (From Kaminskaite, 2019) A) Overall rig set up. B) schematic of Hoek-type cell used. Platens were adapted to include ultrasonic transmitters and receivers (from McPhee et al., 2015).

The axial strain was measured by an axial linear variable differential transformer (LVDT) attached to the loading ram. The lateral strain was measured in two orthogonal directions using gauges mounted onto the sample horizontally. Axial load is measured with a strain gauge-based load sensor which can then be converted to axial pressure using:

$$\sigma_1 = \frac{F}{A} \quad (3-6)$$

Where σ_1 is the axial (maximum) stress (MPa); F is force applied (N); A is the cross-sectional area of the core plug (m²). Compressive stress and compactive strain are treated as positive so shortening and volume reduction are read as positive values. All measurements (axial load, confining pressure, time, strain data) were plotted in real time for the test procedure and data was stored for later analysis.

The platens at each end of the sample were adapted to measure velocity, with an ultrasonic transmitter built into the top platen and an ultrasonic receiver on the bottom platen. These had split transducers capable of measuring compression (P-waves) and two shear (S1 and S2 waves) velocities. Ends of samples are coated with an ultrasound couplant and covered with a round of thin lead foil between the sample and loading platen. P-waves were transmitted at a frequency of 1 MHz and s-waves transmitted at 0.6 MHz. Received signals were acquired by a digital PicoScope oscilloscope and saved every 2 minutes.

3.6.1.2 1-inch samples (no velocity measurement)

Triaxial tests on 1-inch samples were carried out using an MTS rig with a triaxial cell and confining pressure system (Figure 3-6). A separate confining pressure system is used to fill the triaxial rig with confining oil (which surrounds the jacketed core plug), after which the confining pressure could be controlled by the same operating system as the MTS rig. The core was loaded into a rubber sleeve which has o-rings on each end before having a lateral and axial LVDT attached. Only one lateral LVDT was used for the measurement of lateral strain so core plugs with vertical bedding were loaded with lateral LVDT orthogonal to layers. Core plugs with bedding at 45° dip had lateral LVDT placement parallel to dip direction. An external axial LVDT was also placed on the rig by a magnet to quality check axial measurements. Axial load was measured by a strain gauge-based load sensor which was converted to the principle maximum stress using Equation 3-6. All measurements (axial load, confining pressure, time, strain data) were plotted in real time for the test procedure.

3.6.2 Multistage triaxial test procedure

The same multistage triaxial procedure was carried out on both rigs with the only difference being addition of velocity testing on 1.5-inch samples. In both cases, samples were put into a flexible, thin (< 1mm thick) heatshrink wrap to preserve samples once deformed. Each test consisted of three stages at three different confining pressures at 10, 20 and 30 MPa.

Once samples are loaded into the triaxial rig the pressure is increased hydrostatically (i.e., axial load and confining pressure are increased at the same rate) until hydrostatic pressure reaches 10 MPa. The confining pressure is then held at 10 MPa while the axial load increases at a strain rate of $10^{-5}/s$ which is recommended for permeable samples (McPhee et al., 2015). Confining pressure is kept constant until the imminent failure, which was recognised by an inflection in axial strain when plotted against stress and/or an inflection in the lateral strain against stress. After this point, the confining pressure was increased to 20 MPa and then next stage started. The same procedure was then carried out for the second stage, where the axial load increases at constant confining pressure until immanent failure after which the confining pressure was increased to 30 MPa. During the last stage, at 30 MPa, axial load was increased until the sample underwent failure. Once brittle failure of samples occurred axial loading was then decreased at a constant rate. Once axial load decreased to be equivalent to 30 MPa, sample was unloaded hydrostatically at a constant strain rate ($-10^{-5}/s$).

After testing, data was stored and later analysed to assess critical stresses defined by changes in volumetric strain. Volumetric strain was calculated from axial and lateral strains using the following:

$$\varepsilon_v = \varepsilon_a + 2\varepsilon_l \quad (3-7)$$

Where ε_v is volumetric strain, ε_a is axial strain and ε_l is the lateral strain. Note that accuracy and reliability of volumetric strain is lower in samples tested using only one lateral LVDT (e.g., 1-inch samples).

Yield points from each stage for each sample were used to create Mohr circles to derive Mohr-Coulomb failure envelopes defined by the relationship:

$$\tau = C_0 + \sigma \tan \theta \quad (3-8)$$

Where τ is the shear stress (MPa); C_0 is cohesive strength (MPa); σ is normal stress (MPa); and θ is the angle of internal friction. Linear regression of failure envelopes constructed for

samples can use Equation 3-7 to define the cohesive strength (y intercept) and internal friction coefficient (gradient).

As unconfined compressive tests were not carried out on samples, the unconfined compressive strength (UCS) of samples could not be directly measured. Instead, yield point data from each sample was plotted on a principle stress axis plot where the Mohr-Coulomb failure criterion can be expressed in terms of principle stresses (McPhee et al., 2015):

$$\sigma_1 = \sigma_0 + \sigma_3 k \quad (3-9)$$

Where σ_1 is the maximum principal stress (MPa); σ_0 is the unconfined compressive strength (MPa); and σ_3 is the confining stress (MPa) (i.e. minimum principle stress) and k is the triaxial stress factor. The intercept of the line of best fit of this data is therefore equivalent to the UCS (unconfined compressive strength).

In order to derive yield curves for each sample, mechanical data was also plotted in P-Q space where P is the effective mean stress and Q is the differential stress:

$$P = \frac{(\sigma_1 + 2\sigma_3)}{3} \quad Q = \sigma_1 - \sigma_3 \quad (3-10)$$

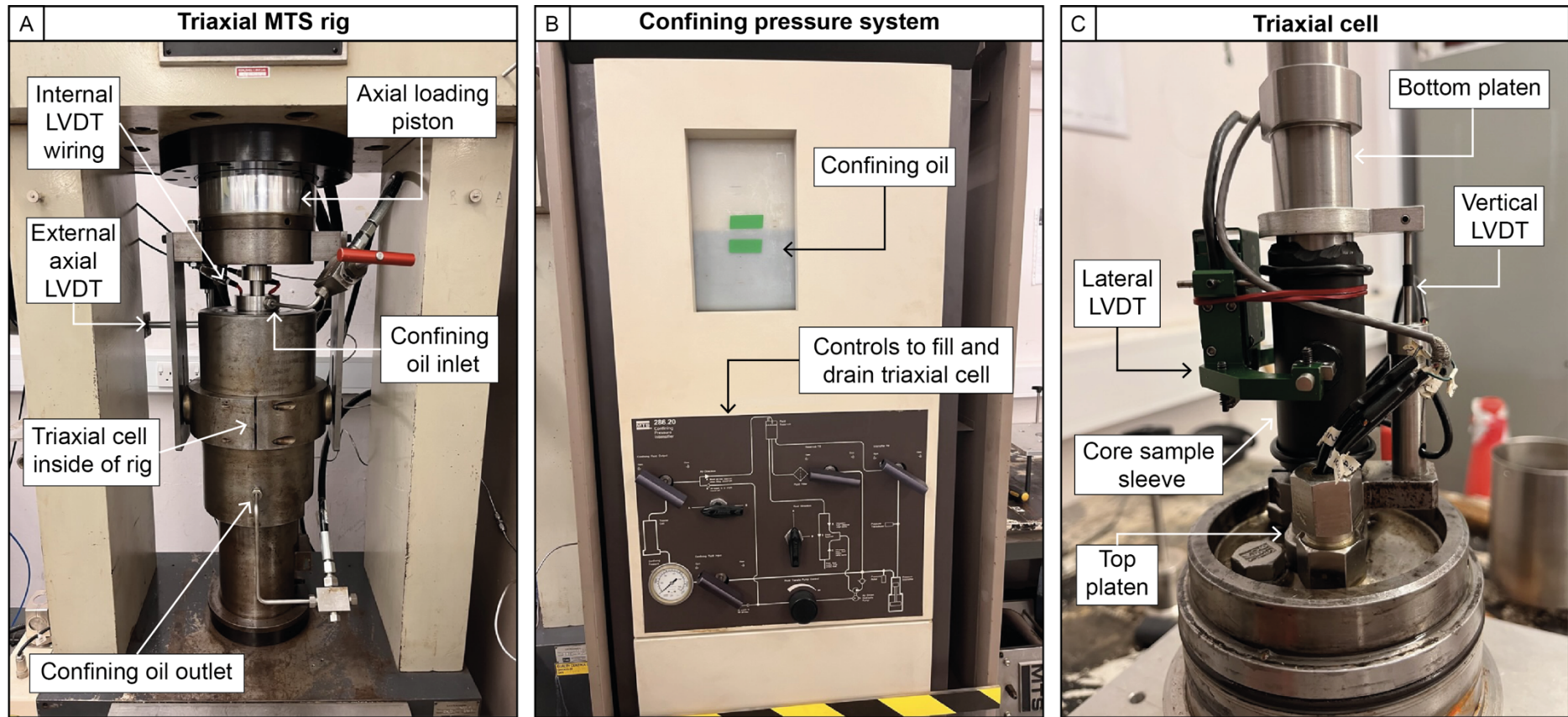


Figure 3-6. MTS triaxial test equipment set up used for 1-inch samples. A) Loaded sample set up of MTS rig. B) Confining pressure system to load and drain MTS triaxial cell with oil. C) Inner triaxial cell.

3.7 CT scanning and image analysis workflow

Axial and helical scans were taken of core plugs using a GE Brivo 385 medical style CT scanner. All scans were taken at 120 kV and 40 μ A producing CT images of 512 x 512 pixels with a pixel size of 187 x 187 μ m². Two perpendicular axial scans were taken of each core plug before and after mechanical failure. Helical (spiral) scans were taken every 0.625 mm along the core with total slices of each sample ranging between 85-98 depending on core length. Core were orientated so scan positions were as close as possible before and after failure. Avizo 3D 2022.1 software was used to create segmented macro-pore volumes from helical scan data. Scans were then segmented using a threshold defined for pore space and rock material. Segmented volumes of pore space were then used to construct a volume from which volume sizes could be defined.

3.8 Microstructural analysis

3.8.1 Undeformed samples

Orientated 2 x 3 cm blocks were cut from samples as close as possible to where core plugs were taken and made into polished thin sections. Thin sections were used for qualitative microstructural observations of host rocks assessing mineralogy and texture using optical microscopy. Scanning Electron Microscopy was also carried out on select samples for textural assessment. A Tescan VEGA3 XM was used to carry out backscattered imaging (BSE) of whole thin sections. Observations from scanning electron microscopy and optical microscopy were used to assess the heterogeneity of mineralogy and pore shape and size.

3.8.2 Deformed core plugs

For samples deformed during triaxial resting, core plug samples were impregnated with resin in a vacuum before being cut into small 2 x 3 cm blocks for polished thin sections. For faulted samples collected in the field (laminated limestones, Crato Formation, Brazil) small blocks were cut directly from the observed fault zones. In both cases, small blocks were orientated to faults planes, both in cross section and in plan view. Polished thin sections were then observed using an optical polarizing microscope to assess texture and deformation microstructure which was used to define deformation mechanisms.

Chapter 4

4. Characterisation of deformation features in non-marine carbonates from field observations

4.1 Introduction

Understanding non-marine carbonate deposits is of increasing importance due to their substantial hydrocarbon reservoir potential, particularly with the development of continental carbonate plays within the 'pre-salt' of the South Atlantic (Carminatti et al., 2008). Similar deposits are also potential reservoir intervals for shallow, low temperature geothermal opportunities (e.g. Aquasanta Terme – Madonna et al., 2005) as well as providing valuable stratigraphic archives of hydrology and palaeoclimate (Anzalone et al., 2007). However, non-marine deposits possess significant heterogeneities related to complex depositional and diagenetic processes, which can be further complicated by deformation during the early stages of their burial (Delle Piane et al., 2017). The nature of faulting within continental-type carbonates and its impact on fluid flow is crucial when considering subsurface permeability in the context of characterizing reservoir quality. Unlike established concepts of fault and fluid flow models within clastic rocks (Knipe, 1992; Yielding et al., 1997; Fisher & Knipe, 1998), the extremely heterogeneous nature of carbonates means that faulting within these deposits is difficult to model and predict (Michie et al., 2018). The difficulty in modelling and prediction of deformation structures within non-marine carbonates is compounded by a relative scarcity of case studies and observations of faulted non-marine carbonates. Though there has been recent significant research into understanding and characterising faults in marine carbonates (Tondi et al., 2006; Billi et al., 2010; Molli et al., 2010; Rath et al., 2011; Michie, 2015; Haines et al., 2016; Delle Piane et al., 2017; Cooke et al., 2018,2019; Ferraro et al., 2019; Kaminskaite et al., 2020; Michie et al., 2014,2020,2021), comparatively little work has been carried out investigating deformation structures in microbial and hydrothermal carbonates. Despite well documented exposures of microbial and hydrothermal carbonates, most existing work has focussed on characterising depositional architecture and palaeoclimate interpretation (e.g., Portman et al., 2005) with no comprehensive investigation into the presence and character of faults within these deposits worldwide.

This study aims to investigate the presence of, and characterise deformation structures within, microbial and hydrothermal carbonate systems to provide key structural analogues, particularly of features that occur within the early burial history of non-marine carbonates. A total of 14 field locations were visited of documented microbial and hydrothermal carbonates exposures deposited prior to or contemporaneous with well-documented structural deformation. The exposures cover a variety of Mesozoic ages (from the Aptian) to the Holocene and tectonic settings, to form a comprehensive atlas of potentially faulted global microbial and hydrothermal exposures (Figure 4-1). This chapter first provides a background of the different non-marine carbonates visited and their depositional setting. Results from an extensive fieldwork campaign is presented, providing insights into faulted outcrops within travertines and laminated limestones. Results are then discussed to assess their deformation mechanisms and possible impacts on fluid flow.

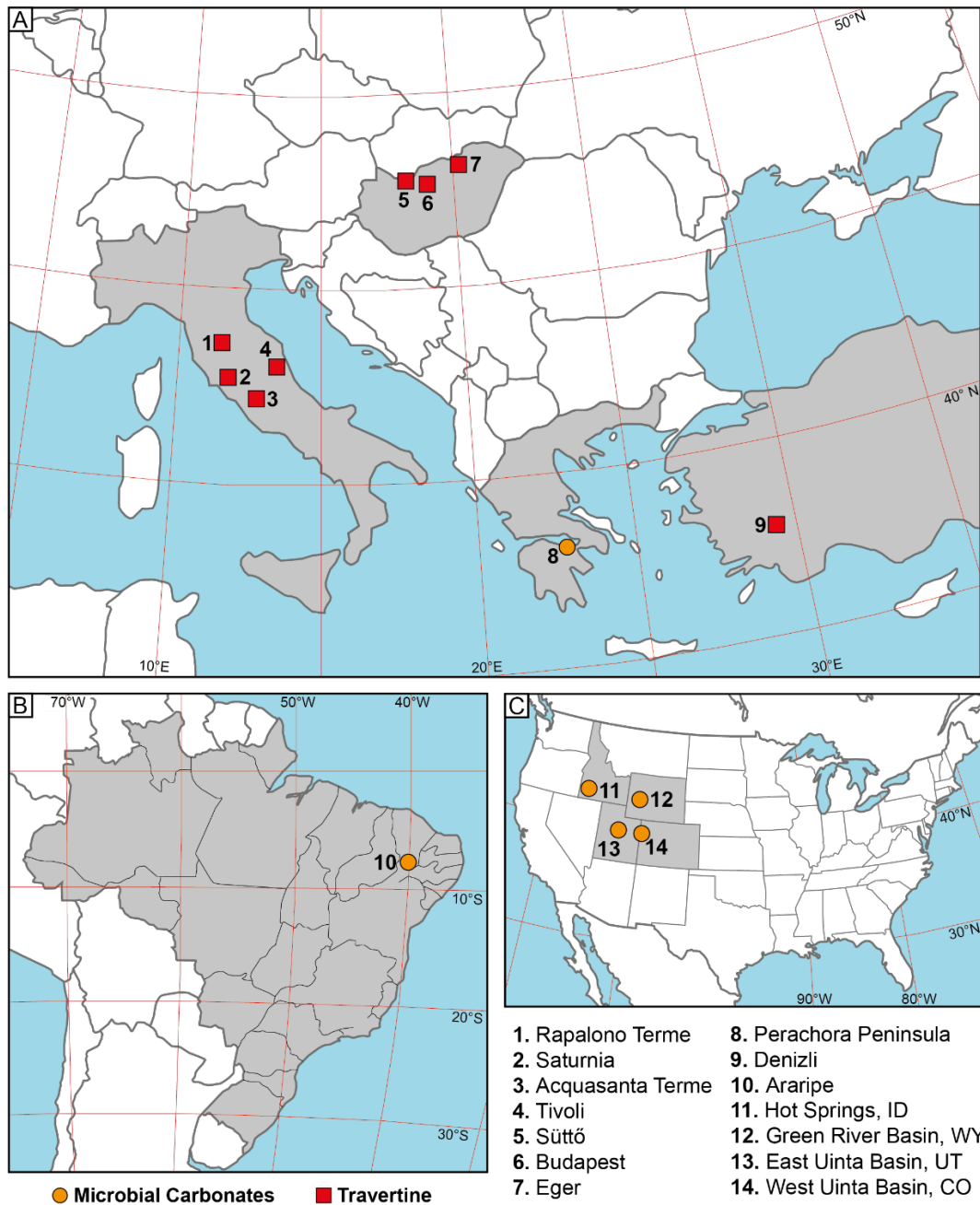


Figure 4-1. Overview of microbial carbonate localities investigated in this study.

4.1.1 Background

This study is comprised of an extensive fieldwork investigation of non-marine carbonates covering multiple localities across the world (Figure 4-1). The investigated exposures of non-marine carbonates can be broadly separated into microbialites (including stromatolites, thrombolites, bioherms) and travertines. Locations were selected based on a preliminary assessment of published non-marine carbonate field case-studies coupled with regional and

local tectonic histories to find suitable formations which may have experienced deformation. Study locations are detailed in Table 4-1 and an overview of the carbonate formations investigated are outlined in Table 4-2.

Table 4-1. Non-marine carbonate formations studied in this thesis with latitude and longitude coordinates.

Formation	Location	Latitude	Longitude
Hot Springs Formation	Idaho, USA	42.759966	-115.75182
		42.764228	-115.74331
		42.767045	-115.73694
Green River Formation	Wyoming, USA	42.368843	-110.23206
		42.364782	-110.19745
Green River Formation	Colorado, USA	39.753887	-109.03968
Green River Formation	Utah, USA	41.224914	-112.87055
		41.219605	-112.85143
		39.831960	-109.11137
		39.815538	-109.10874
Crato Formation	Araripe, Brazil	-7.126377	-39.695873
		-7.113800	-39.697519
Perachora carbonate mounds	Perachora Peninsula, Greece	38.029343	22.851317
		38.036270	22.865323
		38.042193	22.874421
		38.045773	22.880011
Tivoli Travertines	Tivoli, Italy	41.953623	12.742666
Saturnia Travertines	Saturnia, Italy	42.633376	11.511089
		42.688889	11.497942
		42.648061	11.512605
Acquasanta Travertine	Acquasanta Terme, Italy	42.793394	13.438787
		42.785312	13.433826
		42.785312	13.433826
		42.774775	13.424801
Terme San Giovanni fissure-ridge	Rapolano Terme, Italy	42.790933	13.456715
		43.283163	11.591565
Serre di Rapolano Travertines	Rapolano Terme, Italy	43.279367	11.591729
		43.247052	11.617163
		43.248589	11.612326
		43.235734	11.608899
Budakalász travertines/	Buda Hills/	43.236842	11.612399
		47.620556	19.017500
Sütto travertines	Gerecse Hills, Hungary	47.537504	19.028396
		47.742957	18.449612
		47.736446	18.447762
Ballık Travertine Formation	Denizli, Turkey	47.738193	18.459849
		37.872692	29.377373
		37.863392	29.353434
		37.863980	29.339028
		37.923465	29.124104

Table 4-2. Information of different non-marine carbonates investigated in this study.

Formation	Location	Age	Carbonate type	Depositional setting	Tectonic setting	Porosity	References
Hot Springs Formation	Idaho, USA	Miocene	Bioherms	Lacustrine shallow water algal reef	Extensional, early post-rift	5-30%	Straccia et al. (1990) Bohacs et al. (2013)
Green River Formation	Wyoming, USA	Eocene	Caddisfly carbonate mounds	Marginal lacustrine	Compressional, intramontane lakes		Leggit & Cushman (2001)
Green River Formation	Colorado, USA	Eocene	Stromatolites, thrombolites	Marginal lacustrine	Compressional, intramontane lakes	Thrombolite : 2 – 20%	Sarg et al. (2013)
Green River Formation	Utah, USA	Eocene	Stromatolites, thrombolites	Marginal lacustrine	Compressional, intramontane lakes	Stromatolite : 3 – 30% Thrombolite : 10 – 35%	Chidsey et al. (2015)
Crato Formation	Araripe, Brazil	Aptian	Laminated limestones	Biologically induced mineralisation in shallow, epicontinental hypersaline lakes	Extensional, early post-rift		Heimhofer et al., (2010) Catto et al. (2016) Warren et al. (2017)
Perachora carbonate mounds	Perachora Peninsula, Greece	Late Pleistocene	Cynobacterial carbonate mounds	Marginal lacustrine	Extensional, syn-rift		Kershaw & Guo (2003, 2006) Portman et al. (2005)
Tivoli Travertines	Tivoli, Italy	Quaternary	Travertine	Depression fill	Transtensional	2 – 25%	De Filippis et al (2013a,b) Faccenna et al. (2008) Della Porta et al. (2017)

Saturnia Travertines	Saturnia, Italy	Quaternary	Travertine	Smooth slope and terrace system	Transtensional	4 – 30%	Ronchi & Cruciani (2015) Vignaroli et al. (2016) Della Porta et al. (2022)
Acquasanta Travertine	Acquasanta Terme, Italy	Middle Pleistocene	Travertine	Slope apron system	Transtensional	5 – 16 %	Maggi et al. (2015) Della Porta et al. (2017) Jenssens et al. (2020)
Terme San Giovanni fissure-ridge	Rapolano Terme, Italy	Late Pleistocene to present	Travertine	Fissure ridge	Transtensional		Brogi & Capezzouli (2009, 2014) Brogi et al., (2010, 2015)
Serre di Rapolano Travertines	Rapolano Terme, Italy	Middle – Late Pleistocene	Travertine	Slope bodies, terraced mounds, cones and waterfall deposits	Transtensional		Brogi et al. (2009)
Budakalász travertines/ Sütto travertines	Buda Hills/ Gerecse Hills, Hungary	Quaternary	Travertine	Terrace and smooth slopes, reed and marsh pool. Fissure ridge	Extensional within back-arc of Aegean-Carpathian collision	5 - 27 %	Kele et al. (2003) Seirralta et al. (2010) Török et al. (2017, 2019) Claes et al., (2017)
Ballık Travertine Formation	Denizli, Turkey	Pliocene	Travertine	Slopes, depression fill, fissure ridge and mounds	Transtensional and extensional	3 – 30 %	Özkul et al. (2002) El Desouky et al. (2015) Alçiçek et al. (2016) Van Noten et al. (2013, 2019)

4.1.1.1 Microbial carbonates

A total of 6 different microbial carbonate formations were assessed for this study: Hot springs Formation, Idaho, USA; Green River Basin, Wyoming, USA; East Unita Basin, Utah, USA; West Unita and Piceance Creek Basins, Colorado, USA; Perachora Peninsula, Greece; Crato Formation, Brazil. Though these localities have been broadly grouped together as microbial carbonates, they showcase the variability and different types of microbialites, within several different basin settings briefly explained herein.

Hot Springs Formation, Idaho, USA

The Miocene Hot Springs Formation in Southeast Idaho is a lacustrine shallow-water algal reef (Figure 4-2a) which is exposed over an 80 km² area (Straccia et al., 1990; Bohacs et al., 2013). The sequence is characterised by concave-upward conical bioherms separated by grainstones and can develop into bioherm complexes (Bohacs et al., 2013). In a reservoir analogue study carried out by Bohacs et al. (2013), the character of microbialites (i.e. size, type, porosity, permeability) is found to correlate to the stratal position and location along the depositional profile. Microbial morphologies and their dependant porosities (5-30 %) within the Hot Springs formation are seen to be highly variable and connectivity of microbial bioherms and grainstones are dependent on their sequence-stratigraphic position (Bohacs et al., 2013).

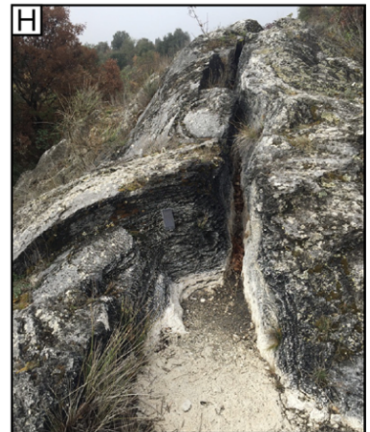
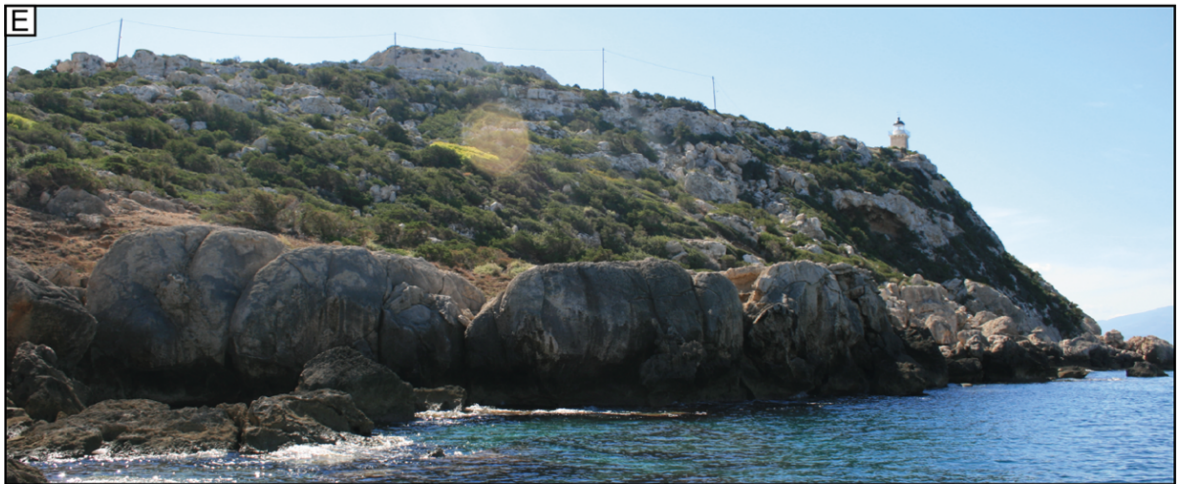
Green River Formation, Wyoming, Utah and Colorado, USA

The Eocene microbial-dominated Laney Member defines a marginal lacustrine system of the Green River Formation (Seard et al., 2013), deposited across the Greater Green River Basin, Uinta and Piceance Creek lacustrine basins which span across modern day Wyoming, Utah and Colorado (Leggitt & Cushman 2001; Seard et al., 2013). These lacustrine basins formed intramontane lakes within the foreland of the Cordilleran fold and thrust belt formed during the Cretaceous to Eocene Laramide Orogeny (Smith et al., 2008).

Along the northern margin of Lake Gosuite, in the Greater Green River Basin, in South-West Wyoming the Green River Formation hosts carbonate mounds up to 9 m in height and 40 m diameter and are observed in reef-like geometries along a 70 km outcrop (Leggitt & Cushman 2001, Figure 2b). These large carbonate mounds (Figure 4-2b) are formed through the coalescence of smaller columns (1-2 m tall) which are composed of caddisfly larval cases surrounded by layers of tufa and stromatolite (Leggitt & Cushman 2001). The Eocene Green River Formation also crops out along the western margin of the Piceance Basin in Western Colorado. Here the formation is characterised by deepening-upward cycles formed of

grainstones and packstones followed by stromatolites and thrombolites and capped by fine-grained stromatolites and/or oil shale deposits (Sarg et al., 2013). The Uinta Basin Green River Formation hosts lacustrine microbial carbonates characterised by thrombolites and stromatolites (Figure 4-2c/d) and are inferred to be deposited in a lake margin setting in the littoral to sublittoral zone (Chidsey et al., 2015).

Figure 4-2. (Next page). Non-marine carbonate examples. A) Bioherm, Hot Springs Formation, Idaho (USA). B) Caddisfly microbial mound, Green River Formation, Wyoming (USA). C) Stromatolite, Green River Formation, Utah (USA). D) Cyanobacterial carbonate mounds, Perachora Peninsula, Greece. E) Saturnia Hot Springs, Italy. F) Saturnia travertine hot springs, Italy. G-H) San Giovanni Fissure Ridge, Italy.



Crato Formation, Brazil

The laminated limestones of the Crato Formation form a part of the Aptian post-rift sequence in the Araripe Basin (Heimhofer et al., 2010), located in NE Brazil. The basin evolution was strongly controlled by extensional tectonics accompanying the opening of the southern and equatorial branches of the South Atlantic rift system during the Early Cretaceous (Catto et al., 2016) resulting in the formation of a suite of NE-SW trending half grabens including the Araripe Basin (Heimhofer et al., 2010). Cessation of rifting in the Aptian was accompanied by deposition of the early post-rift Santana Group (Heimhofer et al., 2010) consisting of deltaic to lacustrine sediments forming the Rio da Batateiras and Crato Formations overlain by evaporates of the Ipubi Formation and marginal marine shales of the Romualdo and Arajara Formations (Heimhofer et al., 2010).

The Nova Olinda member is the thickest limestone horizon of the Crato Formation and is known worldwide as a Fossil Lagerstätte due to the excellent preservation of macrofossils (Catto et al., 2016). Carbon and oxygen isotope analysis, as well as presence of fish fossils indicates that this formation is lacustrine in origin (Warren et al., 2017) and the presence of halite pseudomorphs indicates the system had hyper-saline conditions for periods of deposition (Martill et al., 2007). However, the formative processes of this hypersaline condition have remained somewhat ambiguous (Heimhofer et al., 2010; Catto et al., 2016; Warren et al., 2017). These laminated limestones can be regarded as analogous to the low permeability lacustrine facies in the pre-salt Barra Velha reservoir formation in the Santos Basin (Miranda et al., 2018).

Perachora Peninsula, Greece

Late Pleistocene cyanobacterial carbonate mounds (Figure 4-2e) occur along the western portion of the Perachora Peninsula, an uplifted horst block in the eastern Gulf of Corinth (Kershaw & Guo 2003/2006; Portman et al., 2005). The Gulf of Corinth is a presently active, E-W trending rift basin active since ~5 Ma within the back-arc of the Hellenic orogen (Papanikolou & Royden, 2007; Gawthorpe et al., 2018). The Perachora Peninsula formed as part of the uplifted Gerania block which segmented the main Corinth Gulf from the Alkyonides Gulf and hosts the Perachora Fault Segment Boundary (Kershaw & Guo 2003,2006; Leeder et al., 2005; Portman et al., 2005). Cyanobacterial carbonate mounds or 'bioherms' have been uplifted within the footwall of the Perachora Fault, forming raised wave-notches, dated to relate to several interglacial high-stands throughout the Late Pleistocene and Holocene (Leeder et al., 2005). These mounds measure up to 10 m high and several tens of metres wide with a

bulbous morphology and are thought form in shallow water and follow a palaeo-terrace bounded by steeply dipping coastal faults (Kershaw & Guo 2003/2006; Leeder et al., 2005; Portman et al., 2005).

4.1.1.2 Travertines

The deposition and formation of travertine bodies has been extensively studied and are often used as analogue models for microbial reservoirs such as those in the South Atlantic Pre-Salt sequence (Claes et al., 2015,2017; Ronchi & Cruciani, 2015; Cook & Chafetz, 2017; Giwelli et al., 2017; Chafetz et al., 2018; Mancini et al., 2019; Verbiest et al., 2021). However, these studies focus on reservoir characteristics of travertine facies and their wider deposits and are often discussed as the product of deformation [sometimes termed 'travertonics' (Hancock et al., 1999; Brogi et al., 2021)] (Altunel & Karabacak, 2005; Brogi & Capezzouli 2009; Brogi et al., 2010; Mesci et al., 2020). Here six individual travertine bodies have been studied to evaluate the impact of faulting within these sequences: Tivoli plateau travertines, Italy; San Giovanni Fissure Ridge, Italy; Saturnia, Italy; Acquasanta Terme, Italy, Suttö travertine; Hungary; Ballık travertine; Turkey.

Tivoli plateau travertines, Italy

The extensively quarried plateau travertines, located ~25km east of Rome within the Acque Albule basin (De Filippis et al., 2013a,b), covers a 20 km² region (Faccenna et al., 2008), forming one of the largest known travertine deposits of Quaternary age in the world (De Filippis et al., 2013a,b). The Tivoli plateau is characteristic of massive thermal deposits formed of bedded travertine within a tectonic depression resulting in little development of topography (Faccenna et al., 2008; De Filippis et al., 2013a,b). The Acque Albule basin sits within an eastward piggy-back basin within Late Miocene-Pliocene thrust sheets associated with the central Apennines fold-thrust belt which has undergone post-orogenic extension from the Pliocene onwards in relation to back-arc extension in the Tyrrhenian Sea (Billi & Tiberti, 2009).

These plateau travertines, made up of sub-horizontal benches (Della Porta et al., 2017), separated by erosional surfaces are aligned with a N-S striking strike-slip fault (Faccenna et al., 2008) which fed hydrothermal fluids through a central conduit preserved as several active and inactive vents and springs along the fault (De Filippis et al., 2013a,b).

Saturnia, Italy

Pleistocene to present day travertine deposits are found in the northern part of the Albegna Basin (southern Tuscany, central Italy), a NE-SE trending Neogene basin filled by Miocene to

Quaternary marine and terrestrial deposits (Ronchi & Cruciani, 2015; Vignaroli et al., 2016; Della Porta et al., 2022). Travertine deposition is associated with Neogene and Quaternary magmatic activity promoting an active geothermal system along (Della Porta et al., 2022) a network of N-S and E-W striking transtensional fault arrays (Vignaroli et al., 2016). The depositional setting is characterised by a gentle dipping slope with localised terrace systems (Ronchi & Cruciani, 2015). Present-day travertine deposition along the Gorello waterfall and hot springs in Saturnia (Figure 4-2f) provides a present-day analogue of the terraced slope travertine facies associated with these formation types.

Acquasanta Terme, Italy

The Acquasanta Travertine deposits comprise of Middle Pleistocene travertine slope aprons. The Acquasanta deposits are located on the eastern side of the central Apennines, a Neogene fold and thrust belt formed due to the convergence of the European and Adria-African continental blocks (Maggi et al., 2015; Della Porta et al., 2017; Castorina et al., 2020; Janssens et al., 2020). Travertine overlies Oligocene-Miocene marls which form the upper layer of the folded stratigraphy which form the Acquasanta Anticline, a N-S striking, E-verging fold (Maggi et al., 2015; Della Porta et al., 2017). Travertine slope aprons comprise of three uplifted terraces which prograde towards the Tronto River valley with the oldest terraces at the highest topographic elevations (Jenssens et al., 2020). Deposition is thought to be controlled by NW-SE trending normal faults and N-S trending strike slip faults, which cross-cut the anticline where the folded Mesozoic-Cenozoic carbonate succession provide a Ca-rich source (Maggi et al., 2015). Locally travertine bodies are characterised by several different depositional facies including hydrothermal mounds, moderate to gentle slopes, terraced slopes and shallow ponds (Maggi et al., 2015; Della Porta et al., 2017).

San Giovanni Fissure Ridge, Italy

The San Giovanni fissure ridge (Figure 4-2g/h) is located ~1 km SW of Rapolano Terme, central Italy, located on the eastern side of the Siena Basin (Brogi & Capezzouli, 2009, 2014; Brogi et al., 2010, 2014) within the Northern Apennines fold and thrust chain (Aldinucci et al., 2007; Brogi et al., 2017). The Late Pliocene to Holocene travertines (Brogi et al., 2017) form isolated bodies which can be up to 40 m thick in places (Guo & Riding, 1998). Travertine deposition throughout the Late Pleistocene was driven by springs of hydrothermal fluids (~39°C) originating from a shallow reservoir within a Late Triassic to Early Cretaceous carbonates succession which are still active today (Guo & Riding, 1998, 1999; Brogi & Capezzouli, 2014; Brogi et al., 2017).

Pannonian Basin, Hungary

The late Cenozoic Pannonian Basin hosts widely distributed Quaternary travertine occurrences, though these are predominantly found in the Gerecse (Seirralta et al., 2010; Török et al., 2017,2019; Claes et al., 2020) and Buda Hills (Claes et al., 2017) in northern Hungary. The Pannonian Basin, which covers the central part of the European Alpine belt developed as a result of extensional tectonics originating in the Miocene within the back-arc of the Carpathian and Dinaride collision zones (Matenco & Radivojević, 2012) resulting in the evolution of several sub-basins. This extension has been followed by the formation of several uplifted areas during Miocene-Quaternary inversion, although this is relatively minor (Matenco & Radiojević, 2012). Relatively high geothermal gradients and elevated heat flow associated with this extension in the late Early to Late Miocene provides the region with abundant thermal waters (Török et al., 2017; Claes et al., 2017). Both the Gerecse and Buda Hills are part of the Transdanubian Range; a NE-SW elongated synclinal structure consisting of predominantly Triassic carbonates and hosts an essentially continuous large-scale karstic groundwater reservoir providing carbonate rich thermal fluids for travertine precipitation at the surface (Claes et al., 2017; Török et al., 2017). Studies in this area have largely focussed on travertine deposits in reference to palaeo-terraces of the Danube as they are a key tool in correlating different terrace levels and can be used to estimate uplift rates and river levels with deposits becoming younger towards to River Danube (Kele et al., 2003; Seirralta et al., 2010; Ruszkiczay-Rüdiger et al., 2018; Török et al., 2019).

Travertine formation in the Buda Hills is complex travertine system controlled by a NW-SE trending fault and consists of low angle travertine lobes with terrace slope, smooth slope and reed facies which overall are covered by marsh-pool facies. An analysis of geobody architecture conducted by Claes et al. (2017) illustrates the complex nature of these deposits and shows how, over a km-scale, petrophysical properties can vary widely. In this case porosities varying between 5 – 15% were found in terrace, smooth slope and marsh-pool facies while porosities were found to also reach up to 27% in reed facies (Claes et al., 2017).

Almost 50 travertine bodies have been identified in the Gerecse Hills (Seirralta et al., 2010; Ruszkiczay-Rüdiger et al., 2018). The Sütto travertines are one of the largest of these deposits and represent travertine deposition in reed mound, slope, lacustrine and palustrine environments from fluids likely controlled by underlying faults (Török et al., 2017). Török et al. (2019) also identified a fissure ridge system along a NW-SE trending fault.

Ballık Travertine Formation, Turkey

The Ballık travertine deposits in SW Turkey form part of the recent Neogene fill within the Denizli Graben Horst Structure (DGHS), a WNW-ESE trending structure within the West Anatolian Extensional Province in SW Turkey (Bozkurt & Mittwede, 2005; Koçyiğit, 2005; Kajmakci, 2006; Alçiçek et al., 2007, 2013; Van Noten et al., 2013, 2019; Özkaymak, 2015; Claes et al., 2017). Travertine deposition is thought to be closely related to the local Miocene-Pliocene magmatic activity (El Desouky et al., 2015), which is also why the DGHS is famous for its extensive geothermal fields (Kaypak & Gökkaya et al., 2012; Brogi et al., 2014; El Desouky et al., 2015; Alçiçek et al., 2016), which is considered to promote decarbonisation of Triassic limestones and act as a heat source for hydrothermal fluid circulation (El Desouky et al., 2015).

An extensive structural and paleostress investigation of this area was carried out by Van Noten et al. (2013, 2019) describing the localised multi-phase deformation of the Ballık travertines. The study concluded that WNW-ESE faults within the travertine body formed during a long-lived phase of NNE-SSW extension during the early Pleistocene which were later reactivated as sinistral strike slip faults during in which the Ballık area acted as a transfer zone during NNW-SSE extension. Later NNE-SSW extension during the late Pleistocene to present day was re-established resulting in further deformation and reactivation of existing faults accompanied by active travertine deposition.

4.2 Methodology

4.2.1 Field investigation

Detailed structural observations were taken during several field excursions with a focus on brittle structures. Quarried outcrops provided excellent 2D and 3D exposure of the studied sequences. Fieldwork investigation of brittle features included qualitative observations including fault geometry, fault zone characteristics, fault kinematics and fault rock type/distribution. Quantitative structural data including, fault orientation, apparent displacement, fault thickness and slickenside orientation were also collected. In several instances, certain fault rocks could not be sampled as these consisted of mainly friable material.

4.2.2 Microstructural analysis

Oriented polished thin sections from small-scale faulting (<5 cm) within the Crato Formation, Brazil were analysed using an optical microscope and a Tescan VEGA3 XM was used to carry out backscattered imaging (BSE) of whole thin sections. Observations from scanning electron microscopy and optical microscopy were used to assess texture and deformation microstructure.

4.2.3 Petrophysical analysis

In the case of the Crato Formation, samples of small-scale faults (<5 cm) were collected. Oriented core plugs, perpendicular to the fault plane, were taken from collected samples for porosity and permeability measurements. A full description of the petrophysical methods used for porosity and permeability are outlined in Chapter 3. Briefly, porosity was derived through measuring grain volume using the Boyle's law double-cell method with helium gas and bulk volume measurements of core plugs using a caliper to measure length and diameter (API, 1998). Single phase gas permeability was measured using a pulse-decay method. Testing followed methodology and apparatus set-up detailed in API (1998). Permeability analysis for each sample was conducted at both 1500 and 2500 psi to mimic subsurface condition and evaluate stress dependency. To account for gas slippage effects Klinkenberg corrected permeability was calculated as described by Klinkenberg (1941).

4.3 Results

4.3.1 Microbialites

Of the 6 microbialite localities visited, only the laminated limestones of the Crato Formation exhibited any structural features and are discussed in the following results. Whilst the other formations discussed in section 4.1.1 are in locations where local and regional tectonics are known to produce deformation structures in the area, exposures studied in USA and Greece contained no major structural features within microbialites. In the Perachora Peninsula (Greece), microbialites were observed to be fault bound, but with no observed deformation within the microbialites themselves. Fault structures mapped as offsetting certain bioherms within Portman et al. (2005) produce topographic breaks with no preservation of fault planes or deformation preserved.

4.3.1.1 Small scale faulting of the Crato Formation

Nova Olinda host rock characteristics

The Nova Olinda member of the Crato Formation is exposed in several quarries 2-3 km southwest of the small town of Nova Olinda (Figure 4-3). The Crato Formation is formed of laterally continuous, planar, millimetric layers defined by variable organic content and are often categorised into two facies types: i) those that are characterised by light to dark brown laminations and ii) typical ‘blue’, laminated limestones which have distinct dark-pale alternation or banding (Heimhofer et al., 2010). Pervasive secondary alteration is also observed within the Crato Formation, where yellowish-brown alteration illustrates the oxidation of organic matter from meteoric water circulation (Cabral et al., 2019; Alencar et al., 2021). Pale laminae are characterised by dense and homogenous texture composed of microcrystalline calcite grains (Figure 4-4 to Figure 4-6). The darker layers are characterised by significant concentrations of organic material and clay minerals (Figure 4-4 to Figure 4-6).

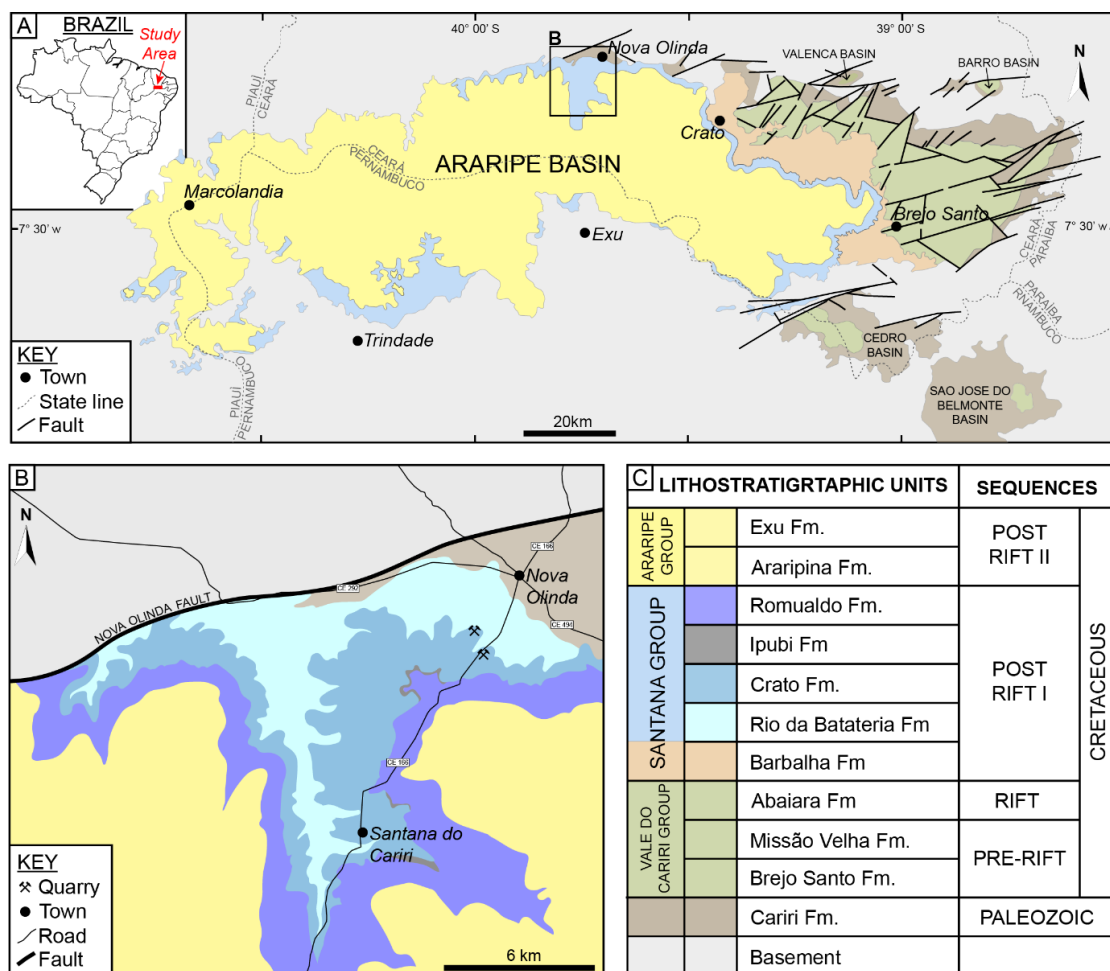


Figure 4-3. A) Regional Geology of the Araripe Basin, Brazil. B) Local Geology of Nova Olinda. Quarry locations indicate laminated limestone exposures. C) Lithostratigraphy of the Araripe Basin. (Modified after Catto et al., 2016)

Deformation features and architecture

The Nova Olinda member of the Crato Formation is observed to be cross-cut by a series of small-scale extensional faults (< 25 cm throw). One set of conjugate faults are observed in the Nova Olinda Formation which trend NNE-SSW. Both have dips ranging from 40-60°. Faults are typically characterised by a complex series of laterally and vertically anastomosing fault planes visible due to the contrast between dark grey/brown organic and clay-rich layers and light grey/white calcite layers.

Figure 4-4 illustrates the common geometry and exposure of faulting observed within the Nova Olinda Member. As the example shows it is common for faults to occur in conjugate sets with a throw up to 20 cm. Generally, these faults are continuous through the whole exposed sequence though commonly anastomose and splay into multiple planes across a very thin fault zone up to 5 cm wide with complex and heterogeneous segmentation (Figure 4-4f/g; Figure 4-5; Figure 4-6). Both the field exposure in Figure 4-4 and hand specimen example in Figure 4-5 have been altered by meteoric waters resulting in oxidation of organic material within the deposits.

Though there are instances where altered laminations appear to be faulted, alteration still appears to have affected the fault itself suggesting that alteration occurred post-faulting as locally uses the fault as a pathway to follow higher permeability layers. As the fault plane is not completely altered it appears that higher permeability layers and vertical fractures controlled alteration. Both bedding parallel and vertical mode 1 fractures are observed to cross-cut faulting and are often observed with an adjacent alteration halo which suggests that these fractures, along with higher permeability laminations, act as fluid pathways for meteoric waters resulting in extensive alteration of the sequence.

Locally, the fault plane can appear darker in colour compared to the host rock, especially in samples with a high concentration of clay rich layers (e.g. Figure 4-5). The individual fault planes of the 2 cm throw fault in Figure 4-5 are millimetric in width and are dark black planar features where the sample is unaltered. Where the fault is altered the faults are recognised by dark brown millimetre thick planes (Figure 4-5a). Thin sections taken from the fault zone permit investigation of the fault material where the dark colourisation of unaltered fault planes is a result of increased organic and clay content smearing into the fault plane (Figure 4-5d-g). The continuity of clay and organic material within the fault planes is limited even at these very low throws, and display thinning and breaking of smearing as observed in Figure 4-5e/f.

In contrast, Figure 4-6 illustrates a fault where the fault planes are not easily identifiable without bedding offsets as kinematic markers. The fault planes show similar geometries but lack the concentration and smearing of organic material as seen in Figure 4-5. Figure 4-6c-k illustrate these small-scale faults in thin section. Figure 4-6i-k shows that fault planes are not as sharp and distinctive as those seen in Figure 4-5 and are characterised by a mm wide zone which lacks any bedding.

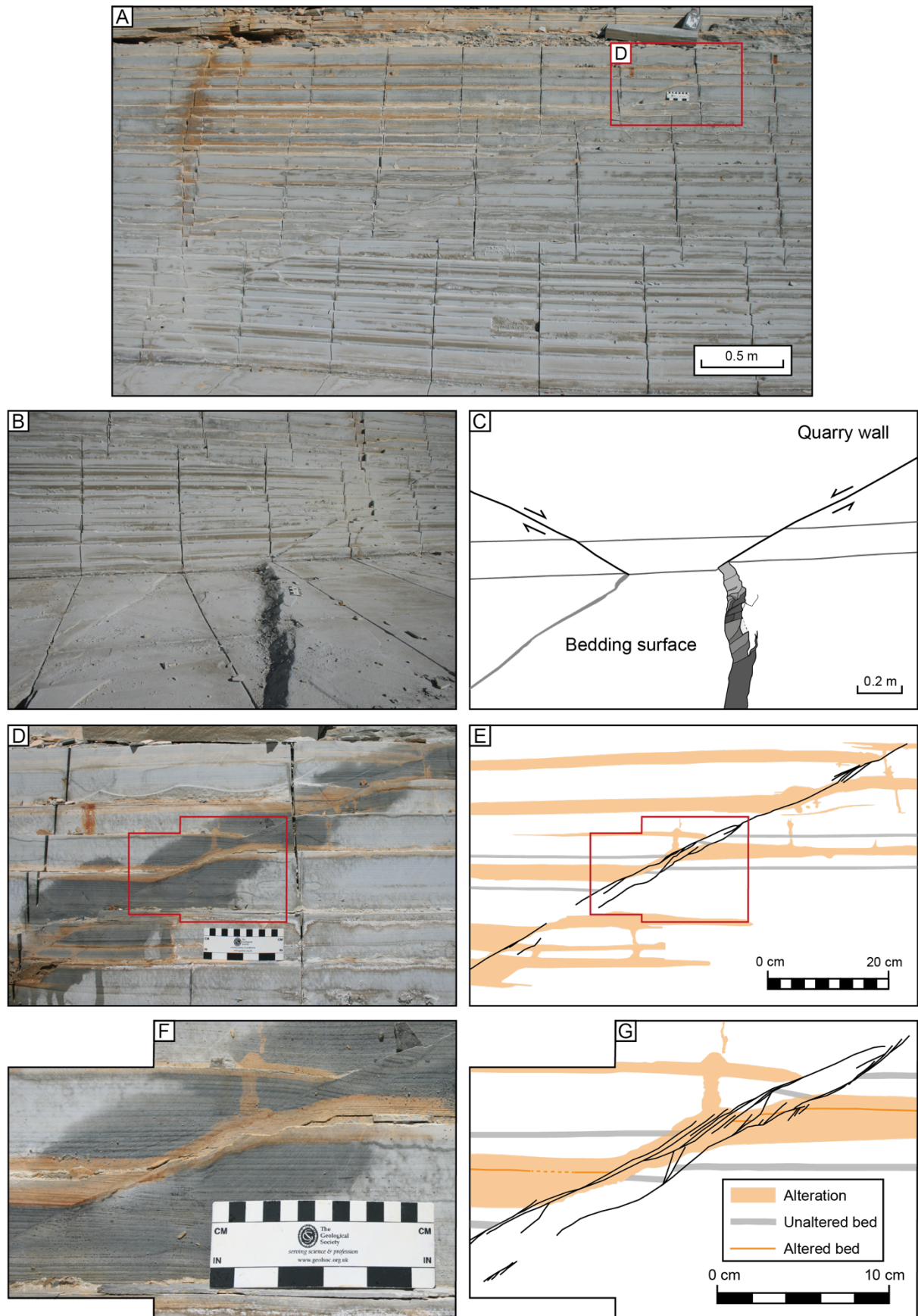


Figure 4-4. Field example and corresponding schematics of small-scale faulting in the Nova Olinda member from the Crato Formation.

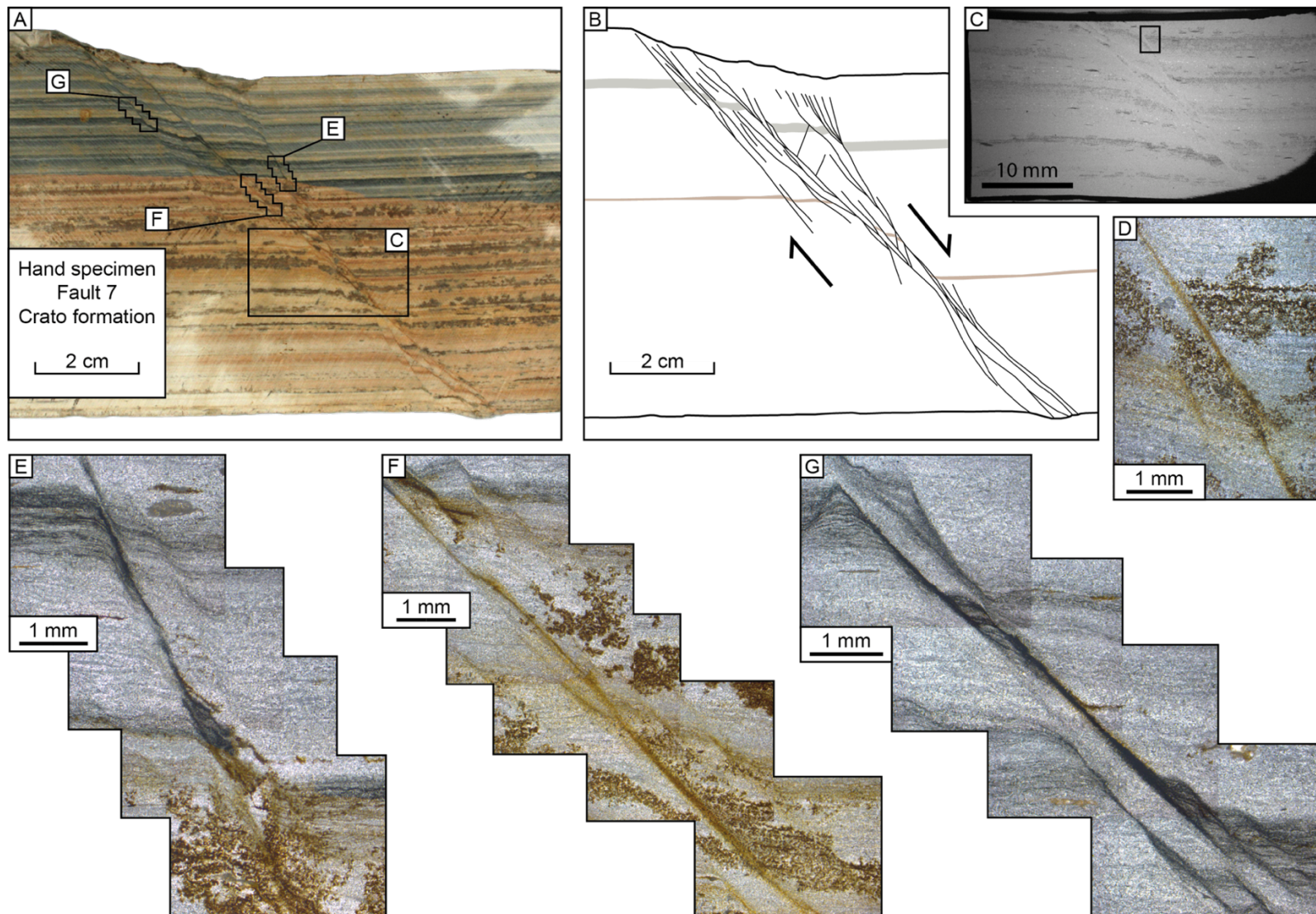


Figure 4-5. A/B) Hand specimen and schematic of faulted laminated carbonates from the Crato Formation. C) SEM image of faulted segment. D-E) Photomicrographs of fault planes taken from specimen.

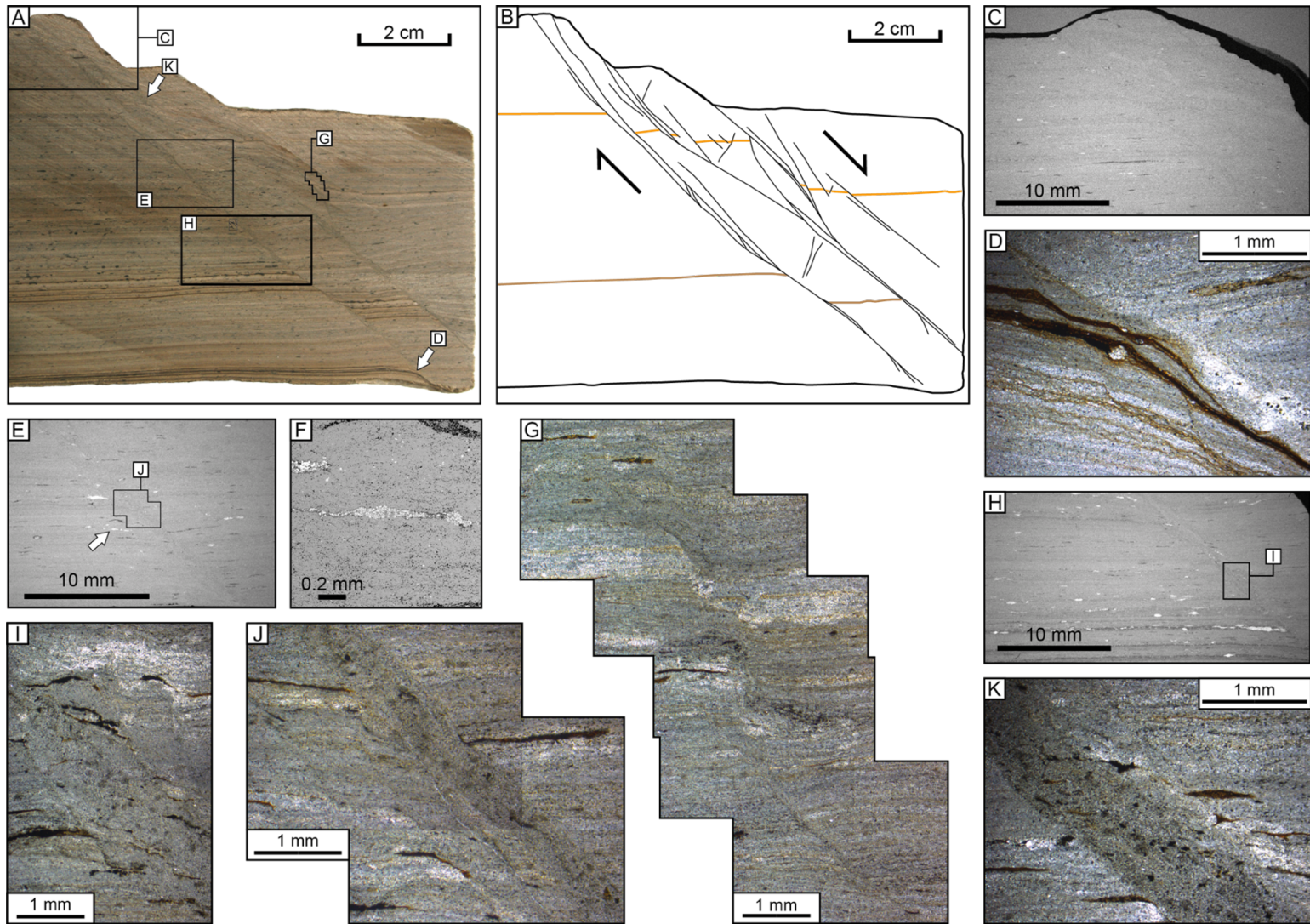


Figure 4-6. A/B) Hand specimen and schematic of faulted segment from the laminated carbonates of the Crato Formation. C-K) SEM and photomicrographs of faulted segments.

Petrophysical analysis of Crato Formation faults

Core plug with a diameter of 1.5 inch were taken from both the host rock and faults of three different faulted sections within the nova Olinda member to assess if there are any changes in porosity and permeability across the small-scale faults. Faulted sections were cored perpendicular to the fault to ensure that measured permeability reflected measurement of fluid flow across the fault.

Table 4-3. Porosity and permeability results from the small-scale faults within the Nova Olinda Member, Araripe Basin, Brazil.

Fault section	Type	Porosity, %	Klinkenberg Permeability, mD
NO Fault 1	Fault	11.72	0.046
	Fault	12.46	0.052
	Host	14.50	0.072
NO Fault 2	Fault	17.59	0.007
	Fault	10.78	0.007
	Host	18.54	0.023
NO Fault 3	Fault	9.53	0.004
	Host	12.82	0.006

The porosity of the host rocks taken from the Nova Olinda member (Table 4-3) adjacent to faults were measured to range from 12.5 to 19% and is predominantly observed to be formed of intergranular matrix porosity (Figure 4-5/4-6). Porosities of cores that included small scale faulting are generally found to decrease compared to the adjacent host rock. The reduction in porosity in cores affected by small scale faulting is variable, ranging from 5 to 40%. However, these decreases are never more than an order of magnitude.

Permeability measurements show that the host rock permeability ranges from 0.006 to 0.072 mD (Table 4-3) and so can be considered a tight carbonate with significant porosity. Permeability measurements of cores that are faulted show a very slight decrease in permeability with values of 0.004 to 0.052 mD. The permeability difference between the host rock and faulted samples highlights this as a minor reduction never more than half an order of magnitude (Figure 4-7a), which may be caused by the incorporation of clay and organic material into the fault or by juxtapositions of calcite layers against organic- and clay-rich layers.

Due to the relatively minor permeability reduction between individual fault and host rock pairs, the overall distribution of fault rock permeabilities within the Nova Olinda Member still strongly reflects the initial distribution of host rock permeabilities. As a result, relatively permeable host rocks (e.g. surrounding NO Fault 1) are able to have fault rock permeabilities that exceed host

rock permeabilities in other tighter/less permeable host rocks (e.g. NO Fault 3) (Table 4-3, Figure 4-7b). At the scale of deformation observed, it therefore remains host rock permeability, and primary diagenetic or depositional fabrics that are likely to exhibit a stronger control on the permeability of a given deformed rock mass. This is in coherency of observations of alteration from meteoric waters which do not appear to be severely impacted by faults but are more strongly controlled by stratigraphic variability (Figure 4-4).

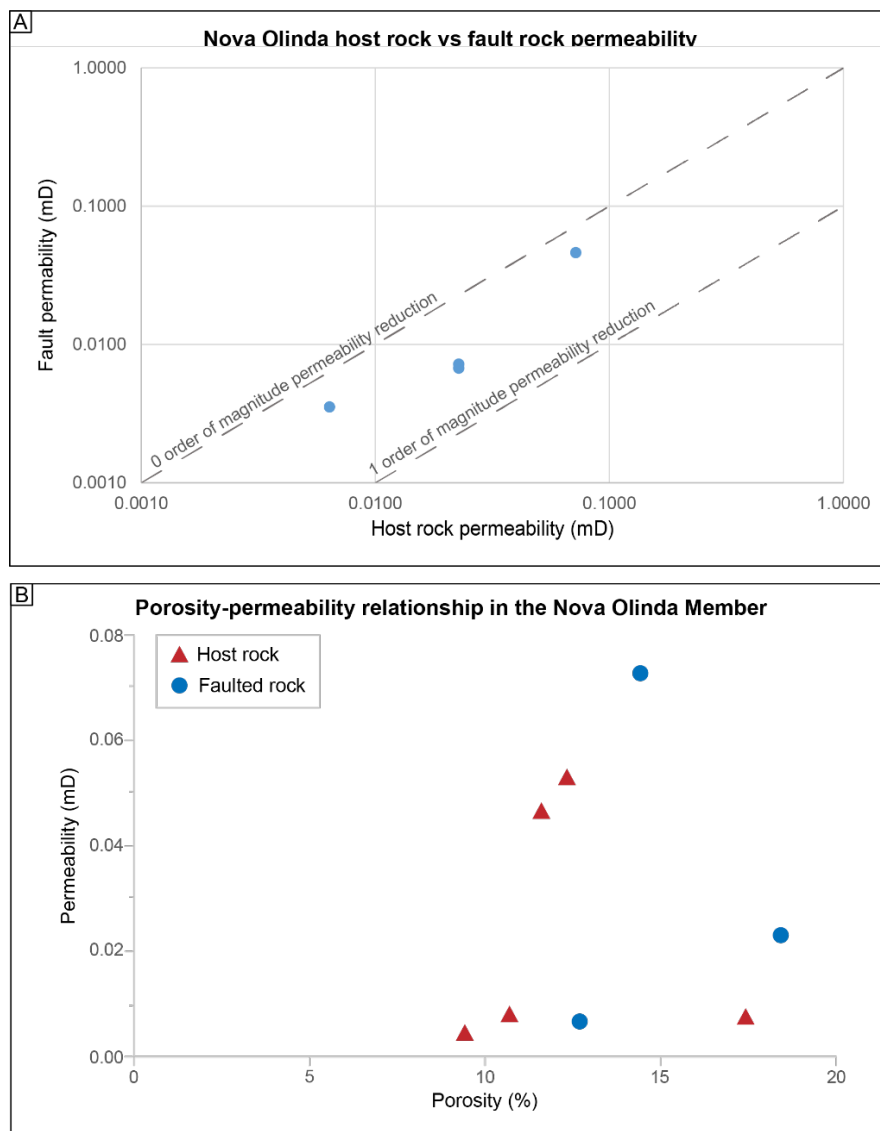


Figure 4-7. A) Graph illustrating permeability reductions between the host rock and across small scale faulting within the Nova Olinda Member (Araripe Basin, Brazil). C) Plot of porosity and permeability of all samples from the Nova Olinda Member.

4.3.2 Travertines

As discussed in section 4.1.1, 7 individual travertine bodies were visited located in Italy, Turkey and Hungary with the focus on characterising deformation features in these travertines. All

travertine bodies assessed are surficial Quaternary deposits, which have not undergone significant burial but are in regions of active tectonics and as such are commonly used in the study of neotectonics (Hancock et al., 1999; Altıntel & Karabacak 2005; Brogi & Capezzuoli 2009; Brogi et al., 2010,2021). The majority of travertine outcrops are affected by fracturing and karstification, but definitive evidence of faulting was only observed in the Ballık Travertines in SW Turkey (Figure 4-8c-d). Therefore, the Ballık travertines form the focus of analysis with respect to faults, whereas observations on karst features and fractures are from both the Ballık and Tivoli travertines in Italy (Figure 4-8a-b). The following results discuss different structural features observed in European travertine outcrops including karsts, fractures, dilational faults and shear strike-slip faulting.

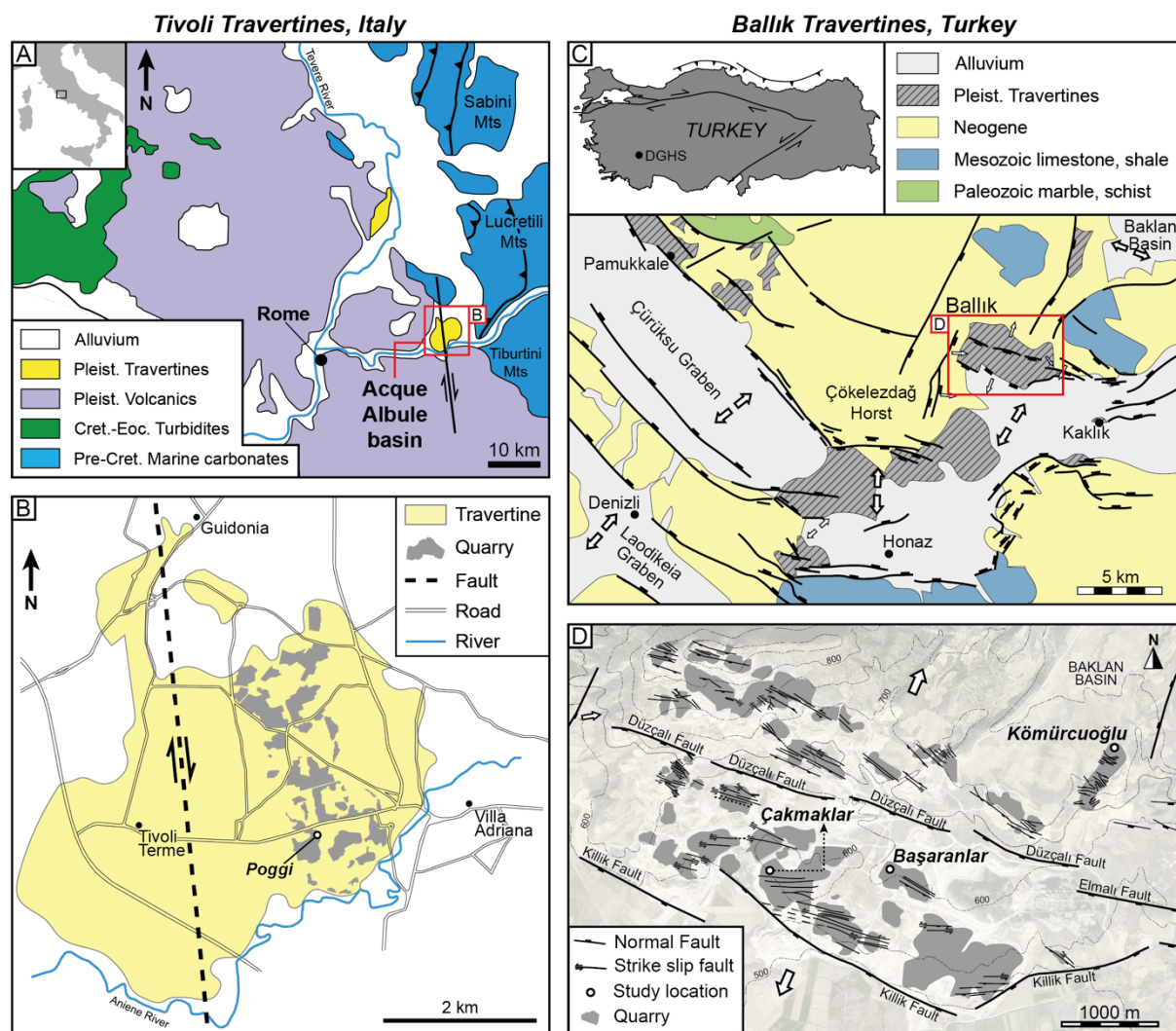


Figure 4-8. Regional geology of the Tivoli travertines, Italy and Ballık travertines, Turkey (edited from Faccenna et al. (2008)). A) Regional Geology of the Acque Albule Basin. B) Tivoli travertine quarried outcrops (edited from Billi et al. 2016). C) Regional geology of the Denizli Horst Graben System (DGHS). (edited from Özkul et al. (2013)). Location of DGHS (study area) marked on inset of Turkey. D) Quarried outcrops of the Ballık travertine body with studies locations indicated (edited from Van Noten et al. (2019)).

4.3.2.1 Travertine karsts

Both the Ballık and Tivoli plateau travertines show the presence of numerous elongate, sub-vertical or bed-parallel chaotic zones, ranging from 30 cm to 10 m wide of heights up to 4 m, which are either partially open, or filled with material of a partly different composition from surrounding wall rock (Figure 4-9, Figure 4-10). The boundaries of these features are commonly irregular or rugose and are ultimately interpreted as karst features.

Heterogeneous travertine breccias can be observed within some karst features (Figure 4-9c). Breccias within sub-vertical karsts are chaotic with a matrix of fine-grained, reddish-brown terrigenous material. Clasts are typically angular to sub-angular, ranging from centimetre scale chips through to metres scale blocks commonly formed of travertine host rock with bedding preserved within larger clasts. Uppermost portions of karst features are commonly defined by slightly rotated metre scale blocks of travertine host rock (Figure 4-9d-f). Figure 4-9d illustrates a complex partially filled elongated karst which has numerous vertical karsts which appear to branch off the main horizontal karst. Bedding can also be observed within the karst infill locally.

Karst features are also observed in the Metemar and Kömürçuoğlu travertine quarries in Turkey. Elongated karst features along bedding are illustrated in Figure 4-10a where the original karst structure is preserved and remains as an open cavity within the travertine. Structures within karsts in the Ballık travertines appear to feature more complex sedimentary features and are often associated with dilational faults and fractures where karsts are observed to spread out from a small point of the fault wall (Figure 4-10c/e). Multiple karst structures are observed to be filled with bedded, fine grained carbonates and clastic sediments (marls, clay and quartz). Sediment fill is likely a combination of reworked travertine sediment and influx of terrigenous material (Figure 4-10c/e). Where karst cavities appear to be filled with bedded clastic sediments, the original karst structure can be defined and illustrates the heterogenous nature of the cavity walls (Figure 4-10c/e). Locally clasts of host rock travertine can be found to be incorporated into the sediment fill as with the Tivoli examples (Figure 4-10c). Larger (up to 10 m width and 5 m in height), more complex karst structures are observed in the Kömürçuoğlu travertine quarries where the original karst structure is difficult to define and is characterised by both sediment fill, large vugs and collapse breccias (Figure 4-10d). In the case of the karst pictured in Figure 4-10c the karst is within the footwall of the adjacent dilational fault but does not appear to show any connectivity with the fault zone. This may reflect along strike variation in the connectivity of karst systems with faults and fractures.

Observations from both Turkey and Italy illustrate that travertine karsts can be divided into three categories:

1. Karst cavities - which can be unfilled (Figure 4-9a/e, Figure 4-10a) or filled (Figure 4-9d), or a combination of fill with localised cavities and vugs (Figure 4-9e).
2. Fault-and fracture-controlled karst networks - commonly filled with reworked travertine (calcite) and terrigenous material (Figure 4-10c/e) are linked with dilational faults or fractures.
3. Karst collapse structures (Figure 4-9c/f): Karsts are defined by travertine breccias and rotated host rocks, usually hosted in a matrix of fine mud and/or clay sediments.

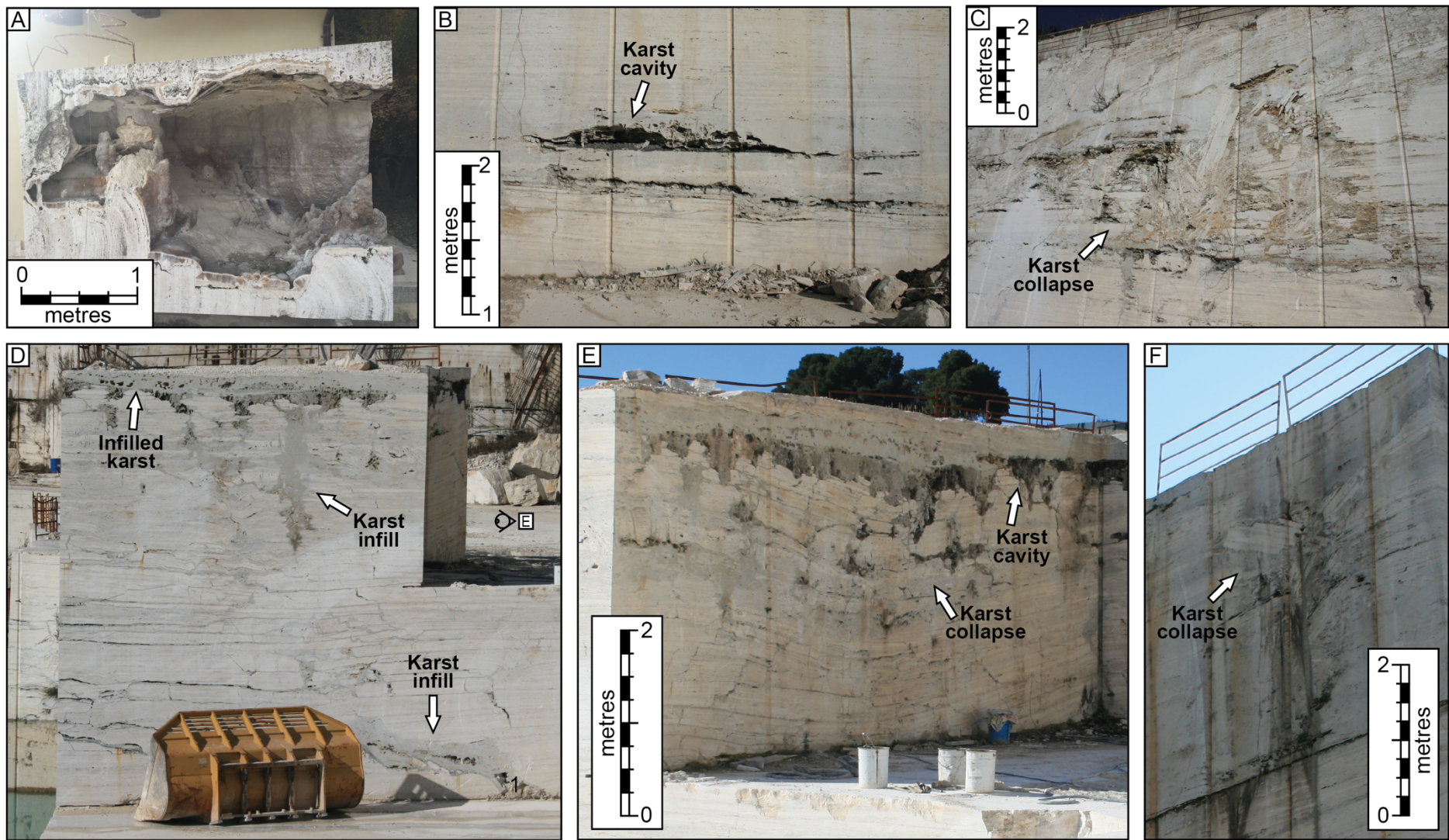


Figure 4-9. Karst features observed in Italian Travertines. A) Example of cavern in a travertine block, Acquasanta Terme. B) Karst cavity, Poggi Quarry, Tivoli. C) Karst collapse feature (Poggi Quarry, Tivoli). D/E) Karst with grey clastic sediment infill and localised cavities (Poggi Quarry, Tivoli). F) Narrow karst collapse feature (Poggi Quarry, Tivoli).

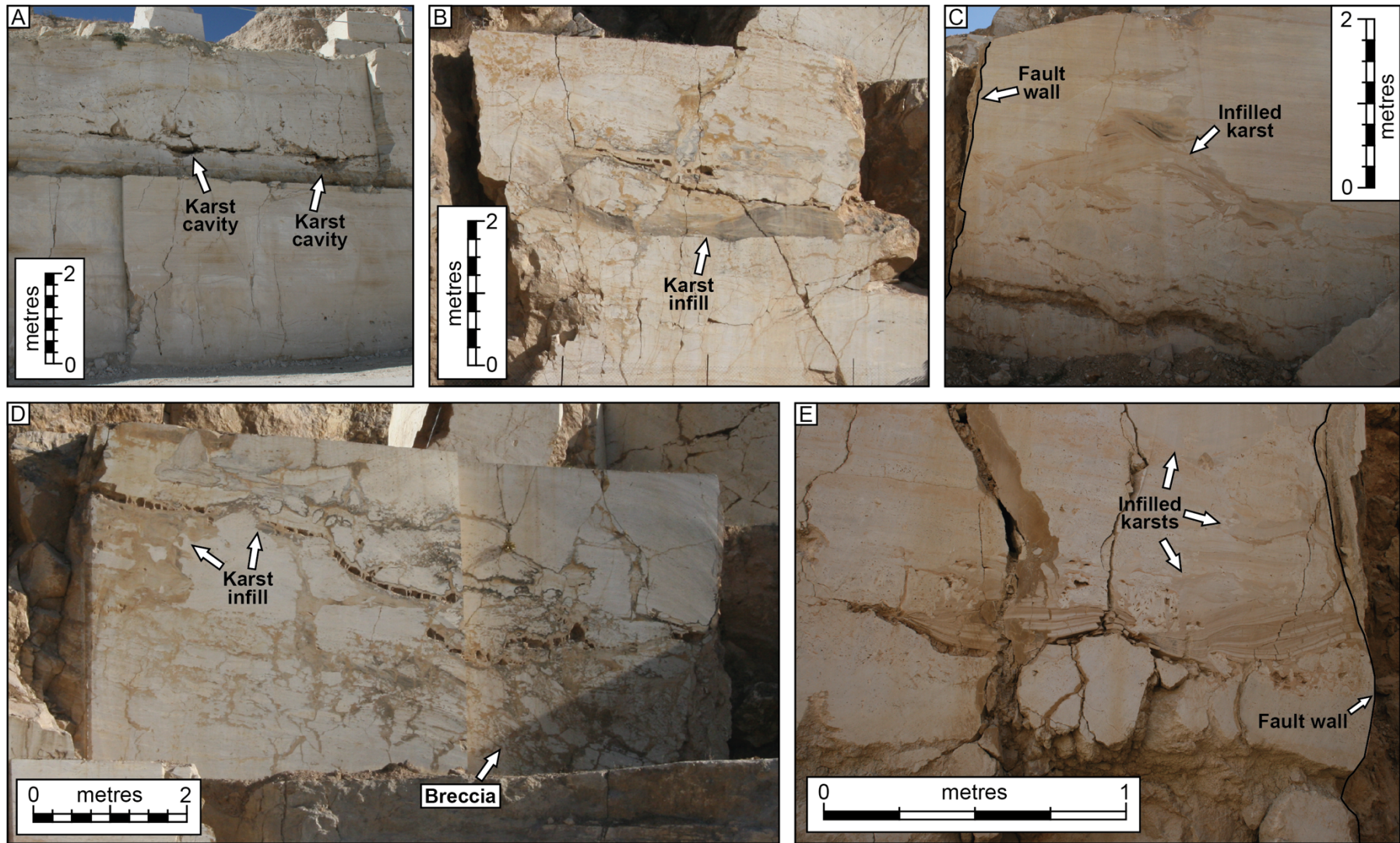


Figure 4-10. Karst features observed in the Ballık travertines, Turkey. A) Elongated, bedding parallel karst cavity. B) Karst with clastic sediment infill and travertine blocks. C) Bedded sediment fill in a karst structure with inclusion of travertine host rock clasts. D) Complex karst structure with transitions between sediment infill, vugs and travertine breccia. E) Elongated karst structure with bedded clastic sediments cross-cut by fractures,

4.3.2.2 Travertine hosted fractures

Mode 1 fractures are observed to be extremely common in the travertine localities across Italy, Hungary and Turkey. Small aperture (< 2 cm) Mode 1 fractures commonly have a stair-step geometry (Figure 4-11), where steps (i.e. changing from vertical to bedding parallel) occur at bedding surfaces. Fracture geometry appears more complex (i.e. higher frequency of 'steps') in sequences with strongly bedded travertine facies as in Figure 4-11a. In more massive or amalgamated travertine sequences, it is observed that there are less 'steps' in fractures resulting in a simpler fracture geometry (Figure 4-11c).

In mode 1 fractures with larger apertures (> 2 cm) which are either near the top travertine body surface or are interbedded with other sedimentary sequences (conglomerate and palaeosols layers) these dilational features are observed to be filled with clastic sediment (Figure 4-12). For example, Figure 4-12, illustrates fractures observed in the Ballık travertine body (Turkey) that intersect a conglomerate layer interbedded with light-brown, fine-grained likely terrigenous material. Both fractures pictured have widths up to 0.5 m and are heterogeneously filled with sediments that have the same composition as and appear to be sourced from this conglomerate layer with inclusion of travertine clasts which have collapsed into the created space. The fracture imaged in Figure 4-12a illustrates the termination of the fracture at the base of a conglomerate layer, the layering of which is deformed into a small ~0.5 m wide concave depression overlying the open fracture. This may suggest that fracture growth occurred soon after conglomerate deposition when the conglomerate layer was poorly consolidated. Unlike the boundaries of the previously described karst features, the edges of Mode 1 fracture infill features are typically more planar and more regular than the diffuse or rugose boundaries of the karsts.

Several fractures are also observed to be cross-cut by younger unfilled mode 1 fractures of different orientation which also cross-cut the conglomerate layers (e.g., Figure 4-12a), suggesting multiple episodes of fracturing during basin extension. Similarly, the filled fracture pictured in Figure 4-12b illustrates a fracture which becomes diffuse when intersecting the conglomerate. However, this fracture appears to be re-fractured with an unfilled mode-1 (up to 5mm aperture) fracture along one of the fracture walls and propagates into the overlying conglomerate, indicated multiple phases of fracturing. Additionally, some dilational fractures, even when cross-cutting a poorly consolidated portion of the conglomerate layer yet remain unfilled (Figure 4-12b). In such cases, the stepping geometry of the fracture where the fracture intersects this poorly consolidated layer may inhibit subsequent filling of the cavity below. The

fracture geometry may, therefore, control the extent of rock-fall deposition that occurs within such dilational structures.

Within the Ballik travertine, it is common to find dilational fractures with sediment infill preserved along the fracture walls surrounding an 'open' central fissure or poorly consolidated, friable material. Figure 4-13 and Figure 4-14 provide examples of such fractures and display the highly heterogeneous and varied nature of such structures. The fractures displayed in Figure 4-13 illustrate how conglomerates are preserved in heterogeneous lenses along the fracture wall with varying thicknesses between 3 and 0.5 m. In both examples of fractures in Figure 4-13, different types of conglomeratic infill can be distinguished. Broadly, fracture parallel 'layers' of different conglomerates are recognised, with differing textures and clast size distributions (Figure 4-13b). For example, Figure 4-13b displays the presence of three different types of conglomerate - one with clasts of light brown fine-grained sedimentary rocks supported by a dark brown matrix; a dark brown matrix-supported conglomerate with clasts of light brown fine-grained sedimentary rocks, calcite clasts and conglomerate clasts (these have relatively smaller clast sizes); and a conglomerate with variable texture (dominantly clast supported) which has a higher proportion of clasts.

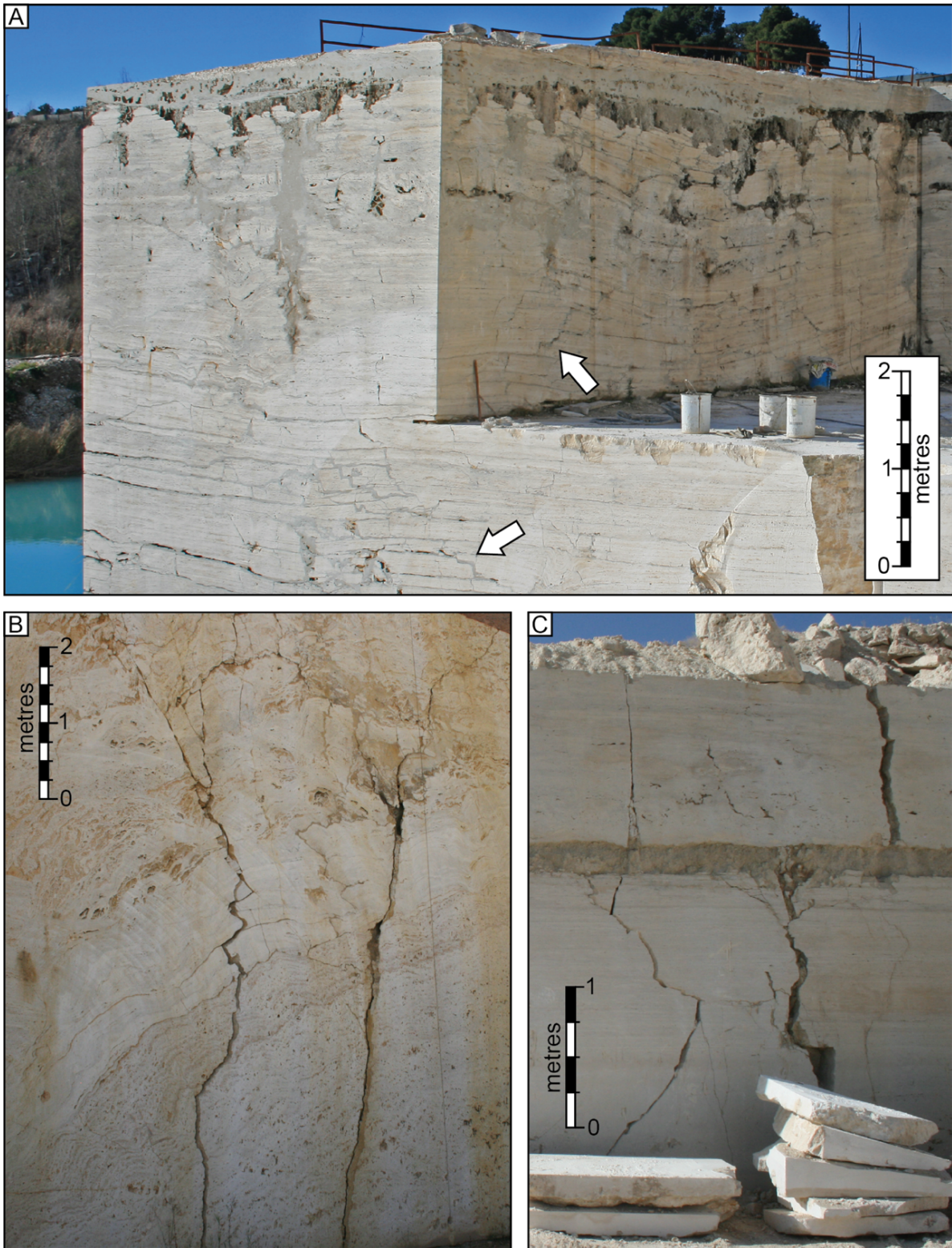


Figure 4-11. Examples of stair-step mode 1 fractures in travertine. A) Complex, highly connected stair-step fractures in a strongly bedded travertine body related to karst collapse feature (Poggi Quarry, Italy). B) Stair-step fracture, (Kömürçuoğlu Quarry, Turkey). C) Mode 1 fractures in a massive travertine block with interbedded clastic sediment layer (Çakmaklar Quarry, Turkey).

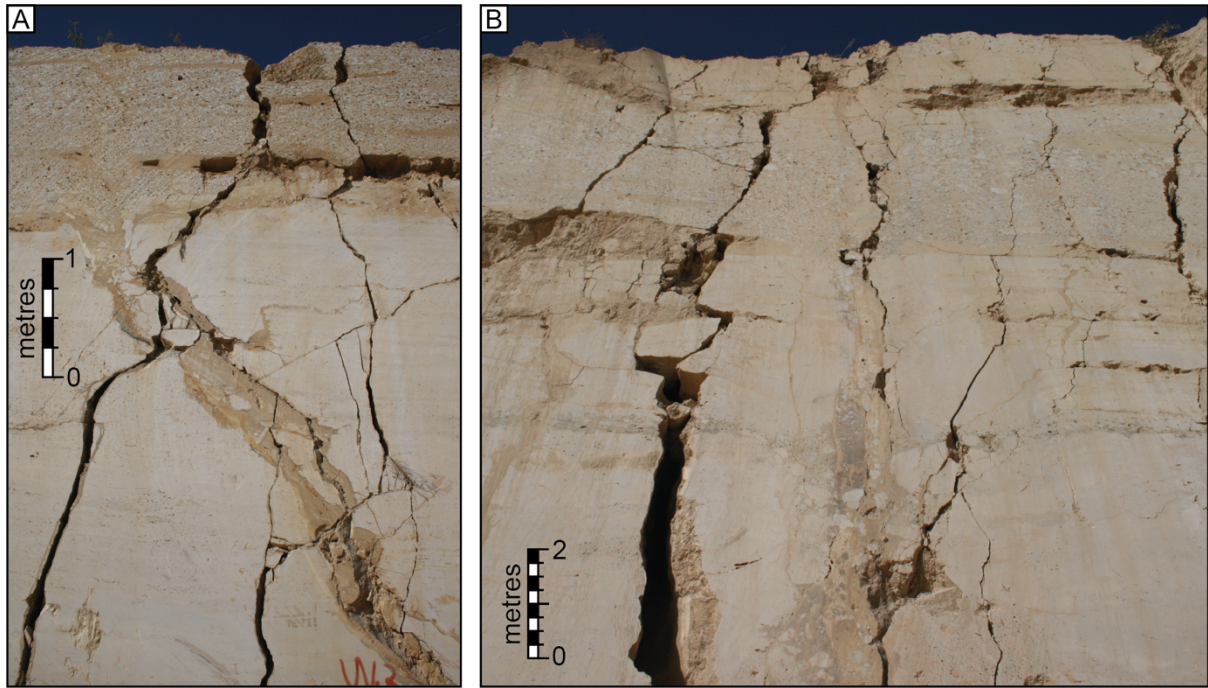


Figure 4-12. Mode 1 fracture with sediment infill in the Ballık travertines (Kömürçuoğlu Quarry, Turkey). A) N dipping fracture filled with conglomerate and terrigenous sediment from overlying sequence. Infilled fracture is cut by near vertical S dipping fractures which cut through the whole sequence and remain unfilled. B) unfilled and conglomerate filled fracture. Filled fracture has heterogenous fracture walls (increases up to 1 m width at bottom of section) which has refractured along the left fracture boundary and propagates through the conglomerate layer.

The fracture shown in Figure 4-13d-e and Figure 4-14c also illustrates variable fracture fill but is instead composed of distinct millimetric to centimetric sub-horizontal layers of conglomerates and fine-grained light to dark brown terrigenous sediments. This change in infill sedimentology may indicate progressive cycles of fracturing and filling of the structure. The sub-horizontal layers observed in these fractures, in contrast, suggests prolonged deposition filling the fracture space. In both examples of fracture infill in Figure 4-13, calcite is found as both veins, cross-cutting the conglomerates (Figure 4-13f), and coatings around clasts. In some fractures, fracture parallel travertine deposition and calcite mineralisation is observed coating the fracture walls. For example, Figure 4-14d/f illustrate a layer of black, manganese-rich, travertine shrubs (e.g., Chafetz et al., 1998) which radiate in their growth direction from the fracture wall. The presence of black travertine shrubs indicates the potential of travertine-precipitating waters with high pH promoting Mn and Fe mineralisation (Chafetz et al., 1998). Pervasive (Figure 4-14e) and localised (Figure 4-13c) manganese alteration of the calcite clasts and/or calcite-rich matrix of some of these infill conglomerates further suggests significant redox reactions and chemical alteration during fluid flow phases.

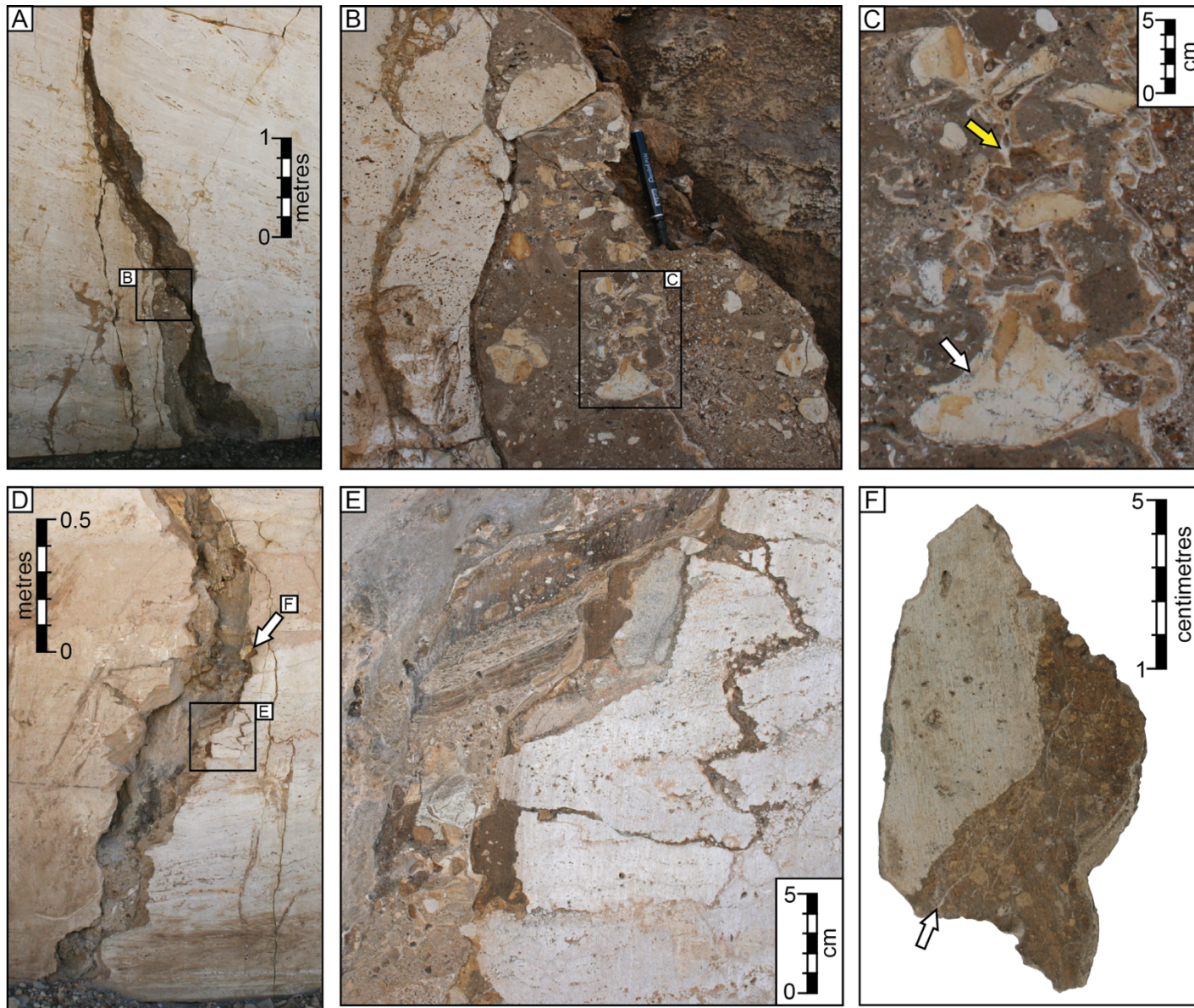


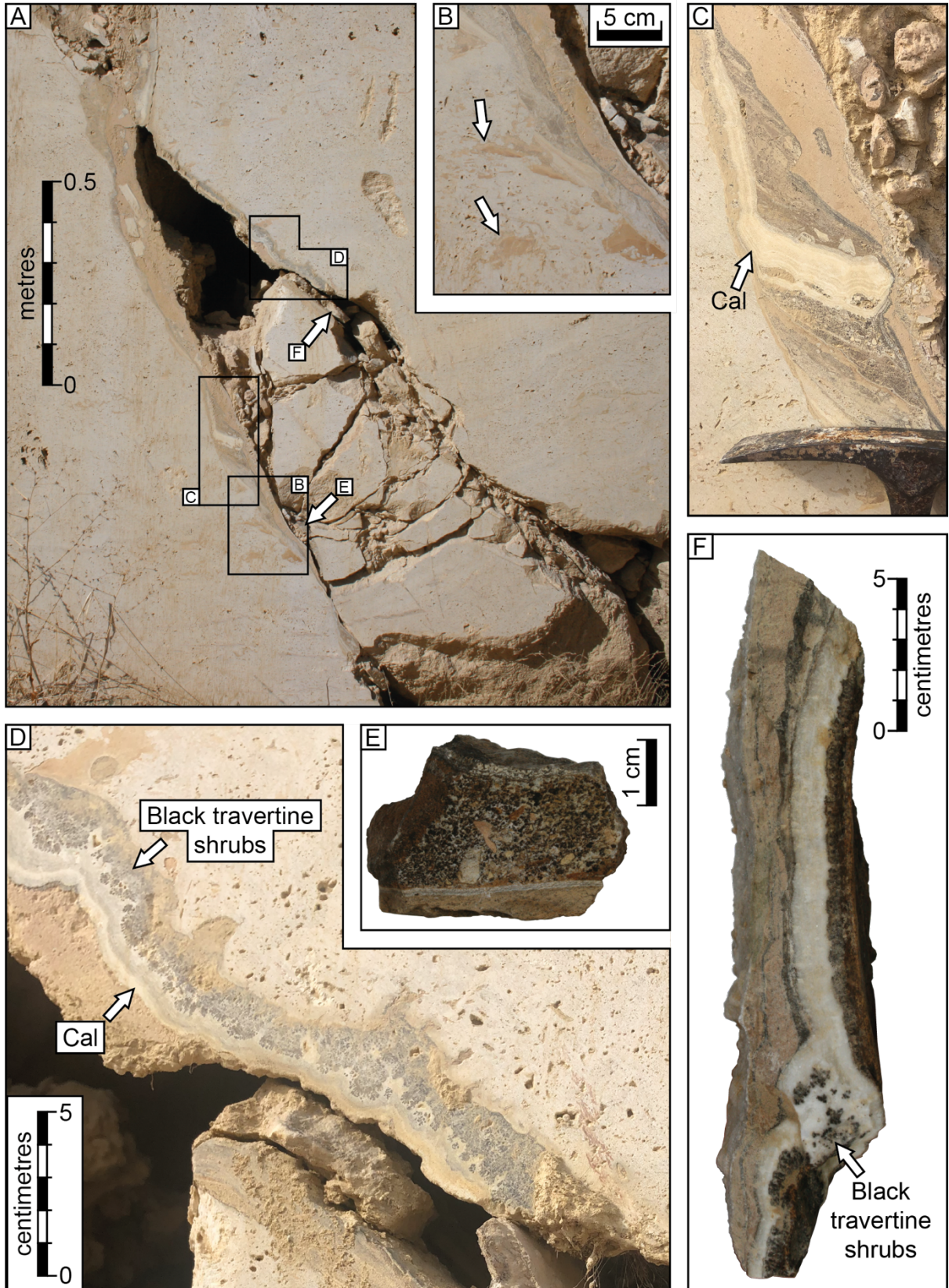
Figure 4-13. Examples of dilational fractures in the Ballık travertines (Kömürçuoğlu Quarry, Turkey). A) Fracture with poorly consolidated centre and locally preserved well cemented infill conglomerate along fracture walls. B) Close-up image of conglomerate infill in fracture from A. 3 different types of conglomerate can be observed: a light brown, matrix-supported conglomerate with travertine and light brown sedimentary clasts; a dark brown matrix-supported conglomerate with clasts of light brown fine-grained sedimentary rocks, calcite clasts and conglomerate clasts (these have relatively smaller clast sizes); and a conglomerate with variable texture (dominantly clast supported) which has a higher proportion of clasts. C) inset from B. White arrow shows black manganese alteration in clasts consisting of calcite. Yellow arrow highlights clasts coated by calcite. D) Dilational fracture with open central cavity with heterogeneous conglomerate infill locally preserved on fracture walls. E) Conglomerate infill from fracture illustrated in D. Distinct sub-horizontal layers of conglomerates and fine-grained light to dark brown terrigenous sediments can be seen. F) Hand specimen taken from fracture in D composed of a travertine clast bounding a brown matrix supported conglomerate infill material. White arrow illustrates example of mm-scale calcite veins that commonly cross-cut secondary fracture infill.

Figure 4-14 b also illustrates how some fractures can have irregular walls similar to those observed in karst systems, with significant inlets up to 30 cm into the host rock. Inlets can be relatively smooth (compared to the rough surface of un-covered fracture surfaces) which are filled with light to dark-orangey brown terrigenous material. The smoothing and karstification of the immediate host rock suggests that dilational fractures may be widened and smoothed by dissolution and karstic processes once it has opened.

Generally, fractures in the observed travertine formations can be classified into three types:

1. Mode 1 fractures with clastic sediment infill. Sediment infill is commonly composed of terrigenous sediments forming matrix supported conglomerates with inclusion of travertine host rock clasts. Secondary manganese alteration and calcite veins are also common.
2. Mode 1 fractures with no fill. Commonly small aperture, < 2 cm, 'stair-step' type fractures, though some larger scale fractures may lack any sediment fill.
3. Partially filled mode 1 fractures. Inner part commonly open or composed of poorly consolidated friable sediments. Fracture walls show wall-parallel travertine and calcite mineralisation and may preserve cemented fracture infill.

Figure 4-14 (next page). Dilation fracture observed in the Ballık travertine (Kömürçuoğlu Quarry, Turkey). A) Lower portion of fracture characterised by open cavities with collapsed travertine infill. Fracture walls preserve fracture parallel calcite veins, travertine layers and light brown fine grained sedimentary fracture infill material. B) Inset from A illustrating irregular, relatively smooth edge of fracture wall and interfingering of fine grained light brown sediment, possible inferring widening of the fracture width by dissolution. C) Focus of fracture wall from A illustrating vertical to sub horizontal mm-cm layers of calcite, fine-grained terrigenous sediments, and conglomerates. D) Close up of black travertine shrubs (Mn or Fe rich) along fracture wall which are coated with a 2cm vein of banded calcite. E) Hand specimen taken from fracture composed of a fine-grained matrix supported conglomerate. Matrix is especially prone to Mn or Fe alteration. F) Hand specimen of fracture wall showing Mn/Fe rich black travertine shrubs surrounded by calcite. mm-scale undulose layers of dark brown/black fine-grained sediments interbedded with fine-grained light brown sediments is observed parallel to the calcite vein.



4.3.2.3 Travertine hosted faults

The few examples of faulting within travertines are within the Ballık travertines, Turkey (Figure 4-8, Figure 4-15, Figure 4-16). An extensive network of normal faults with a NW-SE trend -SE are observed in the K m rcuoglu Quarry at the northernmost boundary of the Ballık travertines (Figure 4-15). These faults are typically steep/sub-vertical ($71-89^\circ$) dilational faults with poorly consolidated internal structure which makes characterisation of these features challenging to put into a fluid dynamic framework. These faults have been split into three categories based on their throw: 1) Small faults with apparent throws less than 0.5 m; 2) Medium faults with apparent throws between 0.5 and 3 m; and 3) Large faults with throw over 3 m. In addition to normal faulting, a NW-SE Strike-slip fault was also observed in the Bařaranlar Quarry (Figure 4-8d, Figure 4-21), which displays complex heterogeneities in its geometry and fault rocks type and continuity.

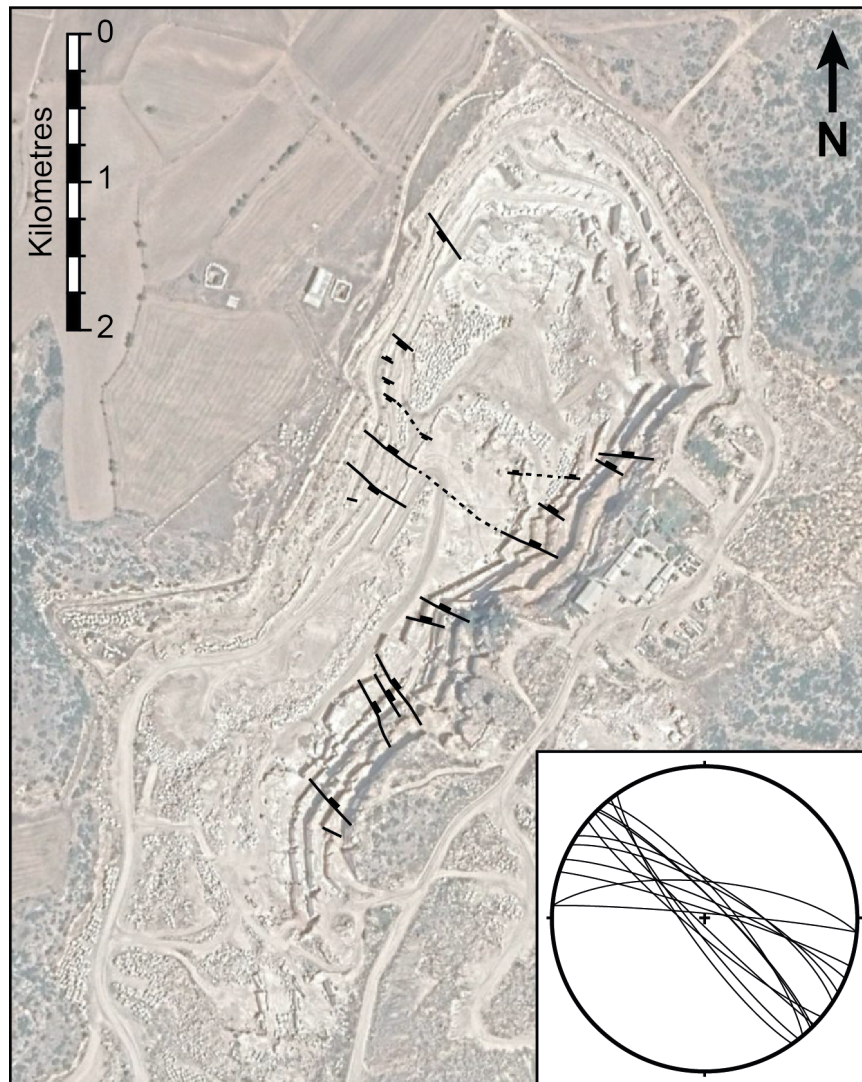


Figure 4-15. Map of K m rcuoglu Quarry, Turkey with fault observed normal faults mapped and plotted onto the inset stereonet.

Small (< 0.5 m) to medium throw (0.5 - 3 m) dip-slip faults

Generally, small to medium normal faults observed in the Kömürçuoğlu quarry, Turkey, are open, dilational features where the fault core is characterised by open voids with variable sediment infill. The infill of these dilational faults vary widely. In some cases, where dilation is minimal (i.e., the fault core dilational zone is less than 20 cm), faults lack infill and the structure remains open. In these cases, minor brecciation of the host rock is observed, where fragments of the host rock from the fault walls have been included and 'fallen' into the space produced (Figure 4-16). For example, Figure 4-16a shows a near vertical apparent reverse fault with a dilational core of up to 6 cm. The apparent reverse offset may actually be a representation of a high angle normal fault with small throw in an oblique view or may be a strike slip fault with reverse offset locally which is more likely in the tectonic regime of the Çakmaklar quarry (Turkey). The lower portion of this fault that is characterised by a singular fault plane is found to lack any infill, especially where the fault plane has gentle undulations in orientation. Localised infill of this fault core is composed of uncemented clasts of the host rock (e.g., Figure 4-16c).

More commonly, the fault core of dilational faults is found to be composed of travertine clasts suspended in a variably cemented matrix of grey to brown clay rich terrigenous sediment (Figure 4-16a/b). In small scale faults (< 0.5 m throw), as in the case illustrated in Figure 4-16b, clasts appear to be fractured off from the host rock with minimal rotation. In medium sized faults (0.5 - 3 m), host rock travertine clasts lack any preferential orientation and are often included in a matrix of poorly cemented, friable material filling the central fissure (e.g., Figure 4-18). This may either illustrate the variable infill of these open fissures created when faulting or may also illustrate the evolution of the fault core from initial formation, with initial fracturing of the wall rock, to a more chaotic fissure fill as a result of prolonging filling and refracturing of initial rockfall deposits.

As with the mode 1 fractures discussed in Section 4.3.2.2, dilational fault cores can also be filled with fault parallel to sub-parallel layers of conglomerates. These are considered conglomeratic deposits rather than fault rock breccias due to the inclusion of clay rich terrigenous material (sourced from palaeosols or the present-day surface) and sedimentary clasts which have not been sourced from the travertine host rock. As a result, they are interpreted as 'rock-fall' deposits rather than directly formed from fault related process. The composition and texture of conglomerates found within these fault cores are highly variable and can also display variable continuity and alteration. Figure 4-17 illustrates a normal fault with a throw of ~0.25 m which has a complex inner fault core composed of fault parallel layers

of different conglomerates and thin layers of calcite mineralisation (1-5 mm thick) with a central poorly consolidated and friable 'centre' of ~20-30 cm thickness. Different conglomerate layers are distinguished by changes in matrix and clast composition and size. Some conglomerate layers are composed of light brown, poorly-sorted angular clasts between 5 cm to 30 cm supported in a calcite cement. In comparison dark grey/brown layers have a clay-rich, fine-grained matrix (Figure 4-17b). Clast composition is variable and includes travertine hosts rock, light to dark brown fine-grained sandstone sedimentary clasts and conglomerate clasts. The fault cross-cuts a conglomerate layer which is composed of clasts that appear similar in composition to those found in the fault infill. Clasts also have no preferred orientation and deposits are generally bimodally sorted, which support deposition due to rock-fall/debris infilling the dilational space (similar to those observed by Gent et al., 2010). The boundaries between different layers can either be sharp and planar or sharp and undulose. Clasts can also be found to line boundaries between different layers. Though different conglomerate layers are easily distinguished, some layers show similarities in their colour, texture and lithology and may be co-genetic, suggesting episodic deposition and re-fracturing/faulting of the fault zone.

Conglomerate layers are commonly interbedded with millimetric to centimetric layers of calcite (Figure 4-17d-f) and in some cases millimetre thick 'microbial black crusts' formed from manganese rich precipitates (Figure 4-17f). These fault parallel layers vary in thickness from 0.5 to ~20 cm's and are generally undulose but conformable to the conglomerate layers and likely formed as a crust on previously exposed surfaces (Figure 4-17d-f). Small calcite veins (< 1mm thick) are observed to cross-cut conglomerate layers and clasts (Figure 4-17d) and calcite is also observed to locally coat grains in some conglomerate layers. These smaller, younger veins are observed to be overprinted with manganese-rich alteration which is pervasive throughout the fault zone. Manganese-rich alteration is also observed in the calcite cement of some conglomerates and around the edges of sedimentary clasts. The extent of manganese alteration is variable across different conglomerates which may indicate preferential fluid flow through certain layers (i.e., more permeable conglomerate layers are those that are more heavily altered) and likely highlight a complex and multi-phase formation history of the fault (i.e., conditions promoting alteration and deposition of manganese may have only occurred early in the faults history before formation/deposition of resulting conglomerate layers.)

No fault cores observed in the Ballik travertine were composed of fully cemented rock-fall deposits. Observed faults either had an open fissure space or a central fissure loosely filled

with poorly consolidated material (Figure 4-17 & Figure 4-18). In most cases, different 'layers' of conglomerates are only preserved locally along fault wall, often in lenses and are often fractured (Figure 4-18b) and included as clasts within the chaotic fissure fill.

In almost all cases, normal faults are found to become increasingly heterogeneous up-dip. Figure 4-16a-c illustrates the splaying of singular fault planes into multiple strands resulting in an increased fault-zone width up-dip, especially at shallow levels where faults intersect with the travertine body surface (as observed in Figure 4-16a). Where normal faults are easily recognised at one quarry level, correlating faults with higher quarried levels provided extremely difficult due to this increasing heterogeneity and dispersal of throw. For example, in Figure 4-16c the fault widens into a v-shaped geometry where the fault intersects a conglomerate interval in the travertine body and becomes much more diffuse. This likely reflects the poorly cemented conglomerate providing a significant mechanical change in the stratigraphy compared to the well cemented, strong travertine. Similarly, in Figure 4-18a the fault core becomes wider where the fault intersects a weakly cemented palaeosol layer which is also more heavily fractured compared to the overlying travertine mass. These changes in fault geometry are likely due to changes in the mechanical stratigraphy occur; either where the travertine is interbedded with sedimentary layers (in this case conglomerate and palaeosol layers) or where the faults intersect what was the ground-surface at time of faulting.



Figure 4-16. Small scale (<0.5 m apparent throw) dip-slip faulting observed in Turkey. A) Near vertical apparent reverse fault observed in Çakmaklar quarry. B) ~ 20 cm throw dilational normal fault observed in the Kömürçuoğlu Quarry, Turkey. C) Normal faulting in travertine interbedded with conglomerate layer (Kömürçuoğlu Quarry, Turkey).

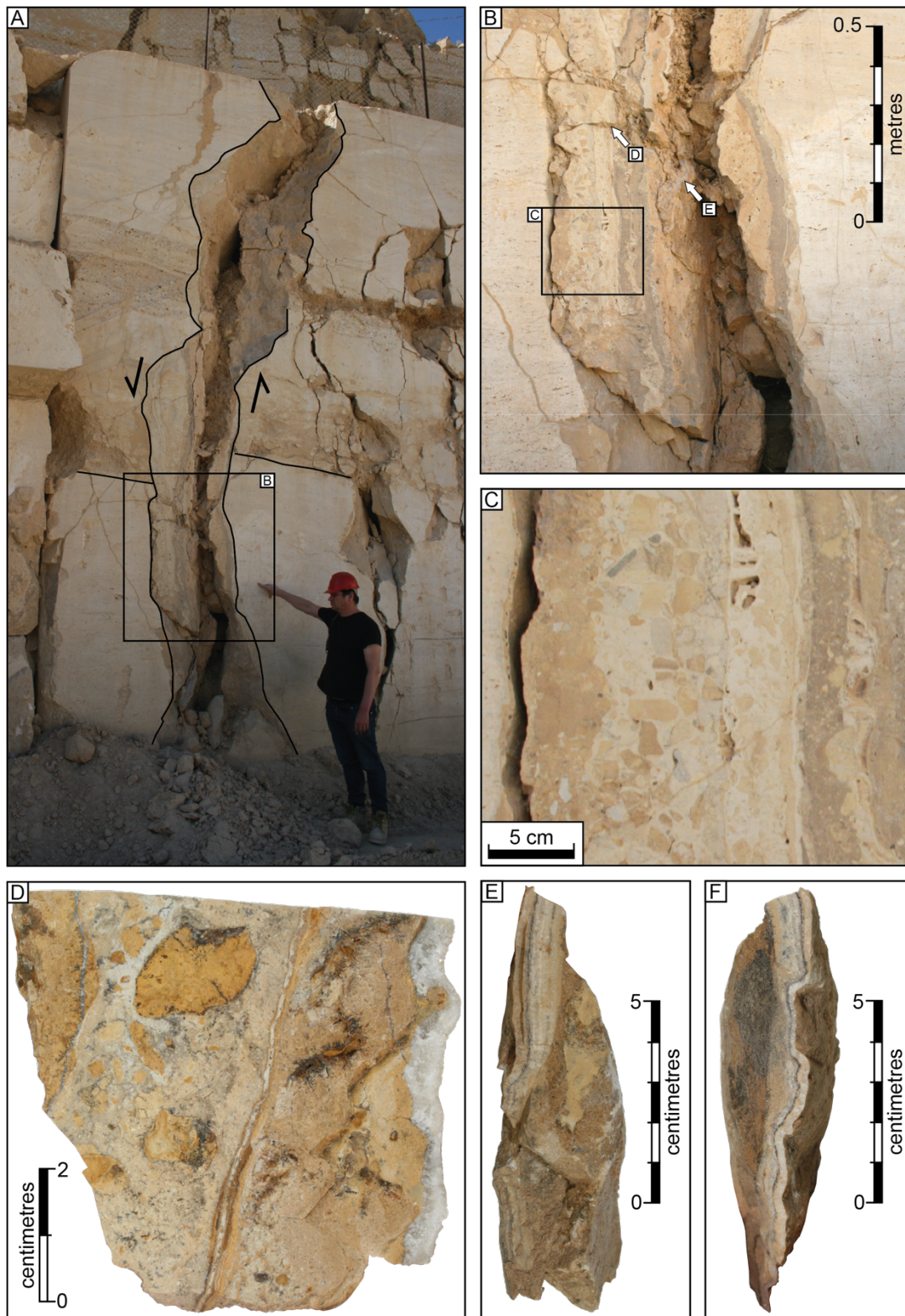


Figure 4-17. Dilational normal fault observed in the K m rcuoglu Quarry, Turkey. A) Overview of fault illustrating heterogeneous fault wall geometries and changing dip. Inner portion of fault is infilled with loose friable material composed of travertine clasts and clay rich sediment. B) Fault parallel layers of well cemented conglomerates with varying textures and matrix and clast composition locally preserved along fault walls. C) Detailed image of fault parallel bands of conglomerates with thin layers of calcite between some different conglomerates. D) Hand specimen from conglomerate bands (location in B) shows distinct bands of conglomerates and calcite veins. Manganese alteration of the calcite matrix and fine-grained sedimentary clasts is pervasive. E-F) Hand specimen taken from fault wall illustrating fault parallel banded undulose calcite vein. Millimetre layer of dark manganese rich layer formed either through alteration of calcite layer or deposited as a microbially induced crust.



Figure 4-18. Dilational normal faults observed in the Kömürçuoğlu Quarry (Turkey) with throws between 1-3 m. A) Dilational normal fault with heterogeneous fault core thickness composed of unconsolidated, friable material. B) Normal fault with partially cemented fault core. C) Dilational normal fault with a poorly consolidated fault core composed of large travertine clasts and brown, clay rich mud.

Large throw (> 3 m) normal faults

Only one fault with a throw more than > 3 m was observed in the Ballık travertine with a throw of 6.7 m (Figure 4-19). The fault has a dilational fault core of up to 10 m width which is predominantly composed of poorly consolidated and friable material with travertine clasts up to 4 m in a matrix of brown coloured, fine-grained terrigenous and altered travertine material.

Though the fault zone width is significantly larger than those observed in small to medium throw faults, the fault zone is still focused along a singular dilational fissure. As observed with smaller faults within the Ballık travertine, the fault walls preserve heterogenous lenses of conglomerates (Figure 4-19b) which are likely initial debris deposits which have been subsequently faulted. Figure 4-19b also illustrates the heterogeneous and sharp boundary between the conglomerate layer and the host rock, interpreted to reflect the widening of the fissure through dissolution of the host rock. This is further evidenced in Figure 4-19c where fine-grained terrigenous sedimentary deposits are found to fill a bedding parallel karst cavity structure and intersect the fault. Karstification within the travertine may therefore be linked to fault formation and suggest an active hydrothermal system throughout the fault network in the travertine body (Cazarin et al., 2019).

Strike slip faults

In the Braşaranlar quarry (Ballık travertines, Turkey) (Figure 4-8d), a WNW-ESE trending strike-slip fault was observed (Figure 4-20). Quantified lateral offsets of the fault were unable to be determined due to lack of confident/visible offset marks within the quarry but horizontal slicken lines were observed at multiple points on the primary slip surface (Figure 4-20b). As such the scale of the true fault cannot be quantified but the fault zone width is observed to be to 4 m and is mapped over a length of ~ 100 m and with a relatively limited vertical throw (< 0.5 m).

The lateral character of the fault is highly heterogeneous, where a singular, near-vertical, fault core (Figure 4-20c) is observed in the western part of the outcrop but becomes segmented, ~ 100 m to the east where multiple slip surfaces are observed (Figure 4-21b). The fault core also become wider towards the east from 0.7 m in the west and 3.5 m in the east. However, this may be due to a lack of sufficient exposure of the fault in the west, where there is not a fully cross-sectional view and so may be exposing only a singular fault segment rather than the whole system. As such, observations largely focus on the eastern segment of the fault where a full cross-section of the fault can be viewed. The core is generally composed of continuous fault parallel layers of travertine, Mn-/Fe- rich black travertine crusts and calcite

veins as well as chaotic poorly cemented fill (Figure 4-21a/b). Travertine deposition is found to be up to 20 cm in thickness and is composed of multiple centimetric layers (Figure 4-21d/e) indicating that the fault had to be 'open', with fluid circulation at several stages of fault evolution to allow prolonged travertine deposition. These observations suggest that the strike slip faulting within the Ballık travertines likely had some dilational or tensional component during the early part of their history. Locally, wall-parallel travertine layers can be found to be heavily fractured (Figure 4-21c) which may reflect later reactivation and deformation of the fault zone through continued strike-slip displacement producing highly variable deformation within the fault-parallel travertine layers along strike (Figure 4-22c/e).



Figure 4-19. Large scale (>6 m displacement) normal fault observed in the Kömürçuoğlu Quarry, Turkey. A) Fault core is composed of poorly consolidated, friable material with large (up to 4 m) travertine host rock clasts in a brown oxidised mud matrix. B) Cemented calcite mineralisation and original 'breccia' along fault wall locally preserved. C) Mud rich cemented breccia locally observed in place along the fault wall.

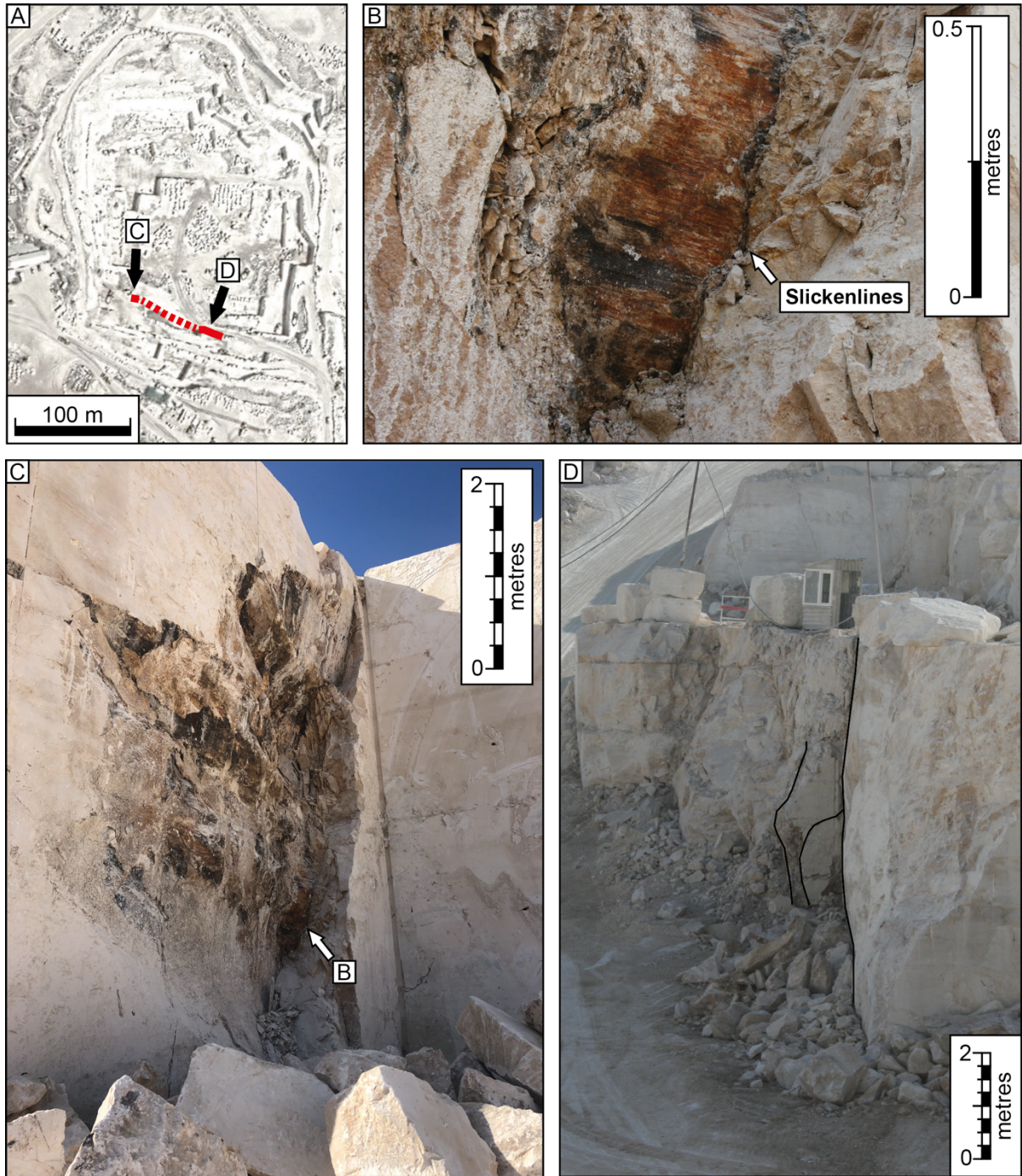


Figure 4-20. WNW-SES trending strike slip fault observed in the Ballık travertine body (Braşaranlar Quarry, Turkey). A) Satellite view of the Braşaranlar quarry with fault outcrop locations marked by red fault line. B) Slicken lines observed on primary slip plane of fault. C) Overview of eastern fault outcrop location illustrating undulose fault plane. D) Overview of second fault outcrop location illustrating multiple fault segments (detailed in Figure 4-22).

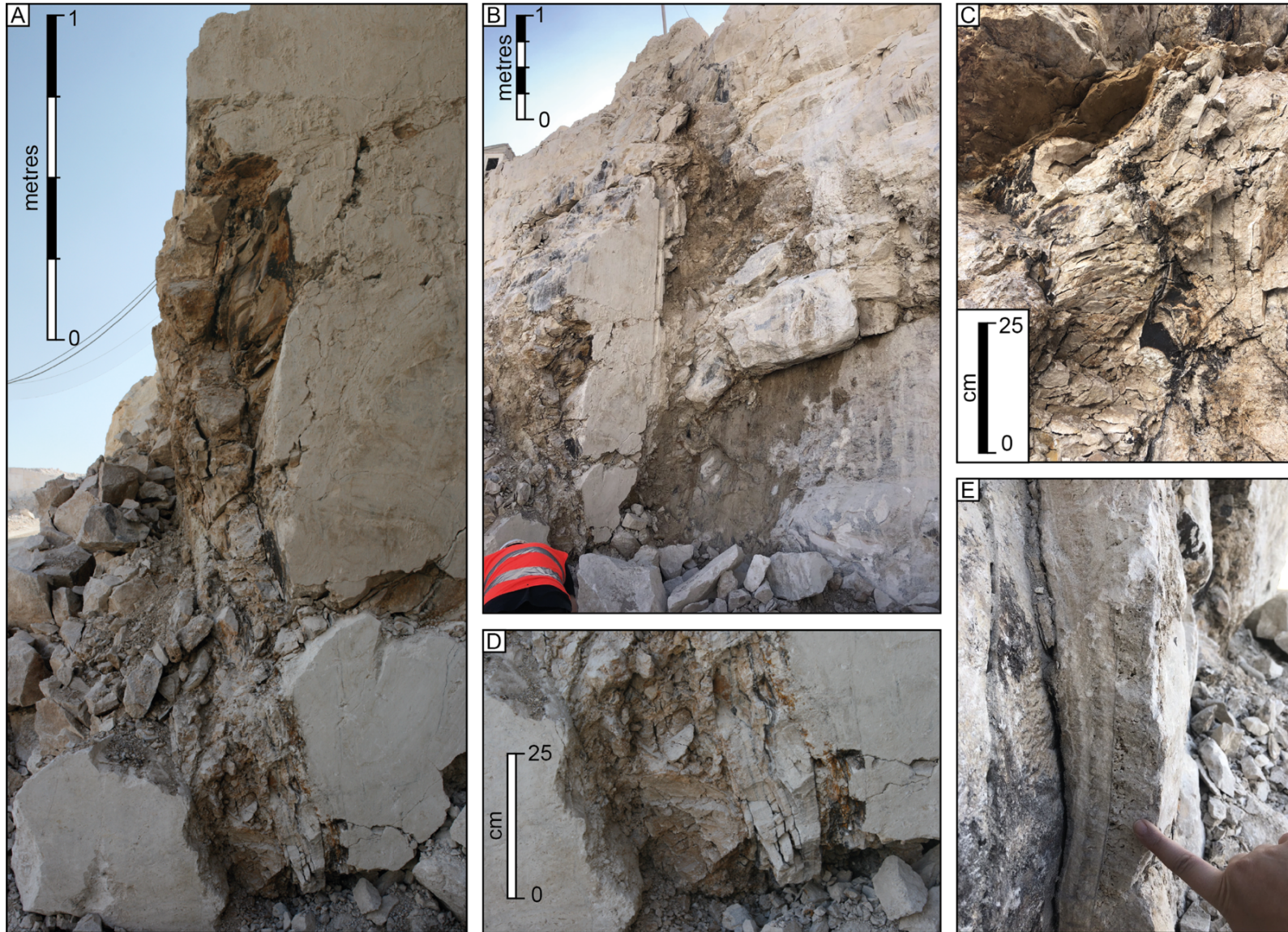


Figure 4-21. Detailed pictures of the strike slip fault observed in Braşaranlar Quarry from Figure 4-20. A) Photograph of west/east? segment from fault. B) Heterogeneous fault core of the strike slip fault with multiple segments. C) Heavily fractured fault parallel travertine and black Fe and Mn rich crusts. D) Detail of fault parallel travertine layers and chaotic poorly cemented material within fault core. E) Example of fault parallel travertine deposition bounding the fault core.

The extent of internal deformation within the fault core may be due to localisation of strain to a particular segment or portion of fault or may be due to different stages of fault evolution, where the un-deformed travertine layers represent a later stage in dilation and deposition that occurred after fracturing of older travertine deposits within the fault core. The variability of this relationship along-strike likely reflects highly compartmentalised periods of deformation and/or fluid flow along a given fault segment which vary temporally and spatially.

Though this strike slip fault generally shows similar characteristics to the normal dilation faulting also observed in the Ballık travertine body, where similar calcite, travertine and Fe- and Mn-rich mineralisation along the dilation fault walls are also observed, the strike slip fault possibly represents a more evolved fault, where internal deformation of the fault zone is observed along with multiple generations of travertine deposition. Additionally, multiple slip surfaces were observed within the massive travertine body illustrating the formation of fault segments. This contrasts with the dilational normal faults, where faults are generally observed to be localised onto a singular dilational fault plane (except for where the fault intersects a layer with significant mechanical differences or the free surface).

Fault core thickness - displacement relationships

Fault core thickness measured from faults observed in the K m rcuoglu Quarry have a very weak positive correlation ($R^2 = 0.28$) with fault throw but cover a substantial spread, especially at lower throws. When analysed alongside data from pre-existing studies of the Ballık travertines ( zkul et al., 2013; Van Noten et al., 2019) this relationship remains though there is increased spread in the data with several faults having less than 10 m throw showing a range of fault core thickness between 0.1 and 10 m.

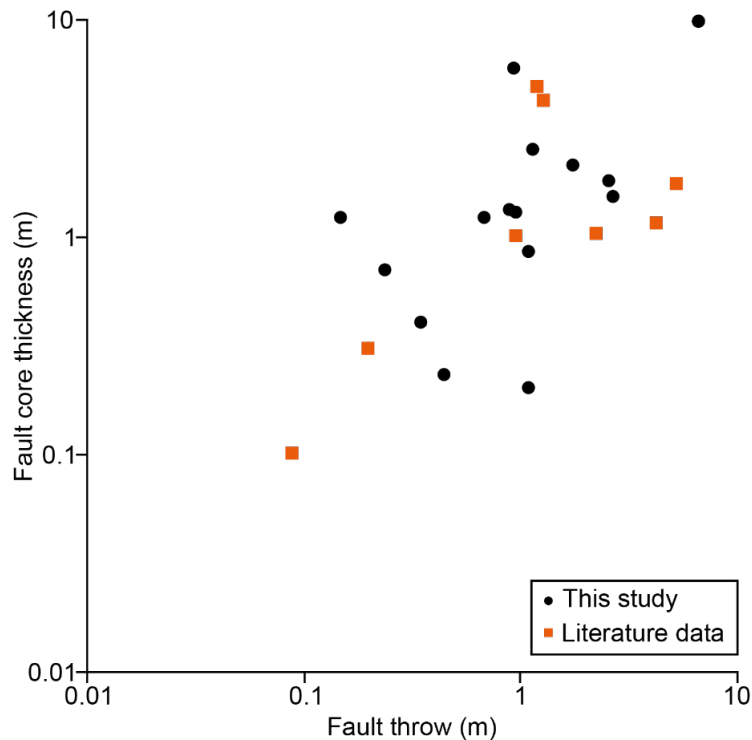


Figure 4-22. Relationship between fault throw and fault core thickness of the faults observed in K m rcuoglu Quarry (field measurements from the study) and the surrounding Ballık travertine body (from literature), Turkey. Data from literature is taken from Van Noten et al. (2019) and  zkul et al. (2013).

4.4 Discussion

4.4.1 The presence of deformation within non-marine carbonates

Though 13 different formations located in tectonically affected areas were visited, only 7 of these provided evidence of deformation (Table 4-4). Of these 7 localities, only the Nova Olinda laminated limestones in Brazil and the Ballık Travertine in Turkey are observed to host faults. The limited extent of known faulted outcrops in non-marine microbial and hydrothermal carbonates may be attributed to limited understanding of what these deposits look like in the ancient historical record and so only those that are relatively young are acknowledged. This is especially true for travertines, where the majority of studied outcrops are of Quaternary age (with many localities are shown to still be actively precipitating). Older travertines, and indeed microbialites, are prone to dissolution, terrestrial erosion, or remineralisation for those which become buried such that their origin becomes unclear (Brasier, 2011) meaning that Cenozoic or older non-marine carbonates may be under-represented in the literature record compared to their actual existence. The low preservation potential of these deposits still poses a difficult challenge and has been addressed in several studies (Capezzouli et al., 2014, 2022; Bosence et al., 2015; De Boever et al., 2022), including the aptly named research paper “Non-marine

carbonate: Wherefore art thou?" by Cappezzouli et al. (2022). It is generally recognised that the effect of erosion and dissolution by meteoric waters in terrestrial environments plays a significant effect on the low preservation potential of non-marine carbonates. This study is therefore limited to deposits, which have undergone little burial and early diagenesis, though provides insights into early deformation commonly observed in deposits which are intrinsically linked to tectonic activity and may form important modifications to deposits prior to deeper burial.

Table 4-4. Overview of different structural features observed in visited non-marine carbonate outcrops for this study. Ages and depositional and tectonic settings detailed in Table 4-2.

Formation	Location	Age	Carbonate type	Deformation features observed		
				Fractures	Karsts	Faults
Hot Springs Formation	Idaho, USA	Miocene	Bioherms			
Green River Formation	Wyoming, USA	Eocene	Carbonate mounds			
Green River Formation	Colorado, USA	Eocene	Stromatolites, thrombolites			
Green River Formation	Utah, USA	Eocene	Stromatolites, thrombolites			
Crato Formation	Araripe, Brazil	Aptian	Laminated limestones	Y		Y
Perachora carbonate mounds	Perachora Peninsula, Greece	Late Pleistocene	Carbonate mounds	Y		
Tivoli Travertines	Tivoli, Italy	Quaternary	Travertine	Y	Y	
Saturnia Travertines	Saturnia, Italy	Quaternary	Travertine	Y	Y	
Acquasanta Travertine	Acquasanta Terme, Italy	Middle Pleistocene	Travertine	Y	Y	
Terme San Giovanni Travertines	Rapolano Terme, Italy	Late Pleistocene to present	Travertine	Y	Y	
Serre di Rapolano Travertines	Rapolano Terme, Italy	Middle – Late Pleistocene	Travertine	Y	Y	
Budakalász/ Sütto travertines	Buda/ Gerecse Hills, Hungary	Quaternary	Travertine	Y		
Ballık Travertine Formation	Denizli, Turkey	Pliocene	Travertine	Y	Y	Y

4.4.2 Structural styles

4.4.2.1 Small scale faulting in laminated limestones

Deformation within the Crato Formation is limited to small-scale (<20 cm) normal faults. These structures are found to occur as conjugate sets with dips ranging from 40-60° and are formed of multiple fault strands within relatively thin (<5 cm), segmented fault zones. Microstructural analysis of these small faults show that the fault zone is observed to have a slight reduction in grain size and, where faulting cross-cuts successions rich in organic material, smearing of clay size organic material has occurred along the fault segments.

Minor normal displacements, variable dips, and ductile deformation features (folds and dragging of laminations in faults) indicate that formation of these small-scale faults likely occurred soon after deposition where the deposits were only partially consolidated with variable extents of cementation. Detailed analysis of additional soft sediment deformation in the Crato Formation was discussed by Alencar et al. (2021) and illustrates evidence of features such as loop bedding, convoluted laminations and load casts which supports a largely ductile formation mechanism. Alencar et al. (2021) infers that the presence of these features as well as of additional soft sediment structures such as fluid escape structures and breccias provide evidence of liquefaction associated with palaeoseismicity. Though the Crato Formation forms part of the post-rift sequence within the Araripe basin, it is thought that this seismicity is caused by reactivation of the adjacent basement shear zone system during redistribution of stress during the continued rifting of the eastern margin of NE Brazil. It is interpreted that these events may have produced minor deformation of the Crato formation producing the small-scale faulting observed in the exposures studied. These deposits provide a useful analogue to the Barra Velha Formation within the Santos Basin (offshore NE Brazil) where smooth and crenulated laminated limestones are found (Terra et al., 2010). The Barra Velha Formation sequence deposited during the late stages of rifting to post rifting during the onset of thermal subsidence and post-rift evolution (Terra et al., 2010; Gomes et al., 2020; Borghi et al., 2022). Given the similar depositional setting and initial tectonic evolution, these small-scale deformation features may be characteristic of post-rift lacustrine marine sequences. However, the deformational features may be affected by reactivation in rift basins with complex structural and stratigraphic evolutions resulting in structural deformation influenced by the existing structural fabric of the sequence.

4.4.2.2 Karst interaction with fractures and faults

Karstification of travertine is commonly observed across different types of facies and travertine types highlighting the important role dissolution has in the low preservation potential of these deposits within the geological record. Karst formation and processes also play an important role in the formation of secondary porosity where deposits are thick enough to remain preserved. Karst features are broadly characterised on their structural style and infill into three distinct types:

1. Karst collapse structures characterised by travertine breccias and rotated host rocks, usually hosted in a matrix of fine mud and/or clay sediments.
2. Karst cavities are unrelated to faulting or fractures and can be unfilled (karst cavities), unfilled or have variable fill.
3. Fault-and fracture-controlled karsts systems which are commonly filled with terrigenous material and reworked travertine sediments and are linked with dilational faults or fractures.

Karst collapse structures

Karst collapse structures are interpreted to originate through collapse of the overlying travertine into karstic cavities resulting in locally brecciated travertine similar to collapse breccias recognised in many karstified carbonate sequences (e.g Woodcock et al., 2014; Daniels et al., 2022). Understanding of the 3D variability of the structure is however poorly constrained in these localities where the spatial variability cannot be observed. However, fracturing of the host rock is common around karst collapse structures, especially below these structures where the initial collapse causes an impact with the underlying strata. As such fracture intensity may increase locally where karst collapse features occur. Brogi et al. (2016) define these shallow karst collapse features as sinkholes which are commonly composed of regolith where the karst either intersects the surface or interbedded palaeosols and thus can pose significant geological hazard due to hidden subsidence.

Karst cavities unrelated to faulting or fractures

Karst cavities that appear to be unrelated to faulting or fractures are often elongated along bedding and may be formed because of particularly high porosity travertine facies or due to significant primary vug formation evolving into karst networks where shallow meteoric waters circulate. Unlike observations in other karstic systems (e.g., reef carbonates of Mississippian Pembroke Limestone Group – Woodcock et al., 2014) where collapse breccias are seen to be

related solely to underlying structures, observations in the Ballık Travertine are not always associated with fault structures and form their own class of deformational features. This may be a result of the potential for very early vug and cavity formation due to deposition near or on the earth-surface for non-marine carbonates. Contrary to marine, reef carbonates which may have more limited vug/cavity formation during their early diagenesis and require exhumation for interaction with meteoric waters, and so will localise along pre-existing zones of weakness, such as faults and fractures related to their exhumation (e.g., Woodcock et al., 2014). Instead, in largely undeformed, recently deposited travertines, and to an extent marginal lacustrine microbialites, early interactions with meteoric waters and resultant dissolution will likely localise along higher permeability stratigraphy (e.g., organic rich, or palaeosol horizons) to promote stratigraphically controlled, rather than structurally-controlled vug and cavity formation. As a result, whilst overall structural frameworks play a clear role in the prediction of such breccias (as seen in the dilational fault infill of the major faults of the Ballık Travertine), important accumulations of poorly sorted breccia pipes and deformed stratigraphy likely exist outside of major fault zones, especially where later deformation or reactivation of faults is minimal.

Fault-and-fracture-controlled karst systems

Figure 4-10c/e illustrated closely related and interacting karst features with dilational faults. The interaction of karsts with dilational structures illustrates how dilational features can act as a significant conduit for fluid flow. Karst systems likely have variable connectivity with the fault system along strike where the karst system is not continuously interconnected to the dilational fault/fracture and also likely shows significant heterogeneity of the extent of dissolution. These complex networks of dilational structures with karsts illustrate the potential for syn-deformational dissolution and precipitation, often resulting in widened ‘fault’ zones where the apparent fault walls do not represent the original fault walls resulting from primary deformation, similar to brecciated, “depositional fault rocks” in Woodcock et al. (2014).

Karsts within the Ballık travertine that are related to faulting are generally found to be filled with layers of fine-grained terrigenous material with inclusions of brecciated travertine clasts broken from the karst walls. In most cases the infill is well cemented with calcite cement, and in places preserved thin laminations onlapping karst walls, suggest a relatively low energy depositional environment of the finer-grained material, contrary to the more chaotic infill suggested by the breccias (Woodcock et al., 2014). Fracturing of karst infill is also common where multiple generations of faulting or fracturing is evident, suggesting that dissolution of the host rock occurs relatively early after initial phases of faulting or prior to generation of faults

along pre-existing collapse breccias (Figure 4-23). The control on the communication of fluids between the host rock and fault conduit is likely the lateral permeability of travertine layers, where travertine facies that typically have high porosities and permeabilities (such as bubble boundstones and shrub facies) will preferentially re-distribute fluids from the fault zone and promote further karstification and precipitation along the walls of the fracture within these sequences. The along strike variability of karsts may therefore also be controlled by the continuity and heterogeneity of travertine facies. Though not assessed in this study, the distribution of fluids along high permeability travertine layers may result in localised enhanced cementation and secondary diagenesis.

The complexity and variability of the interaction between fracture conduits and matrix within carbonates has been evaluated by several authors (Önder et al., 1985; Romanov et al., 2002; Klimchouk et al., 2012; Galloway et al., 2018; Cazarin et al., 2019; Araújo et al., 2021; La Bruna et al., 2021). For example, Cazarin et al. (2019) illustrates how fracture networks control the formation of characteristics of the Toca da Boa Vista and Toca da Barriguda cave systems in NE Brazil. Observations of these cave systems showed how karsts development occurred initially through ascending fluid flow along fractures, with lateral flow between the fracture conduit and host rock controlled by facies variability within stratigraphy. Cazarin et al. (2019) concluded that the stratigraphic control is important to determine overall karst architecture where porosity and permeability will provide lateral pathways for fluids, and those with mineral assemblages susceptible to dissolution (such as travertine) will exhibit a high degree of karstification, as observed in the Ballık travertines.

4.4.2.3 Dilational fractures and faults within travertines

Dilational deformation is common within travertine where neotectonics play an intrinsic role in their deposition and subsequent shallow deformation. Generally, dilational features were observed to have minor vertical throw components (of 1- 6 m) and can be categorised as dilational faults of hybrid mode normal/strike slip faults. Though these two categories represent two different modes of deformation, the characterisation of geometry and fill of the resulting dilationally produced accommodation space within the faults is broadly similar and can be summarised as three different types of dilational feature:

- a. Dilational faults/fractures with a fault core composed of poorly consolidated rock-infill deposits
- b. Dilational faults/fractures with one or more generations of cemented infill conglomerates and/or fault parallel travertine, calcite and manganese mineralisation.

- c. Dilational faults/fractures with a combination of variably cemented infill conglomerates, fault parallel mineralisation with a fault core of poorly consolidated terrigenous material.

The formation and evolution of dilational normal faulting within the Ballık travertines is summarised in Figure 4-23 which illustrates how the three different types of dilational features may represent different maturities of fault growth. The schematic illustrated in Figure 4-23 illustrates the initial hybrid failure of travertine body where changes in the fault architecture are apparent where the succession is interbedded with weaker sedimentary units such as a palaeosol surface. Subsequent dissolution and widening of fault core occurs by meteoric waters with karstification of the immediate wall rock causing any primary slip surface to be destroyed (Figure 4-23-3). Calcite and travertine mineralisation nucleating on the fault walls may also occur when the fault acts as a conduit if temperature, pressure and Ca-concentrations of fluids permit. Stage 4 illustrates the filling of the fault zone by terrigenous sediments from overlying strata and brecciated fragments of travertine sourced from the fault walls. Initial infill is likely to be poorly consolidated formed of clasts within a clay and organic rich matrix (Figure 4-23 & Figure 4-24). Fluid flow through this zone causes cementation and alteration, though the extent of diagenesis may be variable due to the heterogeneous nature of the fault core infill. Stage 5 illustrates reactivation and therefore widening of the fault with a new generation of central fault infill and mineralisation. Hybrid faulting may undergo several generations of reactivation with variable preservation of pre-existing younger generations of fault infill.

The nature of dilation deformation and the controlling failure mechanisms have been discussed in Chapter 2. The observation of opening mode fractures and hybrid mode faults in travertines illustrate the spectrum of brittle deformation types that occur between tensile failure and shearing, where dilational fractures illustrate simple tensile failure and dilational faults display both a tensile and shear component. The dilational brittle failure of travertine bodies is likely due the mechanical strength (due to very early diagenesis as discussed in Chapter 2) of the deposits coupled with the lack of overburden stress in the very shallow subsurface and therefore represent typical structural styles that can form at shallow depths and may be extremely common in deformed, non-marine carbonates.

Though dilational features within travertines have been briefly discussed in neotectonic studies (Van Noten et al., 2019) and in investigation of karst features (Brogi et al., 2016), the detailed characterisation of fault infill, geometry and evolution have not been widely discussed

in literature. Observations of dilational faults and fractures in this study show the highly heterogeneous nature of these faults which likely form complex networks with karst systems. Possible comparative fault examples are those observed in carbonates of the Jebel Hafeet anticline (UAE and Oman) by Gent et al. (2010) where similar fissures features are filled with sediments distinctly different from the host wall rock with inclusion of crushed wall rock and carbonate veins. However, these faults lack the complex evolution of re-faulting and fracturing which results in multiple fault parallel 'layers' of sediment infill with varying degrees of diagenesis and spatial variability. Instead, Gent et al. (2010) observes stratification of this sediment infill illustrating episodic sedimentation through gravity or hydraulic transport which is only observed within a minor number of examples locally within dilational fractures in this study (Figure 4-14).

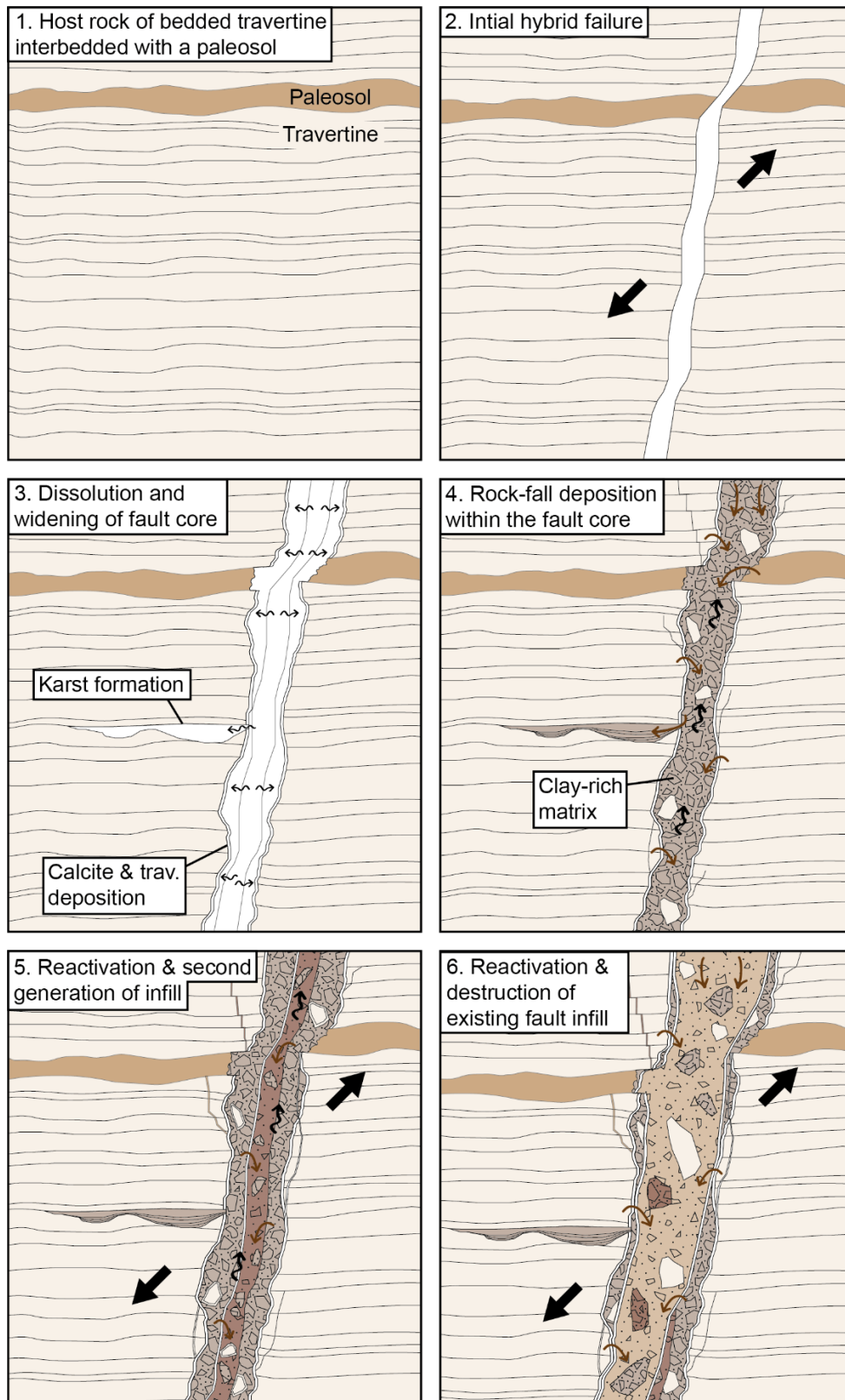


Figure 4-23. Diagram showing possible dilational fault evolution observed in the Ballik Travertines (Turkey). Stage 2 illustrates initial hybrid failure of the travertine, where interbeds of mechanically weaker units such as palaeosols result in changes in fault geometry. Stage 3 illustrates the widening of the fault and formation of a connected karst system through dissolution. Travertine deposition or calcite mineralisation may be deposited onto the fault walls. Stage 4 shows filling of the fault void by terrigenous material sourced from overlying strata and brecciated segments of wall rock. Stage 5 and 6 illustrates the reactivation of the fault through hybrid faulting resulting in new generation of fault infill.

4.4.3 Permeability impacts of shallow deformation features

4.4.3.1 Small scale faulting in laminated limestones

The laminated limestones of the Crato Formation in Brazil provides a potential outcrop to tight low-permeability carbonates similar to some microbial facies observed within the pre-salt reservoirs of the Barra Velha Formation in the Santos Basin. Therefore insights into the style and impact of faulting presented in this study may be characteristic to these formations (Terra et al., 2010; Catto et al., 2016; Miranda et al., 2018).

Though individual faults form complex segmenting and splaying faults, permeability, and porosity reductions relative to the host rock are minor (less than 0.5 magnitude reductions). Alteration by Fe-rich meteoric waters of the formation shows that laminations and fractures have the dominant control on fluid pathways and that faults appear to have limited impact on the overall hydraulic system. Alteration can be observed to locally follow fault segments which provide a pathway between preferentially altered laminations. This is likely due to the host rock porosity and permeability controlling the primary lithology of the faults, whereby parts of the fault cross-cutting clay-poor, higher porosity laminations will also have higher porosity. Alteration is also observed to follow preferred successions across faults where faults are composed of multiple fault strands (over a 5 cm wide zone up to 30 individual fault strands can be observed) so that layers remain juxtaposed. The minor faults in this study do not show preferential growth of calcite cements or pervasive recrystallisation through acting as conduits and precipitation zones for Ca-rich fluids contrary to observations on larger faults in e.g. marine, reefal carbonates (Cooke et al., 2019).

Analysis of mechanical stratigraphy within the Crato laminated limestones by Araujo et al. (2020) supports the notion that heterogeneities within the laminations control the hydraulic system and highlights the impact that this mechanical stratigraphy has on the formation of diagenetic and deformation structures. Araujo et al. (2020) notes that variations in depositional environments between different laminations results in associated variations in diagenesis where very early cementation occurred in layers associated with high deposition rates and high primary porosity allowed significant pore water content. The observations of variations of mineralogy along the dip of faults in this study are directly linked to the fault layer juxtapositions, Where the faults interact with layers which are rich in organics and have relatively lower porosities, fault strands will also be characterised with relatively higher organic material and lower porosities than portions of the fault that interacts with higher porosity layers. In other words, the porosity reduction where the fault interacts with higher porosity layers may still

result in a higher fault porosity than where the fault intersects low porosity, organic rich layers. Despite their abundance and continuity, the permeability impact of the minor faults observed within this study is therefore likely minimal, especially considering the very low permeabilities of the primary host rock.

4.4.3.2 Shallow dilational structures within travertines

The nature of dilational faults and fractures which results in the generation of open voids and fissures, immediately implies the potential for the categorisation of these features as major conduits to fluid flow (Figure 4-24a). This is true during their initial formation, periods of low sedimentation/infill rates and during periods of reactivation evidenced by travertine precipitation, dissolution of wall rocks and calcite rich cementation and vein fills even within terrigenous collapse breccias. This behaviour of the dilational faults observed in the Ballık Travertine is contrary to intra-travertine shear faults in Giwelli et al. (2016a,b) and Delle Piane et al. (2016) where fault rocks developed in shearing of travertine have the ability to act as a baffle to flow due to localised compaction and asperity shearing producing porosity and permeability reductions. In the exposures of the Ballık travertine no faults were observed to be fully-filled, however similar processes may occur as fault infills undergo consolidation during burial and/or experience closure of fissures and fractures. As such the heterogeneity observed within the fill of these structures suggests that the fault zone permeability may change with prolonged development and filling by gravitational or hydraulic transport. Nevertheless, the dilational faults formed through near-surface deformation of the Ballık travertine appear to provide ample vertical fluid pathways.

The most important impact on permeability of these faults however remains their potential as open fluid-conduits (Figure 4-24). As travertines display high permeability anisotropy (Giwelli et al., 2017) where permeability is significantly higher parallel to bedding than across bedding where very low permeability layers (such as micritic microbial mats) controls fluid flow, fault-related conduits provide open, vertical pathways with permeabilities likely several orders of magnitude higher than primary host rock permeability. Karst processes can also be amplified in close relationship with dilational faults due to their high potential for fluid flow, resulting in the development of complex karst systems within and surrounding dilational fault and fracture systems providing further open pathways for fluids.

Even when dilational structures are fully or partly-filled, local changes in the permeability anisotropy may occur where fault parallel deposition of travertine within fault walls occurs (Figure 4-24b). Similar vertically banded travertines are observed within fissure ridge deposits

where ascending hot waters result in carbonate precipitation within the fissure space controlled by underlying faults (De Filippis et al., 2012a,b; Brogi et al., 2014; Chapter 2). Though no spring mound depositional features (Chapter 2) are observed related to the vertically banded travertine; such deposits may occur if/where faults intersect the surface. The presence of vertical layers of travertine may result in a change in the permeability anisotropy from the wall rock where bedding-parallel permeability will be significantly reduced and instead promote vertical fluid flow (Figure 4-24). Unless the fissure is completely filled with the deposition of vertical banded travertine, the central fissure may continue to act as an open fluid pathway though may be inhibited in communication of fluids between the host rock and the central fissure.

Commonly, however, faults are found to be filled with conglomerates. Generally, these are composed of terrigenous sediments which have a clay-rich matrix. As such they likely display reductions in macro-porosity and are likely to result in reductions in permeability compared to the host rock controlled by the extent of diagenesis. Several conglomerates and terrigenous infill portions of the faults within the Ballik travertine are observed to be fractured after their deposition and infilled with calcite cementation within vein fills or pore-space within the conglomerates themselves, indicating the potential for vertical fluid migration through even filled fault structures. However, unlike the partly or fully-open voids, it is apparent that episodes of further deformation are required to trigger fluid flow along the fault, once it is filled. However, if continuous travertine depositional is present through the fault core, then these layers may act as preferred fluid pathways along fault zones (Figure 4-24c). Additionally, faults may display different generations of infill where preservations of early infill and travertine deposition is variable therefore introducing more complex heterogeneities in permeability within the fault zone (Figure 4-24d).

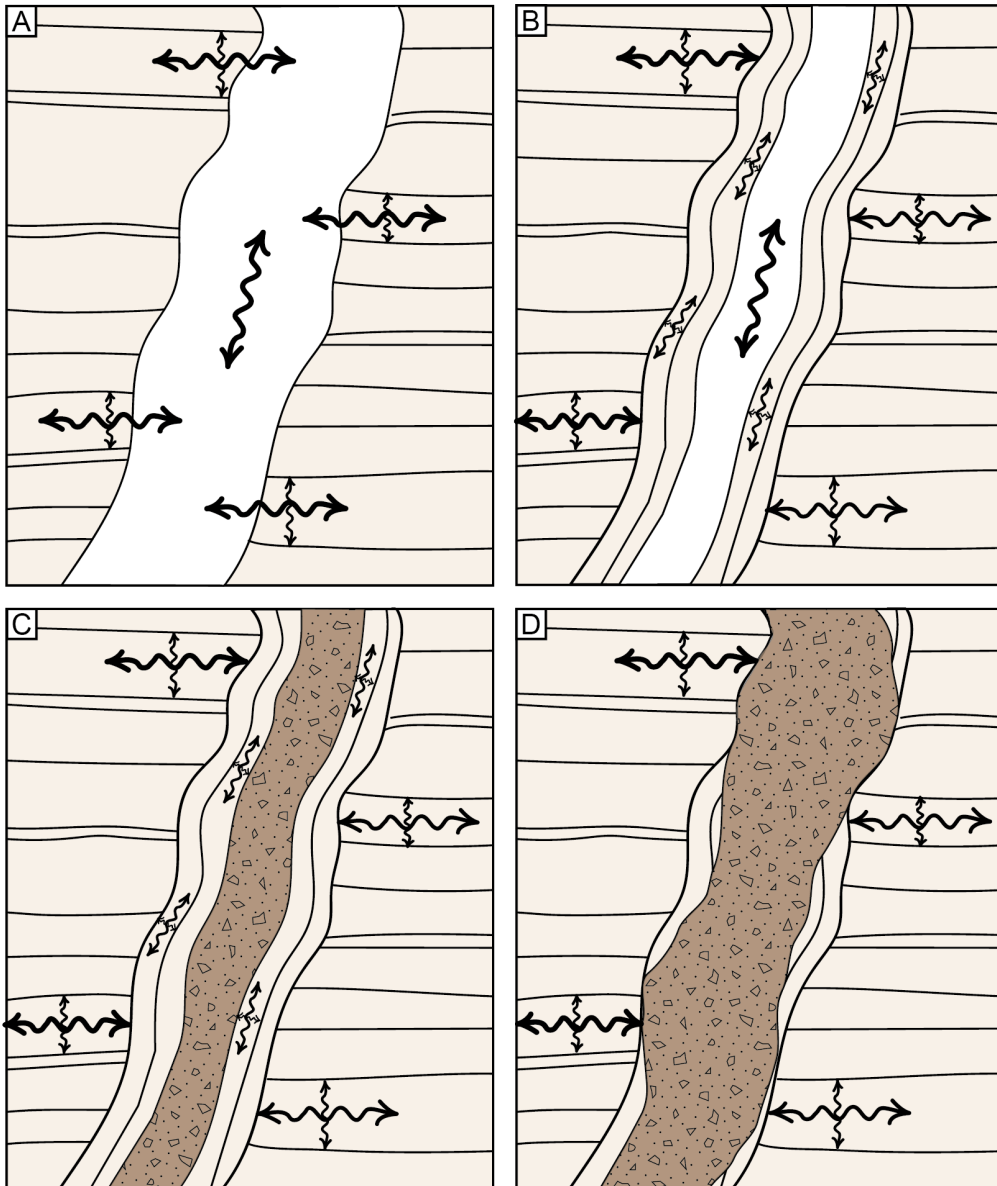


Figure 4-24. Influence of dilational faulting on permeability anisotropy within travertines. A) Dilational faults act as conduits for fluid flow and provide a preferential vertical pathway for fluids as vertical permeability across travertine laminations is much lower than permeability parallel to travertine beds. B) Travertine deposition and calcite mineralisation is common along the fault walls of these faults. Continuous fault parallel travertine will result in a lateral permeability reduction in the fault core. The presence of vertical layers of travertine or additional mineralisation and veins may result in a reduced re-distribution of fluids from the inner fissure acting as a conduit to the surrounding fault rock. C) illustrates a fault where the central fissure is composed of infilled conglomeritic sediment. The permeability within the central part of the fault zone is controlled by the composition and diagenesis of the infill and may represent a permeability decrease compared to the host rock where sediments are clay rich and have undergone significant diagenesis. However, high porosity vertical layers of travertine can act as fluid pathways depending on the continuity D) illustrates a the most common type of dilational faults observed where the preservation of the older deposition within the fault fissure are locally preserved and so the sediment infill of the fault controls the overall hydraulic system along the fault. The central part of the fault is often also composed of different types of conglomerate infill providing further local permeability heterogeneity within the fault zone.

4.5 Conclusions

An extensive fieldwork investigation was carried out to characterise the presence and styles of deformation within exposed microbial and hydrothermal carbonates, with a view to assessing the impact such deformation features may have on fluid flow. A total of 13 global non-marine carbonate formations were visited encompassing the highly variable depositional settings and carbonate types typical of non-marine settings. Only 7 of these deposits were found to host observable deformation features, only 2 of which had faulted exposures (Crato Formation lacustrine microbialites, Brazil; Ballık Travertines, Turkey). The limited extent of deformation suggests most microbial carbonates may have limited deformation in their early history. However, observations may be limited due to the under-representation of ancient microbialites and hydrothermal carbonates in literature due to limited preservation and misidentification (due to diagenesis and destruction of primary depositional features).

The laminated limestones of the Crato Formation are found to develop minor normal faults (< 20 cm throw) related to minor post-rift seismicity in NE Brazil. These faults are shown to have a limited impact on permeability despite being pervasive throughout the studied exposures. Instead, primary depositional fabrics remain the primary control on the hydraulic system.

Deformation within travertines is characterised by dilational faults and fractures as well as karst networks. Dilational faults and fractures illustrate early shallow subsurface deformation which can act as open permeable zones enhancing vertical permeability within travertine bodies. These dilational features can, however, display complex sedimentary infill as a product of gravitational and hydraulic deposition coupled with re-activation of structures and variable extents of diagenesis. A spectrum of deformation styles within karst structures is observed in travertines, where they are found to form either in relation to fault and fracture networks or form separate, stratigraphically defined karsts. These different styles of karst formation, however, can generally have comparatively similar infill character with that of dilational faults and fractures making their identification from limited observations (e.g. core) challenging, but with likely different extents and timing.

Ultimately, quantitative, and qualitative data discussed in this study to assess the impact of deformational features during early burial on permeability provides constraints for similar subsurface deposits where early deformation of non-marine carbonates is more poorly constrained.

Chapter 5

5. Influence of rock fabric on the mechanical behaviour of travertine

5.1 Introduction

Deformation of rocks can have fundamental impact on fluid flow and is an important consideration for a range of applications including reservoir/aquifer management and geotechnical engineering. As discussed in Chapter 2, the complexity of the texture and fabric of carbonates in comparison to sandstones means that modelling and predicting brittle and/or ductile deformation is challenging. Travertine, in particular, is composed of highly heterogenous facies with highly complex pore systems and variable porosity; its layered nature makes it likely that properties will also be anisotropic. Analysis of mechanical data to understand inelastic behaviour, failure mode and the brittle-ductile transition is useful to interpret and predict the occurrence and extent of deformation within such rocks as well as the impact of deformation on fluid flow.

This study uses an integrated approach to quantitatively characterise the porosity and permeability heterogeneity within travertines and understand the impacts this has on the key deformation processes during failure. This is achieved by conducting an initial characterisation of travertine facies for tested samples and petrophysical analysis of different predominant facies types. Mechanical and velocity data from triaxial tests, along with CT scan imaging and optical microscopy captured during different stages of deformation are used to assess the impact of travertine fabrics on rock strength and resulting deformation style and failure mechanisms.

5.2 Mechanical failure within carbonates

The deformational behaviour of porous carbonate rocks has been investigated in several experimental studies (e.g., Vajdova et al., 2004; Baud et al., 2009,2017a,b; Dautriat et al., 2011; Ji et al., 2012; Cilona et al., 2014; Walton et al., 2015,2017; Brantut et al., 2018; Meng

et al., 2020; Chen et al., 2022). A detailed review of compaction, dilatancy and failure in porous carbonate rocks can be found in Chapter 2. In summary, inelastic deformation is generally separated into two regimes reflecting the brittle-ductile transition: 1) dilatancy, associated with low confining pressures and 2) compaction, where distributed cataclastic flow typically occurs at high confining pressures (Wong & Baud, 2012; Bedford et al., 2018). Due to the ability of calcite to easily undergo mechanical twinning and dislocation slip at relatively low-stress and temperature conditions, a comparatively early transition from dilation to compaction is commonly observed in carbonates (Baud et al., 2009; Chen et al. 2022). For example, Baud et al. (2000) found that Solnhofen limestone within porosities as low as 3% displays similar compactive yield similar behaviour to that of sandstones and carbonates with porosities up to 40%. Experimental analyses of porous carbonates illustrate the transition between dilatant and compactive regimes to be highly complex with localised, shear-enhanced compaction (Baud et al., 2000; Wong & Baud 2012; Vajdova et al., 2004).

Experimentally derived mechanical data from carbonate with low to intermediate porosities (3-18% - Vajdova et al., 2004) illustrate that deformation is dominated by dilatancy and shear localisation at low confining pressures, while shear enhanced compaction, with an eventual switch back to dilatancy after a certain amount of strain hardening occurs at higher confining pressures (Baud et al., 2000; Vajdova et al., 2004; Wong & Baud, 2012). Such results illustrate a complex interchange between pore collapse mechanisms and microcracking, which has significant implication for the overall porosity changes experienced throughout deformation (Wong & Baud, 2012). In comparison, high porosity carbonates (>30% - Baud et al., 2009), demonstrate only shear-enhanced compaction failure, even at low confining pressures (Vajdova et al., 2004; Baud et al., 2009).

Overall, initial, host-rock porosity is found to play a significant control on the failure mechanism whereby increasing porosity results in a decrease in the strength and increased compressibility of the rocks (Vajdova et al., 2004; Ng & Santamarina 2022). As a result, porosity often forms a primary parameter used to model deformation within both clastic and well-documented carbonate rocks (e.g. porous sandstones – Rutter & Glover, 2012; chalks – Welch et al., 2015). However, existing studies are limited in the scope of carbonate types, focussing on the variability within limestones (Vajdova et al., 2004,2010; Baud et al., 2009,2017a,b; Zhu et al., 2010; Ji et al., 2012; Regnet et al., 2015; Brantut et al., 2018; Meng et al., 2020; Chen et al., 2022), high porosity but internally homogenous chalks (Welch et al., 2015), or very low porosity carbonates such as marbles (Walton et al., 2015; Tsirikis et al.,

2022). A paucity of observations exists within travertines, which exhibit complex, 3D internal host-rock porosity heterogeneity.

5.3 Materials and methodology

5.3.1 Travertine

Five different travertine bodies across Italy and Hungary (Figure 5-1) were sampled for petrophysical analysis and mechanical testing: 1. Tivoli travertines, Italy; 2. Rapolano Terme travertines, Italy; 3. Saturnia travertines, Italy; 4. Acquasanta Terme travertines, Italy and 5. Ballik travertines, Turkey. An overview of the travertine formations used in this study, including depositional setting, travertine type and ages are detailed in Chapter 4.1.1.

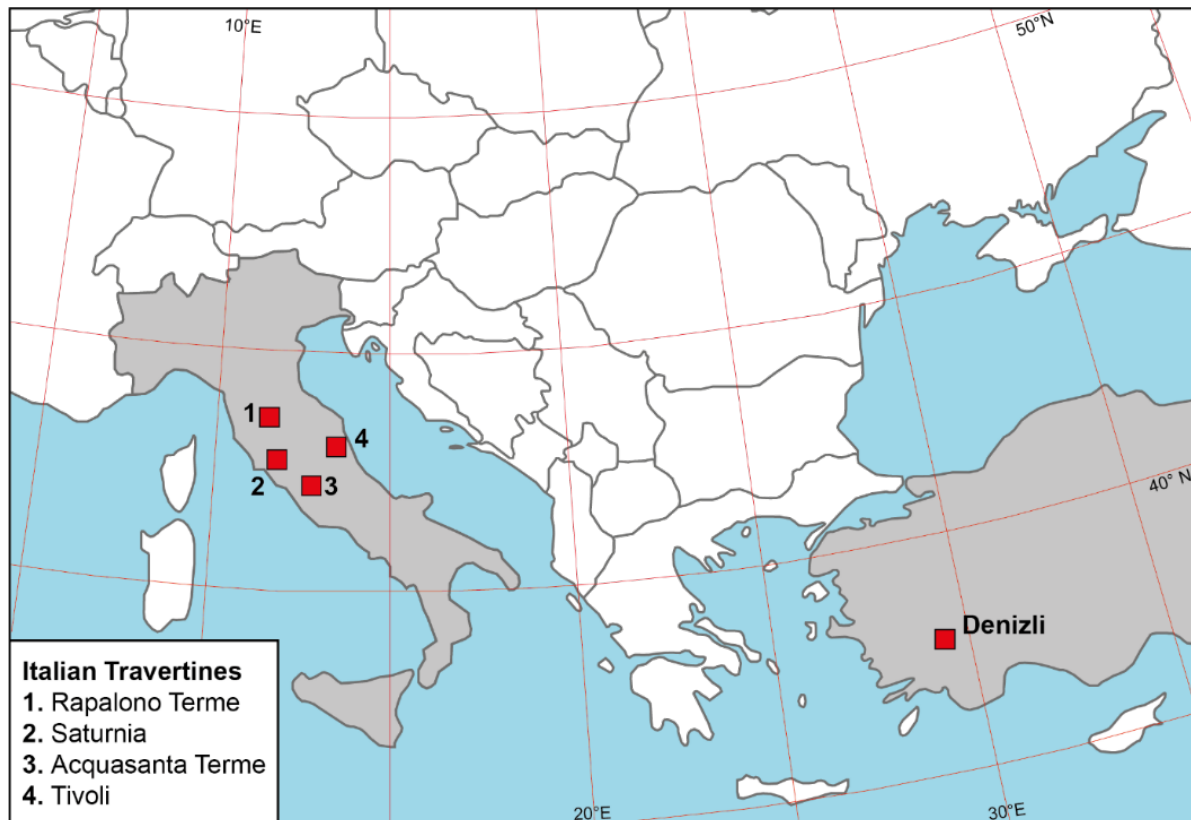


Figure 5-1. Studied travertine locations for mechanical analysis.

Travertines are generally composed of mm to cm thick laminations formed of calcite. The architecture and geometry of travertine laminations can vary widely depending on the depositional setting (Guo & Riding, 1998; Pedley, 2009; Capezzuoli et al., 2014) (Chapter 2.2.1). Largely horizontal travertine deposits can be found in depression depositional systems, as seen in the Tivoli travertines, while complex steep sided construction morphologies are

observed within mound depositional systems and fissure ridge deposits (as observed in Rapolano Terme and Ballik travertines). Slope depositional deposits, such as those observed in Acquasanta Terme result in smooth slopes and complex terrace deposits. Changes in facies within travertines occur over mm to metre scales, depending on the depositional environment (i.e., hydrodynamic setting, surface topography, microbial community etc) (Chafetz & Folk, 1984; Guo & Riding, 1998; Maggi et al., 2015). The travertine material used for mechanical testing can be broadly categorised into 5 different facies types summarised in Table 5-1. Cores from representative samples from each of these samples were used for mechanical testing to understand the control of travertine fabric (controlled by the predominant facies type present) may have on the strength and failure mode.

Table 5-1. Overview of travertine facies found within tested travertine cores.

Facies	Description	Porosity type	Example figures
Clotted peloidal micrite/sparite	Dense clotted peloidal micrite spheroids surrounding by microsparite	Central pore space in some spheroids and intra spheroid pores.	Figure 5-2 a-b
Laminated micrite/microsparite	Undulose, wavy laminations formed of clotted peloidal micrite or microsparite. Laminations are coated in prismatic sparite where layers are not conformable.	Lens shaped pores between laminations.	Figure 5-2 c-d
Shrubs	Dendritic micrite often coated with microsparite layer. Individual dendrites are found to nucleate from a singular point, usually resulting in a layer of parallel shrubs nucleated on the underlying substrate. Density of shrubs within individual layers can vary greatly depending on the extent of dendrite amalgamation.	Inter-dendritic pores. Porosity connectivity and abundance decreases with increasing density and amalgamation of dendrites.	Figure 5-2 e-f
Coated bubbles	Near spherical and convex upwards structures with a clotted peloidal micrite framework. Walls of bubbles are lined with rims of equant sparite.	Inter-bubble pore with poor connectivity.	Figure 5-2 h-i

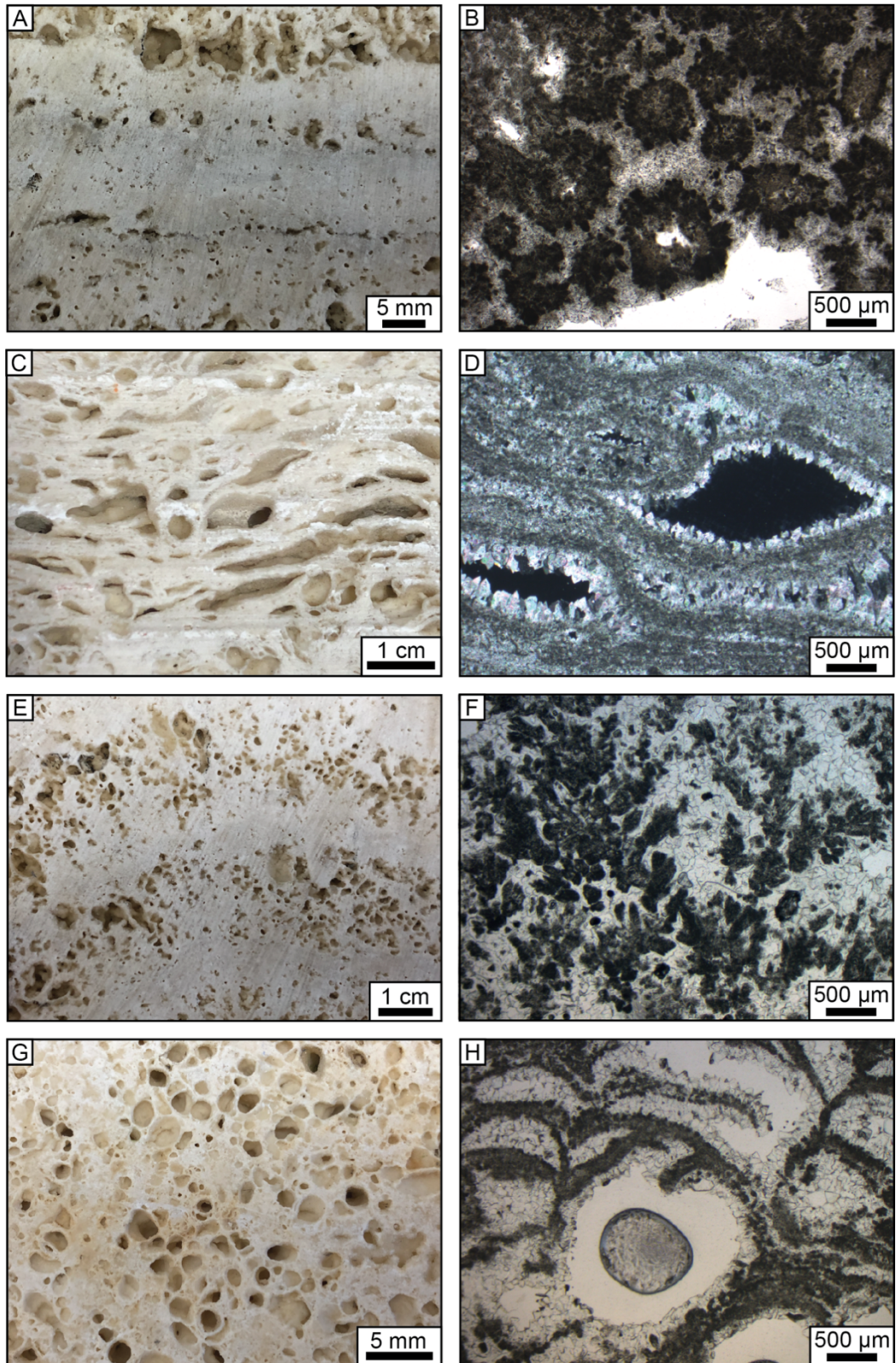


Figure 5-2. Hand specimen and photomicrograph examples of facies found within tested travertine samples. A-B) Clotted peloidal micrite/sparite facies from the Tivoli travertine body. B) illustrates peloidal micrite spheres surrounded by microsparite cement. C-D) Laminated micrite/microsparite with lens shaped porosity. D) illustrates prismatic sparite crystals coating laminations. E-F) Shrubs facies. E) shows layers of dendritic shrubs with alternating layers of shrub density. F) illustrates clotted peloidal dendritic micrite within a sparite cement. H-I) Coated bubble facies. I) illustrates spherical to semi-spherical bubble framework formed of clotted peloidal micrite. Micritic bubble framework is coated with equant to prismatic sparite.

5.3.2 Sample collection and preparation

Representative small blocks (15 – 30 cm³) of travertine were collected from each outcrop location for petrophysical and mechanical analysis. Three orientations (parallel, perpendicular and 45° to bedding) of 1- or 1.5-inch diameter, cylindrical core plugs were drilled from each sample where possible. Core plugs were prepared in accordance with testing standards detailed in API (1998) for mechanical testing with length to diameter ratios between 2 and 2.5 and specimens ends exactly perpendicular to core length and ground flat (see Appendix 1 for core plug data).

5.3.3 Petrophysical analysis

Porosity was derived from bulk and grain volume measurements conducted on core plugs, which had been dried at 60° for at least 4 days. Grain volume was calculated using the Boyle's law double-cell method with helium gas and bulk volume measurement of core plugs was determined using the calliper method (API, 1998).

Single phase gas permeability of cores was measured at a confining pressure of 2500 psi using either the pulse-decay for low permeability samples or steady state method for high permeability samples (Chapter 3). Testing followed the methodology and apparatus set-up detailed in API (1998). To account for gas slippage effects, Klinkenberg corrected permeability was calculated as described by Klinkenberg (1941).

Localised permeability of a sample block from the Tivoli travertines was measured using a probe permeameter at atmospheric pressure along three parallel transects to quantify heterogeneities in permeability across individual travertine beds. Permeability measurements were taken every 2 mm along the transect using a steady-state method with compressed air and then Klinkenberg corrected (full methodology is outlined in Chapter 3). The methodology of probe permeability followed the recommended practice outlined in API (1998) using a 2 mm diameter seal probe.

5.3.4 Triaxial multiphase mechanical testing

Ultrasonic velocity of cores was measured during multistage triaxial tests (full test methodology and equipment is outlined in Chapter 3). The triaxial test was carried out over three stages at confining pressures of 10, 20 and 30 MPa. The end of the first two stages was defined by the Imminent Failure Point (IFP) which occurs just at or after the yield point.

During the final stage, loading continues until full failure of the sample occurs. Ultrasonic velocities were monitored by piezoelectric transducers placed at each end of the core plug and V_p (compressional wave), V_{s1} and V_{s2} (orthogonal fast and slow shear waves) values were recorded every 2 minutes.

5.3.5 CT scan imaging and macro-porosity modelling

The internal structure of core plugs was determined through CT imaging using a GE Bravo 385 medical-style CT scanner (detailed acquisition parameters are outlined in Chapter 3). Helical scans of core plugs were taken before and after mechanical testing to visualise internal structure of cores post deformation. 3D volume generation and macro-pore segmentation was performed using Avizo 3D 2022.1 software providing data visualisation and quantification of macro-porosity.

5.3.6 Optical microscopy

Polished thin sections were made from both the original sample blocks (from which cores were taken from) to evaluate host rock textures and mineralogy, and deformed core plugs following mechanical testing. Deformed core plugs were impregnated with blue-dyed epoxy under a vacuum to preserve the internal structure. Orientated thin sections were then made from small blocks (3 x 2 cm) perpendicular to the main failure plane observed (CT scan images were used where no obvious failure plane/s could be observed). Petrophysical characterisation of travertine.

5.4 Results

5.4.1 Porosity

The petrophysical characteristics of travertine reflects the heterogeneous nature of the wide variety of fabrics that is associated with these deposits. Porosities measured from 106 travertine core plugs are found to have a range between 1 and 46% and have a mean porosity of 14.2%. The distribution of porosities for this sample set (Figure 5-3a) show that over half of the samples (56.6% of samples) have a porosity < 10% with the remaining half of sample distributed over a range from 10 to 46%. High porosity core samples are typically either found to have a high frequency or thickness of facies associated with high porosities, such as bubble boundstones (unconnected inter-bubble pores) and low-density dendritic shrubs (intershrub framework porosity) or host large vugs (Figure 5-3b). Core plugs composed of facies such as

peloidal micrite and crystalline banded travertine are associated with lower porosity values (< 10%) (Figure 5-3b).

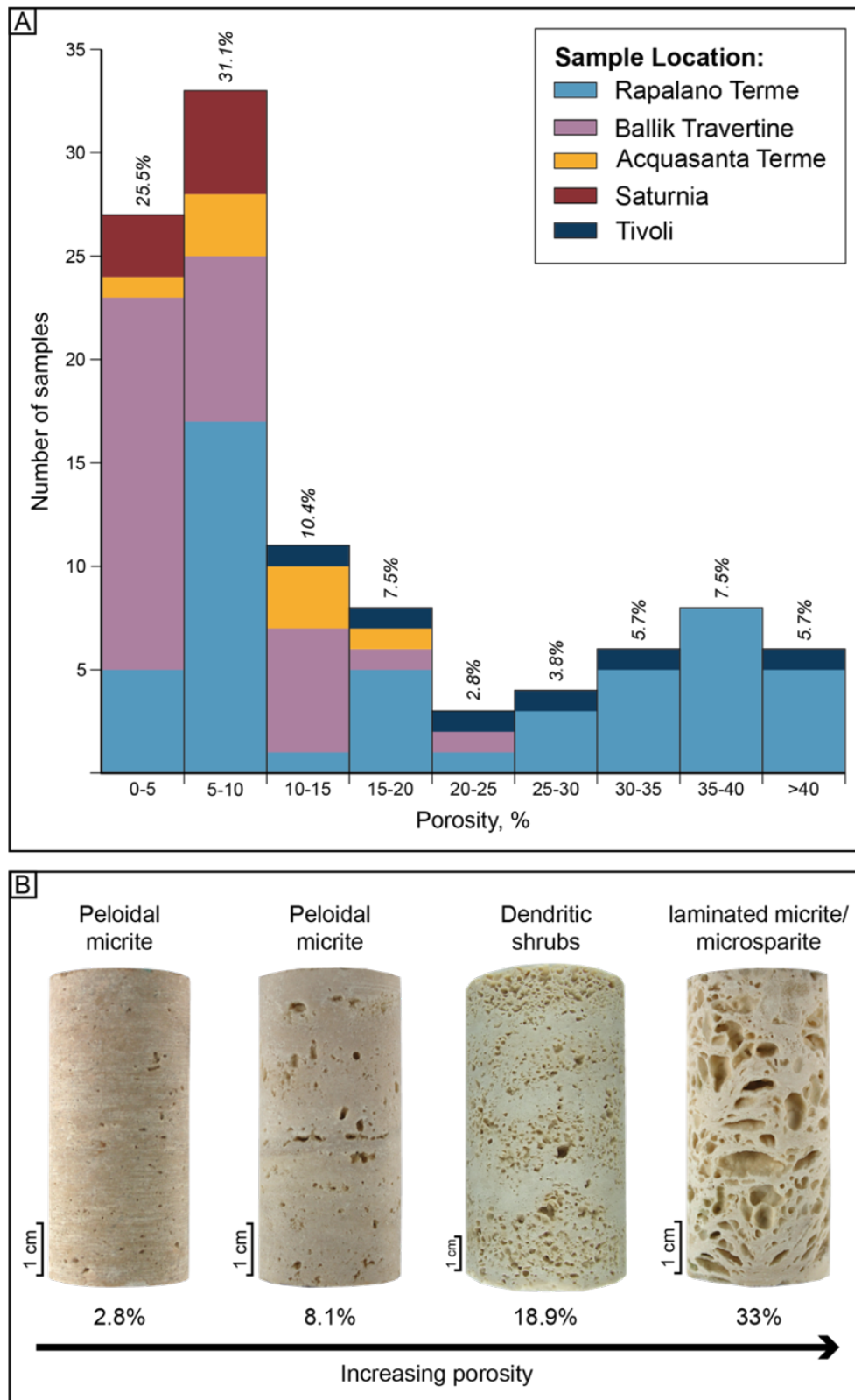


Figure 5-3. A) Porosity distribution of travertine core plugs with percentages of each fraction labelled. B) Core plug examples from low porosity peloidal micrite to high porosity laminated micrite/microsparite with coated bubbles.

5.4.2 Permeability heterogeneity

5.4.2.1 Probe permeability

Probe permeability results across a layered travertine sample from the Tivoli travertine formation illustrates the variability of permeability over several orders of magnitude from 0.1 to > 1000 mD on a 0.5 mm scale (Figure 5-4). The travertine measured is composed of 1 to 2 cm layers which can be categorised into 4 different facies types described in Table 5-2. Probe permeability results illustrate permeabilities within the clotted peloidal micrite/sparite (F3) type facies are typically < 10 mD. Comparatively, permeability within micritic dendrite (F2) and coated bubble facies (F4) are measured to be > 100 mD. The dendrite crust facies (F1) is found to display a range of permeability from 1 – 1000 mD where the lower permeability reading may relate to layers with denser and thicker lamina. Though the coated bubble facies (F4) consist of a poorly connected pore network, probe permeability results are very high (> 1000 mD). This may be a result of the small radius over which the permeability is measured, whereby permeability may only be measured between 2 or 3 coated bubbles. As such, the permeability measured of a larger framework may be significantly lower.

Table 5-2. Description of facies identified in Figure 5-4 with associated pore type and typical abundance.

Facies label	Description	Porosity	Pore type
F1	Shrubs: dendritic crust	$\phi < 5\%$	Inter-dendrite pores
F2	Shrubs: micritic dendrite	$\phi = 5-15\%$	Inter-dendrite pores
F3	Clotted peloidal micrite/sparite	$\phi < 5\%$	Minor porosity commonly found between laminations
F4	Coated bubbles	$\phi = 15-40\%$	Spherical poorly connected pores within cemented bubbles

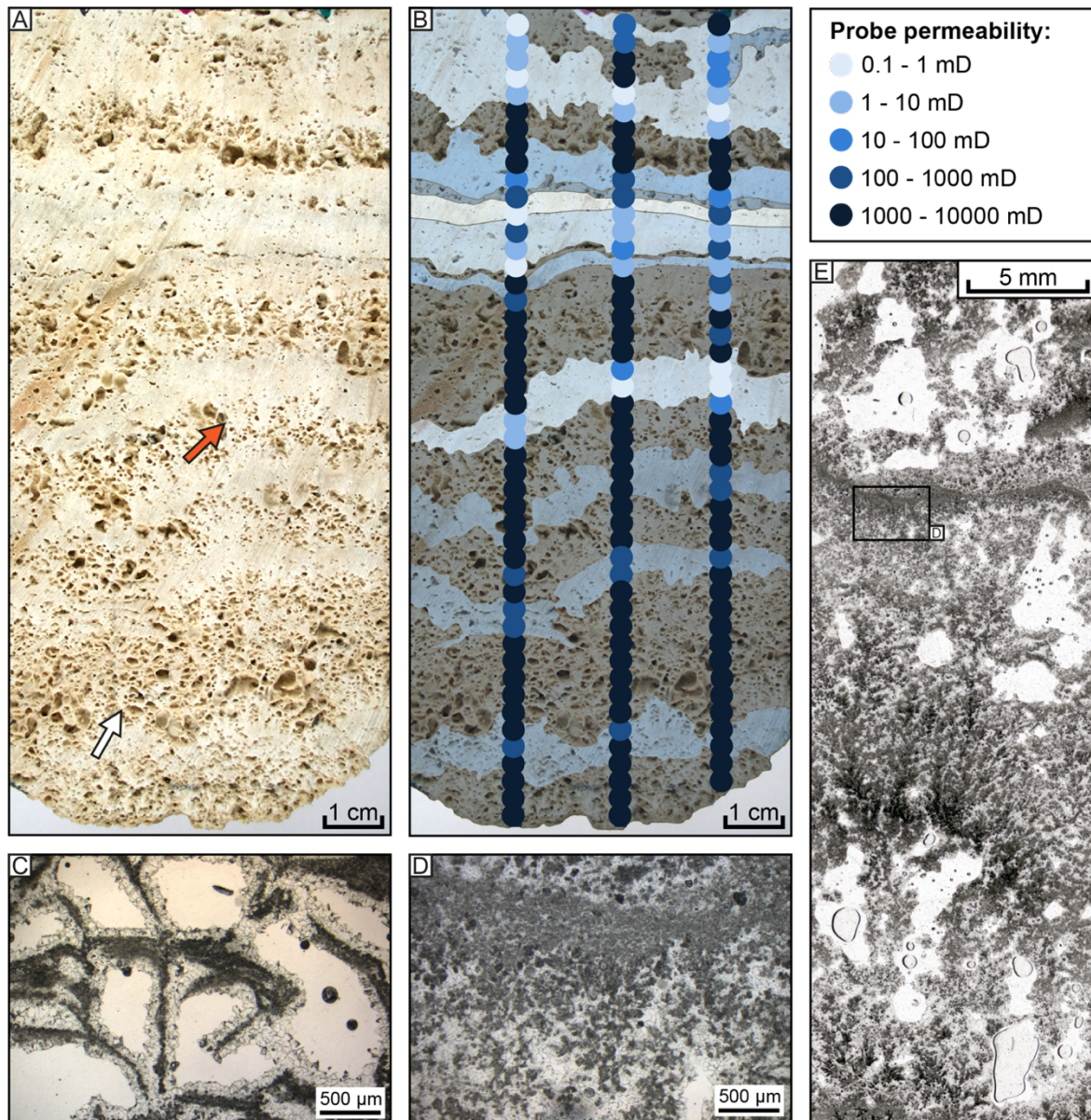


Figure 5-4. A) Travertine block composed of layers of Dendritic crusts (F1), micritic dendrite shrubs (F2), clotted peloidal micrite/microsparite (F3) and Coated bubbles (F4). Red arrow highlights shrub facies illustrated in photomicrograph E. White arrow highlights coated bubbles illustrated in photomicrograph C. B) Probe permeability results along three vertical transects. Each circle represents a Klinkenberg corrected measurement. D) Photomicrograph illustrating partially collapsed coated bubbles from A. D-E Photomicrographs showing clotted peloidal dendritic texture of shrub layers.

5.4.2.2 Permeability anisotropy

Permeability measured cores with variable orientation to bedding (parallel, perpendicular and 45°) in three different facies (laminated micrite/microsparite; peloidal micrite/microsparite and shrubs). Facies descriptions detailed in Table 5-1) illustrates the dependency of permeability on overall flow direction. Figure 5-5 illustrates permeability data measured from travertine cores categorised by both the core orientation and the dominant facies type. Permeabilities measured in cores where bedding is perpendicular to flow direction make up the largest

fraction of samples below 1 mD (54%) and show an approximate normal distribution on a logarithmic scale with a peak at 0.01 to 0.1 mD (Figure 5-5). Permeability measured in cores 45° to bedding show a similar approximate normal distribution of frequencies observed in those measured perpendicular to bedding with frequency peak at 0.01 to 0.1 mD. Core plugs which are orientated parallel to bedding (where flow is measured along travertine laminations) make up the largest fraction of sample with permeabilities > 1 mD (73%).

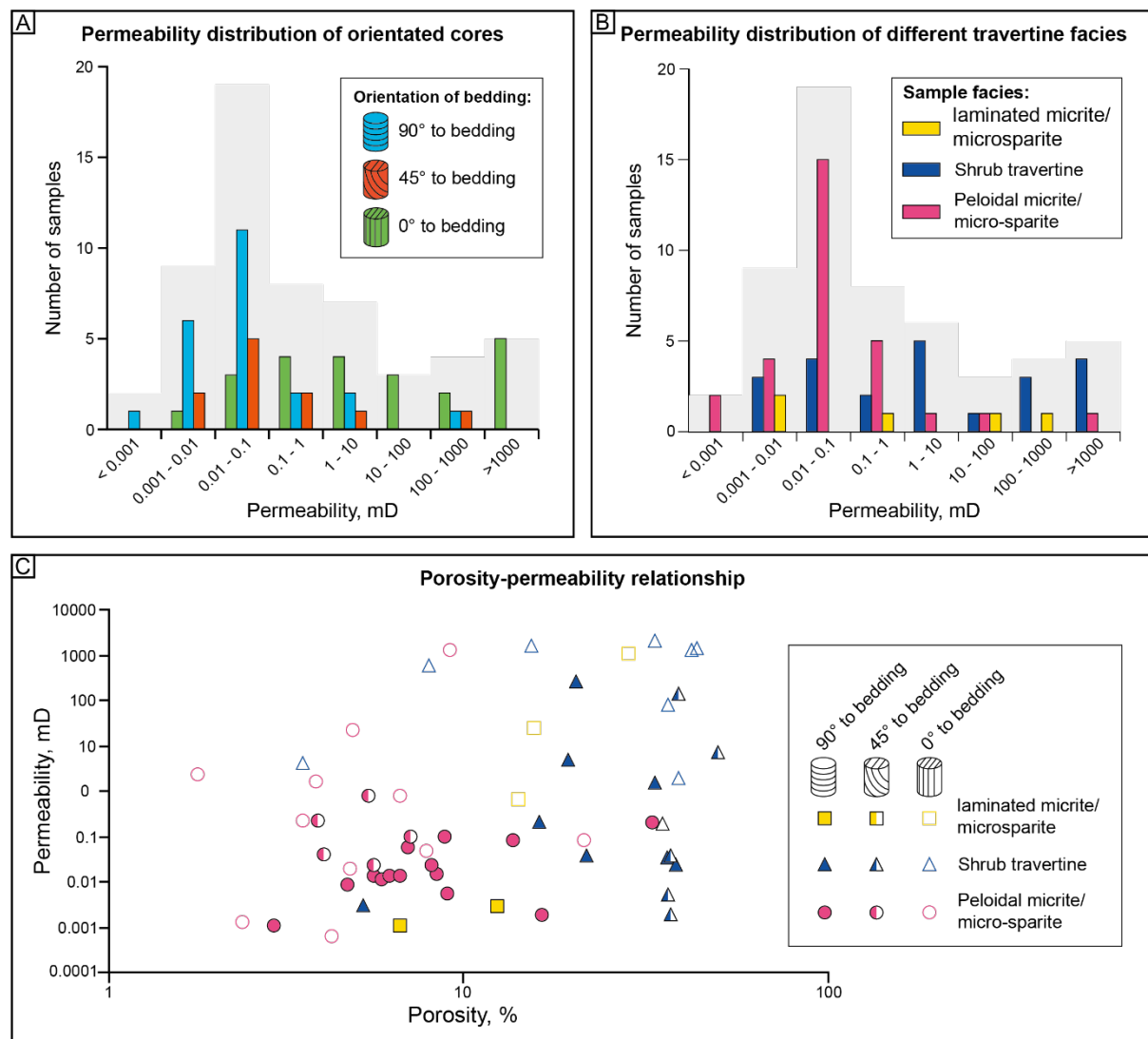


Figure 5-5. A-B) Permeability distribution of measured travertine core plugs. A) Permeability distribution categorised based on core orientation. B) Permeability distribution categorised based on predominant facies of cores of all sample orientations. C-D) Relationship of permeability with porosity categorised by facies and core orientation.

All facies' types show greater arithmetic and geometric mean permeabilities in samples orientated parallel to bedding than those oblique or perpendicular to bedding. However, such a comparison is fairly simplistic and negates the spread of distributions of porosity and

permeability within and between samples. Evaluation of both linear, and logarithmic potential best-fit curves on data presented in Figure 5-5c, separated by facies and angle of bedding with respect to long-axis of core plugs, demonstrates extremely weak to absent porosity-permeability correlations (Figure 5-5). However, peloidal micrites show a substantial increase in the strength of a positive correlation between permeability and porosity with increasing angle to bedding (Table 5-3). This is also reflected in the ‘narrowing’ of the spread of permeabilities, denoted by the decrease of standard deviation of the log of permeability ($\sigma_{\log k}$) from samples orientated parallel to bedding (1.4) samples orientated perpendicular to bedding (1.17) (Table 5-4). Shrub facies exhibit an extremely large spread of data for all angles of samples, with a total absence of any correlation between porosity and permeability (Table 5-4). Whilst a similar decrease in $\sigma_{\log k}$ is observed in shrub facies, there remains a substantial magnitude of variance of permeability and porosity (Table 5-4). Despite this, shrub facies show the largest differences in arithmetic and geometric mean permeability between bed-parallel or oblique and bed-perpendicular orientated samples of 1-2 orders of magnitude (Table 5-4). However, this may reflect their overall higher permeability than peloidal micrites (Figure 5-5, Table 5-4). Laminated micritic facies, show similar large differences in arithmetic and geometric mean permeability for core-axis orientation however are limited by the number of samples.

Table 5-3. Summary of distribution properties for porosity measurements of samples from Italy and Turkey used in poro-perm anisotropy analyses.

Property	Facies	n, samples	Arithmetic mean (%)	Standard deviation	Variance	Skewness	Kurtosis
Porosity	All	57	16.5	14.1	197.4	0.7974	2.142
Porosity	Shrubs	22	29.1	13.3	178.2	-0.593	2.177
Porosity	Laminated micrite/microsparite	5	15.1	8.0	64.2	0.819	2.616
Porosity	Peloidal micrite	30	7.6	6.3	39.3	2.679	10.630

The progression of peloidal micrites towards higher permeabilities for a given porosity and decrease in permeability perpendicular to bedding is interpreted to represent control by the more coherent geometry of layering within peloidal micrite favouring enhanced, layer-parallel permeability in bed-parallel samples, as opposed to the more variable and occasionally interconnected layering seen within shrub facies (e.g. Figure 5-4). As a result, permeability measurements in peloidal micrites are more likely to experience and ultimately be controlled by across-bed baffles within samples orientated orthogonal to bedding with a reduction of

geometric mean permeability of approximately an order of magnitude from bed-parallel or oblique orientated samples to bed-perpendicular oriented samples (Table 5-4). Conversely, the highly variable and interconnected pore-network of shrub facies means that there is a great likelihood of more permeable pathways in all orientations. Whilst the data on laminated micrite/microsparite facies are limited, their pore network character is more similar to that of shrub facies. Permeability anisotropy in shrub and laminated micrite/microsparite facies are likely to be controlled more by the orientation and connection of pore network distributions, rather than intrinsic depositional layering. Where these are orientated favourably for flow this can produce substantially enhanced permeability (e.g. > 100 mD reflected in the relatively high average permeabilities for shrub facies). However, this results in a much less predictable permeability anisotropy which may or may not be coincident with bedding.

Table 5-4. R² values for linear and logarithmic regression lines for Peloidal Micrite and Shrub facies samples at different core-plug angles. Data in raft facies is omitted due to a limited number of samples for best fit curves.

Facies	Angle of long-axis of core plug to bedding	R² for linear best fit	R² for logarithmic best fit
Peloidal Micrite	0	0.0265	0.0828
Peloidal Micrite	45	0.189	0.1664
Peloidal Micrite	90	0.659	0.522
Shrubs	0	0.0085	0.001
Shrubs	45	0.0012	0.0037
Shrubs	90	0.0085	0.001

5.5 Mechanical properties of travertine

5.5.1 Stress-strain response to failure

Multistage triaxial tests were carried out on 15 samples from four different travertine bodies (Table 5-5). Stress-strain curves are used to analyse the mechanical behaviour and quantify the critical stresses experienced at three stages of confining pressure (10, 20 and 30 MPa). Figure 5-6a & c illustrate the typical axial stress-strain curves for i) shrub facies and ii) laminated and peloidal micrite/microsparite. For all samples, irrespective of facies, an increase of the yield point (marking the onset of inelastic deformation) is observed with decrease angle to bedding; i.e., samples where bedding is orientated parallel to σ_1 (i.e vertical bedding), typically fail at higher effective stresses than samples whose bedding are an angle or perpendicular to σ_1 .

Shrub type (typically associated with moderate to high porosity facies) facies are associated with variable stress-strain responses during triaxial testing (Figure 5-6a-b; Table 5-5). Two samples (TIV-1-P1, perpendicular, and RT8 H2, parallel to σ_1) presented stress-strain paths, which resulted in a sudden drop of stress at the post peak stage, interpreted to be brittle failure (Figure 5-6a). The volumetric response to stress of these samples shows a decrease in the volumetric strain during failure at each stage, which are interpreted as the onset of brittle deformation (C') (Figure 5-6b). Strain hardening with eventual softening (only observable at 30 MPa confining pressure) is observed in all remaining shrub facies samples, to varying extents (Figure 5-6a; Appendix B). Such samples typically show volumetric strain increases during failure at 30 MPa confining pressure with a final volumetric strain decrease, here interpreted as the transition from compaction to dilation (C^{*}). The decrease in volumetric strain, however, is insubstantial compared to the volumetric strain increase (i.e., volumetric strain increase \gg volumetric strain decrease) inferring that deformation in the compressional regime is substantial. The changes in volumetric strain during the final triaxial stage are interpreted to be due to initial compaction causing substantial volumetric strain increase followed by a switch to brittle deformation resulting in a relatively small amount of volumetric strain decrease (Figure 5-6b). The volumetric response to failure at confining pressures of 10 and 20 MPa are variable, either undergoing a volumetric strain increase, interpreted as C^* (onset of compaction) or decrease (onset of dilation, C').

Table 5-5. Overview of travertine samples tested under triaxial conditions. Φ : porosity pre-deformation (%); k : Permeability pre-deformation; C_0 : cohesion (MPa); μ : internal friction coefficient; C^* : transition from compaction to dilation during triaxial test; SEC: Localised shear enhanced compaction; LC: Localised compaction; BD: Brittle deformation.

Travertine locality	Facies	Pore type	Sample name	Bedding orientation	Φ , %	k , mD	UCS, MPa	Vp, m/s	Fracture angle	C_0	μ	Failure mode	C^*
Tivoli	Shrubs with coated bubbles	Inter-dendrite and intra-bubble pores	TIV-1-P1	90°	18.9	3.90	97.3	5291	< 45°	35	0.31	LSEC	
			TIV-8-P1	90°	21.33	0.03	70.5	4804	Horizontal	14	0.21	LC	
Rapalano Terme	Shrubs (clotted peloidal micrite dendrites and dendritic crusts)	Inter-dendrite pores	RT1-H2	0°	33	1.18	57.4	5447	> 45°	16.5	0.65	LSEC	✓
			RT1-P5	90°	38	0.02	16.0	5673	< 45°	7	0.24	LSEC	✓
			RT8-P1	90°	13.4	2.52	35.8		Horizontal	-	-	LC	
			RT8-P3	90°	16.4	0.67	34.7		Horizontal	-	-	LC	✓
			RT8-H2	0°	12	27.3	80.5		> 45°	26	0.45	BD	
			RT8-A1	45°	10.6	1.49	40.1		> 45°	16	0.17	SEC	✓
			RT8-A2	45°	10.6	3.30	47.6		> 45°	17	0.29	SEC	
Saturnia	Shrubs (clotted peloidal micrite dendrites and dendrite crusts)	Inter-dendrite pores	SAT1-P7	90°	7.9	0.002	74.5		> 45°	27	0.28	BD	
Acquasanta Terme	Peloidal micrite/microsparite	Inter-peloidal pores	AT6-P1	90°	8.52	0.09	48.1	4850	> 45°	12.4	0.44	BD	
			AT6-H1	0°	4.66	19.40	59.8	5509	> 45°	15.9	0.72	BD	
			AT6-H2	0°	8.88	1144	72.2	-	> 45°	24	0.39	BD	
	Laminated micrite/microsparite	Bedding parallel lenses	AT7-P2	90°	6.4	0.003	34.7	4975	Horizontal	10	0.57	BD	
			AT7-H2	90°	13.8	0.60	72.2	4961	Horizontal	17	0.69	BD	

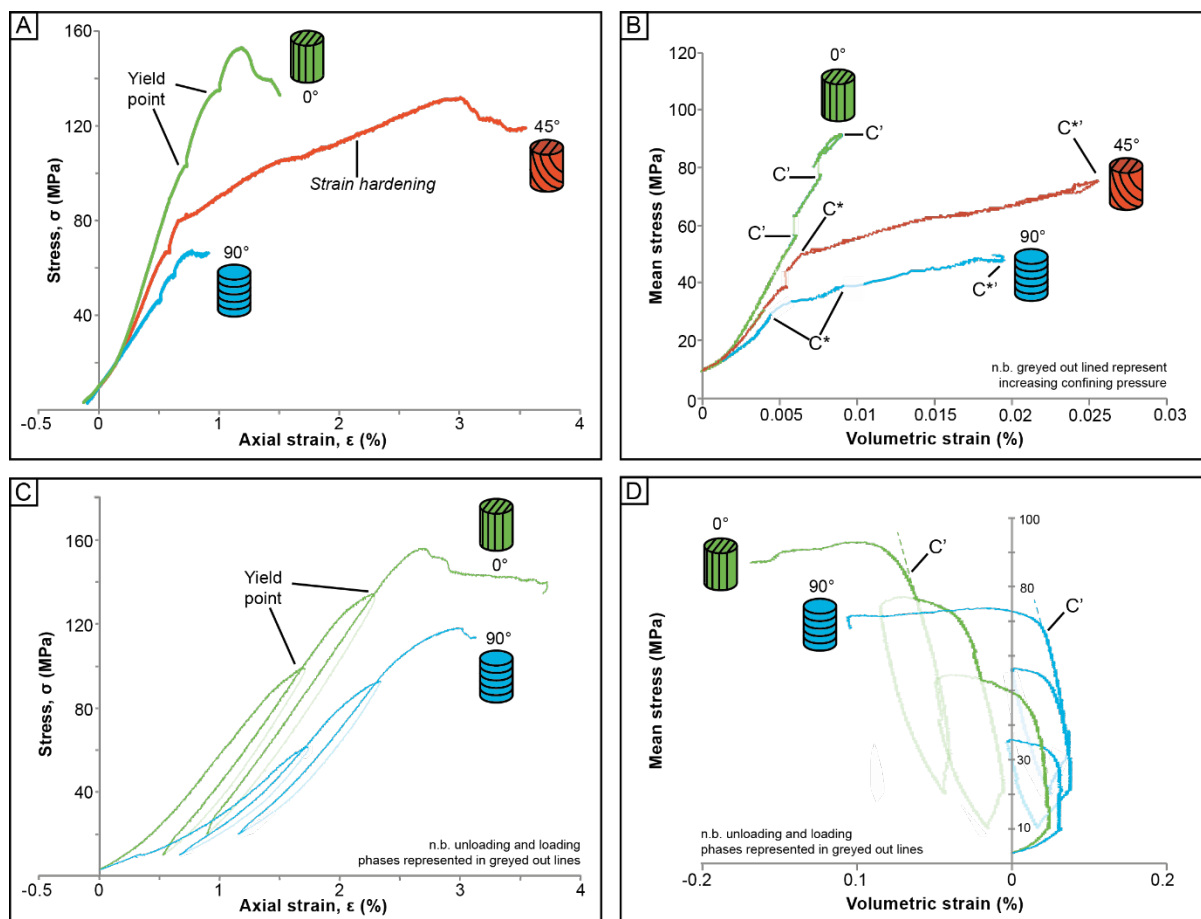


Figure 5-6. Representative multi-stage triaxial test data measured in travertines at 10, 20 and 30 MPa confining pressure. A) and B) present data from shrub facies (samples RT8 H2, RT8 A1 and RT8 P1). A) Axial stress and strain of raft facies illustrate increasing yield points with decreasing angle of bedding. Shrub samples show variable extents of strain hardening. B) Mean stress and volumetric strain data from shrub facies illustrate variable volumetric responses during failure with associated critical stress states. C' indicates the onset of dilatancy defined by a decrease in volumetric strain; C^* indicates onset of shear enhanced compaction marked by an increase in volumetric strain; and C^{*} marks transition from shear enhanced compaction to dilatancy marked by switch from increasing volumetric strain to a decrease in volumetric strain. C) and D) present the typical stress-strain response in laminated and peloidal micrite/microsparite (samples AT27H2 and AT27P2). C) Axial stress-strain data illustrate typical curves ending in brittle failure. D) Volumetric strain changes with mean stress illustrating volumetric strain decreases with critical stress C' points. (Note greyed out lines represent loading and unloading phases between triaxial stages). (Sample information: Table 5-2).

Cohesion (C_0) and internal friction (μ) parameters derived from Mohr-Coloumb failure curves of deformed samples show a substantial range of values for travertines (Figure 5-7). Cohesive strength of samples can range from 7 to 35 MPa. Cores perpendicular to bedding show the greatest range (7-35 MPa) of cohesive strength compared to those parallel the bedding (15-26 MPa). Only two samples with dipping beds (at 45°) were measured and so may not be representative of intermediate angles of bedding. The internal friction coefficient of samples are found to be < 1 and can be as low as 0.17. Generally, the spread of μ data for samples parallel to bedding are higher than those derived from samples parallel to bedding though overlap significantly.

Unconfined compressive strength (UCS) for samples was also derived from triaxial mechanical data and are observed to have a large range of values (16 – 92 MPa). UCS appears to be broadly related to the orientation of bedding with respect to σ_1 (

Figure 5-7c). The mean UCS for samples of each bedding orientation show that mean UCS is at its lowest when orientated 45° to the mean principal stress. However, the spread of data shows that samples with horizontal bedding (i.e., 90° to σ_1) can have lower UCS values than those with bedding angles of 45° to σ_1 . However, this may be due to the low number of samples with bedding at 45° and therefore does not reflect the true variation that may exist.

The relationship between porosity and UCS of samples (Figure 5-8) shows a very poor negative correlation ($R^2 = 0.051$). UCS values measured from shrub facies show a substantial spread from 16 – 92 MPa. Meanwhile, laminated micrite/microsparite and peloidal micrite/microsparite facies have lower ranges of UCS values, however this may reflect the comparatively small number of samples from these facies. The categorisation of data according to facies type does not resolve the poor correlation which may suggest that bedding orientation has a larger control on UCS than facies within travertine carbonates. As such the porosity cannot be used to predict the mechanical properties of different travertine facies.

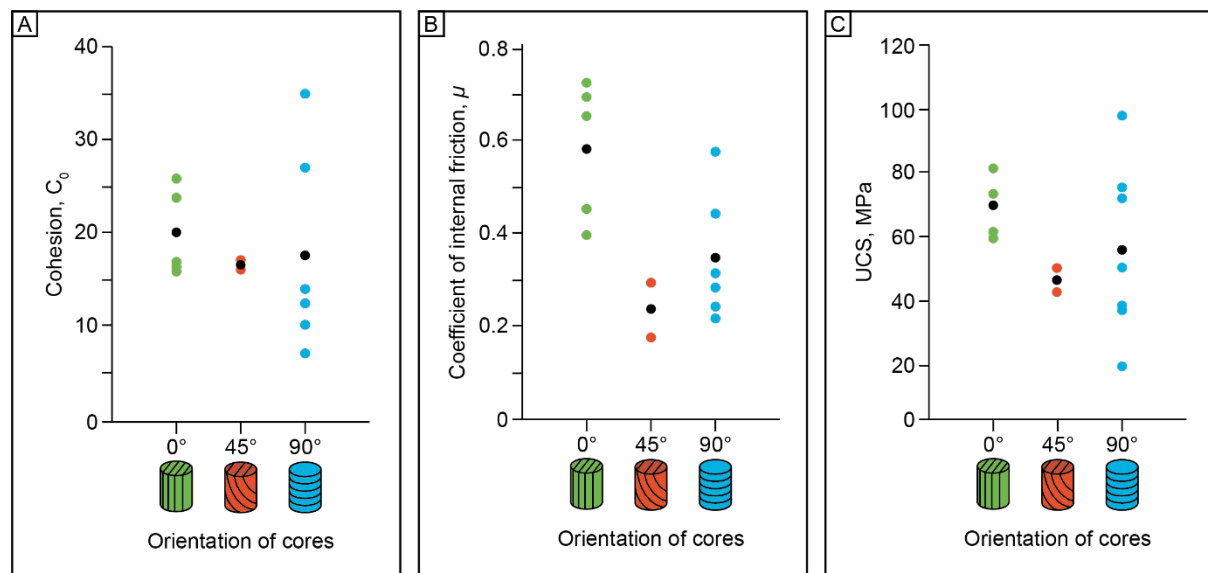


Figure 5-7. Cohesion (A), internal friction (B) and UCS (C) data for tested travertine samples with different bedding orientations.

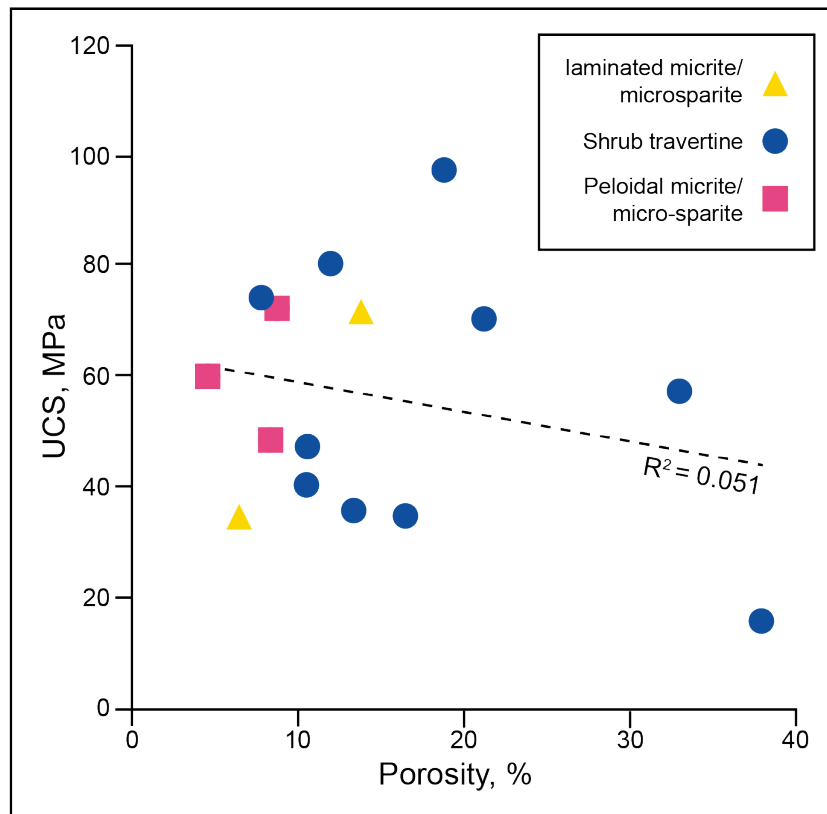


Figure 5-8. UCS data (derived from triaxial mechanical testing against porosity), characterised by facies type. Dashed line represents the linear, best fit trend line for all data points demonstrating a very weak/absent, likely non-significant correlation.

5.5.2 Critical stresses and yield envelopes

The critical stresses, C' (onset of dilatancy), C^* (onset of compaction) and C^{**} (transition from compaction to dilatancy) quantified from stress-strain data has been used to infer partial yield envelopes in P-Q space, (P = effective mean stress, Q = differential stress) (Figure 5-9). Data has been further categorised depending on orientation of bedding, which illustrates the relationship between bedding orientation and yield envelope geometries. However, it should be noted that some sample data sets only have three data points resulting in reduced reliability of interpreted yield curve geometry. Observations from original mechanical data are therefore depended upon to infer the likelihood of best-fit curves.

C' critical stresses for both laminated micrite/microsparite (Figure 5-9a) and peloidal micrite/microsparite (Figure 5-9b) show positive correlations of P and Q which are interpreted to fall within the dilational regime. However, though volumetric strain decrease is observed at all failure points, strain hardening is observed in the stress-strain curve for sample AT26 P1 (perpendicular to bedding) which suggested the presence of compactive processes. The overall volumetric strain decrease however, suggests that dilation is the dominant deformation

mode in laminated micrite/microsparite and peloidal micrite/microsparite up to 30 MPa. The partial yield slope for vertically bedded travertine (parallel to σ_1) is observed to be steeper than observed for horizontally bedded travertine (perpendicular to σ_1). Critical stress show that vertically bedded travertine is able to accommodate higher differential pressures and confining stresses before brittle dilation occurs compared to horizontally bedded travertine.

Figure 5-9c illustrates critical stresses (C' , C^* and C^{**}) measured in shrub facies. Similar to results observed in laminated micrite/microsparite and peloidal micrite/microsparite facies, critical stresses in vertically bedded travertines are noticeably higher compared to those observed in horizontal and 45° dip travertine. The yield curve for vertically bedded travertine displays an initial high angle positive correlation which shallows towards 120 MPa differential stress (Figure 5-9c). The presence of both C' and C^* towards the top of the curve are interpreted to be due to the transition between dilatancy and compaction. The apex/curvature of the yield curve may be under-estimated here, where a lack of data within the compaction regime means construction of the full yield envelope is limited. Comparatively, C' and C^* data in shrub facies samples with bedding at 45° and 90° are observed to form a cloud of data and lack good correlation between P and Q values. Best-fit polynomial trendlines for both samples sets show weak positive correlations (Figure 5-9c). However, these correlations are not considered an accurate representation of the yield curve due to very low R^2 values ($R^2 = 0.34$ for 45° orientated samples: $R^2 = 0.47$ for samples 90° to bedding). As C' and C^* are poorly defined in P-Q space (i.e., there is an overlap of C' and C^* data) this distribution may be due to variations of lithotypes within shrub facies samples, where small differences in the pore-network distribution not quantified here may have a substantial control on the mechanical response. As C^* points are present within this data set, this distribution of data within horizontally bedded and dipping travertine are interpreted to represent the dilation-compaction transition.

The switch from shear enhanced compaction to dilation was observed in four of the nine shrub facies tested (Table 5-5), where an eventual decrease in the volumetric strain is observed. C^{**} stresses are presented in Figure 5-9c which demonstrated the evolution from compaction to dilation. C^{**} values are typically higher than the associated C^* of the same sample, which suggests that the yield curve expands to accommodate this switch in deformation regime. However, very limited data of C^{**} values means that the change in yield envelope stress state is unable to be reliably determined. The change in deformation mechanism does not appear to be controlled by sample orientation as C^{**} points are observed in samples of all orientations. However, the change in dominant deformation mode (from compaction to dilation) suggests

that dilational processes play a key role even when sample appear to undergo shear enhanced compaction.

Overall, mechanical results from triaxial testing generally illustrate that there is a mechanical dependency on the orientation of the travertine fabric with respect the principal stresses, regardless of travertine facies, where the compressive strength increases with increasing angle between σ_1 and bedding. However, the mechanical response has been found to vary depending on the primary facies present in travertine sample. The mechanical response can broadly be divided into two broad types:

1. Dilational in the brittle regime which is observed in laminated micrite/microsparite and peloidal micrite/microsparite travertine facies.
2. Complex variable compactive and dilational deformation in the transitional regime observed in shrub facies.

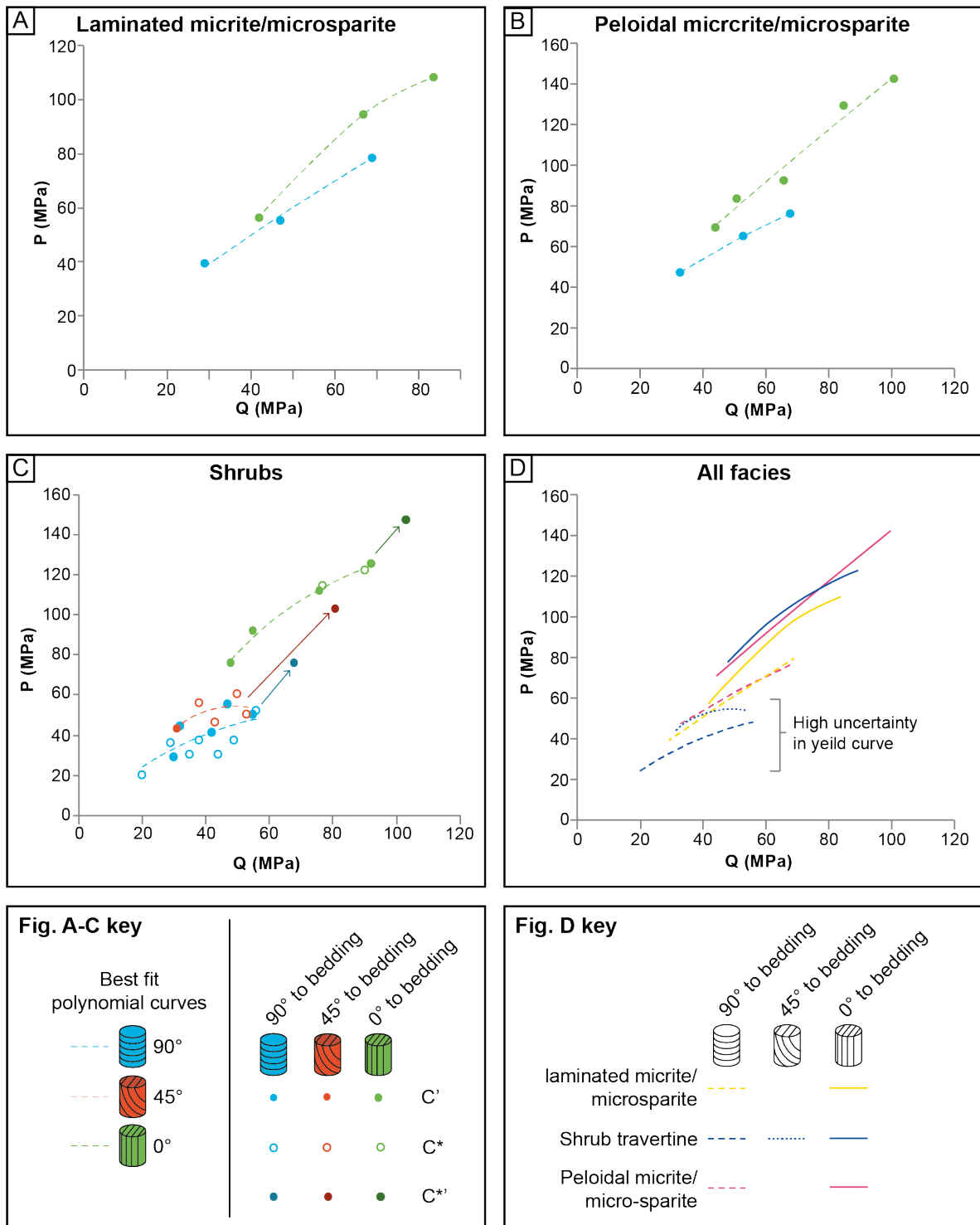


Figure 5-9. Critical stress states (C' , C^* , C^{*}) presented in P - Q space (P : Mean stress; Q : differential stress) with best fit polynomial curves representing partial yield curves for each facies tested. A) Partial yield curves of laminated micrite/microsparite samples. Yield curves for samples both orientated vertical and perpendicular to bedding fall within the dilational regime. Yield curve for vertically bedded travertines show higher critical stresses than those in horizontally bedded samples. B) Partial yield curves of peloidal micrite/microsparite samples. Yield curves for samples both orientated vertical and perpendicular to bedding fall within the dilational regime. Yield curve for vertically bedded travertines show higher critical stresses than those in horizontally bedded samples. C) Critical stress data from shrub facies. Vertically bedded travertine illustrates higher critical stresses with a transition to compaction at the highest stresses observed. Critical stresses in horizontally and dipping travertine show a substantial spread in data with high uncertainty in best fit curves ($R_2 = 0.34$ for 45° orientated samples; $R_2 = 0.47$ for samples 90° to bedding). C^{*} critical stress states illustrate the expansion and change in yield envelope. D) Illustrates all best fit yield envelopes.

5.5.3 Velocity analysis

Ultrasonic velocity of compressional waves, V_p , measured in samples at 10 MPa hydrostatic pressure show that samples have a large spread of V_p between 4804 and 5673 m/s highlighting the heterogenous natures of the samples tested (Figure 5-10). V_p is found to show very little correlation with travertine rock properties such as UCS, porosity or density (Figure 5-10). There is a very weak atypical positive correlation of V_p and porosity (Figure 5-10a). When these data are categorised by facies, V_p is found to decrease within laminated micrite/microsparite and peloidal micrite/microsparite. However, only two samples for each of those facies were able to be tested for velocity, so this is unreliable. High porosity (> 10%) shrubs appear to control the positive correlation between V_p and porosity.

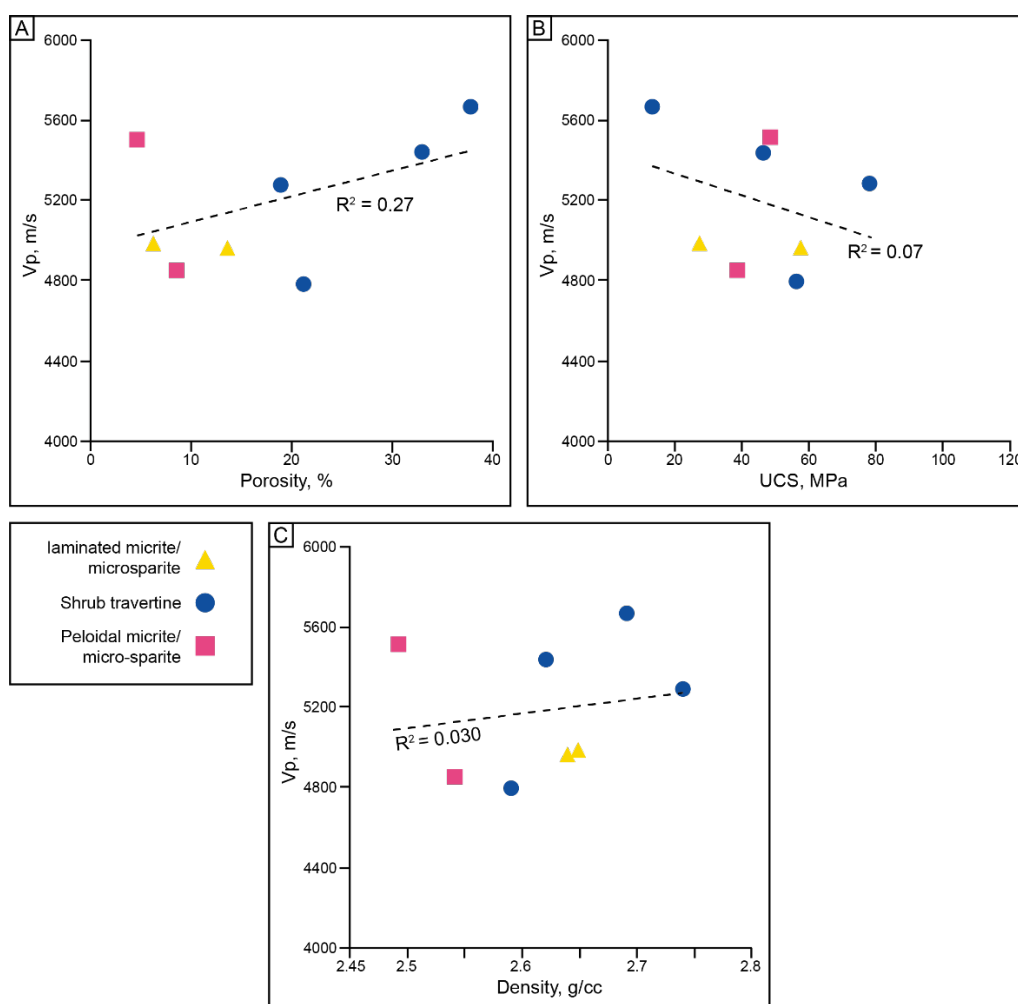


Figure 5-10. V_p (compressional wave velocity) measured on dry travertine samples at 10 MPa confining pressure. Data is categorised by travertine facies. A) V_p versus porosity shows no correlation. B) V_p and UCS show a weak positive correlation with an R^2 of 0.43. C) V_p and Density show little correlation.

Vp and UCS have a weak negative correlation within travertines (Figure 5-10b). As the R² value of the trendline is considered to be very low (0.073) this correlation is considered unreliable and as such no correlation can be defined between UCS and Vp. Vp and density show a weak positive correlation with density (Figure 5-10c), though the R² value is similarly very low and cannot therefore be considered a reliable correlation.

Ultrasonic velocity changes of Vp (compressional waves) and Vs (shear waves) were measured during triaxial testing to observe the velocity response during failure. Initially, Vp and Vs are observed to increase marginally with increasing confining pressure and axial stress (Figure 5-11). However, Vp is observed to decrease in most samples during the final stage of triaxial testing where the sample is allowed to fail at high differential stresses (Figure 5-11a). The magnitude of the drop in Vp observed in this final stage of failure is variable across samples from ~ 70 to 800 m/s (Figure 5-11). The greatest decrease (~ 800 m/s) in velocity is observed in sample TIV-8-P1, in which a bedding parallel, horizontal fracture formed, which likely inhibited the propagation of ultrasonic waves through the sample. Decreases in Vs are also observed in samples with increasing axial strain, though with a weaker correlation than observed with Vp. As such, the ratio of Vp and Vs (Vp/Vs) gently increases with axial strain (average increase of Vp/Vs of 0.05 between undeformed and deformed samples). No clear relationships between the orientation of bedding within cores and velocity are observed within the data.

Initial increases of Vp with axial strain and stress during the early stages of the tests are interpreted to represent the initial closure of microcracks and collapse of smaller pore spaces. Fracture generation/failure produces the onset of a negative correlation between both Vp and Vs with axial strain and stress. The decrease in Vp is observed in all samples, including those that are interpreted to undergo shear enhanced compaction suggesting that dilatational microcracking mechanisms still play a role in deformation during shear enhanced compaction. The increase in Vp/Vs suggests that microcracking dilatational behaviour does not have as strong a control on Vs as it does on Vp. Vs may therefore be more affected by compactional, pore collapse than Vp. Overall, dilatancy is therefore interpreted as having a greater control on velocity than pore collapse processes, resulting in a 'slower' rock following deformation.

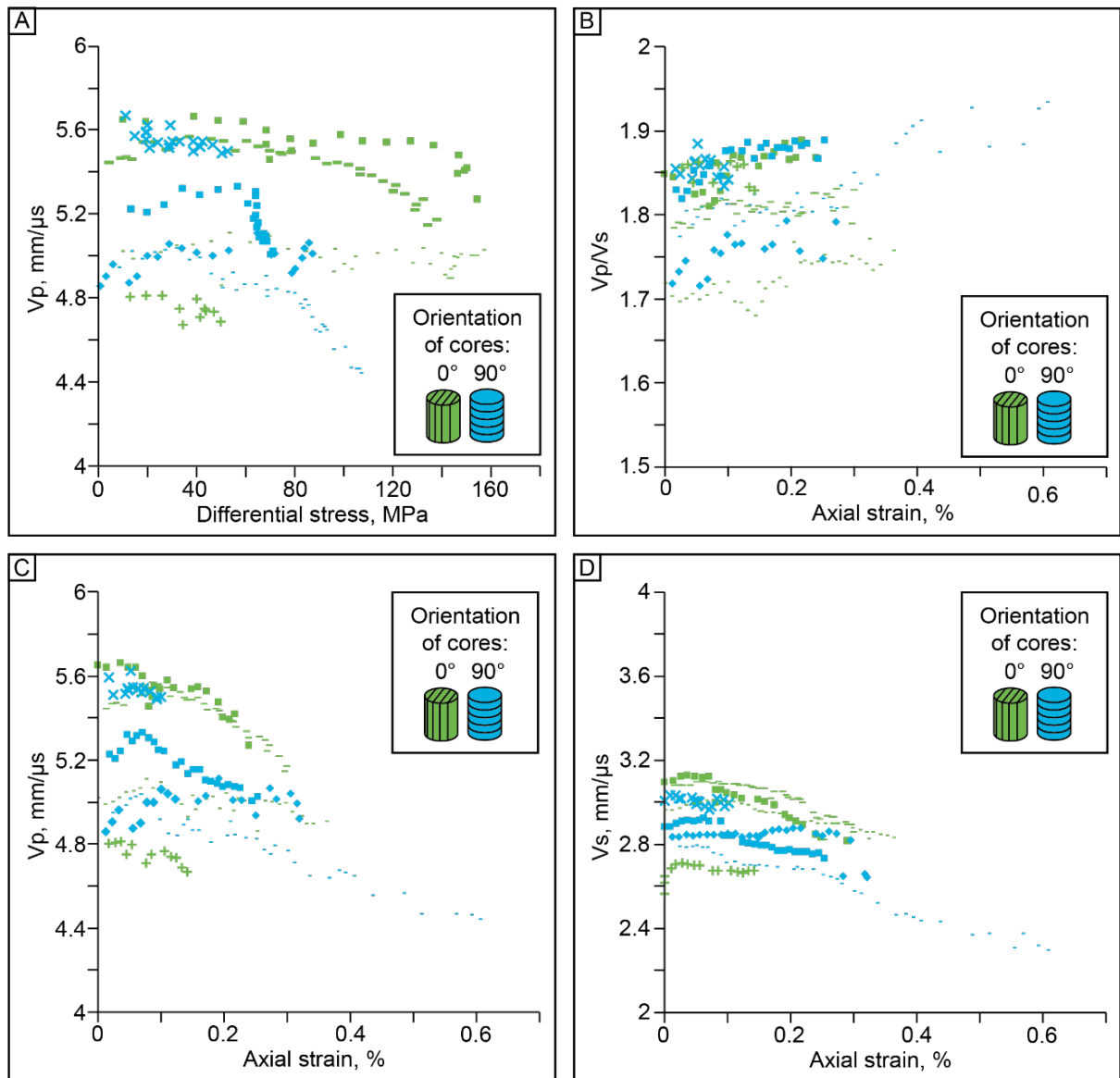


Figure 5-11. Velocity data measured during triaxial testing of travertine. Symbols signify individual samples tested. A) V_p evolution with increasing differential stress. B) V_p/V_s (ratio of V_p and V_s) changes with axial strain. C) V_p changes with increasing axial strain. D) V_s changes with increasing axial strain.

5.5.4 Failure plane orientation

Samples post deformation are found to have a macroscopic failure plane. In most tests, samples were broken into two or more pieces. Where samples could be held intact (using a thin plastic casing) CT scans were taken to assess the internal architecture of deformation (Figure 5-12). Figure 5-12a shows samples where the long axis of the core plug is perpendicular to bedding, where samples display shallow dip ($< 30^\circ$) fractures which occur parallel to bedding within, or at the boundary of high porosity layers. Changes in dip angle and geometry are common across layers in within these low angle planes, which is interpreted to be due to mechanical differences in layers. Failure observed within samples where the core

plug long axis is oblique to bedding are also found to result in bedding parallel failure associated with high porosity layers producing fractures of 45° to 60° dip (Figure 5-12b). In samples parallel to bedding, failure is observed to occur along ~ 60° dipping planes and crosscut bedding (Figure 5-12b). Fractures can be locally observed to change dip where either porosity or the contacts between travertine laminations are intersected (Figure 5-12b). The differences of fracture orientation between oriented samples are interpreted to reflect bedding planes/depositional fabrics providing mechanically feasible failure planes. Bed-parallel fabrics are likely weaker than the strength of inter-layer material, and so form a locus for later deformation when they are preferentially aligned with respect to maximum principal stress (e.g., parallel or 45° to) or intersect with non-aligned deformational fabrics (e.g. Figure 5-12b).

5.6 Structural analysis of failure in travertine

5.6.1 Macro-porosity evolution

The changes in macro-porosity of three shrub facies samples from Rapolano Terme, each with a different orientation to bedding, were analysed by modelling macro-porosity volumes from CT scan images (Figure 5-13). Macro-porosity (pore space > 5 mm) is identified by black, low-density portions of the CT scans (Figure 5-13d). Volumes created through segmentation of CT imaging illustrate the pore network formed in shrub type facies (Figure 5-13). Pore volumes modelled in samples prior to triaxial testing illustrate a pore network within shrub facies with a highly irregular surface in 3D (Figure 5-13a/d/g). High porosity layers are associated with high inter-dendritic porosity regions between individual ‘shrubs’ and are separated by low porosity layers where dendrites are more densely amalgamated (Figure 5-13d). The macro-pore volumes also illustrate the poor pore-connectivity of the pore network across travertine laminations (Figure 5-13a/d/g). As such, cores with long axis parallel to bedding have axial connectivity while cores perpendicular and at an angle to bedding have no or very limited axial macro-pore connectivity (Figure 5-13a/d/g). Pore-connectivity anisotropy supports permeability results presented in Section 5.3.3 where the micro-porosity (not imaged here) within the tighter travertine layers control vertical fluid flow where beds are oblique to flow direction.

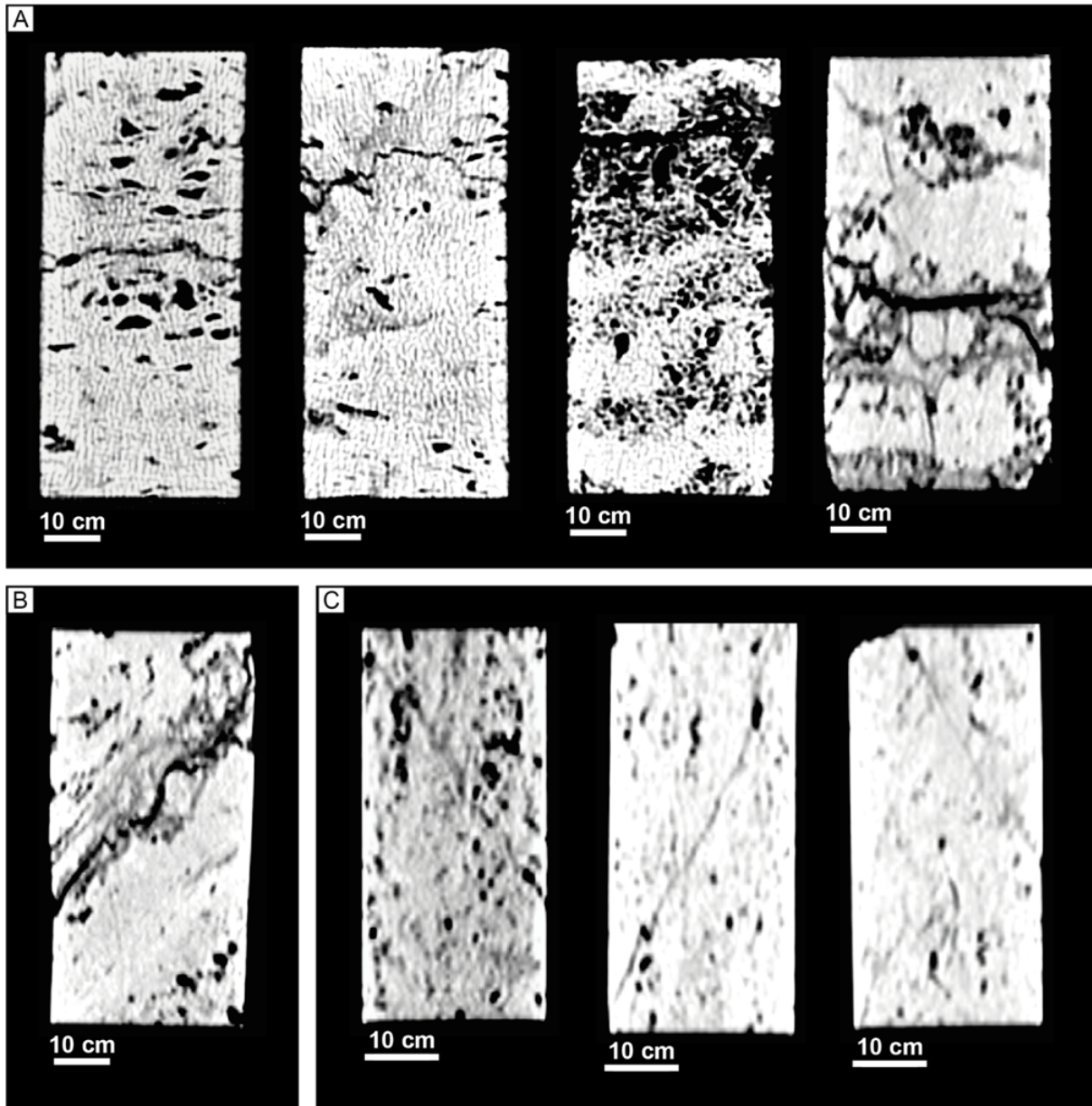


Figure 5-12. CT scan images from deformed travertine samples illustrating the different angles of fracture formation. A) Cores with long-axis orientated horizontal bedding often show open mode fractures parallel to bedding resulting in near horizontal fractures. B) Core with long axis orientated at 45° to bedding where fracture forms along bedding. C) CT scans of cores with long-axis orientated parallel to bedding. Fractures are commonly observed to have dips ranging from 60° to 70°.

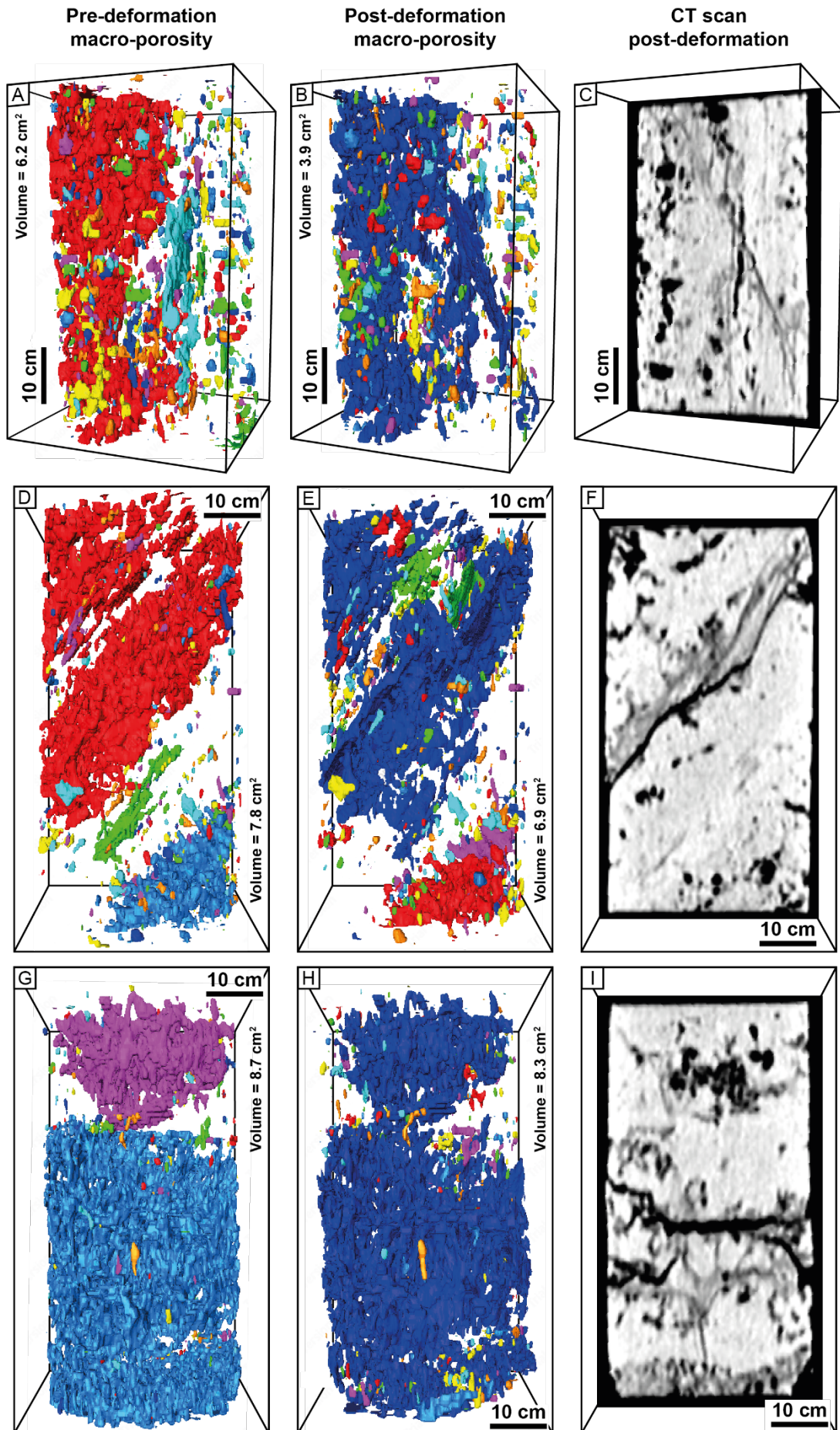
A reduction in the modelled macro-porosity is observed (Table 5-1) in all three samples, with the greatest decrease observed in the sample parallel to bedding (21.1% volume) and smallest decrease measured in the sample perpendicular to bedding (4.9% reduction). Though data is limited to only one sample set, results suggest an increasing extent of porosity reduction with long-axis angle to bedding. In sample RT8 P1 (perpendicular to bedding), and RT8 H2 (parallel to bedding), the largest pore networks become connected after failure (Figure 5-13b/h). This is especially prominent in sample RT8 P1, where two vertically separated pore networks (coloured purple and light blue in Figure 5-13d) become connected after undergoing triaxial

failure (blue pore network imaged in Figure 5-13e), resulting in a higher axial connectivity. Additionally, following testing, the 3D macro-porosity networks display a more regular surface which appears smoother (Figure 5-13b/e/h). Changes in the macro-pore network character may be due to pore collapse processes accompanied with localised fracturing at the edges of pore networks and connectivity of individual pre-existing pore space.

Table 5-6. Overview of modelled macro-porosity volumes of RT8 (Rapalano Terme, Italy).

Sample	Core orientation	Original macro ϕ volume, cm ³	Post-deformation macro ϕ volume, cm ³	Volume decrease, %
RT8 P1	Perpendicular	8.7	8.3	4.9 %
RT8 A1	45°	7.8	6.9	11.2 %
RT8 H2	Parallel	6.2	4.9	21.1 %

Figure 5-13. (Next page) 3D macro-porosity volumes derived from CT scan data for three samples of different orientations to bedding (parallel, perpendicular and 45°) before and after triaxial testing. Colours demark isolated, internally connected pore volumes determined using Avio3D. A-C) 3D macro-porosity volume pre- (A) and post deformation (B) with 2D CT scan (C) of failure plane in sample parallel to bedding. D-F) 3D macro-porosity volume pre- (D) and post deformation (E) with 2D CT scan (F) of failure plane in sample 45° to bedding. G-I) 3D Macro-porosity volume pre- (A) and post deformation (B) with 2D CT scan (C) of failure plane in sample perpendicular to bedding. Colours of pore volumes illustrate different connected pore segments.



5.6.2 Microstructure

Polished thin sections taken from deformed samples following the triaxial tests were analysed to identify key structural features to understand the deformational processes and products of deformation. The main structural components observed within deformed travertine falls into two categories: i) samples that deform in the brittle regime with little to no strain hardening (which included all peloidal micrite and laminated micrite samples and some shrub facies samples) and ii) samples which undergo strain hardening with eventual brittle failure (only present in shrub type travertines).

5.6.2.1 Failure in the brittle regime

Samples that failed in the brittle regime during triaxial testing (i.e., no evidence of strain hardening) are dominated by fracturing and micro-cracking processes. Figure 5-14a-f shows photomicrographs typical of the fractures and microcracks that formed, which are particularly common within laminated micrite/microsparite and peloidal micrite/microsparite samples. Within laminated micrite/microsparite, fractures are observed to cross-cut laminations with a stepped geometry (Figure 5-14a/b/e). Pore collapse is also observed and is interpreted to form due to microcracking of the pore walls.

In samples where bedding is perpendicular to σ_1 , shallow or near horizontal ($< 20^\circ$ dip) fractures up to 0.1 mm wide are parallel and sub-parallel to bedding and often step between laminations and beds (Figure 5-14e). Minor, tensile through-going (e.g., layer-cutting) microcracks are also common (Figure 5-14), which often intersect the primary horizontal fractures. Minor occurrences of pore emanating cracks and fractures are also observed (Figure 5-14d). In samples with long axis parallel to bedding, open, tensile fractures are common and occur along bed or lamination boundaries (Figure 5-14c). Micro-cracking and inclusion of grains into pore space is also locally observed in samples, particularly within pores > 0.5 mm width (Figure 5-14a/c). Nevertheless, all samples deformed in the brittle regime are observed to preserve the bulk of primary pore spaces (Figure 5-14a-f).

Minor occurrences of mechanical twinning of sparite cements are observed within all samples which suggest minor components of plastic deformation are present. However, they play a minor, localised role in deformation with the majority of strain being accommodating through fracturing and shearing, in the brittle regime.

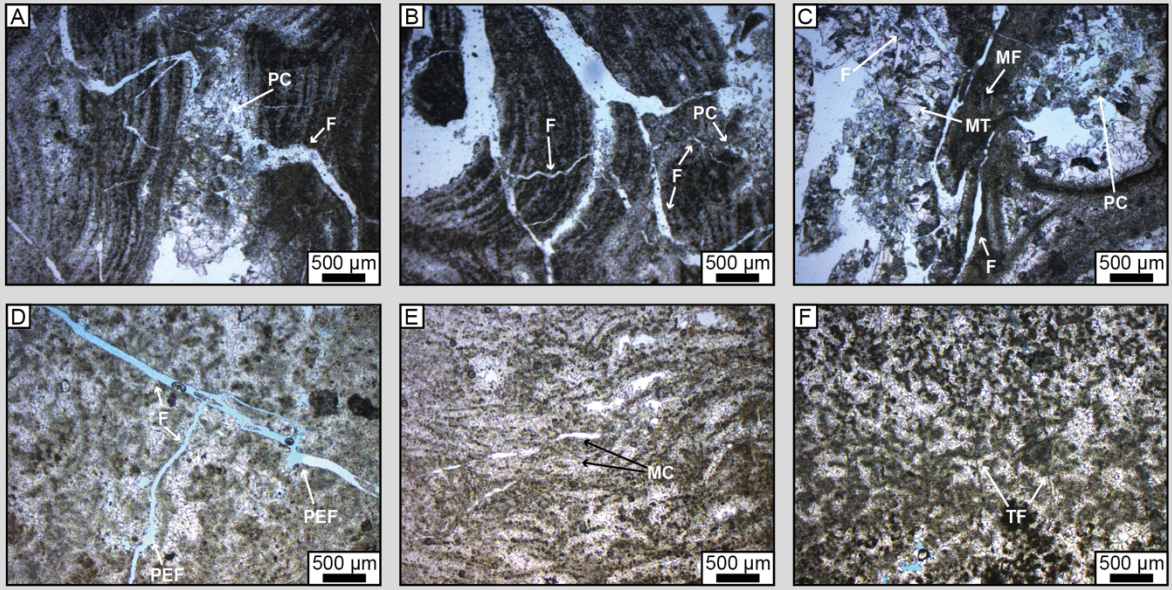
5.6.2.2 Failure within the transitional regime

Eight shrub travertine samples deformed within the transitional regime (i.e., samples with strain hardening) where grain crushing, compaction and microcracking are commonly observed (Figure 5-14g-o). Grain crushing and compaction is localised to thin, 0.2 mm wide, planar structures (Figure 5-14h/j/k/l/o) which represent zones of grain size reduction. These are interpreted to be localised compaction bands where no evidence of shearing is observed. Where en-echelon structures and offsets are observed (Figure 5-14g-h), these bands are interpreted to be shear enhanced compaction bands. Often these individual compaction strands occur in 1-3 mm bands of multiple strands which segment and bifurcate (Figure 5-14g/j/n/o). The thickness and extent of grain crushing along these bands varies and can coalesce to form more densely packed regions of the localised compaction band (Figure 5-14j). Pore collapse is observed to be a result of microcracking and grain crushing of the pore walls (Figure 5-14h/m). Primary porosity is observed to be locally preserved outside of localisation compaction bands, however, is severely reduced within compaction bands. In samples where bedding is 90° to the maximum principal stress, low angle conjugate compaction bands are observed (Figure 5-14j-k) whilst samples where bedding is at 45° and 0° typically only resolves higher angle features.

Localised compaction and shear-enhanced compaction bands represent zones up to 3 mm wide regions of low porosity (not considering fracture porosity) due to grain crushing and pore collapse. In most cases, however, shear enhanced compaction bands are overprinted or crosscut by fractures (Figure 5-14g-o). Evidence of brittle dilation (i.e., microcracks and through going fractures) is observed in all samples that are interpreted to deform in the transitional regime, though is more extensive in samples where a switch to dilation from compaction was interpreted in the triaxial mechanical data. Brittle deformation is therefore interpreted to occur alongside compaction processes. However, the extent of dilation within shear enhanced compaction bands is variable and can vary along individual bands.

Mechanical twinning is also observed to be a major deformation mechanism (Figure 5-14f-l) and is closely associated with areas of pronounced shear deformation, such as in the grains surrounding shear planes (Figure 5-14g), areas of intense cracking/fracturing (Figure 5-14c) and pore collapse (Figure 5-14j/f). The extent and abundance of mechanical twinning is more pronounced in areas with pervasive sparite grains > 0.1 mm in size (Figure 5-14g-h). The presence of both compactive shear bands, mechanical twinning and fractures illustrates a complex interplay of brittle and ductile processes that occur within the transition between these regimes resulting in complex structural features.

BRITTLE DILATION



COMPACTION AND DILATION

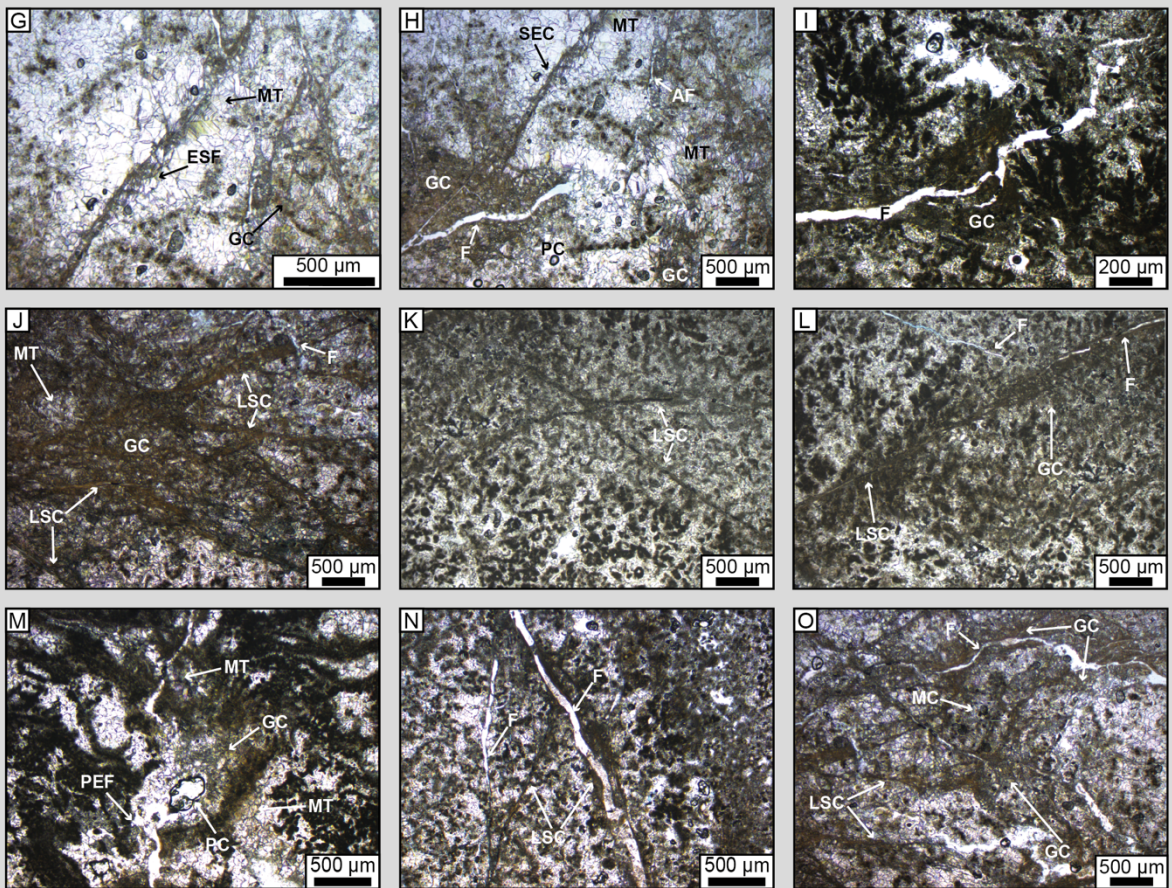


Figure 5-14. (Previous page) Photomicrographs of deformed samples. All images are orientated so that the maximum principal stress is vertical. Label abbreviations: PC: pore collapse; F: fracture; MC: microfracture; PEF: pore emanating fracture; LC: localised compaction; LSC: localised shear compaction; ESF: enechelon shear fracture; MT: mechanical twinning; GC: grain crushing. Photomicrographs A to F are from samples interpreted to deform in the brittle regime. A) Pore collapse feature with through going fracture across bedding. Fracture has an irregular geometry. Minor micro-fractures are also present. B) Brittle fractures at multiple orientations. Fractures cut through bedding with stepping geometry and locally follow bedding parallel pores. C) Pore collapse structures are common within large pores > 0.5 mm wide. Mechanical twinning is also observed within sparite cements. D) Pore emanating fractures. Both low angle and tensile fractures are present. E) low angle fractures in horizontally bedded samples. Stepping of fractures across laminations/beds is common in laminated micrite/microsparite facies). F) Tensile fractures. G) Enechelon geometry fractures within a shear band with localised compaction. H) Localised compaction defined by grain crushing and packing. Tensile and shear fractures cross-cut areas of localised compaction. I) Low angle stepping fracture in horizontally bedded shrub samples. Grain crushing and packing is observed locally at bends in the fracture. J) Shear compaction band formed of multiple compaction strains. K) Conjugate shear enhanced compaction bands. L) Shear enhanced compaction band which has been partially fractured. M) Pore collapse with pore emanating fracture. N) High angle shear enhanced compaction band overprinted by throughgoing fracture. Multiple fractures and shear enhanced strands are observed to splay from the primary failure plane. O) complex zone of localised compaction bands and cross cutting fractures.

5.7 Discussion

5.7.1 Deformation mechanisms within travertine

Deformation within travertine samples at confining pressures up to 30 MPa are found to either fail within the brittle regime or at the transition between the brittle and ductile regime. The style of deformation is summarised in Figure 5-16 and has been found to be dependent on both the orientation of bedding with respect to σ_1 and the travertine facies. Overall, deformation can be categorised as either:

1. Dilation and localisation where microcracking and brittle shear are the dominant failure mechanisms; or
2. Localised shear compaction, dominated by grain crushing, pore collapse and mechanical twinning, which is overprinted by dilational fracturing during the final stages of deformation.

5.7.1.1 Dilation and brittle failure

Deformation within the dilational regime is observed in samples of laminated micrite/sparite and peloidal micrite/microsparite facies, which have moderate porosities (6.4 – 13.8%). Deformation within these samples results in brittle shear failure within zones of high porosity, which typically occurs between laminations/layers within these facies types. Strain is interpreted to localise in high porosity layers, which occur between laminations in laminated micrites and between beds in peloidal micrites. Unlike deformation analysis of other porous carbonates (Baud et al., 2000 – Solnhofen limestone; Baud et al., 2009 - Majella Limestone,

$\phi = 30\%$; Vajdova et al., 2014 - Indiana limestone, $\phi = 15.6\%$ and Tavel limestone, $\phi = 10.4\%$; Cilona et al., 2014 - Bolognano limestones, $\phi = 29\%$), laminated micrite/sparite and peloidal micrite/microsparite facies in this study results in an atypical, purely dilational, response to compression at confining pressures up to 30 MPa. Generally, the yield strength of carbonates is inversely proportional to porosity and grain size (Cilona et al., 2014). As such, the response of laminated micrite/sparite and peloidal micrite/microsparite facies would be predicted to fall within the transitional or compactive deformation regime comparable to Tavel and Indiana limestones analysed by Vajdova et al. (2014) (Figure 5-15). Instead, however, dilational mechanisms dominate. This may be due to very stable fabrics formed from the construction of self-supporting framework fabrics and very early constructive diagenesis which is common in travertines (Anselmetti & Eberli, 1993). The lack of compactive and transitional regime deformation during triaxial testing in this study reinforces the difficulty in predicting yield envelopes in carbonates and highlights the potential error in using porosity as a proxy for estimating conditions for strain localisation.

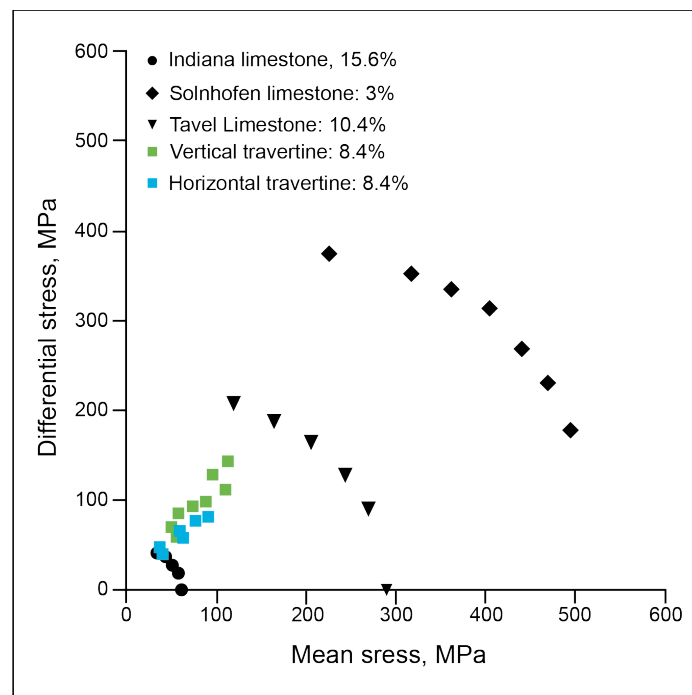


Figure 5-15. Comparison of critical stress data from peloidal and laminated micrite travertine samples deformed in this study compared to published carbonate data. Data for additional carbonates: Indiana limestone and Tavel Limestone: Vajdova et al. (2014); Solnhofen Limestone: Baud et al. (2000a)

5.7.1.2 Localised shear compaction and late-stage dilation

Localised compaction and localised shear-enhanced compaction is observed in shrub facies which have porosities of 10.6 to 38%. The variable porosities between cores taken from the same sample are the likely cause of the spread of critical stresses observed in the analysis and may reflect smaller-scale intra-facies/sample porosity variations in porosity which cannot be quantified in this study. Generally, shrub facies deform within the transitional regime which results in the formation of localised compaction and shear-enhanced compaction bands. These bands, up to 3 mm wide zones of reduced grain size and porosity, formed as a result of grain crushing and pore collapse. Brittle dilation is however observed to be present and form both through going and cross-cutting fractures. This brittle deformation is also present in samples where a switch from compaction to dilation (at critical stress C^*) is not interpreted suggesting that both brittle and compactive processes occur in the brittle-ductile regime. Compactive processes are however interpreted to be the dominant process in this stress regime which results in strain hardening. Baud et al. (2000) interprets the transition from shear-enhanced compaction to dilation as the point at which cumulative dilation due to cracking exceeds the concomitant compaction due to pore collapse. Observations of micro-structure in this study support this interpretation where microcracks are observed to overprint compaction similar to results of mechanical tests in the Indiana Limestone of 10-16% porosities (Vajdova et al., 2014). Vajdova et al. (2014) suggests that deformation twinning slip, which is commonly observed in sparite cements in deformed samples within this study, may induce local tensile stress concentration and nucleate cracks, promoting evolution towards dilatant cataclastic flow. Macro-porosity observations in this study show a decrease in overall porosity is observed suggesting that brittle and compactive pore collapse and grain crushing is the primary control on final, post-deformation porosity with reductions between 4.9-21%. Deformation within the transitional regime therefore displays a complex interplay between dilation and compaction mechanisms and results in complex changes of the micro- and macro-porosity networks. Results from travertine though remain inconclusive for predicting reliable stress responses within shrub facies, where a larger data set and measurements of more diverse datasets are needed to constrain yield curves in the compactive regime especially.

5.7.1.3 Velocity response to failure in travertine

Changes in V_p and V_s observed during triaxial testing show that V_p is characterised by an initial increase which is interpreted to be due to the initial closure of existing cracks, and then decreases during inelastic deformation controlled by brittle microcracking processes. This is in broad agreement with the initial velocity response observed by Nicolas et al. (2016) and

Baud et al. (2017a) from mechanical experiments carried out in high porosity limestone. However, Baud et al. (2017a) observed an eventual increase in V_p which is controlled by pore collapse which is not observed in this study. This is likely due to the dominant control of brittle mechanisms within travertines at the confining stresses measured in this study. It should also be noted that mechanical triaxial tests carried out in this study were performed on dry samples and so the velocity response of saturated samples is likely to a different response as elastic wave velocities are dramatically affected by pore fluid properties (Fortin et al., 2007).

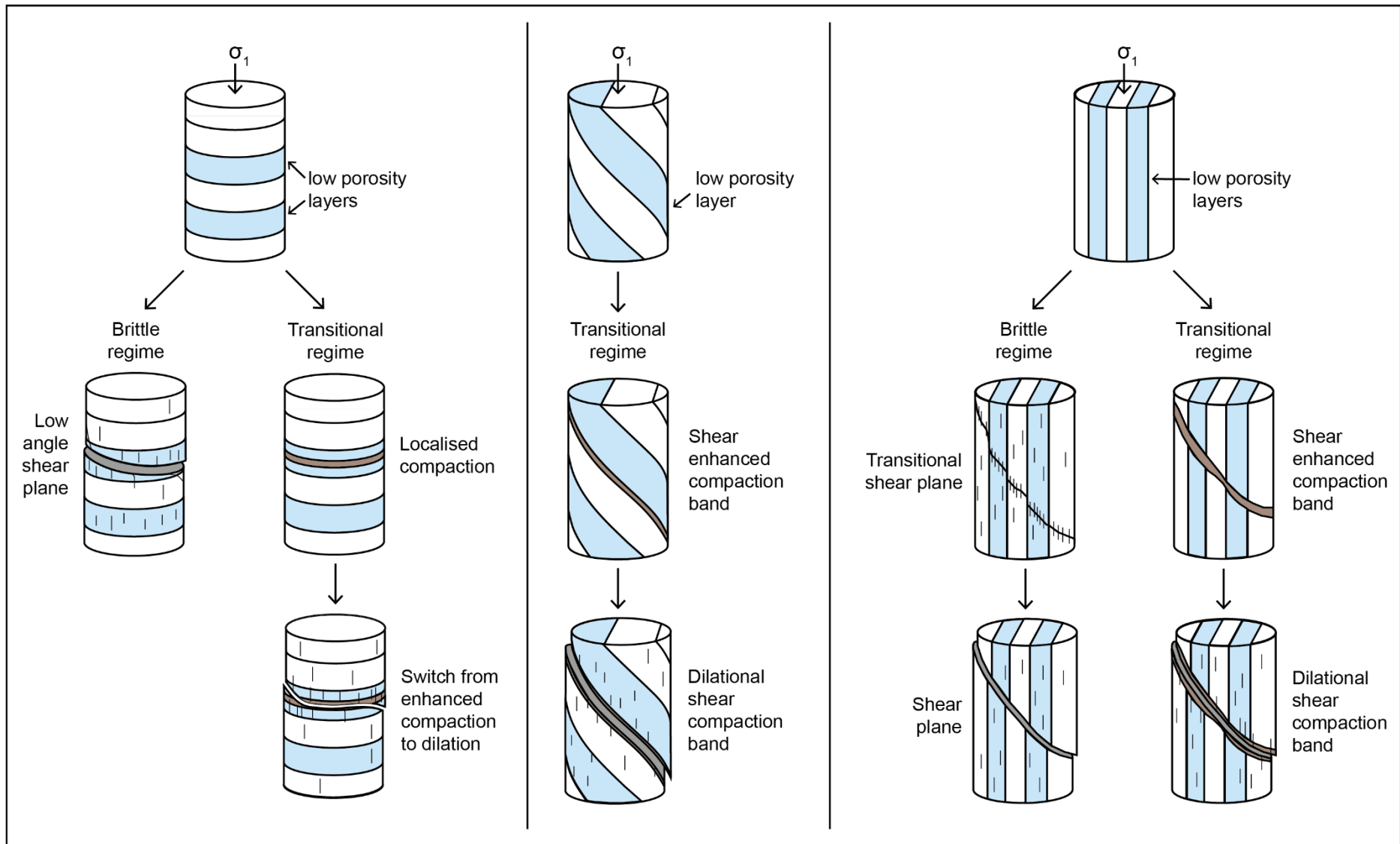


Figure 5-16. Summary of deformation styles observed in differently orientated travertine cores.

5.7.2 The control of travertine heterogeneity on failure

5.7.2.1 Control of travertine facies on deformation style

Petrophysical results illustrate the large-scale ranges of porosity (1 - 16%) and permeability (0.002 - >1000 mD) at millimetric scales within travertines as a result of the broad variety of depositional facies. This range is shown to be due to the mm and cm scale changes in facies types, which are associated with pre-existing, depositional, pore network variability. Scale and styles of variability in this study are similar to results presented in Soete et al. (2022) where samples of sub-horizontal, biostromal reed, cascade and waterfall travertine facies are found to have porosity ranges of 3 - 25% and a permeability range 0.004 – 3675 mD. Soete et al. (2022) provided further analysis of mercury injection capillary pressure and nuclear magnetic resonance to illustrate that the pore size distribution (i.e., bimodal versus unimodal) rather than porosity or pore type control the permeability within travertines. This may explain the large range of porosity and permeability data that is observed within individual facies type and the atypical relationships observed between V_p and the host rock properties measured in this study. Published data from marine carbonates show that typically, V_p decreases with increasing porosity and increases with increasing UCS (e.g., Palchil, 2012; Al-Osta et al., 2014; Reyer & Phillip, 2014). The absence of such a strong relationship between V_p , UCS and deformation style in this study may be a result of the complex nature of different facies, and intra-facies fabrics associated with travertines. Mechanical data illustrates the difference in mechanical response due to compressional stress within three different facies types (shrubs, laminated micrite/microsparite and peloidal micrite/microsparite). Within laminated micrite/microsparite (6.4 – 13.8% porosity) and peloidal micrite/microsparite (4.66 – 8.88% porosity) deformation can be predicted to fall within the dilational regime, irrespective of bedding orientation, up to 30 MPa confining pressures. Comparatively, the correlation of yield envelopes within shrub facies samples is harder to define. Shrub samples show a wide variety of lithotypes, which as discussed by Soete et al. (2022) represents substantial changes in the material framework. Whilst pore sizes were not quantified in this study (due to low resolution of CT scanning), visual inspection of shrub facies samples in comparison to laminated and peloidal micrite/microsparite qualitatively highlight a far greater variety of size and shape of pores which may explain the greater variety of deformational styles. As such, more detailed analysis of deformation within different shrub facies sub-divisions are needed to quantify the effect changes in lithofacies has on deformation.

5.7.2.2 Control of travertine bedding orientation on failure plane geometry

The final geometry of both dilatant brittle fractures/shearing and shear compaction bands are observed to be affected by the orientation of bedding (Figure 5-16). Results are comparable to studied anisotropic rock mediums such as hard foliated rocks (Cho et al., 2012), shales (Fjær and Nes, 2014; Gholami & Rasouli, 2014), sandstones (Tavallali et al., 2010), and experimental compounds (Zhang et al., 2019). Travertines in this study are found to localise in beds/laminae of high porosity or along bedding planes when their orientation is favourable. Generally, dip of the failure plane (either brittle or compactive) increases with decreasing bedding angle measured from the principal stress direction. Modelling of a transversely isotropic rock (i.e., those that have one plane of elastic symmetry such as layered shales) by Zhang et al. (2019) also demonstrate this relationship where shear cracking is the dominant process along dipping or horizontal weak layers while tensile cracking is more important when bedding is parallel (resulting in high angle failure planes $> 60^\circ$ failure planes). This is similar to results found in travertines, where either high porosity layers or bedding planes localise failure when their orientation is suitable. Though deformation structure can only be observed at one confining stress due to triaxial testing set-up, similar geometries across differently orientated samples suggest that this relationship may also be true for travertine. Further analysis of structure at different confining pressures by conducting single stage triaxial tests is needed to confirm this.

The observation in this study of low angle ($< 30^\circ$) brittle shear planes in horizontally oriented travertines are not observed in existing studies of mechanically anisotropic media (Tavallali et al., 2010; Cho et al., 2012; Fjær and Nes, 2014; Gholami and Rasouli, 2013; Zhang et al., 2019). Fjær and Nes (2014) and Cho et al. (2012) did observe low dips of $15 - 30^\circ$ locally in heterogeneous failure planes, however, these were in samples with beds dipping $15-30^\circ$ (i.e., inflections in the failure plane occur co-planar with bedding) and so are not comparable. As such, it is difficult to resolve a mechanical model for near horizontal failure under compression and falls outside of classic Andersonian theory (1951) (which predicts that only normal faults with $> 45^\circ$ dips can form). Zhang et al. (2019) illustrate that distribution of microcracks is more diffuse in samples which are horizontally bedded. It is therefore suggested that the mechanical response of sub-horizontal brittle shear is likely a pseudo-shear plane where strain localisation occurs within high porosity layers with the eventual collapse of such layers through diffuse microcracking resulting in the splitting and breaking of cores and formation of a low angle plane slightly oblique to bedding/layering.

Overall, the mechanical anisotropy is therefore considered a key control on deformation localisation. Modelling local stresses may be complex in heterogenous travertine bodies such as mound and slope deposits where a range of bedding geometries are observed both laterally and vertically. The changing mechanical response depending on bedding orientation therefore has implications for the types of deformation features likely to be encountered within a given body of travertine.

5.7.3 Possible impacts of failure within travertine on fluid flow

It was not possible to measure permeability changes in samples after undergoing deformation, however, observations of the macro-and micro porosity changes can be used to hypothesise the impacts on fluid flow. For travertine facies that are more likely to deform within the dilational regime, fracture porosity may provide fluid pathways and decrease the permeability anisotropy in the rock mass, where tensile fracture provides vertical pathways. If dilatant fracturing is pervasive permeability anisotropy may be reversed, with substantially weaker horizontal permeability than vertical fracture permeability. Comparatively, prior to eventual dilation, shrub facies (and potentially other high porosity travertine facies not assessed here) are observed to undergo localised compaction resulting in bands of decreased porosities and grain size which may act as narrow barriers to fluid flow. Shear experiments conducted on travertine by Giwelli et al. (2016a,b); Delle Piane et al. (2016); Kiewiet et al. (2020) illustrate similar microstructural characteristics, where shearing even at low (2 cm) displacements results in porosity and permeability reductions associated with localised compaction and asperity shearing. Comparison of microstructure of cataclastic development in sheared travertine (Delle Piane et al., 2016) show a similar internal structure to that observed in compaction bands (note these are on a smaller scale) within deformed travertine in this study. However, key structural differences remain (likely due to the different stress regimes tested) whereby mechanical twinning is an important deformation mechanism observed in travertine samples deformed in this study. Additionally, comparisons are based only on microstructural observation of thin sections, which may not image/represent the true micro-porosity network between grains in three dimensions. Additional work is therefore needed to assess the impact such deformation may have on permeability, ideally on samples pre- and post-deformation. Samples in this study are observed to a switch from shear enhanced localised compaction to dilation, which introduces microcracks and fractures crosscutting compaction bands which may reduce or negate the overall possible permeability decrease of compaction bands but provide complex and likely poorly connected fluid pathways. This influence of late-stage brittle

failure will likely be dependent on the connectivity and size of microcracks and fractures produced which is observed to be variable within deformed samples in this study.

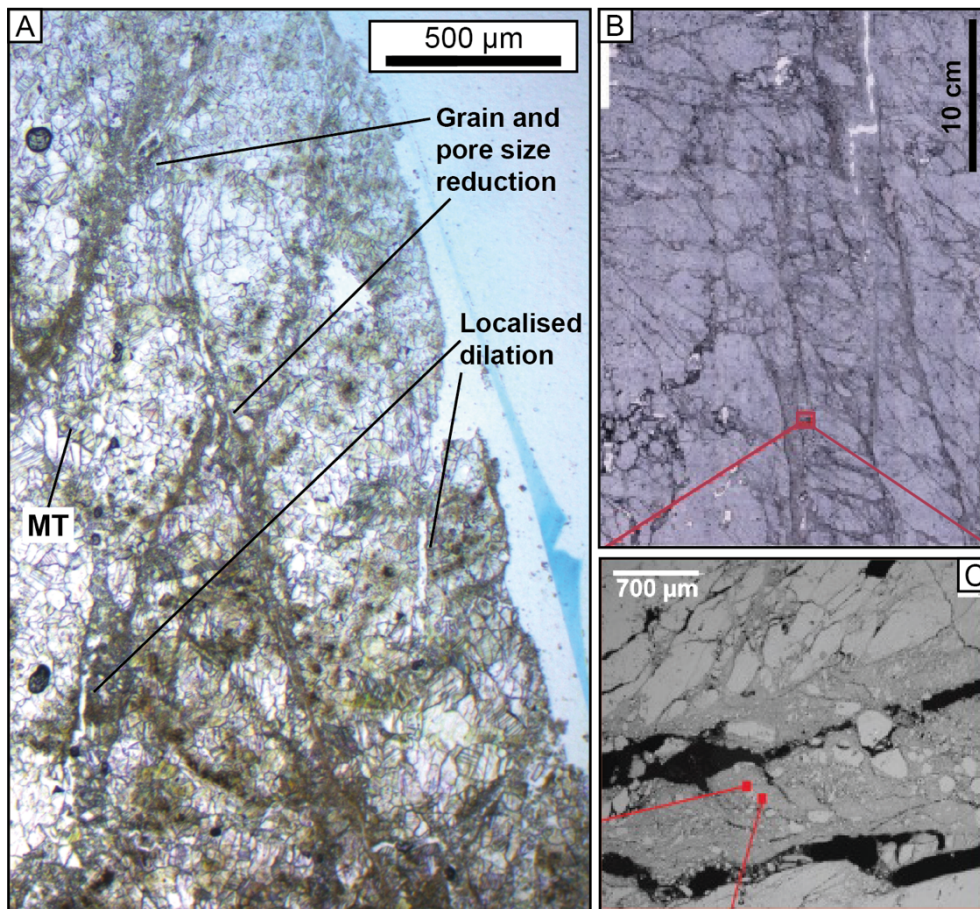


Figure 5-17. Comparison of microstructure within deformed travertine samples. A) Photomicrograph from this study illustrating enhanced shear compaction bands with localised dilation. B) Sample photograph and C) SEM image from Delle Piani et al., 2016 of experimentally sheared travertine. SEM image from A (red inset identifies location) illustrates grain size reduction and fracturing.

5.8 Summary

Integrated analysis of porosity-permeability measurements, mechanical triaxial test data, CT scan modelling and optical microscopy is used to understand the deformation mechanisms typical for travertine. Due to heterogeneous nature of travertines, this study focuses on the impact bedding orientation and facies has on deformation to aid prediction of modelling faults of analogous deposits (such as those in the South Atlantic pre-salt) in the subsurface.

Preliminary analysis of permeability anisotropy within travertines illustrate that porosity-permeability relationships can be recognised on a facies level with permeability anisotropy most predictable in peloidal micrite/microsparite facies and though a correlation exists,

anisotropy has a more random distribution within shrub and laminated micrite/microsparite facies.

Results from mechanical testing and structural observations show that the existing travertine fabric, which is associated with travertine facies, has a primary control on the deformation mechanisms within travertine. Results show that deformation is either accommodated by dilational processes, such as micro-cracking, in moderate porosity laminated micrite/microsparite (porosity: 10.8%) and peloidal micrite/microsparite facies (porosity: 7.5%); or results in localised shear compaction (associated with grain size reduction and pore collapse) with a subsequent switch to dilational micro-cracking in higher porosity shrub facies (porosity: 19.4%). Further quantification of variations in critical stresses with bedding orientation illustrate that the angle of bedding with respect to the principal σ_1 stress controls the geometry of failure plane. Results provide broad predictions for failure plane angle, which are observed to increase with decreasing angle in σ_1 to the bedding plane. The impact such inelastic deformation has on permeability is discussed qualitatively and highlights that compaction band formation within travertines may act as barriers to fluid flow due to localised decreases in grain size and porosity. However, this is interpreted to be controlled by the extent of brittle deformation process that can occur within the brittle-ductile transition. This may negate possible permeability reductions if microcracking is pervasive enough to form a connected fracture framework. The validity of such a hypothesis, however, requires further work to quantify the permeability response to failure within travertine.

Overall, this study provides quantitative data to illustrate travertine porosity-permeability and mechanical properties with conceptual hypotheses for how deformation may vary as a function of the orientation of fabrics with respect to the principal stress orientations within complex travertine bodies.

Chapter 6

6. Discussion

6.1 Introduction

Understanding the structural elements of fault zones, including fault rock distribution and continuity, fault zone architecture, petrophysical and microstructural properties, is crucial to understanding the generation of faults and predicting and modelling their impact on fluid flow in the subsurface (Knipe, 1992; Knipe et al., 1997). Chapter 2 explores the current understanding of carbonate fault rocks which are found to be considerably more variable and complex than siliciclastic sequences (Delle Piane et al., 2017; Michie et al., 2018, 2020). Although substantial work has been carried out to understand faults in carbonate rocks (e.g., Agosta et al., 2007; Michie and Haines, 2016; Giwelli et al., 2016; Michie et al., 2018,2020,2021; Delle Piane et al., 2017; Cooke et al., 2018; Wu et al., 2020) there still exists a relative paucity of data and models on how host rock properties such as mineralogy, porosity and facies can be reliably used as a predictive tool in fault seal analysis compared to siliciclastic fault rocks. Similarly, in reviewing the current understanding of carbonate fault rocks (Chapter 3), the lack of research on the structural geology of non-marine carbonates is apparent. Three main research questions were recognised to address key knowledge gaps within the context of carbonate fault rocks:

1. What are the structural characteristics of faults within non-marine carbonates?
2. What is the impact of deformation within non-marine carbonates on fluid flow in the subsurface?
3. Can non-marine carbonate host rock characteristics be used to predict petrophysical characteristics of faults in space and time?

Interest and research in non-marine carbonates has increased significantly in recent years following the discovery of extensive Early Cretaceous, non-marine carbonate, hydrocarbon reservoirs in the South Atlantic rifted margins (e.g., Bohacs et al., 2013; Bosence et al., 2015; Gallois et al., 2015; Ronchi & Cruciani, 2015; Wright & Rodriguez, 2018; Lima & De Ros, 2019; Gomes et al., 2020; Capezzouli et al., 2022). Key concepts relating to their distribution,

processes, and depositional models, remain challenging, requiring frontier research (Capezzouli et al., 2022). One of the main challenges associated with studying non-marine carbonates are their limited global distribution due to low preservation potential within the geological record and tendency to having experienced complete diagenetic alteration (e.g., Capezzouli et al., 2022). This provided a challenging aspect to this project, which aimed to understand and quantify fault characteristics within non-marine carbonates. Due to a lack of known and published examples of faulted non-marine carbonates, an extensive global field study was undertaken to visit potential faulted outcrops to address the outlined research questions (Chapter 4). Alongside this, an experimental mechanical approach was taken to address the deformational response under a range of confining pressures (up to 30 MPa) (Chapter 5). This chapter aims to summarise and discuss the results of work carried out during this study with comparisons to existing carbonate fault models to assess the validity and implications of research outcomes.

6.2 What are the structural characteristics of faults within non-marine carbonates?

Although an extensive fieldwork campaign was carried out visiting a diverse collection of different non-marine carbonate rock types in various tectonic settings, only two different types of non-marine carbonates showed evidence of shear deformation. Observations from these field outcrop locations provide characterisation of fault zone characteristics within Quaternary travertines (Ballık, Turkey) and Aptian laminated microbialites (Crato formation) (Chapter 4), providing insights into shallow deposits, which have undergone very little burial. Additional mechanical experiments were taken out to compare deformation under laboratory conditions to that observed in the field. Across field observations and mechanical data, three styles of deformation are observed within non-marine carbonate assessed in this study:

1. **Brittle shear faults:** Observed in small-scale faulting (< 20 cm throw) in laminated limestones and in mechanically deformed travertine samples (laminated micrite/microsparite and peloidal micrite/microsparite facies).
2. **Dilational deformation, including fractures, faults and karsts systems:** Observed in the Ballık travertines, Turkey.
3. **Localised compaction and localised shear enhanced compaction bands with late fracturing:** Observed in mechanically deformed travertine shrub facies.

6.2.1 Faulting within laminated limestones

Small scale (< 20 cm throw) conjugate faults within laminated limestones of the Crato Formation (Araripe Basin, Brazil) were interpreted to have formed soon after deposition within partially consolidated sediments resulting in moderate-angle (40 – 60°) fault planes and associated soft sediment, ductile features (folds, dragging and loop bedding). Generally, faults are found to form 5 cm wide bands of highly segmented and bifurcated shear planes, which can have gouge material preferentially composed of organic clays where organic rich layers are intersected. Though normal faults observed in outcrops of laminated limestones and travertines are interpreted to form during similar burial depths, the deformation styles are markedly different. Laminated limestones are characterised by compactional shear faulting while dilational hybrid faulting is observed in travertines. As burial depths are similar at the near surface, the difference in deformation style is interpreted to be controlled by the extent of cementation. Poor cementation in laminated limestone muds leads to deformation in a compactional manner while well cemented travertine, composed of framework building calcite deform in dilation. As cementation and total porosity of carbonates is found to have a fundamental control of carbonate rock strength (Croizé et al., 2010), the style of deformation that laminated limestones may experience may evolve with increasing burial and diagenesis.

6.2.2 Dilational faulting within travertines

Dilational fractures, faulting and karst features are observed within travertines in outcrop. Chapter 4 concludes that these faults in shallow travertines are predominantly normal, hybrid failure faults where failure occurs at the transition between extension and shear failure. These faults are characterised by their dilational or “open” nature and often complex infill. The dilational nature of faulting is suggested to be due to the low confining stresses coupled with high rock strength as a result of very early diagenesis and cementation resulting in failure that occurs within the brittle dilation regime (i.e., on the left side of P-Q yield envelope). Dilational faults are common near the surface where tensile fracturing is common (e.g. basalts of north eastern Iceland - Angelier et al., 1997) and Chapter 4 discusses the similarities with dilational faults in Tertiary carbonates on Jebel Hafeet (UAE/Oman) presented by Gent et al. (2010). Additional scaled models were carried out by Gent et al. (2010) constructed of hemihydrate powder (analogous to layered cohesive rocks) interbedded with weaker sand layers. Modelling illustrates the relationship of failure mode with depth where tensile and hybrid failure modes are observed at and near the surface while faults evolve to shear failure at depth (Figure 6-1). Fault geometries observed in the travertines examined during this study display similar

geometries to these modelled near-surface faults modelled by Gent et al. (2010) (Figure 6-1). Gent et al. (2010) suggests that hybrid failure dominates failure between 7 and 14 cm depth in the experiments, which corresponds to 600 – 1400 m in nature. Outcrops of travertines in the Ballik travertines (Chapter 4) provide exposure up to 140 m below the surface and are buried by up to 40 m of cover sediments (conglomerates and sands). As a result, their setting is considered analogues to the extensional models proposed by Gent et al. (2010). However, the observations of minor influences of shear amongst dominantly dilational faulting at burial depths of 180 m are not in keeping with the predictions from numerical modelling in Gent et al. (2010) where hybrid deformation is believed to be at considerably deeper depths. Importantly, the models in Gent et al. (2010) rely on a purely uniaxial extension, with no oblique or transtensional component. This contrasts with the Ballik travertine outcrops where the structural setting has a moderate transtensional component, demonstrated by the fault-strike parallel slickensides described in Chapter 4. It may be that any minor transtensional component of deformation, combined with the elastic and physical properties of travertines (highly brittle and porous) permit shallower depths of hybrid failure.

The abundance of dilational normal faults differs from many of the recently published carbonate fault rock models (e.g., Tondi et al., 2006; Agosta et al., 2007; Antonellini et al., 2014; Cilona et al., 2014; Michie et al., 2014,2021; Rotevatn et al., 2017; Solum & Huisman, 2017; Cooke et al., 2018; Ferraro et al., 2019), which are dominated by shear to compactive failure. Cemented carbonates can sustain open fractures and dilational as well as large voids (such as karsts) over an extended range of burial depths (Bussolotto et al., 2007; Gent et al., 2010), consideration of dilational failure modes may be important at present shallow depths of burial, but also in more deeply buried non-marine carbonates as a key-element of their early burial history. Modelling of travertine faults within similar sequences will also need to consider the infill of dilational faults, which are observed to be variable and often display several generations of infill of terrigenous material, re-worked travertine, secondary vertical travertine deposition and calcite veins.

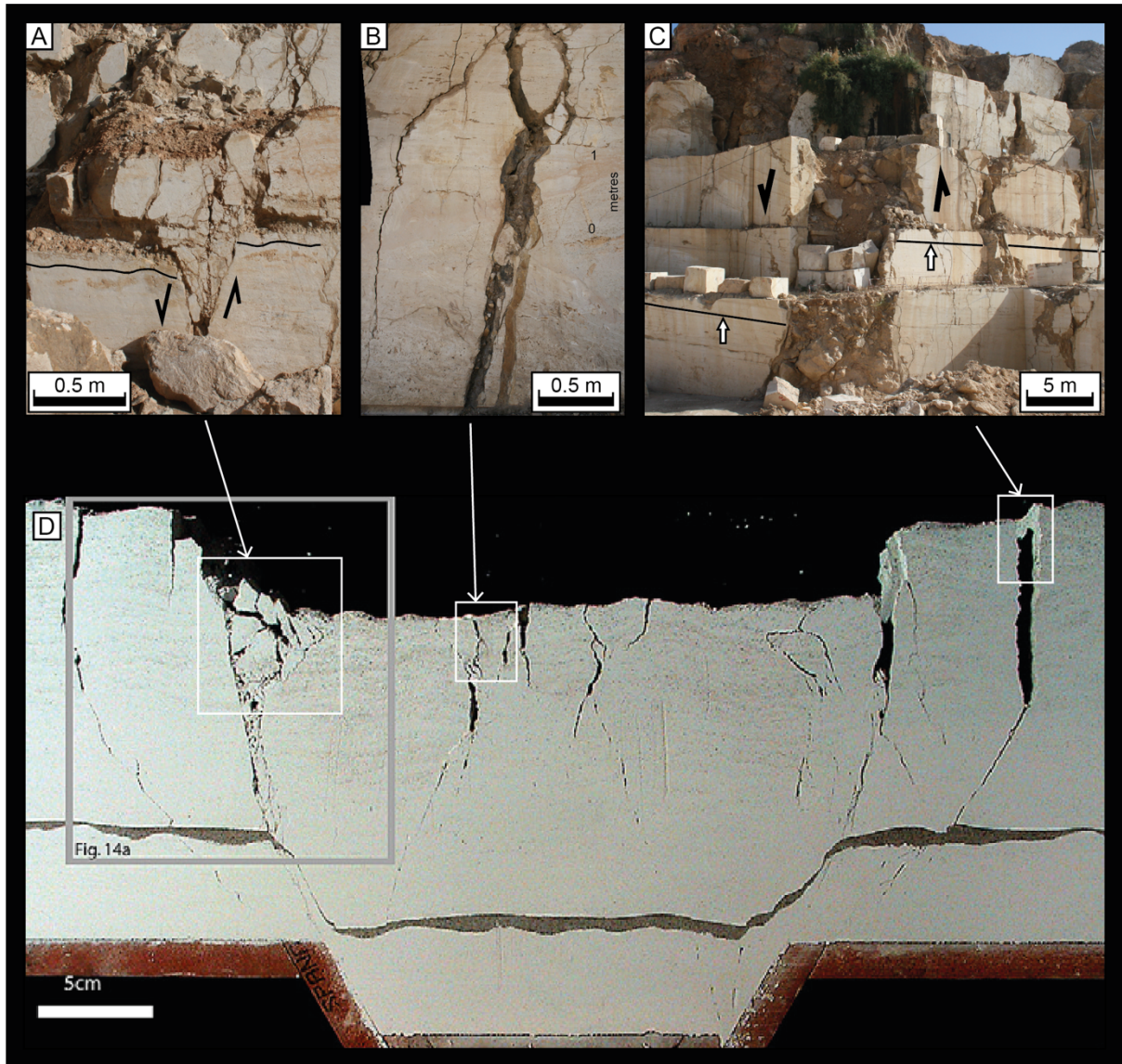


Figure 6-1. Comparison of dilational structures observed in the Ballık travertines (Turkey) with scale model presented by Gent et al., 2010. A) 10 cm offset normal fault with widening of fault core and brecciation of travertine and conglomerate layer. Similar structure observed in scale structure indicated by arrow. B) Dilational fracture with terrigenous infill and travertine clasts which show similarities to scale model where tensile fracturing is common at the near surface. C) ~ 7 m throw dilational fault which formed at the surface of the travertine body. D) scale model formed of hemihydrate and a sand layer (dark band) with horizontal elongation of 7% (Gent et al., 2010). Model illustrates tensile and hybrid failure mode in the top 10 mm and shear failure modes in the lower half of the model.

6.2.3 Fault- and fracture-related karst systems within travertine

Chapter 4 discusses observations of karsts within travertines. Within relatively undeformed travertine sequences (e.g., Tivoli travertine, Italy), karst features are observed to be largely associated with stratigraphic intervals where dissolution occurs at or near the palaeosurface. The collapse of these types of karst structures is common and is associated to high fracture frequencies. Karsts within deformed travertine (Ballık travertine, Turkey) are associated closely with faults and fractures. These karst features are interpreted to form after dilational failure, which forms fluid conduits and results in the preferred dissolution of higher porosity

layers. Variability of the lateral continuity and geometry of these karst systems is likely to result in stratigraphic zones of high karst frequency in heavily faulted sections. In many cases, karsts in deformed sequences are filled with fine grained sediments formed of reworked travertine grains (calcite) and clay-rich material (thought to be terrigenous), which are observed to host internal sedimentary bedding structures. Sediment infill shows variable cementation by calcite, which fills inter-granular porosity. The fault-controlled karsts observed in travertines are similar to observations of other fault-controlled karst systems (e.g., Lu et al., 2017; Cazarin et al., 2019; Li et al., 2019; Araújo et al., 2021) where stratigraphic control as well as fault/fracture networks will determine overall karst structure. The distinction between fault-controlled karsts and paleo-surface karst systems may be difficult to characterise without the context to faulting. Fault-controlled karsts, however, are commonly observed to be filled with stratified sediments, which is not observed within karsts unrelated to faulting. Additionally, karsts in undeformed sections (i.e. 'sink holes') are, however, observed to be more chaotic associated with karst collapse, though this is not exclusive to non-fault related karsts.

6.2.4 Comparison of field observations and mechanical failure

Triaxial tests (Chapter 5) showed that deformation in travertine under compression at up to 30 MPa confining pressure occurred either within the brittle regime resulting in shear brittle failure or at the brittle-ductile transition resulting in localised compaction and shear enhanced compaction bands which are overprinted by dilational microcracking. Although geometric variations (i.e., dip and width) were observed in outcrops containing faults relating to layering of travertine, the style of faulting (i.e., hybrid brittle failure) does not appear to be controlled by facies suggesting low confining pressures (< 10 MPa). This is interpreted to be due to the early cementation of travertine so that stresses fall on the left side of yield curves in P-Q spaces for all travertine facies resulting in brittle dilational failure (Figure 6-2). However, as facies have substantially different petrophysical properties (i.e., porosity/pore type), P-Q curves are found to vary with facies and orientation (Figure 6-2). On stress paths at confining pressures > 10 MPa, failure may fall on different parts of the yield curve (i.e., dilation on the left or compaction on the right side of yield curves) depending on the facies and orientation of bedding (Figure 6-2) at conditions similar to those observed in this study (i.e., confining pressure at 30 MPa, equivalent to ~ 1.2 km at lithostatic pressure). Therefore, depending on stresses, localised compaction may be observed in high porosity layers of shrubs alongside brittle structures within lower porosity micrite-dominated facies (i.e., laminated micrite/microsparite and peloidal micrite/microsparite). Projection of these relationships suggests that at higher confining pressures not assessed in this study, lower porosity micrite-

dominated facies may also experience shear enhanced compaction where sufficiently high differential pressures are reached for stresses to fall on the right side of P-Q yield curves (Figure 6-2).

Although carbonates may experience crystal plastic deformation at relatively low confining pressures (e.g. Vajdova et al., 2004,2010; Baud et al., 2017a; Brantut et al., 2018), travertine appears to predominantly undergo brittle failure at low P_c , typical of the near surface, especially within moderate porosity micrite/microsparite dominant facies (4.66 – 13.8% porosity). This tendency for relatively early brittle failure suggests that the strong role of mechanical twining and dislocation in calcite observed in other carbonates (e.g., Vajdova et al., 2004,2010; Baud et al., 2017a; Brantut et al., 2018) may be subdued within travertines or cannot be sustained at high strain rates.

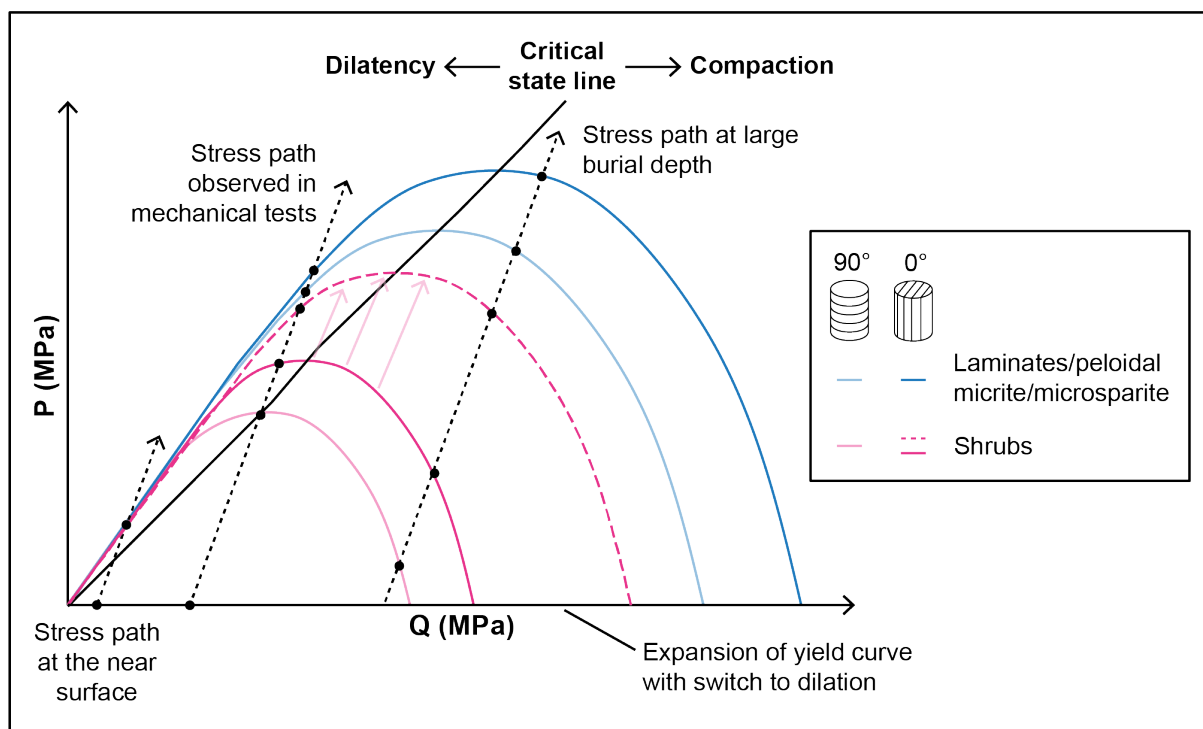


Figure 6-2. Schematic yield curves for travertine facies studied based on mechanical observations. Three example stress paths are mapped in dashed, black lines. A stress path equivalent of very shallow faulting at the near surface illustrates deformation within all travertine facies and orientation will fail on left side of P-Q yield curve. Stress path at confining stress of ~ 30 MPa will result in a variety of deformation styles depending on the facies type. Stress path at high confining pressures (i.e., large burial depth) will result in compactive deformation of all facies depending on differential stress. Dashed yield curves illustrate the expansion of yield curves after shear enhanced compaction.

Mechanical testing provides insight into the failure modes that will dominate in these travertine sequences at deeper burial depths than experience by the Ballik travertine and agrees with Gent et al. (2010) where hybrid open faults evolve into shear faults at depth. Mechanical testing also illustrates that deformation in these moderate porosity micrite/microsparite dominant facies will undergo brittle failure up to 30 MPa (~ 1.2 km of overburden pressure),

due to their high strength related to cementation. The brittle behaviour of these facies is unusual in comparison to carbonates of similar porosities, which are observed to undergo compaction at similar confining pressures (Vajdova et al., 2014). Comparatively, shrub facies, which have higher variability of porosities (7.7 – 38%), are observed to deform in the dilatant-compaction transition resulting in formation of localised compaction bands and shear enhanced compaction bands with a late phase of dilation (i.e. late phase of tensile fracturing and brittle shearing). This style of deformation, however, was variable between samples at different confining pressures (i.e. volumetric strain increase or decrease was not consistently observed across all samples at the same confining pressures) which is interpreted to be caused by smaller variations in shrub types, which were not quantified here.

6.3 What is the impact of deformation within non-marine carbonates on fluid flow in the subsurface?

6.3.1 Small-scale faults within laminated limestones

Evaluation of deformation within laminated limestones of the Crato Formation has contributed new data on the microstructural character and petrophysical properties of fault within mudstone carbonate lithologies (Figure 6-3). Small-scale faults studied within the laminated limestones of the Crato Formation show relatively minor porosity (a few %) and permeability reductions (up to half an order of magnitude) compared to host rocks (Chapter 4) (Figure 6-3). However, the permeability may be more significantly impacted in more mature, high displacement faults, given the tendency to incorporate organic and clay materials even at low throws. Such faults, however, are not captured within this study and the permeability impact at larger displacements therefore remains uncertain.

Within the Crato Formation the host rock depositional fabric is interpreted to be the main control on the hydraulic system evidenced by extensive alteration along preferential laminates. As discussed in Section 6.2.1, faults form dispersed zones of multiple slip surfaces. As well as low throws (<0.2 m), the accommodation of strain across a zone (up to 5cm) of multiple slip surfaces produces several instances of individual laminae sets in self-juxtaposition. Additionally, little to no grain fracturing occurs producing only negligible grain size reductions. These characteristics of deformation mean that the smaller-scale faults within laminated limestones have only minor impacts on permeability compared to undeformed host-rocks.

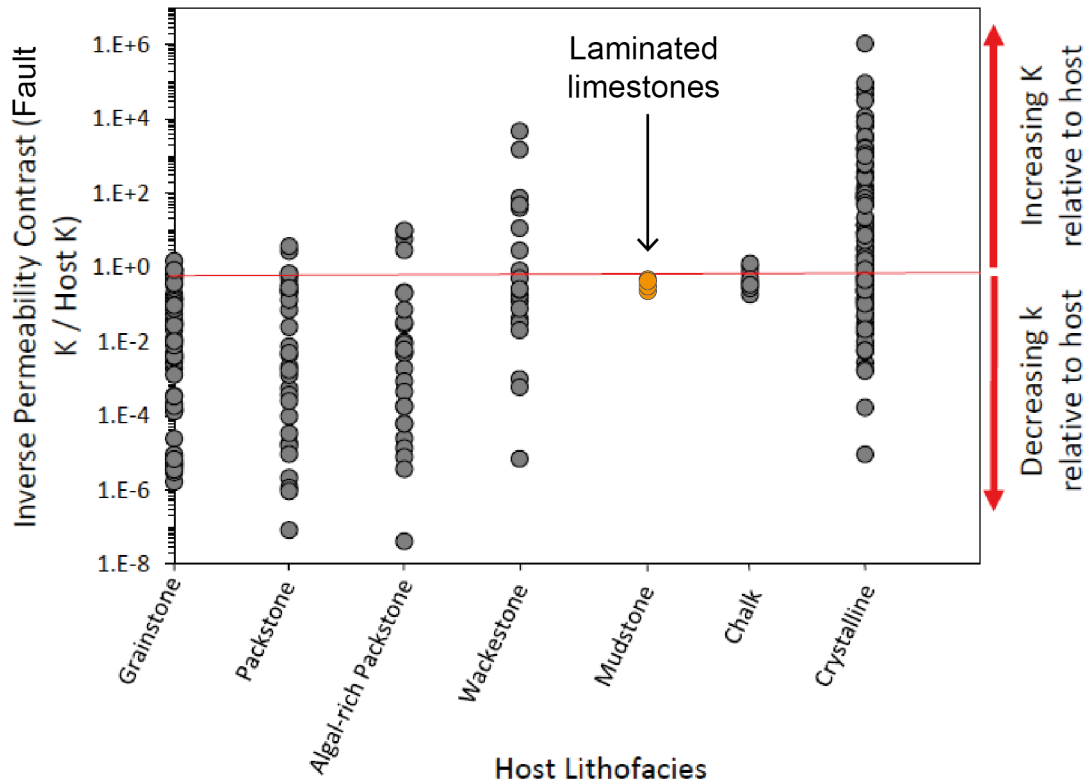


Figure 6-3. Plot of inverse permeability contrast (fault rock permeability divided by host rock permeability) for different carbonate faults from Michie et al. (2020). Measurements from laminated limestones (classified as mudstones using Dunham classification) from the Crato Formation have been added to this global data base and show a permeability reduction. Note that data are from faults < 0.2 m throw and are therefore not representative of larger scale structures.

Additionally, initial brittle shear failure within laminated limestones of the Crato Formation (this study) demonstrates a relatively limited impact on the pervasive alteration fabrics present, suggesting a more complex interaction with fluid-flow within the subsurface. The permeability reduction that is observed is interpreted to be due to the inclusion of abundant, fine-grained, organic material into slip planes. However, due to low throws and variability of organic/clay-rich layers, the incorporation/smearing of organic matter within the failure plane is variable and is not observed to be continuous. It should also be noted that faults have an early post-depositional timing at low stresses, with deformation within the Crato Formation interpreted as ‘seismites’ by Alencar et al. (2021). This places the timing of the deformation within poorly lithified, low-cohesion stratigraphy under low confining pressures. As such, deformation subsequent to cementation (which likely results in an increase of rock strength) remains uncertain within laminated lacustrine limestones and is likely to be characterised by different deformation styles than that observed in this study. Further work to test cemented samples is

needed to map yield curves to understand the control of stresses and cementation on failure modes.

As such the scalability of the petrophysical characterisation of faults within the Crato Formation to larger structures remains uncertain. Additionally, deformation in laminated limestones within the Crato Formation is observed to be relatively evenly distributed throughout the exposure within consistent orientation of conjugate fault sets and should therefore be considered separately to fracture/deformation zones closely associated with faults. The intensity of faulting throughout the formation is therefore unlikely to impact the bulk permeability on a reservoir scale. Small-scale faults formed at low burial depths in laminated limestones observed in this study can be broadly compared to disaggregation bands observed in sandstones, which show limited permeability reduction dependent on clay content (e.g., Fisher & Knipe 2001; Fossen 2010). Similar observations are also found within deformation bands formed within chalk by Kaminskaite et al. (2019), where the matrix within deformation bands shows no evidence of grain fracturing and experience only slightly reduced interparticle microporosity due to compaction.

6.3.2 Dilation vs compaction in travertine

Host rocks within travertines are found to be highly heterogenous with different depositional facies characterised by varying pore types and abundance. Additionally, travertine host rocks display strong permeability anisotropy where permeability across travertine layers is much lower than along individual travertine beds. As such, understanding depositional models is crucial to understand reservoir characteristics and several studies have been conducted to create geobody models for different travertine deposits (e.g., Ballık travertines: Claes et al., 2015; Van Noten et al., 2019; Tivoli travertine: Della Porta et al., 2016; Süttö travertine: Török et al., 2017). Therefore, the petrophysical characterisation of faulting in travertine is likely to reflect primary, depositional, heterogeneity observed within these complex deposits dependant on the stresses at time of deformation.

Dilational faults and fractures, which dominate deformation within shallowly buried travertine is likely to result in substantially increased vertical permeability with open fractures and faults acting as conduits to fluid flow. This is demonstrated by the extensive dissolution and widening of fault cores and formation of fault associated karst systems in the Ballık travertines example. However, karst and fault infill and subsequent diagenesis will control the later permeability characteristics of these features and so the period of enhanced vertical permeability may be

relatively short-lived. Chapter 4 discusses how the infill characteristic may be especially important in controlling the fault zone fluid flow, where dilational structures may evolve from open, very high permeability conduits to lower permeability zones which are commonly filled with matrix supported conglomerates (either sourced from overlying deposits or reworked travertine). Unfortunately, permeability of different types of infill could not be quantified due to the inability to sample these zones, which are commonly formed of friable sediments, and so impacts on fluid subsequent to cementation of these fault zones are purely hypothetical. Fault-parallel calcite veins and vertical precipitates of travertine within these zones, however, can be inferred to provide horizontal baffles to fluid flow, which will create local variations in the permeability anisotropy.

Where dilational deformation occurs in travertines with confining stresses less than < 30 MPa, initial deformation will likely be characterised by fracturing and increased permeability. This is also likely to reduce the permeability anisotropy where fracturing provides vertical fluid pathways. With the development of more mature faults this may result in a permeability decrease, where grain size reduction and pore collapse occurs with progressive brecciation as observed in low porosity, marine carbonates (Molli et al., 2010; Bussolotto et al 2015; Michie, 2015; Haines et al., 2016; Delle Piane et al., 2017; Cooke et al., 2018). Conversely at stresses where compaction becomes the dominant deformation mechanism (the threshold of which is observed to vary between different travertine facies), grain size reduction is common and localised compaction and shear enhanced compaction band formation will likely result in permeability reductions.

6.4 Can host rock characteristics be used to predict the style of deformation and permeability in space and time within non-marine carbonates?

6.4.1 Combined depositional and deformation models for non-marine carbonates

The two different deposits of faulted non-marine carbonates observed in this study display differing degrees of heterogeneity. The laminated limestones studied are formed of laterally continuous, mm-cm scale thin layers with sequences up to 25 m in thickness. Observations in the Crato Formation (Chapter 4) support a general deformation model of dispersed, brittle fault formation during early burial throughout the whole deposit with relatively little impact of

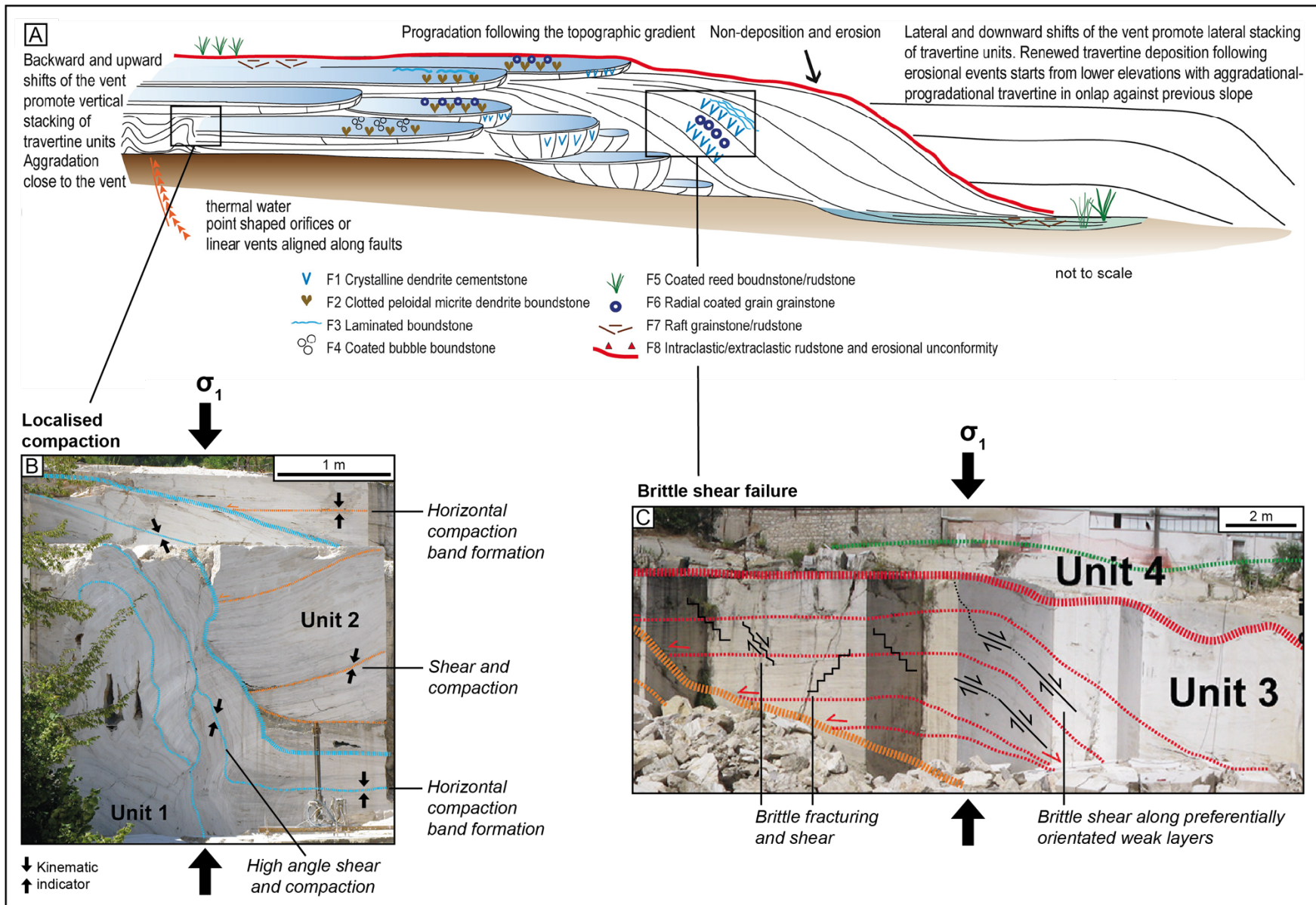
differences in mechanical stratigraphy. The fairly consistent nature of deformation is likely a result of faulting within poorly lithified sediments, with relatively homogenous mechanical properties beyond individual laminae. At the scale of individual laminae, observations suggest that host rock clay and/or organic content provide a strong control on the character of the fault zone, and so it is likely that permeability changes are associated with variable clay contents (e.g. Fisher & Knipe, 2001) may operate at the scale of individual laminae. However, even at the relatively small displacements (< 20 cm) observed, the continuity of clay/organic prone fault gouge is limited (although extremely variable). This variability, and heterogenous fault character, even at low throws, suggests that correlation with host rock characteristics for laminated limestones may be fairly minimal, mirroring recent developments of fault clay-permeability relationships in clastic fault rocks (e.g. Fisher et al., 2018). In laminated limestones, the homogenous variability of depositional facies probably means it is primary and secondary diagenetic changes that likely form a stronger control on the bulk permeability. The predictability of such changes is considerably more difficult than prediction of facies trends and will require reconstruction of stress and strength histories. Observations of along- and cross- fault palaeo fluid flow, which are more strongly bound by distinct stratal levels evidenced by Fe-rich alteration within the laminated carbonates, support this limited impact.

Variations in travertine bodies (both facies and bedding orientation) does not appear to have a dominant control on fault formation at shallow burial depths as similar high angle dilational faults are observed through the whole Ballık travertine sequence. As such, brittle hybrid failure can be predicted to dominate deformation within travertine up to confining pressures of 10MPa (~ 500 m depth). However, interbedded sedimentary layers introduce significant mechanical variations, which is observed to alter the fault dips at low throws (< 3 m). Although dilational faults are not controlled by facies, karst formation is usually associated with relatively high permeability facies when they are associated with faults. Karst systems are also common at palaeosol surface levels where the control on formation is not apparent in this study. Generally, there is a higher probability of karst systems where faults intersect high permeability facies intervals or below palaeosol intervals.

Comparatively, facies variations in travertine deposits are found to have a dominant control on fault geometry and deformation mechanisms when under confining stresses > 10 MPa (> 500 m depth). Mechanically deformed travertine samples analysed in Chapter 5 show that orientation of bedding strongly controls the dip of failure planes/deformation bands while the strength in different facies and principal stresses controls the style of deformation (e.g., Figure 6-2). Deformation is predicted to be brittle within laminated micrite/micro-sparite (common

within slope travertines) and peloidal micrite/microsparite (common in depression travertine deposits) (Capazzouli et al., 2014; Delle Piane et al., 2017). Under the same stress conditions, localised compaction and shear-enhanced compaction bands are compaction is associated with shrub facies, which are common in sub-horizontal layers of pools in terraced slopes and ponds (Capazzouli et al., 2014; Delle Piane et al., 2017). Figure 6-4 illustrates possible local variation in deformation style that may occur at stresses achieved in this study (i.e., ~ 30 MPa, 1.2 km depth) within a slope travertine body modelled from the Acquasanta Terme travertine deposits (Italy) by Della Porta et al. (2016). By applying findings from this study it is predicted that deformation between 0.5 and 1.2 km depth (with high differential stresses up to 160 MPa) within smooth slopes, likely forms through dilational fracturing processes initially localised in high porosity layers, while compaction localisation occurs within shrub facies in terraced slopes. As pools within terrace slopes are not laterally continuous (Capazzouli et al., 2014; Delle Piane et al., 2017), the extent and frequency of localised compaction will be controlled by the size and frequency of the terraces under these stress conditions.

Figure 6-4 (next page). Conceptual model and outcrop photographs from Della Porta et al. (2016) with possible deformation model from mechanical observations with broadly equivalent stresses to 1.2 km burial depth from this study. A) Slope Apron depositional model of the Acquasanta Terme (Italy) travertine slope apron. B) Outcrop from the Cardi Quarry (Acquasanta Terme, Italy) illustrating variation of travertine sequence. Unit 2 is dominated by shrubs, and coated bubble travertines. Kinematic indicators illustrate the preferential orientation for formation of compactive deformation of high porosity layers (adapted from Della Porta et al., 2016). C) Field exposure of smooth slope travertines (composed of laminated micrite/microsparite, crystalline dendrites, and radial coated grain grainstone) with possible brittle deformation styles



A clear correlation was also observed between failure plane and bedding orientation where failure plane dip increases with bedding dip, which is similar to many mechanical studies of other rocks with layered fabrics (Tavallali et al., 2010; Cho et al., 2012; Fjær and Nes, 2014; Gholami and Rasouli, 2014; Zhang et al., 2019). As travertine deposits commonly display a variation of morphologies, bedding orientation can be heterogenous across a range of scales. Figure 6-4 illustrates the orientation of failure planes within a slope travertine body which includes clinoform geometries where horizontal layers are observed to onlap onto dipping sequences. Facies modelling and geobody architecture is therefore interpreted to be essential to predicting the style of deformation and resultant hydraulic system observed within travertines.

6.4.2 Implications for reservoir characterisation in South Atlantic Pre-Salt basins

As mentioned in Section 6.1, Early Cretaceous lacustrine deposits form important reservoir intervals of the giant pre-salt oilfields in the Santos and Campos Basins, offshore Brazil. The discovery of pre-salt reservoirs (mostly within coquinas and microbialites) in offshore Brazil resulted in a renewed focus on understanding exhumed lacustrine, microbialite carbonates along with increased exploration for similar basins (such as on the conjugate rifted margin of West Africa, e.g. Toca Formation, Kwanza Basin, offshore Angola, Saller et al., 2016). As a result, the understanding of processes (Dupraz et al., 2009; Capezzouli et al., 2014; Catto et al., 2016), depositional conditions (Bahniuk et al., 2015; Buckley et al., 2015; Gallois & Bosence, 2019) and facies characterisation (Heimhofer et al., 2010; Rezende et al., 2013; Della Porta, 2015; Muniz & Bosence, 2015; Gomes et al., 2020; Basso et al., 2022) of microbial carbonates has improved in recent years. However, decoding microbial influences on deposition and diagenetic processes as well as establishing consistent facies models remains debated within literature. Within the past 5 years, a number of outcrops were established as possible analogue models, including the Aptian Crato Formation (NE Brazil) and travertine bodies across Europe which were considered to show similar carbonate textures (Heimhofer et al., 2010; Della Porta, 2015; Claes et al., 2015, 2017; Giwelli et al., 2016a, b; Miranda et al., 2018). However, with recent availability of data from pre-salt reservoirs (from both offshore Brazil and along the West African Margin) the suitability of travertines as an analogue has been brought into question. It is now recognised that the Barra Velha Formation within the Santos Basin lacustrine pre-salt stratigraphy is characterised by calcite shrubs and spherulites (Basso et al., 2022) and reworked facies such as intraclastic grainstones and laminated

mudstones (Gomes et al., 2020; Basso et al., 2022; He et al., 2022). Although shrub facies observed in pre-salt reservoir units may not be defined as travertines, it may be that travertines form more localised deposits within the larger lacustrine depositional environment within pre-salt reservoirs (Wright & Barnett, 2015). Ultimately, the origin and control on morphology of lacustrine carbonate facies is observed to vary widely. The similarities and complexities that exist within such varied facies associated with lacustrine carbonates highlights the importance of facies modelling and the need for lacustrine depositional models. Although travertine facies may not represent key reservoir intervals within pre-salt reservoirs, they are still observed to form reservoir scale deposits, such as the Tivoli travertine which covers an area of $\sim 8 \text{ km}^2$ with up to 70 m thickness (Faccenna et al., 2008; Della Porta et al., 2017).

6.4.3 Crato Formation as a pre-salt reservoir analogue

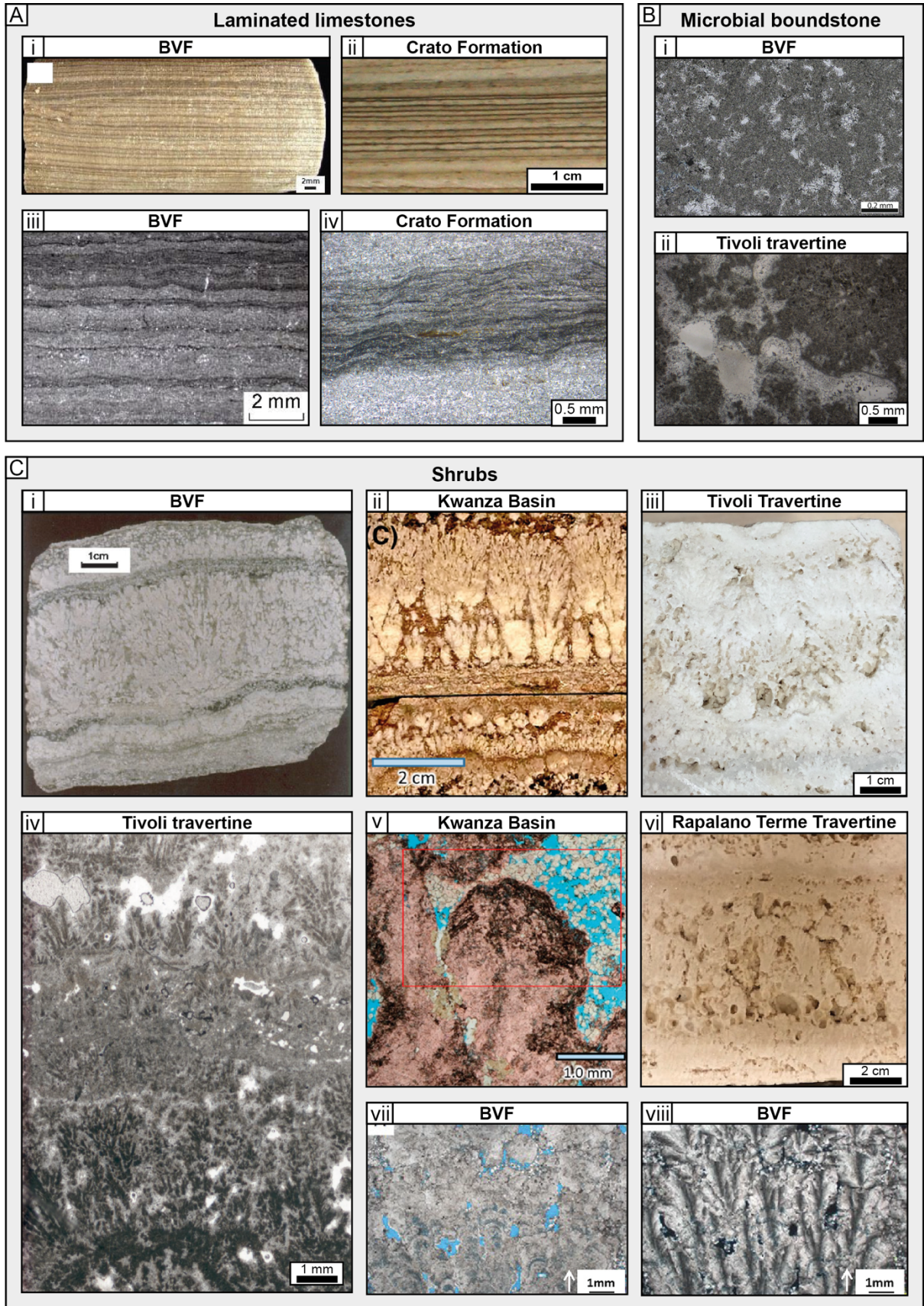
The laminated Crato Formation is stratigraphically equivalent to the Barra Velha Formation (BVF) in the Santos Basin (NE Brazil) and can display similar textures and mineralogy (Terra et al., 2010; Miranda et al., 2018; He et al., 2022). Figure 6-5a illustrates the similarities between laminated limestones from the Barra Velha Formation and samples collected from the Crato Formation (Chapter 3). Laminates within the BVF display planar-to-wavy laminations of mm to cm thickness formed of calcite and secondary dolomite, which is thought to replace authigenic magnesium silicates (Lima & De Ros, 2019). Observations in this study suggest that small-scale faults formed during thermal subsidence soon in laminated limestones are unlikely to affect the bulk permeability (Section 6.3.1). However, laminated deposits found in pre-salt stratigraphy can also have much higher organic and clay rich layers with interbedded clays intervals (Claes et al., 2021; Basso et al., 2022). As a result, the potential of permeability reductions is higher in clay-rich laminate sequences due to incorporation of clay into fault gouge.

6.4.4 Travertines as a pre-salt reservoir analogue

Micritic boundstones observed by Pietzsch et al. (2020) show similar clotted microfabric to the peloidal micrite/microsparite facies observed in this study (Figure 6-5b). However, micritic boundstones from the BVF are extensively dolomitised and locally silicified (Pietzsch et al., 2020). This illustrates that observations from this study may only apply to early deformation of travertines before pervasive diagenesis as changes in porosity and mineralogy are likely to influence the mechanical characterisation of the rock.

Shrub dominated facies are considered to form the best sag-phase reservoir within pre-salt reservoirs due to their high porosity and moderate permeability (Basso et al., 2022). Shrubs facies from the BVF analysed by Basso et al. (2021) and Campos Basin shrubs by Herlinger et al. (2017) have a wide range of poroperm values. In particular, porosity varies between 0.2 and 17.44% whereas permeability varies between <0.001 and 25 mD (BVF) or 295 mD (Campos Basin) (Figure 6-6). Poroperm data from travertine shrub facies (Rapolano Terme, Italy; Tivoli, Italy and Ballik travertines, Turkey) also show variability in poroperm data but are observed to host substantially higher porosities and permeabilities (dependent on bedding direction) with porosities ranging between 3.42 and 50% and permeabilities ranging between 0.02 and > 1000 mD (Figure 6-6). The differences of poroperm between the different shrub formations may be due to differences in the extent of diagenesis experienced.

Figure 6-5 (next page) Comparison of non-marine reservoir carbonate examples with similar facies of carbonates studied within this project. A) Laminates limestones. Ai) Planar laminates from the Barra Velha Formation (BVF) (Santas Basin, SE Brazil) (from Terra et al., 2010). Aii) Laminated limestone from the Crato Formation (Araripe Basin, NE Brazil). Aiii) Photomicrograph of laminated limestone from BVF (from He et al., 2022). Aiv) Photomicrograph of laminated limestone from the Crato formation displaying similar slightly dentate laminations. B) Microbial boundstones: Bi) Microbial boundstone from the BVF with microbial peloids (from Pietzsch et al., 2020). Bii) Photomicrograph of clotted dense micrite from Tivoli Travertine body (Italy) illustrating similar micritic texture. C) Shrubs: Ci) Hand specimen of shrub textures found within the BVF (after Wright & Tosca, 2016). Cii) Shrub textures observed in pre-salt lacustrine carbonates within the Kwanza Basin (after Saller et al., 2016). Ciii) Example of typical travertine shrub facies from Tivoli travertine body (Italy). Civ) Photomicrograph of dendritic shrub growth within travertines (Tivoli, Italy). Cv) Photomicrograph of shrubby calcite growth with microcrystalline bands and dolomite between growths (after Saller et al., 2016). Vi) hand specimen of shrub interval layer in travertine from Rapolana Terme (Italy). Vii) and Viii) Photomicrographs of crystal shrub growth from BVF (after Hosa et al., 2020). Shrubs within the BFV are characterised by fibrous calcitic crystal aggregates.



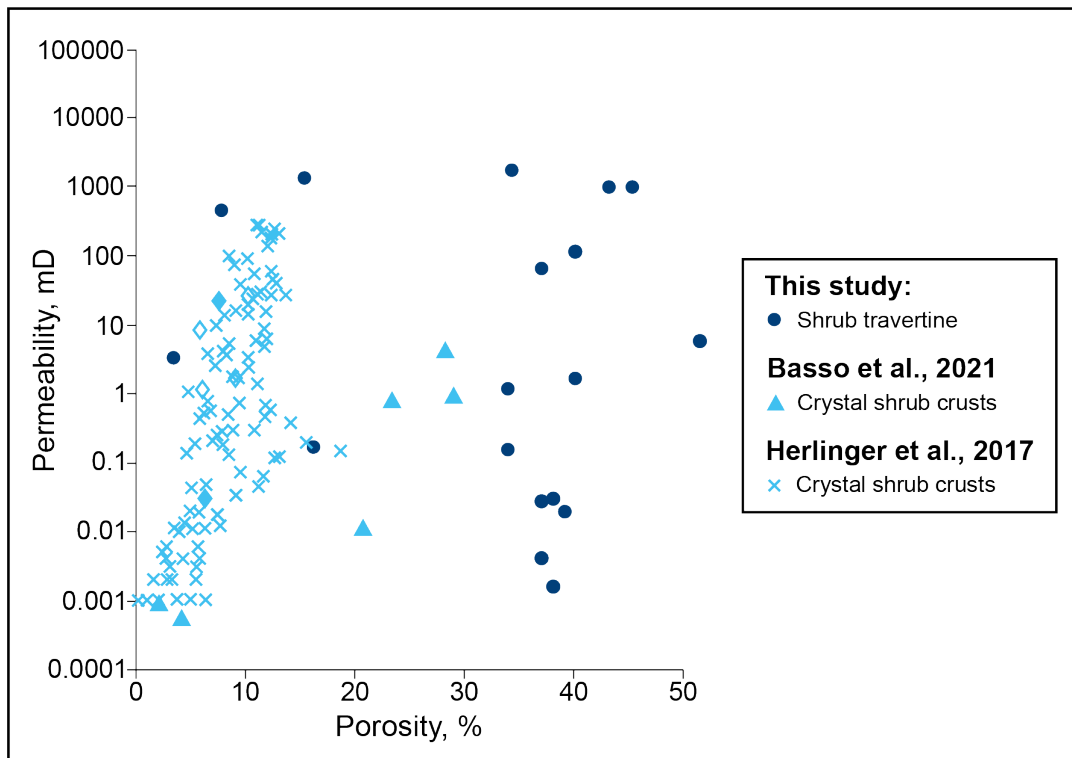


Figure 6-6. Poroperm plot comparing shrub facies within travertines (this study) and pre-salt shrub facies from the Campos and Santos basins (Herlinger et al., 2017; Basso et al., 2021).

Although macrostructure of shrub facies within travertines and shrub-like facies from pre-salt microbialites appear similar (Figure 6-5c), their microstructures are markedly different. A comparison of the major pore network associated with shrubs in travertines and pre-salt reservoirs is illustrated in Figure 6-7. Shrub textures in the BVF are characterised by radial fibrous calcite (Figure 6-5c), which form layers of bifurcating shrubs, commonly interpreted to form as a result of an abiotic depositional process (Herlinger et al., 2017; Hosa et al., 2020; Basso et al., 2021). Conversely, shrubs in travertines are microbially mediated and formed of irregular dendritic micrite and sparite cements (Figure 6-5cv/vii/viii). Microstructural analysis of shrubs found in pre-salt lacustrine carbonates in the Kwanza basin have, however, complex textures of fibrous-to-prismatic calcite crystals with micritisation at terminations of fibrous growth (Figure 6-5v), suggesting alteration and local erosion by microbes (Saller et al., 2016). Porosity within crystalline shrubs is predominantly denominated by growth framework pores within crustal shrubs (Figure 6-5cvii-cviii) (Hosa et al., 2020; Basso et al., 2021). Figure 6-7 compares macro-pore networks within shrub facies between travertines within the BVF. A segmented pore volume of a shrub interval presented by Basso et al. (2021) illustrates the typical macro pore network within crystal shrubs, which are found to form high porosity peaks in high growth framework porosity shrubby framestones (Figure 6-7a). Comparatively,

microporosity modelled from low resolution CT scans of the Tivoli Travertines (Chapter 5) show similar high porosity intervals within shrubs. The pore framework within travertine shrubs, however, appear to be more interconnected with comparatively large (up to 2 cm) pore spaces formed between individual shrubs. Both pore networks (this study, and Basso et al., 2021) derived from CT scans probably underestimate the total porosity where micro-porosity cannot be imaged. Additionally, deposits within the BVF are found to be significantly affected by diagenesis during deeper burial (Herlinger et al., 2017; Barro et al., 2021).

Diagenesis plays a key role in the present-day characterisation of pre-salt reservoir facies and controls the porosity and permeability (Hosa et al., 2020). Dolomite is found to be the main diagenetic product within sag deposits in the Kwanza basin, which probably precipitated during very shallow burial (Saller et al., 2016). Dissolution of stevensite (Mg-rich clay) is common within the Campos Basin, resulting in the replacement of shrubs with silica and dolomite cement filling growth-framework porosity (Herlinger et al., 2017; Basso et al., 2021). As such, not only is the petrophysical characterisation substantially affected by diagenesis in pre-salt reservoirs (Herlinger et al., 2017; Basso et al., 2021; Lupinacci et al., 2022), but the mechanical properties are likely to be affected due to a change in the mineralogy and porosity resulting from differences in the amount of dolomite and silica present (Lupinacci et al., 2022). Extensive silicification of carbonates may result in a more brittle rock mass compared to the original calcite dominated mineralogy (Sartorato et al., 2020; Wennberg et al., 2021; Lupinacci et al., 2022). Mechanical property results from travertines analysed in this study may therefore not be applicable to sequences that are dominated by silica-prone diagenesis.

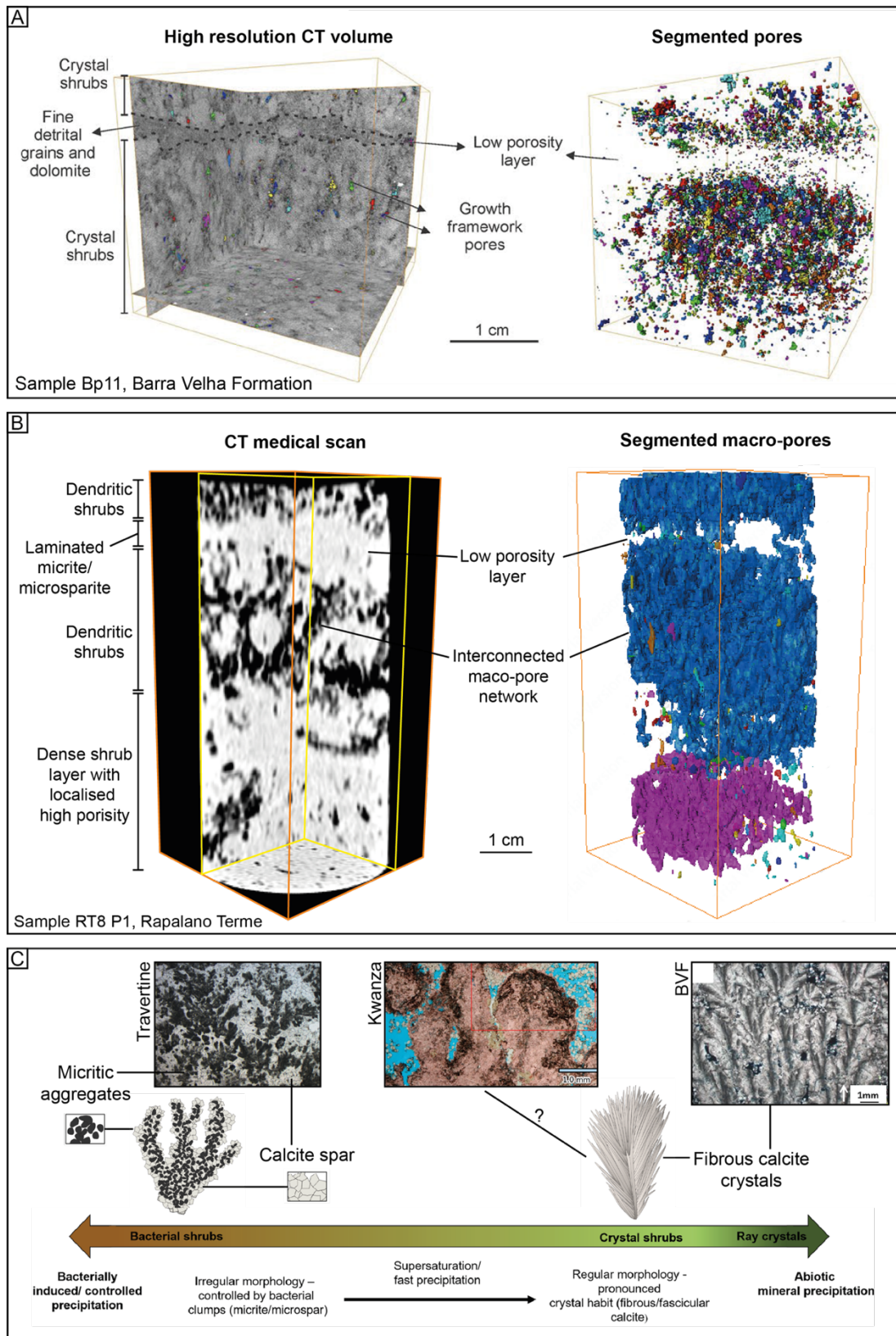


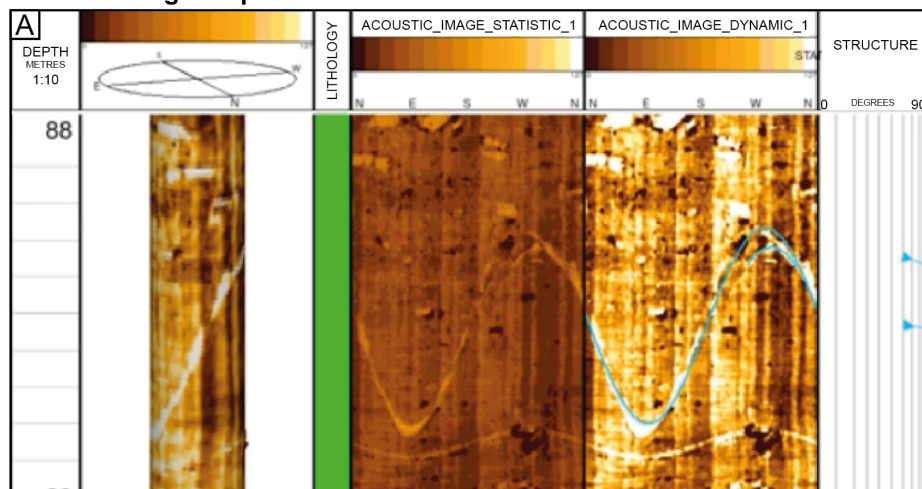
Figure 6-7 Comparison of porosity networks between crystal shrubs from the Barra Velha Formation (Santos Basin, offshore Brazil) and micritic shrubs in travertine (Rapalano Terme, Italy). A) CT volume of crystal shrubs from BVF with segmented pore model illustrating growth framework pores separated by low porosity layers. B) Low resolution CT scan images from shrub travertine facies with modelled macro pore network. High inter-dendrite porosity form large connected networks separated by low-porosity layers. C) model adapted from Basso et al. (2021) illustrating different in shrub morphologies between travertines and those found within pre-salt reservoirs.

6.4.5 Faults within sag stage sequences

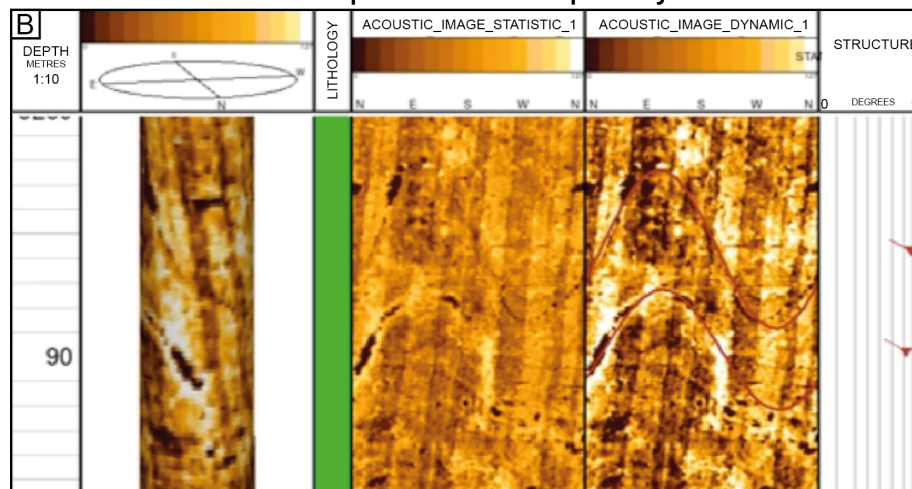
Pre-salt non-marine carbonate reservoirs are associated with deposition during an early post-rift stage (subsequent to passive margin basin formation during the breakup of Gondwana) during thermal subsidence (Basso et al., 2022). As a result, faulting within the post-rift sequence is found to be less intense than within the underlying rift strata (Basso et al., 2022). Although sag-basin fill is associated with a period of tectonic quiescence, fault and fracture zones have been observed within the BVF (Wennberg et al., 2021; Basso et al., 2022; Lupinacci et al., 2022). Fractures are strongly associated with dissolution zones (which can be up to 7 m in height) and strongly silicified intervals (Sartorato et al., 2020; Wennberg et al., 2021). Acoustic borehole image logs, presented by Wennberg et al. (2021), illustrate the variety of structure observed in the Barra Velha Formation (Figure 6-8), which can be partially or fully filled. Wennberg et al. (2021) note that fractures with high amplitude signals in acoustic borehole images may either be veins or could possibly be deformation bands, both of which provide baffles to flow. Open fractures (vuggy fractures – Figure 6-8b) are commonly observed within pre-salt strata and provide open pathways for fluid flow. Fractures are also associated with karst intervals and form complex fracture patterns within brecciated units above karsts. The application of karst observations from this study may therefore aid the understanding of which deposits are more likely to host karst features and could therefore aid prediction of fracture modelling and permeability heterogeneity.

Both high and low amplitude expressions of faults are observed within borehole images from the BVG (Figure 6-8c/d) suggesting that the properties of fault zones and fault development differ within the same deposit. Fault damage zones are also presented by Wennberg et al. (2021) that show dispersed deformation with high intensity fracturing with multiple slip surfaces which this study predicts for brittle deformation within micritic laminated and peloidal travertines. The variation in style of faulting is likely a reflection of the heterogeneities observed within such lacustrine basins, which have quantifications on dimensions and spatial scales from non-marine carbonates within this study, which display equally complex lacustrine carbonate deposits.

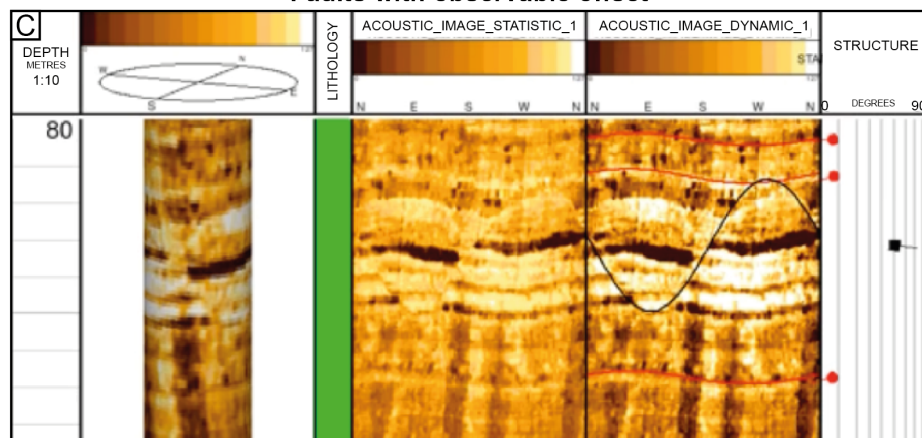
High amplitude fractures: deformation bands or veins



Variable amplitude fractures: partially filled



Faults with observable offset



Faults with throw > observed section

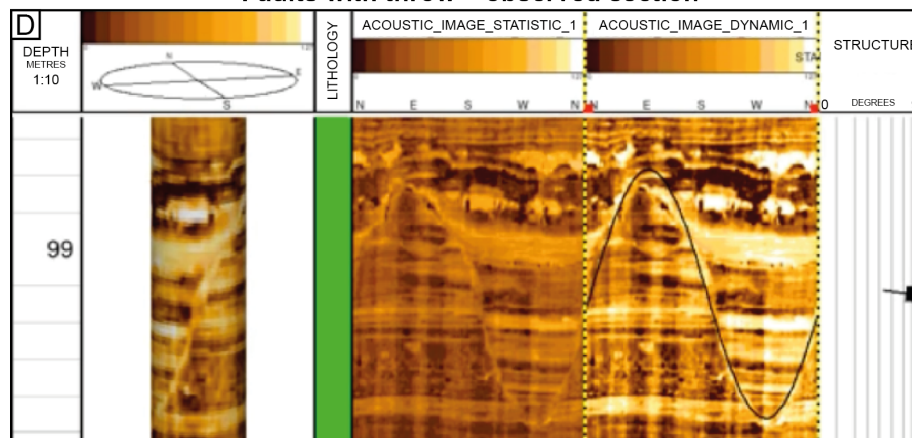


Figure 6-8. Fracture examples in static and dynamic normalised acoustic borehole image logs from Berra Velha Formation (pre-salt lacustrine carbonates in the Santos Basin, SE Brazil) (after Wennberg et al., 2021). A) High amplitude (bright) fracture which could be deformation bands or veins. B) Low amplitude vuggy fractures. C) Minor fault with observed offset. D) Fault with un-known offset.

Chapter 7

7. Conclusions and Further Work

7.1 Aims and objective

The research presented in this thesis aims to provide a greater understanding of the key controls on fault formation within non-marine carbonates to assess the implications of faulting within different lacustrine carbonate facies on fluid flow in the sub surface. Three key objectives were outlined based on significant knowledge gaps that exist within this research field:

1. Conduct a detailed field investigation of faulting within non-marine carbonates to characterise deformation styles within different lacustrine carbonate lithology types (Chapter 4).
2. Investigate the control of host rock heterogeneity on deformation mechanisms of non-marine carbonates through integration of field observations (Chapter 4) and mechanical data (Chapter 5).
3. Determine the control of non-marine carbonate fault rocks on permeability (Chapter 5) and discuss the implications of fault heterogeneity on bulk permeability on a reservoir scale (Chapter 6).

7.2 Key findings

7.2.1 Structural characteristics of faults within non-marine carbonates

An initial literature and field investigation in this study illustrates not only the heterogenous nature of non-marine carbonates, in which many different lithology types are observed (e.g. travertines, stromatolites, microbial mounds, tufas, laminated limestones), but also highlights the scarcity of outcrops of these rock types containing faults. Although field observations were limited due to the under-representation of ancient non-marine carbonates due to poor preservation, observations shows that shallow deformation can vary greatly within different non-marine carbonate deposits. At burial depths < 200 m, faulting within the Ballik travertine

body (Turkey) is observed to be characterised by localised dilational normal faults with complex infill. On the other hand, laminated limestones of the Crato Formation (Brazil) accommodate deformation through formation of small-scale normal faults, which form ~ 5cm width fault zones hosting distributed deformation across multiple slip surfaces. Differences in faulting style are a reflection of tectonic regime (transtensional tectonics in Ballik travertines, thermal subsidence in Crato Formation) and lithology (mechanically strong travertine vs poorly consolidated laminated limestones).

At burial depths > 300 m travertine facies are found to have a greater control on the deformation mechanism where brittle deformation (dominated by microcracking) is observed within moderate porosity laminated micrite/microsparite (average porosity: 10.8%) and peloidal micrite/microsparite (average porosity: 7.5%) while a combination of localised shear compaction (dominated by grain crushing and mechanical twinning) and dilation occurs within high porosity shrub facies (average porosity: 19.4%). Based on mechanical testing and microstructural observations, it is concluded that heterogeneity of fault zones within travertines will reflect the heterogeneity of travertine morphology.

7.2.2 Impact of deformation in non-marine carbonate on permeability

While early deformation at shallow depths (< 200 m) within travertine results in increased flow path connectivity with creation of fluid conduits formed by dilational faulting and karst formation, small scale faults in laminated limestones are concluded to have an insignificant effect on the bulk permeability of the formation and are considered to be comparative to disaggregation bands observed within clastic formations.

At burial depth's > 0.2 and < 1.5 km permeability within travertines is concluded to be dominated by initial brittle deformation in laminated micrite/microsparite and peloidal micrite/microsparite which will likely result in permeability enhanced zones. It is hypothesised that permeability reductions may be observed in mature fault zones within these facies deformed at these stresses due to grain reduction from progressive microcracking and brecciation processes. Conversely, at these stresses shrub travertine facies are observed to deform by compactional processes resulting in localised bands defined by reductions in grain size and porosity which are likely to act as a baffle to fluid flow. However, this relationship is poorly constrained and requires quantitative analysis of permeability changes due to deformation. It is predicted that at pressures > 30 MPa laminated micrite/microsparite and peloidal micrite/microsparite will fail with compactive processes. Therefore, at high stresses,

travertine may have the potential to reduce the bulk permeability as a result of compactive deformation.

7.2.3 Using host rock characteristics to predict deformation style and permeability within non-marine carbonates

Small-scale faulting, similar to that observed within laminated limestones of the Crato Formation, are predicted to be a common feature within similar deposits formed during post-rift thermal subsidence such as the laminated limestones within the Barra Velha Formation, Brazil. Deformation is observed to show limited heterogeneity throughout the sequence where faults exhibit similar orientation, length, throw and fault zone width across the observed outcrops. Similar styles of faulting are therefore predicted to occur throughout the entire sequence depending on extent of cementation and the rates and variation of thermal subsidence.

Comparatively, faulting within travertine sequences is predicted to be dependent on the effective stresses and mechanical heterogeneity observed within different facies and orientations. Faulting at near-surface depths (< 200 m) is predicted to be largely dilational with the formation of dilational faults and fractures as well as pervasive karst systems. At moderate stress (MPa between 10 and 30 MPa), deformation is found to be dependent on facies and can result in the formation of both compactional and brittle structures within different facies within the same sequence. Failure plane dip is found to be controlled by bedding angle dip in relation to the principal stress direction, where the angle of the failure plane increases with increasing dip. This is predicted to result in stepping fractures (which are commonly observed in layered travertines) horizontal travertine stratigraphy. As travertine bodies are commonly associated with complex bedding geometries, such as mounds, fissure ridges, terraced/smooth slopes and depressional (Chafetz & Folk, 1984; Ford & Pedley 1996; Pentecost, 2005), it is predicted that fault orientation and travertine facies will have a strong control the geometry and style of faulting at depths > 200 m. As such, it is concluded that geobody modelling of travertine is essential to predict local variations in permeability anisotropy which may be important within reservoir production.

7.3 Future work

This study aimed to characterise faulting in non-marine carbonate rocks and assess the impact deformation in these rocks may have on fluid flow in the subsurface. Although outcomes from

the research conducted in this study has contributed towards understanding the main controls of faulting in non-marine carbonates, limited exposure of faults and limitations of time and scope of work means there is still some way to go to modelling faults in these rocks. The following outlines work recommended to provide further insights into this frontier research subject.

The observations from this work alongside existing research of carbonate fault rocks (e.g., Michie, 2015; Solum & Huisman, 2017; Delle Piane et al., 2017; Cooke et al., 2018; Michie et al., 2020) illustrate the complexity of deformation, which is dependent on a number of controls. Work needs to be carried out to increase the diversity of non-marine carbonates included in carbonate fault rock databases (e.g., Solum & Huisman, 2017). This can be accomplished by structurally investigating additional lacustrine carbonates not assessed in this study (for example China: Qiu et al., 2021; Japan: Shiraishi et al., 2022; Iran: Mohajjel & Taghipour, 2014; Mohammadi et al., 2019; New Mexico: Ricketts et al., 2014 among others) and by also including a more diverse range of facies and non-marine carbonate types (e.g. stromatolite/thrombolites) in mechanical analysis. Additionally, the formations observed and used for samples in mechanical testing have undergone little to no burial. As such the diagenetic character of these sequences differs substantially to similar rock types in the subsurface (i.e., in pre-salt reservoirs). With the increasing availability of data from Brazilian Pre-salt reservoirs as secrecy regarding these deposits becomes less of an issue, it would be advantageous to carry out a mechanical characterisation on pre-salt reservoir rocks for comparison with analogue studies to understand the role of diagenesis on deformation.

Additionally, CT scan imaging of collected samples provided useful insights into the macropore network within travertines. However, this was limited by the resolution of CT scanning and would benefit from μ CT scan imaging from which higher resolution pore volumes can be extracted. This will provide greater accuracy of pore size, shape and connectivity within non-marine carbonates and provide improved imaging of deformation post-mechanical testing.

Mechanical testing provides insights into the style of deformation characteristic in travertines at varying confining pressures. However, full yield curves were unable to be determined for samples tested. Triaxial tests conducted at higher confining pressures (> 30 MPa) and measurement of apparent pre-consolidation pressure, P^* , (stress required for yield under hydrostatic stress) will provide needed data to construct larger correlation of failure curves and perhaps quantify the brittle-ductile transition with more accuracy. Additionally, due to low sample preservation, permeability was not able to be measured in samples after undergoing

failure in triaxial testing, which limits the understanding that deformation has on fluid flow. As such, key findings from this study will also benefit from both numerical and physical modelling calibrated to mechanical data from thesis to aid prediction of deformation and model fluid flow.

References

- Agosta, F. and Aydin, A. 2006. Architecture and deformation mechanism of a basin-bounding normal fault in Mesozoic platform carbonates, central Italy. *Journal of Structural Geology*. **28**(8), pp.1445–1467.
- Agosta, F., Prasad, M. and Aydin, A. 2007. Physical properties of carbonate fault rocks, fucino basin (Central Italy): Implications for fault seal in platform carbonates. *Geofluids*. **7**(1), pp.19–32.
- Alçıçek, H., Varol, B. and Özkul, M. 2007. Sedimentary facies, depositional environments and palaeogeographic evolution of the Neogene Denizli Basin, SW Anatolia, Turkey. *Sedimentary Geology*. **202**(4), pp.596–637.
- Alçıçek, H. and Jiménez-Moreno, G. 2013. Late Miocene to Plio-Pleistocene fluvio-lacustrine system in the Karacasu Basin (SW Anatolia, Turkey): Depositional, paleogeographic and paleoclimatic implications. *Sedimentary Geology*. **291**, pp.62–83.
- Alçıçek, H., Bülbül, A. and Alçıçek, M.C. 2016. Hydrogeochemistry of the thermal waters from the Yenice Geothermal Field (Denizli Basin, Southwestern Anatolia, Turkey). *Journal of Volcanology and Geothermal Research*. **309**, pp.118–138.
- Aldinucci, M., Ghinassi, M. and Sandrelli, F. 2007. Climatic and Tectonic Signature in the Fluvial Infill of a Late Pliocene Valley (Siena Basin, Northern Apennines, Italy). *Journal of Sedimentary Research*. **77**(May 2014), pp.398–414.
- Alencar, M.L., Correia Filho, O.J., Miranda, T.S. de, Barbosa, J.A., Celestino, M.A.L., Ramos, G.M.S., Araújo, A.F.L. de, Neumann, V.H., Topan, J.G. de O. and Roemers-Oliveira, E. 2021. Soft-sediment deformation structures in Aptian lacustrine laminites: Evidence of post-rift paleoseismicity in the Araripe basin, NE Brazil. *Journal of South American Earth Sciences*. **105**, p.102955.
- Altunel, E. and Hancock, P.L. 1993. Morphology and structural setting of Quaternary travertines at Pamukkale, Turkey. *Geological Journal*. **28**(3–4), pp.335–346.
- Altunel, E. and Karabacak, V. 2005. Determination of horizontal extension from fissure-ridge travertines: a case study from the Denizli Basin, southwestern Turkey. *Geodinamica Acta*. **18**(3–4), pp.333–342.
- Anderson, E.M. (1951) The dynamics of faulting and dike formation with application to Britain. Oliver and Boyd, 2nd Edition, Edinburgh, 133147.
- Angelier, J., Bergerat, F., Dauteuil, O. and Villemin, T. 1997. Effective tension-shear relationships in extensional fissure swarms, axial rift zone of northeastern Iceland. *Journal of Structural Geology*. **19**(5), pp.673–685.
- Anselmetti, F.S. and Eberli, G.P. 1993. Controls on sonic velocity in carbonates. *Pure and Applied Geophysics PAGEOPH*. **141**, pp.287–323.
- Antonellini, M., Petracchini, L., Billi, A. and Scrocca, D. 2014. First reported occurrence of deformation bands in a platform limestone, the Jurassic Calcare Massiccio Fm., northern Apennines, Italy. *Tectonophysics*. **628**, pp.85–104.
- Antonellini, M., Petracchini, L., Billi, A. and Scrocca, D. 2014. First reported occurrence of deformation bands in a platform limestone, the Jurassic Calcare Massiccio Fm., northern Apennines, Italy. *Tectonophysics*. **628**, pp.85–104.

- Anzalone, E., Ferreri, V., Sprovieri, M. and D'Argenio, B. 2007. Travertines as hydrologic archives: The case of the Pontecagnano deposits (southern Italy). *Advances in Water Resources*. **30**(10), pp.2159–2175.
- API 1998. Recommended Practices for Core Analysis RB 40. Second Edition. *American Petroleum Institute*. Washington, D.C., USA.
- Araujo, A.F.L., Ramos, G.M.S., Barbosa, J.A., Correia Filho, O.J., Alencar, M.L., De Miranda, T.S., Neumann, V.H., Celestino, A.M. and Topan, J.G. 2020. Depositional and diagenetics controls on the mechanical stratigraphy of aptian laminated limestones of crato formation. *Rio Oil and Gas Expo and Conference*. **20**(2020), pp.35–36.
- Armenteros, I. 2010. Chapter 2 Diagenesis of Carbonates in Continental Settings *In*: A. M. Alonso-Zarza and L. H. Tanner, eds. *Carbonates in Continental Settings: Geochemistry, Diagenesis and Applications*. Developments in Sedimentology. Elsevier, pp.61–151.
- Ashby, M.F. and Sammis, C.G. 1990. The damage mechanics of brittle solids in compression. *Pure and Applied Geophysics*. **133**, p.33.
- Ayling, M.R., Meredith, P.G. and Murrell, S.A.F. n.d. Microcracking during triaxial deformation of porous rocks monitored by changes in rock physical properties, I. Elastic-wave propagation measurements on dry rocks. *Tectonophysics*. **245**(3–4), pp.223–235.
- Baechle, G.T., Colpaert, A., Eberli, G.P. and Weger, R.J. 2008. Effects of microporosity on sonic velocity in carbonate rocks. *The Leading Edge*. **27**(8), pp.1012–1018.
- Bahniuk, A.M., Anjos, S., França, A.B., Matsuda, N., Eiler, J., Mckenzie, J.A. and Vasconcelos, C. 2015. Development of microbial carbonates in the lower cretaceous codó formation (north-east Brazil): Implications for interpretation of microbialite facies associations and palaeoenvironmental conditions. *Sedimentology*. **62**(1), pp.155–181.
- Balsamo, F., Clemenzi, L., Storti, F., Solum, J. and Taberner, C. 2019. Tectonic control on vein attributes and deformation intensity in fault damage zones affecting Natih platform carbonates, Jabal Qusaybah, North Oman. *Journal of Structural Geology*. **122**, pp.38–57.
- Basso, M., Belila, A.M.P., Chinelatto, G.F., Souza, J.P. da P. and Vidal, A.C. 2021. Sedimentology and petrophysical analysis of pre-salt lacustrine carbonate reservoir from the Santos Basin, southeast Brazil. *International Journal of Earth Sciences*. **110**(7), pp.2573–2595.
- Basso, M., Souza, J.P.P., Honório, B.C.Z., Melani, L.H., Chinelatto, G.F., Belila, A.M.P. and Vidal, A.C. 2022. Acoustic image log facies and well log petrophysical evaluation of the Barra Velha Formation carbonate reservoir from the Santos Basin, offshore Brazil. *Carbonates and Evaporites*. **37**(3), p.50.
- Bastesen, E., Braathen, A., Nøttveit, H., Gabrielsen, R.H. and Skar, T. 2009. Extensional fault cores in micritic carbonate - Case studies from the Gulf of Corinth, Greece. *Journal of Structural Geology*. **31**(4), pp.403–420.
- Baud, P., Schubnel, A. and Wong, T. 2000. Dilatancy, compaction, and failure mode in Solnhofen limestone. *Journal of Geophysical Research: Solid Earth*. **105**(B8), pp.19289–19303.
- Baud, P., Vinciguerra, S., David, C., Cavallo, A., Walker, E. and Reuschlé, T. 2009. Compaction and Failure in High Porosity Carbonates: Mechanical Data and Microstructural Observations. *Pure and Applied Geophysics*. **166**(5–7), pp.869–898.
- Baud, P., Exner, U., Lommatzsch, M., Reuschlé, T. and Wong, T. 2017a. Mechanical behavior, failure mode, and transport properties in a porous carbonate: Mechanical Behavior of Porous Limestone. *Journal of Geophysical Research: Solid Earth*. **122**(9), pp.7363–7387.

- Baud, P., Schubnel, A., Heap, M. and Rolland, A. 2017b. Inelastic Compaction in High-Porosity Limestone Monitored Using Acoustic Emissions: Compaction in Limestone Monitored by AE. *Journal of Geophysical Research: Solid Earth*. **122**(12), pp.9989–10,008.
- Bauer, H., Schröckenfuchs, T.C. and Decker, K. 2016. Hydrogeological properties of fault zones in a karstified carbonate aquifer (Northern Calcareous Alps, Austria). *Hydrogeology Journal*. **24**(5), pp.1147–1170.
- Bedford, J.D., Faulkner, D.R., Leclère, H. and Wheeler, J. 2018. High-Resolution Mapping of Yield Curve Shape and Evolution for Porous Rock: The Effect of Inelastic Compaction on Porous Bassanite. *Journal of Geophysical Research: Solid Earth*. **123**(2), pp.1217–1234.
- Berner, R.A., 1980. *Early diagenesis: a theoretical approach* (No. 1). Princeton University Press.
- Billi, A. 2010. Microtectonics of low-P low-T carbonate fault rocks. *Journal of Structural Geology*. **32**(9), pp.1392–1402.
- Billi, A., Salvini, F. and Storti, F. 2003. The damage zone-fault core transition in carbonate rocks: Implications for fault growth, structure and permeability. *Journal of Structural Geology*. **25**(11), pp.1779–1794.
- Billi, A. and Tiberti, M.M. 2009. Possible causes of arc development in the Apennines, central Italy. *Geological Society of America Bulletin*. **121**(9–10), pp.1409–1420.
- Billi, A., De Filippis, L., Poncia, P.P., Sella, P. and Faccenna, C. 2016. Hidden sinkholes and karst cavities in the travertine plateau of a highly-populated geothermal seismic territory (Tivoli, central Italy). *Geomorphology*. **255**(December), pp.63–80.
- Bohacs, K.M., Lamb-Wozniak, K., Demko, T.M., Eleson, J., McLaughlin, O., Lash, C., Cleveland, D.M. and Kaczmarek, S. 2013. Vertical and lateral distribution of lacustrine carbonate lithofacies at the parasequence scale in the Miocene Hot Spring limestone, Idaho: An analog addressing reservoir presence and quality. *AAPG Bulletin*. **97**(11), pp.1967–1995.
- Bonson, C.G., Childs, C., Walsh, J.J., Schöpfer, M.P.J. and Carboni, V. 2007. Geometric and kinematic controls on the internal structure of a large normal fault in massive limestones: The Maghlaq Fault, Malta. *Journal of Structural Geology*. **29**(2), pp.336–354.
- Borghesi, L., Da Silva, M.C.A.S., Favoreto, J. and Santos, J. 2022. Defining a new common language: a multi-scale descriptive classification for the pre-salt carbonates of the Barra Velha Formation. *Rio Oil and Gas Expo and Conference*. **22**(2022), pp.26–27.
- Bosence, D., Gibbons, K., Le Heron, D.P., Morgan, W.A., Pritchard, T. and Vining, B.A. 2015. Microbial carbonates in space and time: introduction *In*: D. W. Bosence, K. A. Gibbons, D. P. Le Heron, W.A Morgan, T Pritchard and B. A. Vining, eds. *Geological Society Special Publication No. 418, Microbial Carbonates in Space and Time: Implications for Global Exploration and Production.*, pp.1–15.
- Bozkurt, E. and Mittwede, S.K. 2005. Introduction: Evolution of continental extensional tectonics of western Turkey. *Geodinamica Acta*. **18**(3–4), pp.153–165.
- Bramham, E.K., Wright, T.J., Paton, D.A. and Hodgson, D.M. 2021. A new model for the growth of normal faults developed above pre-existing structures. *Geology*. **49**(5), pp.587–591.
- Brantut, N., Heap, M.J., Baud, P. and Meredith, P.G. 2014. Mechanisms of time-dependent deformation in porous limestone. *Journal of Geophysical Research: Solid Earth*. **119**(7), pp.5444–5463.

- Brantut, N., Baker, M., Hansen, L.N. and Baud, P. 2018. Microstructural Control of Physical Properties During Deformation of Porous Limestone. *Journal of Geophysical Research: Solid Earth*. **123**(6), pp.4751–4764.
- Brasier, A.T. 2011. Searching for travertines, calcretes and speleothems in deep time: Processes, appearances, predictions and the impact of plants. *Earth-Science Reviews*. **104**(4), pp.213–239.
- Brogi, A. and Capezzuoli, E. 2009. Travertine deposition and faulting: The fault-related travertine fissure-ridge at Terme S. Giovanni, Rapolano Terme (Italy). *International Journal of Earth Sciences*. **98**, p.47.
- Brogi, A. and Capezzuoli, E. 2014. Earthquake impact on fissure-ridge type travertine deposition. *Geological Magazine*. **151**(06), pp.1135–1143.
- Brogi, A., Capezzuoli, E., Aqué, R., Branca, M. and Voltaggio, M. 2010. Studying travertines for neotectonics investigations: Middle-Late Pleistocene syn-tectonic travertine deposition at Serre di Rapolano (Northern Apennines, Italy). *International Journal of Earth Sciences*. **99**.
- Brogi, A., Capezzuoli, E., Alcicek, M.C. and Gandin, A. 2014. Evolution of a fault-controlled fissure-ridge type travertine deposit in the western Anatolia extensional province: the Cukurba fissure-ridge (Pamukkale, Turkey). *Journal of the Geological Society*. **171**(3), pp.425–441.
- Brogi, A., Alçiçek, M.C., Yalçiner, C.Ç., Capezzuoli, E., Liotta, D., Meccheri, M., Rimondi, V., Ruggieri, G., Gandin, A., Boschi, C., Büyüksaraç, A., Alçiçek, H., Bülbül, A., Baykara, M.O. and Shen, C.-C. 2016. Hydrothermal fluids circulation and travertine deposition in an active tectonic setting: Insights from the Kamara geothermal area (western Anatolia, Turkey). *Tectonophysics*. **680**, pp.211–232.
- Brogi, A., Capezzuoli, E., Kele, S., Baykara, M.O. and Shen, C.-C. 2017. Key travertine tectofacies for neotectonics and palaeoseismicity reconstruction: Effects of hydrothermal overpressured fluid injection. *Journal of the Geological Society*. **174**(4), pp.679–699.
- Brogi, A., Capezzuoli, E., Karabacak, V., Alcicek, M.C. and Luo, L. 2021. Fissure Ridges: A Reappraisal of Faulting and Travertine Deposition (Travitonics). *Geosciences*. **11**(7), p.278.
- Buckley, J.P., Bosence, D. and Elders, C. 2015. Tectonic setting and stratigraphic architecture of an Early Cretaceous lacustrine carbonate platform, Sugar Loaf High, Santos Basin, Brazil *In*: D. W. Bosence, K. A. Gibbons, D. P. Le Heron, W. A. Morgan, T. Pritchard and B. A. Vining, eds. *Geological Society of London Special Publication No. 418. Microbial Carbonates in Space and Time: Implications for Global Exploration and Production*. Geological Society of London. pp. 175–191
- Burchette, T.P. 2012. Carbonate rocks and petroleum reservoirs: a geological perspective from the industry *In*: J. Garland, J. E. Neilson, S. E. Laubach and K. J. Whidden, eds. *Geological Society Special Publication No. 370. Advances in Carbonate Exploration and Reservoir Analysis* pp.17–37.
- Burne, R.V. and Moore, L.S. 1987. Microbialites: Organosedimentary Deposits of Benthic Microbial Communities. *PALAIOS*. **2**(3), pp.241–254.
- Bussolotto, M., Benedicto, A., Invernizzi, C., Micarelli, L., Plagnes, V. and Deiana, G. 2007. Deformation features within an active normal fault zone in carbonate rocks: The Gubbio fault (Central Apennines, Italy). *Journal of Structural Geology*. **29**(12), pp.2017–2037.
- Bussolotto, M., Benedicto, A., Moen-Maurel, L. and Invernizzi, C. 2015. Fault deformation mechanisms and fault rocks in micritic limestones: Examples from Corinth rift normal faults. *Journal of Structural Geology*. **77**, pp.191–212.

- Byerlee, J.D. 1968. Brittle-ductile transition in rocks. *Journal of Geophysical Research*. **73**(14), pp.4741–4750.
- Cabral, F.A. de A., Silveira, A.C. da, Ramos, G.M.S., Miranda, T.S. de, Barbosa, J.A. and Neumann, V.H. de M.L. 2019. Microfacies and diagenetic evolution of the limestones of the upper part of the Crato Formation, Araripe Basin, northeastern Brazil. *Brazilian Journal of Geology*. **49**(1), p.e20180097.
- Caine, J.S., Evans, J.P. and Forster, C.B. 1996. Fault zone architecture and permeability structure. *Geology*. **24**(11), pp.1025–1028.
- Capezzuoli, E., Gandin, A. and Pedley, M. 2014. Decoding tufa and travertine (fresh water carbonates) in the sedimentary record: The state of the art. *Sedimentology*. **61**(1), pp.1–21.
- Capezzuoli, E., Della Porta, G., Rogerson, M. and Tagliasacchi, E. 2022. Non-marine carbonate: Wherefore art thou? *The Depositional Record*. **8**(1), pp.4–8.
- Carminatti, M., Wolff, B. and Gamboa, L. 2008. New exploratory frontiers in Brazil *In: Proceedings of the 19th World Petroleum Congress*. Madrid, Spain: One Petro, pp.28–37.
- Castorina, F., Masi, U. and Billi, A. 2020. Assessing the origin of Sr and Nd isotopes and (REE+Y) in Middle-Upper Pleistocene travertines from the Acquasanta Terme area (Marche, central Italy) and implications for neotectonics. *Applied Geochemistry*. **117**, p.104596.
- Catto, B., Jahnert, R.J., Warren, L.V., Varejao, F.G. and Assine, M.L. 2016. The microbial nature of laminated limestones: Lessons from the Upper Aptian, Araripe Basin, Brazil. *Sedimentary Geology*. **341**(July), pp.304–315.
- Cazarin, C.L., Bezerra, F.H.R., Borghi, L., Santos, R.V., Favoreto, J., Brod, J.A., Auler, A.S. and Srivastava, N.K. 2019. The conduit-seal system of hypogene karst in Neoproterozoic carbonates in northeastern Brazil. *Marine and Petroleum Geology*. **101**, pp.90–107.
- Chafetz, H.S. and Folk, R.L. 1984. Travertines: Depositional Morphology and the Bacterially Constructed Constituents. *Journal of Sedimentary Petrology*. **54**(1), pp.289–316.
- Chafetz, H., Barth, J., Cook, M., Guo, X. and Zhou, J. 2018. Origins of carbonate spherulites: Implications for Brazilian Aptian pre-salt reservoir. *Sedimentary Geology*. **365**, pp.21–33.
- Chafetz, H.S., Akdim, B., Julia, R. and Reid, a. 1998. Mn- and Fe-rich black travertine shrubs; bacterially (and nanobacterially) induced precipitates. *Journal of Sedimentary Research*. **68**(3), pp.404–412.
- Chen, X., Regenauer-Lieb, K. and Roshan, H. 2022. Temperature-Induced Ductile–Brittle Transition in Porous Carbonates and Change in Compaction Band Growth Revealed by 4-D X-Ray Tomography. *Rock Mechanics and Rock Engineering*. **55**(3), pp.1087–1110.
- Chester, F.M. and Logan, J.M. 1986. Implications for mechanical properties of brittle faults from observations of the Punchbowl fault zone, California. *Pure and Applied Geophysics*. **124**(1–2), pp.79–106.
- Chester, F.M., Chester, J.S., Kirschner, D.L., Schulz, S.E. and Evans, J.P. 2004. *Structure of Large-Displacement, Strike-Slip Fault Zones in the Brittle Continental Crust*. Columbia University Press, pp.223–260.
- Chester, F.M., Chester, J.S., Kirschner, D.L., Schulz, S.E. and Evans, J.P. 2016. 8. Structure of Large-Displacement, Strike-Slip Fault Zones in the Brittle Continental Crust *In: G. D. Karner, B. Taylor, N. Driscoll and Kohlstedt, eds. Rheology and Deformation of the Lithosphere at Continental Margins*. MARGINS Theoretical and Experimental Earth Science Series. Columbia University Press.

- Chidsey, T.C., Vanden Berg, M.D. and Eby, D.E. 2015. Petrography and characterization of microbial carbonates and associated facies from modern Great Salt Lake and Uinta Basin's Eocene Green River Formation in Utah, USA *In*: D. W. Bosence, K. A. Gibbons, D. P. Le Heron, W. A. Morgan, T. Pritchard and B. A. Vining, eds. *Geological Society Special Publication No. 418 Carbonates in Space and Time: Implications for Global Exploration and Production*. Geological Society of London, pp.261–286.
- Childs, C., Manzocchi, T., Walsh, J.J., Bonson, C.G., Nicol, A. and Schöpfer, M.P.J. 2009. A geometric model of fault zone and fault rock thickness variations. *Journal of Structural Geology*. **31**(2), pp.117–127.
- Cho, J.-W., Kim, H., Jeon, S. and Min, K.-B. 2012. Deformation and strength anisotropy of Asan gneiss, Boryeong shale, and Yeoncheon schist. *International Journal of Rock Mechanics and Mining Sciences*. **50**, pp.158–169.
- Cilona, A., Faulkner, D.R., Tondi, E., Agosta, F., Mancini, L., Rustichelli, A., Baud, P. and Vinciguerra, S. 2014. The effects of rock heterogeneity on compaction localization in porous carbonates. *Journal of Structural Geology*. **67**, pp.75–93.
- Cilona, A., Baud, P., Tondi, E., Agosta, F., Vinciguerra, S., Rustichelli, A. and Spiers, C.J. 2012. Deformation bands in porous carbonate grainstones: Field and laboratory observations. *Journal of Structural Geology*. **45**, pp.137–157.
- Claes, H., Soete, J., Van Noten, K., El Desouky, H., Marques Erthal, M., Vanhaecke, F., Özkul, M. and Swennen, R. 2015. Sedimentology, three-dimensional geobody reconstruction and carbon dioxide origin of Pleistocene travertine deposits in the Ballık area (south-west Turkey). *Sedimentology*. **62**, pp.1408–1445.
- Claes, H., Marques Erthal, M., Soete, J., Özkul, M. and Swennen, R. 2017. Shrub and pore type classification: Petrography of travertine shrubs from the Ballık-Belevi area (Denizli, SW Turkey). *Quaternary International*. **437**, pp.147–163.
- Claes, H., Miranda, T., Falcão, T.C., Soete, J., Mohammadi, Z., Zieger, L., Erthal, M.M., Aguillar, J., Schmatz, J., Busch, A. and Swennen, R. 2021. Model for calcite spherulite formation in organic, clay-rich, lacustrine carbonate shales (Barbalha Formation, Aptian, Araripe Basin, NE Brazil). *Marine and Petroleum Geology*. **128**, p.104988.
- Claes, H., Török, Á., Soete, J., Mohammadi, Z., Vassilieva, E., Hamaekers, H., Marques Erthal, M., Aratman, C., Cheng, H., Edwards, R.L., Shen, C.-C., Özkul, M., Kele, S., Mindszenty, A. and Swennen, R. 2020. U/Th dating and open system behavior: implications for travertines based on the study of Süttő (Hungary) and Ballık (Turkey) sites. *Quaternaire. Revue de l'Association française pour l'étude du Quaternaire*. (31/2), pp.117–132.
- Cook, M. and Chafetz, H.S. 2017. Sloping fan travertine, Belen, New Mexico, USA. *Sedimentary Geology*. **352**, pp.30–44.
- Cooke, A.P., Fisher, Q.J., Michie, E.A.H. and Yielding, G. 2018. Investigating the controls on fault rock distribution in normal faulted shallow burial limestones, Malta, and the implications for fluid flow. *Journal of Structural Geology*. **114**, pp.22–42.
- Cooke, A.P., Fisher, Q.J., Michie, E.A.H. and Yielding, G. 2019. Permeability of carbonate fault rocks: a case study from Malta. *Petroleum Geoscience*. **2008**, pp.petgeo2019-055.
- Crawford, B.R., Myers, R.D., Woronow, A., Faulkner, D.R. and Rutter, E.H. 2002. Porosity-permeability relationships in clay-bearing fault gouge *In*: *Conference Proceedings of the SPE/ISRM Rock Mechanics Conference 2002*. Irving, Texas: Society of Petroleum Engineers, p1-13

- Croizé, D., Renard, F., Bjørlykke, K. and Dysthe, D.K. 2010. Experimental calcite dissolution under stress: Evolution of grain contact microstructure during pressure solution creep. *Journal of Geophysical Research: Solid Earth*. **115**(B9).
- Curran, J.H. and Carroll, M.M. 1979. Shear stress enhancement of void compaction. *Journal of Geophysical Research: Solid Earth*. **84**(B3), pp.1105–1112.
- da Rocha, H.O., da Costa, J.L.S., Carrasquilla, A.A.G. and Carrasco, A.M.V. 2019. Petrophysical characterization using well log resistivity and rock grain specific surface area in a fractured carbonate pre-salt reservoir in the Santos Basin, Brazil. *Journal of Petroleum Science and Engineering*. **183**, p.106372.
- Daniels, S.E., Tucker, M.E., Mawson, M.J., Holdsworth, R.E., Long, J.J., Gluyas, J.G. and Jones, R.R. 2022. Nature and origin of collapse breccias in the Zechstein of NE England: local observations with cross-border petroleum exploration and production significance, across the North Sea *In*: S. Patruno, S. G. Archer, D. Chiarella, J. A. Howell, C. A.-L. Jackson and H. Kombrink, eds. *Geological Society of London Special Publication No. 494. Cross-Border Themes in Petroleum Geology I: The North Sea*. Geological Society of London, pp.269–299.
- Dautriat, J., Bornert, M., Gland, N., Dimanov, A. and Raphanel, J. 2011. Localized deformation induced by heterogeneities in porous carbonate analysed by multi-scale digital image correlation. *Tectonophysics*. **503**(1–2), pp.100–116.
- De Boever, E., Brasier, A.T., Foubert, A. and Kele, S. 2017. What do we really know about early diagenesis of non-marine carbonates? *Sedimentary Geology*. **361**, pp.25–51.
- De Boever, E., Jaramillo-Vogel, D., Bouvier, A., Frank, N., Schröder-Ritzrau, A., Baumgartner, L., Swennen, R. and Foubert, A. 2022. The fate of a travertine record: Impact of early diagenesis on the Y-10 core (Mammoth Hot Springs, Yellowstone National Park, USA). *The Depositional Record*. **8**(1), pp.220–250.
- De Filippis, L. and Billi, A. 2012a. Morphotectonics of fissure ridge travertines from geothermal areas of Mammoth Hot Springs (Wyoming) and Bridgeport (California). *Tectonophysics*. **548–549**, pp.34–48.
- De Filippis, L., Faccenna, C., Billi, A., Anzalone, E., Brillì, M., Özkul, M., Soligo, M., Tuccimei, P. and Villa, I.M. 2012b. Growth of fissure ridge travertines from geothermal springs of Denizli Basin, western Turkey. *Bulletin of the Geological Society of America*. **124**(9–10), pp.1629–1645.
- De Filippis, L., Faccenna, C., Billi, A., Anzalone, E., Brillì, M., Soligo, M. and Tuccimei, P. 2013a. Plateau versus fissure ridge travertines from Quaternary geothermal springs of Italy and Turkey: Interactions and feedbacks between fluid discharge, paleoclimate, and tectonics. *Earth-Science Reviews*. **123**, pp.35–52.
- De Filippis, L., Anzalone, E., Billi, A., Faccenna, C., Poncia, P.P. and Sella, P. 2013b. The origin and growth of a recently-active fissure ridge travertine over a seismic fault, Tivoli, Italy. *Geomorphology*. **195**, pp.13–26.
- Della Porta, G. 2015. Carbonate build-ups in lacustrine, hydrothermal and fluvial settings: comparing depositional geometry, fabric types and geochemical signature *In*: D. W. Bosence, K. A. Gibbons, D. P. Le Heron, W. A. Morgan, T. Pritchard and B. A. Vining, eds. *Microbial Carbonates in Space and Time: Implications for Global Exploration and Production*. of London Special Publication No. 418. Microbial Carbonates in Space and Time: Implications for Global Exploration and Production. Geological Society of London, pp.17–68.
- Della Porta, G., Capezzuoli, E. and De Bernardo, A. 2016. Facies character and depositional architecture of hydrothermal travertine slope aprons (Pleistocene, Acquasanta Terme, Central Italy). *Marine and Petroleum Geology*. **87**, pp.171–187.

- Della Porta, G., Croci, A., Marini, M. and Kele, S. 2017. Depositional architecture, facies character and geochemical signature of the Tivoli travertines (Pleistocene, Acque Albule Basin, central Italy). *Rivista Italiana di Paleontologia e Stratigrafia*. **123**(3), pp.487–540.
- Della Porta, G., Hoppert, M., Hallmann, C., Schneider, D. and Reitner, J. 2022. The influence of microbial mats on travertine precipitation in active hydrothermal systems (Central Italy). *The Depositional Record*. **8**(1), pp.165–209.
- Delle Piane, C., Giwelli, A., Clennell, M.B., Esteban, L., Nogueira Kiewiet, M.C.D., Kiewiet, L., Kager, S. and Raimon, J. 2016. Frictional and hydraulic behaviour of carbonate fault gouge during fault reactivation — An experimental study. *Tectonophysics*. **690**(PartA), pp.21–34.
- Delle Piane, C., Clennell, M.B., Keller, J.V.A., Giwelli, A. and Luzin, V. 2017. Carbonate hosted fault rocks: A review of structural and microstructural characteristic with implications for seismicity in the upper crust. *Journal of Structural Geology*. **103**, pp.17–36.
- Desouky, H.E., Soete, J., Claes, H., Özkul, M., Vanhaecke, F. and Swennen, R. 2015. Novel applications of fluid inclusions and isotope geochemistry in unravelling the genesis of fossil travertine systems. *Sedimentology*. **62**(1), pp.27–56.
- Dimmen, V., Rotevatn, A., Peacock, D.C.P., Nixon, C.W. and Nærland, K. 2017. Quantifying structural controls on fluid flow: Insights from carbonate-hosted fault damage zones on the Maltese Islands. *Journal of Structural Geology*. **101**, pp.43–57.
- Dimmen, V., Rotevatn, A. and Nixon, C.W. 2020. The Relationship between Fluid Flow, Structures, and Depositional Architecture in Sedimentary Rocks: An Example-Based Overview. *Geofluids*. **2020**, p.e3506743.
- Dunham, R.J. 1962. Classification of Carbonate Rocks According to Depositional Textures. **38**, pp.108–121.
- Dupraz, C., Reid, R.P., Braissant, O., Decho, A.W., Norman, R.S. and Visscher, P.T. 2009. Processes of carbonate precipitation in modern microbial mats. *Earth-Science Reviews*. **96**(3), pp.141–162.
- Eberli, G.P., Baechle, G.T., Anselmetti, F.S. and Incze, M.L. 2003. Factors controlling elastic properties in carbonate sediments and rocks. *The Leading Edge*. **22**(7), pp.654–660.
- Faccenna, C., Soligo, M., Billi, A., De Filippis, L., Funicello, R., Rossetti, C. and Tuccimei, P. 2008. Late Pleistocene depositional cycles of the Lapis Tiburtinus travertine (Tivoli, Central Italy): Possible influence of climate and fault activity. *Global and Planetary Change*. **63**(4), pp.299–308.
- Faulkner, D.R., Mitchell, T.M., Rutter, E.H. and Cembrano, J. 2008. On the structure and mechanical properties of large strike-slip faults In: C. A. J. Wibberly, W. Kurz, J. Imber, R. E. Holdsworth and C. Collettini, eds. *Geological Society Special Publication No. 299: The Internal Structure of Fault Zones: Implications for Mechanical and Fluid-Flow Properties* Geological Society of London, pp.139–150.
- Ferraro, F., Grieco, D.S., Agosta, F. and Prosser, G. 2018. Space-time evolution of cataclasis in carbonate fault zones. *Journal of Structural Geology*. **110**(June 2017), pp.45–64.
- Ferraro, F., Agosta, F., Ukar, E., Grieco, D.S., Cavalcante, F., Belviso, C. and Prosser, G. 2019. Structural diagenesis of carbonate fault rocks exhumed from shallow crustal depths: An example from the central-southern Apennines, Italy. *Journal of Structural Geology*. **122**(February), pp.58–80.
- Ferrill, D.A. and Morris, A.P. 2003. Dilational normal faults. *Journal of Structural Geology*. **25**(2), pp.183–196.

- Ferrill, D.A., McGinnis, R.N., Morris, A.P. and Smart, K.J. 2012. Hybrid failure: Field evidence and influence on fault refraction. *Journal of Structural Geology*. **42**, pp.140–150.
- Ferrill, D.A., Morris, A.P., McGinnis, R.N., Smart, K.J., Wigginton, S.S. and Hill, N.J. 2017. Mechanical stratigraphy and normal faulting. *Journal of Structural Geology*. **94**, pp.275–302.
- Ferrill, D.A., Smart, K.J. and Morris, A.P. 2020. Resolved stress analysis, failure mode, and fault-controlled fluid conduits. *Solid Earth*. **11**(3), pp.899–908.
- Fisher, Q.J. and Knipe, R.J. 1998. Fault sealing processes in siliciclastic sediments *In*: G. Jones, Q. J. Fisher and R. J. Knipe, eds. *Geological Society of London Special Publication No. 147. Faulting, Fault Sealing and Fluid Flow in Hydrocarbon Reservoirs*. Geological Society of London, pp.117–134.
- Fisher, Q.J. and Knipe, R.J. 2001. The permeability of faults within siliclastic petroleum reservoirs of the North Sea and Norwegian Continental Shelf. *Marine and Petroleum Geology*. **18**, pp.1063–1081.
- Fisher, Q.J., Haneef, J., Grattoni, C.A., Allshorn, S. and Lorinczi, P. 2018. Permeability of fault rocks in siliciclastic reservoirs: Recent advances. *Marine and Petroleum Geology*. **91**, pp.29–42.
- Fjær, E. and Nes, O.-M. 2014. The Impact of Heterogeneity on the Anisotropic Strength of an Outcrop Shale. *Rock Mechanics and Rock Engineering*. **47**(5), pp.1603–1611.
- Flügel, E. 2010. Diagenesis, Porosity, and Dolomitization *In: Microfacies of Carbonate Rocks*. Springer Berlin Heidelberg, pp.267–338.
- Folk, R.L. 1962. Spectral Subdivision of Limestone Types. **38**, pp.62–84.
- Ford, T.D. and Pedley, M. 1996. A review of tufa and travertine deposits of the world. *Earth-Science Reviews*. **41**(3–4), pp.117–175.
- Fortin, J., Schubnel, A. and Guéguen, Y. 2005. Elastic wave velocities and permeability evolution during compaction of Bleurswiller sandstone. *International Journal of Rock Mechanics and Mining Sciences*. **42**(7–8), pp.873–889.
- Fossen, H. 2010. *Structural Geology*. Cambridge: Cambridge University Press.
- Fortin, J., Guéguen, Y. and Schubnel, A. 2007. Effects of pore collapse and grain crushing on ultrasonic velocities and V_p/V_s . *Journal of Geophysical Research*. **112**(B8), p.B08207.
- Fredrich, J.T., Evans, B. and Wong, T.-F. 1989. Micromechanics of the brittle to plastic transition in Carrara marble. *Journal of Geophysical Research: Solid Earth*. **94**(B4), pp.4129–4145.
- Frery, E., Gratier, J.P., Ellouz-Zimmerman, N., Loiselet, C., Braun, J., Deschamps, P., Blamart, D., Hamelin, B. and Swennen, R. 2015. Evolution of fault permeability during episodic fluid circulation: Evidence for the effects of fluid-rock interactions from travertine studies (Utah-USA). *Tectonophysics*. **651**, pp.121–137.
- Frisia, S., Borsato, A. and Hellstrom, J. 2018. High spatial resolution investigation of nucleation, growth and early diagenesis in speleothems as exemplar for sedimentary carbonates. *Earth-Science Reviews*. **178**, pp.68–91.
- Gabrielsen, R.H., Braathen, A., Kjemperud, M. and Valdresbråten, M.L.R. 2017. The geometry and dimensions of fault-core lenses *In*: C. Childs, R. E. Holdsworth, C. A.-L. Jackson, T. Manzocchi, J. J. Walsh and G. Yielding, eds. *ty of London Special Publication No. 439. The Geometry and Growth of Normal Faults*. Geological Society of London, pp.249–269.

- Gallois, A. and Bosence, D. 2017. Syn-rift lacustrine carbonates. Cycles, microbial mounds, brackish-hypersaline facies. The Purbeck Limestone Group, Wessex Basin, UK. *Poster Presentation at Petroleum Exploration Society of Great Britain 16th African E&P Conference, London, UK.*
- Gallois, A., Bosence, D. and Burgess, P. 2015. Non-marine carbonate facies, facies models and palaeogeographies of the Purbeck Formation (Late Jurassic to Early Cretaceous) of Dorset (Southern England). *In: European Geosciences Union (EGU) General Assembly 2015 Vienna, Austria: European Geosciences Union.*
- Galloway, E., Hauck, T., Corlett, H., Pană, D. and Schultz, R. 2018. Faults and associated karst collapse suggest conduits for fluid flow that influence hydraulic fracturing-induced seismicity. *Proceedings of the National Academy of Sciences.* **115**(43), pp.E10003–E10012.
- Gawthorpe, R.L., Leeder, M.R., Kranis, H., Skourtsos, E., Andrews, J.E., Henstra, G.A., Mack, G.H., Muravchik, M., Turner, J.A. and Stamatakis, M. 2018. Tectono-sedimentary evolution of the Plio-Pleistocene Corinth rift, Greece. *Basin Research.* **30**(3), pp.448–479.
- Gent, H.W., Holland, M., Urai, J.L. and Loosveld, R. 2010. Evolution of fault zones in carbonates with mechanical stratigraphy – Insights from scale models using layered cohesive powder. *Journal of Structural Geology.* **32**(9), pp.1375–1391.
- Gholami, R. and Rasouli, V. 2014. Mechanical and elastic properties of transversely isotropic slate. *Rock Mechanics and Rock Engineering.* **47**(5), pp.1763–1773.
- Gierlowski-Kordesch, E.H. 2010. Chapter 1 Lacustrine Carbonates *In: A. M. Alonso-Zarza and L. H. Tanner, eds. Developments in Sedimentology. Carbonates in Continental Settings: Facies, Environments, and Processes.* Elsevier, pp.1–101.
- Giwelli, A., Delle Piane, C., Esteban, L., Clennell, M.B., Dautriat, J., Raimon, J., Kager, S. and Kiewiet, L. 2016a. Laboratory observations of fault transmissibility alteration in carbonate rock during direct shearing. *Geofluids.* **16**(4), pp.658–672.
- Giwelli, A., Esteban, L., Delle Piane, C. and Clennell, M.B. 2016b. Fault reactivation in travertine and its impact on hydraulic transmissibility: laboratory experiments and mesoscale structures. *Petroleum Geoscience.*, pp.petgeo2016-025.
- Giwelli, A., Esteban, L., Lemiale, V., Piane, C.D., Clennell, M.B., Raimon, J., Price, G., Kiewiet, M.C.D.N. and Falcão, F. 2017. Hydromechanical Behavior of a Synthetic Homogenous Carbonate Rock During Direct Shear. *Procedia Engineering.* **191**, pp.811–820.
- Golubić, S., Violante, C., Plenković-Moraj, A. and Grgasović, T. 2008. Travertines and calcareous tufa deposits: an insight into diagenesis. *Geologia Croatica.* **61**(2–3), pp.363–378.
- Gomes, J.P., Bunevich, R.B., Tedeschi, L.R., Tucker, M.E. and Whitaker, F.F. 2020. Facies classification and patterns of lacustrine carbonate deposition of the Barra Velha Formation, Santos Basin, Brazilian Pre-salt. *Marine and Petroleum Geology.* **113**, p.104176.
- Guo, L. and Riding, R. 1998. Hot-spring travertine facies and sequences, Late Pleistocene, Rapolano Terme, Italy. *Sedimentology.* **45**(1), pp.163–180.
- Guo, L. and Riding, R. 1999. Rapid facies changes in Holocene fissure ridge hot spring travertines, Rapolano Terme, Italy. *Sedimentology.* **46**(6), pp.1145–1158.
- Haines, T.J., Michie, E.A.H., Neilson, J.E. and Healy, D. 2016. Permeability evolution across carbonate hosted normal fault zones. *Marine and Petroleum Geology.* **72**, pp.62–82.
- Hancock, P.L., Chalmers, R.M.L., Altunel, E. and ??akir, Z. 1999. Travertines: Using travertines in active fault studies. *Journal of Structural Geology.* **21**(8–9), pp.903–916.

- Hausegger, S., Kurz, W., Rabitsch, R., Kiechl, E. and Brosch, F.J. 2010. Analysis of the internal structure of a carbonate damage zone: Implications for the mechanisms of fault breccia formation and fluid flow. *Journal of Structural Geology*. **32**(9), pp.1349–1362.
- Heard, H.C. 1960. Chapter 7: Transition from Brittle Fracture to Ductile Flow in Solenhofen Limestone as a Function of Temperature, Confining Pressure, and Interstitial Fluid Pressure *In: Geological Society of America Memoir 79: Rock Deformation (A Symposium)*. Geological Society of America, pp.193–226.
- He, S., Li, G., Wu, C., Liu, S., Zhang, Z., Su, Y., Zhu, Y., He, Z., Ren, J., Wang, Yuchen, Zhou, W. and Wang, Yajie 2022. Sedimentary filling characteristics and controlling factors of lacustrine microbial carbonates sequence in the Santos Basin, Brazil. *Petroleum Exploration and Development*. **49**(4), pp.785–796.
- Heimhofer, U., Ariztegui, D., Lenniger, M., Hesselbo, S.P., Martill, D.M. and Rios-Netto, A.M. 2010. Deciphering the depositional environment of the laminated Crato fossil beds (Early Cretaceous, Araripe Basin, North-eastern Brazil). *Sedimentology*. **57**(2), pp.677–694.
- Henchiri, M., Ben Ahmed, W., Brogi, A., Alçiçek, M.C. and Benassi, R. 2017. Evolution of Pleistocene travertine depositional system from terraced slope to fissure-ridge in a mixed travertine-alluvial succession (Jebel El Mida, Gafsa, southern Tunisia). *Geodinamica Acta*. **29**(1), pp.20–41.
- Herlinger, R., Zambonato, E.E. and De Ros, L.F. 2017. Influence of Diagenesis On the Quality of Lower Cretaceous Pre-salt Lacustrine Carbonate Reservoirs from Northern Campos Basin, Offshore Brazil. *Journal of Sedimentary Research*. **87**(12), pp.1285–1313.
- Higgins, M.W., 1971. *Cataclastic rocks* (Vol. 687, pp. 1-97). US Government Printing Office.
- Hosa, A., Wood, R.A., Corbett, P.W.M., Schiffer de Souza, R. and Roemers, E. 2020. Modelling the impact of depositional and diagenetic processes on reservoir properties of the crystal-shrub limestones in the ‘Pre-Salt’ Barra Velha Formation, Santos Basin, Brazil. *Marine and Petroleum Geology*. **112**, p.104100.
- Janssens, N., Capezzuoli, E., Claes, H., Muchez, P., Yu, T.-L., Shen, C.-C., Ellam, R.M. and Swennen, R. 2020. Fossil travertine system and its palaeofluid provenance, migration and evolution through time: Example from the geothermal area of Acquasanta Terme (Central Italy). *Sedimentary Geology*. **398**, p.105580.
- Jefferies, S.P., Holdsworth, R.E., Shimamoto, T., Takagi, H., Lloyd, G.E. and Spiers, C.J. 2006. Origin and mechanical significance of foliated cataclastic rocks in the cores of crustal-scale faults: Examples from the Median Tectonic Line, Japan. *Journal of Geophysical Research: Solid Earth*. **111**(B12).
- Ji, Y., Baud, P., Vajdova, V. and Wong, T. -f. 2012. Characterization of Pore Geometry of Indiana Limestone in Relation to Mechanical Compaction. *Oil & Gas Science and Technology – Revue d’IFP Energies nouvelles*. **67**(5), pp.753–775.
- Jolley, S.J., Fisher, Q.J. and Ainsworth, R.B. 2010. Reservoir compartmentalization: an introduction *In: S. J. Jolley, Q. J. Fisher, R. B. Ainsworth, P. J. Vrolik and S. Delise, eds. Geological Society of London SPecial Publication No. 347. Reservoir Compartmentalisation* Geological Society of London, pp.1–8.
- Jones, S.C. 1997. A Technique for Faster Pulse-Decay Permeability Measurements in Tight Rocks. *SPE Formation Evaluation*. **12**(01), pp.19–25.
- Kaminskaite, I., Fisher, Q.J. and Michie, E.A.H. 2020. Faults in tight limestones and dolostones in San Vito lo Capo, Sicily, Italy: Internal architecture and petrophysical properties. *Journal of Structural Geology*. **132**, 103970

- Kaminskaite, I., Fisher, Q.J. and Michie, E.A.H. 2019. Microstructure and petrophysical properties of deformation bands in high porosity carbonates. *Journal of Structural Geology*. **119**, pp.61–80.
- Kaypak, B. and Gökkaya, G. 2012. 3-D imaging of the upper crust beneath the Denizli geothermal region by local earthquake tomography, western Turkey. *Journal of Volcanology and Geothermal Research*. **211–212**, pp.47–60.
- Kaymakci, N. 2006. Kinematic development and paleostress analysis of the Denizli Basin (Western Turkey): implications of spatial variation of relative paleostress magnitudes and orientations. *Journal of Asian Earth Sciences*. **27**(2), pp.207–222.
- Kele, S., Vaselli, O., Szabó, C. and Minissale, A. 2003. Stable isotope geochemistry of Pleistocene travertine from Budakalász (Buda Mts, Hungary). *Acta Geologica Hungarica*. **46**(2), pp.161–175.
- Kershaw, S. and Guo, L. 2003. Pleistocene cyanobacterial mounds in the Perachora Peninsula, Gulf of Corinth, Greece: Structure and applications to interpreting sea-level history and terrace sequences in an unstable tectonic setting. *Palaeogeography, Palaeoclimatology, Palaeoecology*. **193**(3–4), pp.503–514.
- Kershaw, S. and Guo, L. 2006. Pleistocene calcified cyanobacterial mounds, Perachora Peninsula, central Greece: a controversy of growth and history *In*: Pedley and G. Caranante, eds. *Geological Society of London Special Publication No. 255. Cool-water Carbonates: Depositional Systems and Palaeoenvironmental Controls*. Geological Society of London, pp.53–69.
- Kettermann, M. and Urai, J.L. 2015. Changes in structural style of normal faults due to failure mode transition: First results from excavated scale models. *Journal of Structural Geology*. **74**, pp.105–116.
- Kettermann, M., Weismüller, C., von Hagke, C., Reicherter, K. and Urai, J.L. 2019. Large near-surface block rotations at normal faults of the Iceland rift: Evolution of tectonic caves and dilatancy. *Geology*. **47**(8), pp.781–785.
- Kiewiet, M.N., Lima, C., Giwelli, A., Delle Piane, C., Lemiale, V., Esteban, L., Falcao, F., Clennell, M.B., Dautriat, J., Kiewiet, L. and Raimon, J., 2020. An experimental and numerical investigation on the hydromechanical behaviour of carbonate fault zones upon reactivation: the impact of carbonate mud sealing layers and overall research outcomes. *Geological Society, London, Special Publications*, 496(1), pp.39-73.
- Killick, A.M. 2003. Fault Rock Classification: An aid to structural interpretation in mine and exploration geology. *South African Journal of Geology*. **106**(4), pp.395–402.
- Kim, Y.S., Peacock, D.C.P. and Sanderson, D.J. 2004. Fault damage zones. *Journal of Structural Geology*. **26**(3), pp.503–517.
- Klimchouk, A., Tymokhina, E. and Amelichev, G. 2012. Speleogenetic effects of interaction between deeply derived fracture-conduit flow and intrastratal matrix flow in hypogene karst settings. *International Journal of Speleology*. **41**(2), pp.161–179.
- Klinkenberg, L.J., 1941. The permeability of porous media to liquids and gases. *Am. Petrol. Inst., Drilling and Production Practice*, 2, pp.200-213.
- Klein, E., Baud, P., Reuschlé, T. and Wong, T. 2001. Mechanical behaviour and failure mode of bentheim sandstone under triaxial compression. *Physics and Chemistry of the Earth, Part A: Solid Earth and Geodesy*. **26**(1), pp.21–25.
- Knipe, R.J. 1992. Faulting processes and fault seal *In*: R. M. Larsen, H. Brekke, B. T. Larsen and E. Talleraas, eds. *Structural and Tectonic Modelling and its Application to Petroleum Geology*. Norwegian Petroleum Society Special Publications. Amsterdam: Elsevier, pp.325–342.

- Knipe, R.J., Fisher, Q.J., Jones, G., Clennell, M.R., Farmer, A.B., Harrison, A., Kidd, B., Mcallister, E., Porter, J.R. and White, E.A. 1997. Fault seal analysis: successful methodologies, application and future directions. *Norwegian Petroleum Society Special Publications*. **7(C)**, pp.15–38.
- Koçyiğit, A. 2005. The Denizli graben-horst system and the eastern limit of western Anatolian continental extension: Basin fill, structure, deformational mode, throw amount and episodic evolutionary history, SW Turkey. *Geodinamica Acta*. **18(3–4)**, pp.167–208.
- La Bruna, V., Bezerra, F.H.R., Souza, V.H.P., Maia, R.P., Auler, A.S., Araujo, R.E.B., Cazarin, C.L., Rodrigues, M.A.F., Vieira, L.C. and Sousa, M.O.L. 2021. High-permeability zones in folded and faulted silicified carbonate rocks – Implications for karstified carbonate reservoirs. *Marine and Petroleum Geology*. **128**, p.105046.
- Leeder, M.R., Portman, C., Andrews, J.E., Collier, R.E.LI., Finch, E., Gawthorpe, R.L., McNeill, L.C., Perez-Arlucea, M. and Rowe, P. 2005. Normal faulting and crustal deformation, Alkyonides Gulf and Perachora peninsula, eastern Gulf of Corinth rift, Greece. *Journal of the Geological Society*. **162(3)**, pp.549–561.
- Leggitt, V.L. and Cushman, R.A. 2001. Complex caddisfly-dominated bioherms from the Eocene Green River Formation. *Sedimentary Geology*. **145(3–4)**, pp.377–396.
- Li, Y., Sun, J., Wei, H. and Song, S. 2019. Architectural features of fault-controlled karst reservoirs in the Tahe oilfield. *Journal of Petroleum Science and Engineering*. **181**, p.106208.
- Li, M., Wu, S., Hu, S., Zhu, R., Meng, S. and Yang, J. 2021. Lamination Texture and Its Effects on Reservoir and Geochemical Properties of the Palaeogene Kongdian Formation in the Cangdong Sag, Bohai Bay Basin, China. *Minerals*. **11(12)**, p.1360.
- Lima, B.E.M. and De Ros, L.F. 2019. Deposition, diagenetic and hydrothermal processes in the Aptian Pre-Salt lacustrine carbonate reservoirs of the northern Campos Basin, offshore Brazil. *Sedimentary Geology*. **383**, pp.55–81.
- Lu, X., Wang, Y., Tian, F., Li, X., Yang, D., Li, T., Lv, Y. and He, X. 2017. New insights into the carbonate karstic fault system and reservoir formation in the Southern Tahe area of the Tarim Basin. *Marine and Petroleum Geology*. **86**, pp.587–605.
- Lupinacci, W.M., Abdul Fatah, T.Y., Menezes Freire, A.F. and Pierantoni Gamboa, L.A. 2022. Controls of fracturing on porosity in pre-salt carbonate reservoirs. *Energy Geoscience*. **4(2)**, p.100146.
- Madonna, R., Signanini, P., Crema, G., Sabatino, B.D., Rainone, M.L. and Nunzio, A.D. n.d. The Geothermal Area of Acquasanta Terme (Central Italy): Main Characteristics and an Attempt of Field Evaluation *In: Proceedings of the World Geothermal Congress 2005*. Antalya, Turkey, pp.1–8.
- Maggi, M., Cianfarra, P., Salvini, F. and De Lima, C.C. 2015. Staircase fractures in microbialites and the role of lamination-related mechanical anisotropy: The example of the Acquasanta Terme travertine deposits (central Italy). *Bulletin of the Geological Society of America*. **127(5–6)**, pp.879–896.
- Makhnenko, R.Y. and Labuz, J.F. 2016. Elastic and inelastic deformation of fluid-saturated rock. *Philosophical Transactions of the Royal Society A: Mathematical, Physical and Engineering Sciences*. **374(2078)**, p.20150422.
- Mancini, A., Capezzuoli, E., Erthal, M. and Swennen, R. 2019. Hierarchical approach to define travertine depositional systems: 3D conceptual morphological model and possible applications. *Marine and Petroleum Geology*. **103**, pp.549–563.

- Martill, D.M., Loveridge, R. and Heimhofer, U. 2007. Halite pseudomorphs in the Crato Formation (Early Cretaceous, Late Aptian-Early Albian), Araripe Basin, northeast Brazil: further evidence for hypersalinity. *Cretaceous Research*. **28**(4), pp.613–620.
- Matenco, L. and Radivojević, D. 2012. On the formation and evolution of the Pannonian Basin: Constraints derived from the structure of the junction area between the Carpathians and Dinarides: The Evolution of The Pannonian Basin. *Tectonics*. **31**(6), TC6007.
- McPhee, C., Reed, J. and Zubizarreta, I. 2015. *Core Analysis: A Best Practice Guide*. Elsevier.
- Meng, Q., Qian, W., Liu, J., Zhang, M., Lu, M. and Wu, Y. 2020. Analysis of triaxial compression deformation and strength characteristics of limestone after high temperature. *Arabian Journal of Geosciences*. **13**(4), p.153.
- Mercuri, M., Carminati, E., Tartarello, M.C., Brandano, M., Mazzanti, P., Brunetti, A., McCaffrey, K.J.W. and Collettini, C. 2020. Lithological and structural control on fracture frequency distribution within a carbonate-hosted relay ramp. *Journal of Structural Geology*. **137**(May), p.104085.
- Mesci, B.L., Gürsoy, H., Ghaleb, B. and Tatar, O. 2019. Kuzey Anadolu Fay Zonu'nda Traverten Çökeliminde Sıcak Su Kaynağı Olarak Görev Yapan Bir Açılma çatlak: Reşadiye Çatlak Sırtı. *Türkiye Jeoloji Bülteni / Geological Bulletin of Turkey*., pp.1–1.
- Micarelli, L., Benedicto, A. and Wibberley, C.A.J. 2006. Structural evolution and permeability of normal fault zones in highly porous carbonate rocks. *Journal of Structural Geology*. **28**(7), pp.1214–1227.
- Michie, E.A.H. and Haines, T.J. 2016. Variability and heterogeneity of the petrophysical properties of extensional carbonate fault rocks, Malta. *Petroleum Geoscience*. **22**(2), pp.136–152.
- Michie, E.A.H., Haines, T.J., Healy, D., Neilson, J.E., Timms, N.E. and Wibberley, C.A.J. 2014. Influence of carbonate facies on fault zone architecture. *Journal of Structural Geology*. **65**, pp.82–99.
- Michie, E.A.H., Yielding, G. and Fisher, Q.J. 2018. Predicting transmissibilities of carbonate-hosted fault zones. *Geological Society Special Publication*. **459**(1).
- Michie, E.A.H., Cooke, A.P., Kaminskaite, I., Stead, J.C., Plenderleith, G.E., Tobiss, S.D., Fisher, Q.J., Yielding, G. and Freeman, B. 2020. Key controls on the hydraulic properties of fault rocks in carbonates. *Petroleum Geoscience*. **27**(2), pp.petgeo2020-034.
- Michie, E.A.H., Kaminskaite, I., Cooke, A.P., Fisher, Q.J., Yielding, G. and Tobiss, S.D. 2021. Along-strike permeability variation in carbonate-hosted fault zones. *Journal of Structural Geology*. **142**.
- Michie, E.A.H. 2015. Influence of host lithofacies on fault rock variation in carbonate fault zones: A case study from the Island of Malta. *Journal of Structural Geology*. **76**, pp.61–79.
- Miranda, T.S., Santos, R.F., Barbosa, J.A., Gomes, I.F., Alencar, M.L., Correia, O.J., Falcão, T.C., Gale, J.F.W. and Neumann, V.H. 2018. Quantifying aperture, spacing and fracture intensity in a carbonate reservoir analogue: Crato Formation, NE Brazil. *Marine and Petroleum Geology*. **97**, pp.556–567.
- Mitchell, T.M. and Faulkner, D.R. 2009. The nature and origin of off-fault damage surrounding strike-slip fault zones with a wide range of displacements: A field study from the Atacama fault system, northern Chile. *Journal of Structural Geology*. **31**(8), pp.802–816.
- Mogi, K., 1966. Some precise measurements of fracture strength of rocks under uniform compressive stress. *Rock Mech. Eng. Geol.*, **4**(1), p.41.
- Mohajjel, M. and Taghipour, K. 2014. Quaternary travertine ridges in the Lake Urmia area: active extension in NW Iran. *Turkish Journal Of Earth Sciences*. **23**, pp.602–614.

- Mohammadi, Z., Capezzuoli, E., Claes, H., Alipoor, R., Muchez, P. and Swennen, R. 2019. Substrate geology controlling different morphology, sedimentology, diagenesis and geochemistry of adjacent travertine bodies: A case study from the Sanandaj-Sirjan zone (western Iran). *Sedimentary Geology*. **389**, pp.127–146.
- Molli, G., Cortecchi, G., Vaselli, L., Ottria, G., Cortopassi, A., Dinelli, E., Mussi, M. and Barbieri, M. 2010. Fault zone structure and fluid-rock interaction of a high angle normal fault in Carrara marble (NW Tuscany, Italy). *Journal of Structural Geology*. **32**(9), pp.1334–1348.
- Moore, C.H. 1989. *Carbonate Diagenesis and Porosity*. Elsevier.
- Moore, C.H. and Wade, W.J. 2013. Carbonate diagenesis: Introduction and tools *In*: A. M. Alonso-Zarza and L. H. Tanner, eds. *Carbonates in Continental Settings: Geochemistry, Diagenesis and Applications. Developments in Sedimentology*. Elsevier B.V., pp.67–89.
- Muniz, M.C. and Bosence, D.W.J. 2015. Pre-salt microbialites from the Campos Basin (offshore Brazil): image log facies, facies model and cyclicity in lacustrine carbonates *In*: D. W. Bosence, K. A. Gibbons, D. P. Le Heron, W. A. Morgan, T. Pritchard and B. A. Vining, eds. *Geological Society of London Special Publications No 418. Microbial Carbonates in Space and Time: Implications for Global Exploration and Production*. Geological Society of London, pp.221–242.
- Ng, K. and Santamarina, J.C. 2022. Mechanical and hydraulic properties of carbonate rock: The critical role of porosity. *Journal of Rock Mechanics and Geotechnical Engineering*, p.S1674775522001718.
- Nicolas, A., Fortin, J., Regnet, J.B., Dimanov, A. and Guéguen, Y. 2016. Brittle and semi-brittle behaviours of a carbonate rock: influence of water and temperature. *Geophysical Journal International*. **206**(1), pp.438–456.
- Nixon, C.W., Nærland, K., Rotevatn, A., Dimmen, V., Sanderson, D.J. and Kristensen, T.B. 2020. Connectivity and network development of carbonate-hosted fault damage zones from western Malta. *Journal of Structural Geology*. **141**, p.104212.
- Önder, H. 1985. Interaction Between Conduit Type Flow and Diffuse Flow In Karst Formations *In*: *Karst Water Resources (Proceedings of the Ankara-Antalya Symposium 1985)*. IAHS Publication No 161. Ankara, Turkey: IAHS, pp.371–384.
- Osmond, J.C. 2000. West Willow Creek Field; first productive lacustrine stromatolite mound in the Eocene Green River Formation, Uinta Basin, Utah. *The Mountain Geologist*. **37**(3), pp.157–170.
- Ostermeijer, G.A., Mitchell, T.M., Aben, F.M., Dorsey, M.T., Browning, J., Rockwell, T.K., Fletcher, J.M. and Ostermeijer, F. 2020. Damage zone heterogeneity on seismogenic faults in crystalline rock; a field study of the Borrego Fault, Baja California. *Journal of Structural Geology*. **137**(February), p.104016.
- Özkul, M., Kele, S., Gökgöz, A., Shen, C.C., Jones, B., Baykara, M.O., Fórizs, I., Németh, T., Chang, Y.W. and Alçiçek, M.C. 2013. Comparison of the Quaternary travertine sites in the Denizli extensional basin based on their depositional and geochemical data. *Sedimentary Geology*. **294**, pp.179–204.
- Özkaymak, Ç. 2015. Tectonic analysis of the Honaz Fault (western Anatolia) using geomorphic indices and the regional implications. *Geodinamica Acta*. **27**(2–3), pp.110–129.
- Papanikolaou, D.J. and Royden, L.H. 2007. Disruption of the Hellenic arc: Late Miocene extensional detachment faults and steep Pliocene-Quaternary normal faults-Or what happened at Corinth? *Tectonics*. **26**(5), TC5003.
- Paterson, M.S. and Wong, T.F., 2005. *Experimental rock deformation: the brittle field* (Vol. 348). Berlin: Springer.

- Peacock, D.C.P., Fisher, Q.J., Willemse, E.J.M. and Aydin, A. 1998. The relationship between faults and pressure solution seams in carbonate rocks and the implications for fluid flow. *Geological Society, London, Special Publications*. **147**(1), pp.105–115.
- Pedley, M. 2009. Tufas and travertines of the Mediterranean region: A testing ground for freshwater carbonate concepts and developments. *Sedimentology*. **56**(1), pp.221–246.
- Pentecost, A. 2005. Hot springs, thermal springs and warm springs. What's the difference? *Geology Today*. **21**(6), pp.222–224.
- Pentecost, A. and Viles, H. 1994. A Review and Reassessment of Travertine Classification. *Géographie physique et Quaternaire*. **48**(3), p.305.
- Pietzsch, R., Tedeschi, L.R., Oliveira, D.M., dos Anjos, C.W.D., Vazquez, J.C. and Figueiredo, M.F. 2020. Environmental conditions of deposition of the Lower Cretaceous lacustrine carbonates of the Barra Velha Formation, Santos Basin (Brazil), based on stable carbon and oxygen isotopes: A continental record of pCO₂ during the onset of the Oceanic Anoxic Event 1a (OAE 1a) interval? *Chemical Geology*. **535**, p.119457.
- Pijnenburg, R.P.J., Verberne, B.A., Hangx, S.J.T. and Spiers, C.J. 2019. Inelastic Deformation of the Slochteren Sandstone: Stress-Strain Relations and Implications for Induced Seismicity in the Groningen Gas Field. *Journal of Geophysical Research: Solid Earth*. **124**(5), pp.5254–5282.
- Platt, N.H. and Wright, V.P. 1991. Lacustrine Carbonates: Facies Models, Facies Distributions and Hydrocarbon Aspects *In: Lacustrine Facies Analysis*. John Wiley & Sons, Ltd, pp.57–74.
- Portman, C., Andrews, J.E., Rowe, P.J., Leeder, M.R. and Hoogewerff, J. 2005. Submarine-spring controlled calcification and growth of large *Rivularia* bioherms, Late Pleistocene (MIS 5e), Gulf of Corinth, Greece. *Sedimentology*. **52**(3), pp.441–465.
- Qiu, S., Wang, F., Dong, F., Tian, F., Zhao, X., Dai, Q., Li, Q., Zhu, Y. and Wang, Y. 2022. Sedimentary evolution of the Dawan travertines and their geological environmental significance, Huanglong, China. *The Depositional Record*. **8**(1), pp.251–265.
- Rath, A., Exner, U., Tschegg, C., Grasemann, B., Laner, R. and Draganits, E. 2011. Diagenetic control of deformation mechanisms in deformation bands in a carbonate grainstone. *AAPG Bulletin*. **95**(8), pp.1369–1381.
- Regnet, J.B., David, C., Fortin, J., Robion, P., Makhoulfi, Y. and Collin, P.Y. 2015. Influence of microporosity distribution on the mechanical behavior of oolitic carbonate rocks. *Geomechanics for Energy and the Environment*. **3**, pp.11–23.
- Reijmer, J.J.G. 2021. Marine carbonate factories: Review and update. *Sedimentology*. **68**(5), pp.1729–1796.
- Rezende, M.F., Tonietto, S.N. and Pope, M.C. 2013. Three-dimensional pore connectivity evaluation in a Holocene and Jurassic microbialite buildup. *AAPG Bulletin*. **97**(11), pp.2085–2101.
- Ricketts, J.W., Karlstrom, K.E., Priewisch, A., Crossey, L.J., Polyak, V.J. and Asmerom, Y. 2014. Quaternary extension in the Rio Grande rift at elevated strain rates recorded in travertine deposits, central New Mexico. *Lithosphere*. **6**(1), pp.3–16.
- Riding, R. 1991. Classification of Microbial Carbonates *In: Robert Riding, ed. Calcareous Algae and Stromatolites*. Berlin, Heidelberg: Springer, pp.21–51.
- Riding, R. 2012. *Calcareous Algae and Stromatolites*. Springer Science & Business Media.
- Rodríguez-Berriguete, Á., Dal' Bo, P.F., Valle, B. and Borghi, L. 2022. When distinction matters: Carbonate shrubs from the Aptian Barra Velha Formation of Brazilian's Pre-salt. *Sedimentary Geology*. **440**, p.106236.

- Rodríguez-Berriguete, Á. 2020. Early diagenetic features in Holocene travertine and tufa from a volcanic setting (Azuaje, Gran Canaria, Spain). *Facies*. **66**(3).
- Romanov, D., Dreybrodt, W. and Gabrovsek, F. 2002. Interaction of Fracture and Conduit Flow in the Evolution of Karst Aquifers. *Speleogenesis and Evolution of Karst Aquifers*. **1**(3), pp.1–6.
- Ronchi, P. and Cruciani, F. 2015. Continental carbonates as a hydrocarbon reservoir, an analog case study from the travertine of Saturnia, Italy. *AAPG Bulletin*. **99**(04), pp.711–734.
- Rotevatn, A. and Bastesen, E. 2014. Fault linkage and damage zone architecture in tight carbonate rocks in the Suez Rift (Egypt): implications for permeability structure along segmented normal faults. *Geological Society, London, Special Publications*. **374**(1), pp.79–95.
- Rotevatn, A., Fossmark, H.S., Bastesen, E., Thorsheim, E. and Torabi, A. 2017. Do deformation bands matter for flow? Insights from permeability measurements and flow simulations in porous carbonate rocks. *Petroleum Geoscience*. **23**(1), pp.104–119.
- Rutter, E.H. and Glover, C.T. 2012. The deformation of porous sandstones; are Byerlee friction and the critical state line equivalent? *Journal of Structural Geology*. **44**, pp.129–140.
- Rutter, E.H. 1986. On the nomenclature of mode of failure transitions in rocks. *Tectonophysics*. **122**(3–4), pp.381–387.
- Saller, A., Rushton, S., Buambua, L., Inman, K., McNeil, R. and Dickson, J.A.D. (Tony) 2016. Presalt stratigraphy and depositional systems in the Kwanza Basin, offshore Angola. *AAPG Bulletin*. **100**(07), pp.1135–1164.
- Sarg, F.J., Tānavsuu-Milkeviciene, K. and Humphrey, J.D. 2013. Lithofacies, stable isotopic composition, and stratigraphic evolution of microbial and associated carbonates, Green River Formation (Eocene), Piceance Basin, Colorado. *AAPG Bulletin*. **97**(11), pp.1937–1966.
- Sartorato, A.C.L., Tonietto, S.N. and Pereira, E. 2020. Silicification and dissolution features in the brazilian Pre-salt Barra Velha formation: impacts in the reservoir quality and insights for 3D geological modeling. *Rio Oil and Gas Expo and Conference Proceedings*. **20**(2020), pp.68–69.
- Savage, H.M. and Brodsky, E.E. 2011. Collateral damage: Evolution with displacement of fracture distribution and secondary fault strands in fault damage zones. *Journal of Geophysical Research: Solid Earth*. **116**(3).
- Scholz, C.H. 2019. *The Mechanics of Earthquakes and Faulting*. Cambridge University Press.
- Schröckenfuchs, T., Bauer, H., Grasemann, B. and Decker, K. 2015. Rock pulverization and localization of a strike-slip fault zone in dolomite rocks (Salzach-Ennstal-Mariazell-Puchberg fault, Austria). *Journal of Structural Geology*. **78**, pp.67–85.
- Seard, C., Camoin, G., Rouchy, J.M. and Virgone, A. 2013. Composition, structure and evolution of a lacustrine carbonate margin dominated by microbialites: Case study from the Green River formation (Eocene; Wyoming, USA). *Palaeogeography, Palaeoclimatology, Palaeoecology*. **381–382**, pp.128–144.
- Sierralta, M., Kele, S., Melcher, F., Hambach, U., Reinders, J., van Geldern, R. and Frechen, M. 2010. Uranium-series dating of travertine from Süttó: Implications for reconstruction of environmental change in Hungary. *Quaternary International*. **222**(1), pp.178–193.
- Shipton, Z.K. and Cowie, P.A. 2003. A conceptual model for the origin of fault damage zone structures in high-porosity sandstone. *Journal of Structural Geology*. **25**(3), pp.333–344.
- Sibson, R.H. 1977. Fault rocks and fault mechanisms. *Journal of the Geological Society*. **133**(3), pp.191–213.

- Sibson, R.H. 1994. Crustal stress, faulting and fluid flow. *Geological Society, London, Special Publications*. **78**(1), pp.69–84.
- Shiraishi, F., Morikawa, A., Kuroshima, K., Amekawa, S., Yu, T.L., Shen, C.C., Kakizaki, Y., Kano, A., Asada, J. and Bahniuk, A.M. 2020. Genesis and diagenesis of travertine, Futamata hot spring, Japan. *Sedimentary Geology*. **405**.
- Smith, M.E., Carroll, A.R. and Singer, B.S. 2008. Synoptic reconstruction of a major ancient lake system: Eocene Green River Formation, western United States. *Geological Society of America Bulletin*. **120**(1–2), pp.54–84.
- Soete, J., Kleipool, L.M., Claes, H., Claes, S., Hamaekers, H., Kele, S., Özkul, M., Foubert, A., Reijmer, J.J.G. and Swennen, R. 2015. Acoustic properties in travertines and their relation to porosity and pore types. *Marine and Petroleum Geology*. **59**, pp.320–335.
- Soete, J., Claes, S., Claes, H., Erthal, M.M., Hamaekers, H., De Boever, E., Foubert, A., Klitzsch, N. and Swennen, R. 2022. Unravelling the pore network and its behaviour: An integrated NMR, MICP, XCT and petrographical study of continental spring carbonates from the Ballık area, SW Turkey. *The Depositional Record*. **8**(1), pp.292–316.
- Solum, J.G. and Huisman, B.A.H. 2017. Toward the creation of models to predict static and dynamic fault-seal potential in carbonates. *Petroleum Geoscience*. **23**(1), pp.70–91.
- Straccia, F.G., Wilkinson, B.H. and Smith, G.R. 1990. Miocene lacustrine algal reefs- south-western Snake River Plain, Idaho. *Sedimentary Geology*. **67**, pp.7–23.
- Tavallali, A. and Vervoort, A. 2010. Effect of layer orientation on the failure of layered sandstone under Brazilian test conditions. *International Journal of Rock Mechanics and Mining Sciences*. **47**(2), pp.313–322.
- Terra, J.G.S., Spadini, A.R., França, A.B., Leite, C., Zambonato, E.E., Costa, L., Arienti, L.M., Erthal, M.M., Blauth, M., Franco, M.P., Matsuda, N.S., Goulart, N., Augusto, P., Junior, M., Francisco, R.S., Avila, D., Souza, R.S.D., Tonietto, S.N. and Maria, S. 2010. Classificações Clássicas De Rochas Carbonáticas. *B. Geoci. Petrobras, Rio de Janeiro*. **18**(1), pp.9–29.
- Tondi, E., Antonellini, M., Aydin, A., Marchegiani, L. and Cello, G. 2006. The role of deformation bands, stylolites and sheared stylolites in fault development in carbonate grainstones of Majella Mountain, Italy. *Journal of Structural Geology*. **28**(3), pp.376–391.
- Török, Á. and Vászárhelyi, B. 2010. The influence of fabric and water content on selected rock mechanical parameters of travertine, examples from Hungary. *Engineering Geology*. **115**(3–4), pp.237–245.
- Török, Á., Mindszenty, A., Claes, H., Kele, S., Fodor, L. and Swennen, R. 2017. Geobody architecture of continental carbonates: “Gazda” travertine quarry (Süttő, Gerecse Hills, Hungary). *Quaternary International*. **437**, pp.164–185.
- Török, Á., Claes, H., Brogi, A., Liotta, D., Tóth, Á., Mindszenty, A., Kudó, I., Kele, S., Huntington, K.W., Shen, C. and Swennen, R. 2019. A multi-methodological approach to reconstruct the configuration of a travertine fissure ridge system: The case of the Cukor quarry (Süttő, Gerecse Hills, Hungary). *Geomorphology*. **345**, p.106836.
- Tsikrikis, A., Papaliangas, T. and Marinos, V. 2022. Brittle-Ductile Transition and Hoek–Brown mi Constant of Low-Porosity Carbonate Rocks. *Geotechnical and Geological Engineering*. **40**(4), pp.1833–1849.
- Tucker, M.E. and Bathurst, R.G.C., 1990. Meteoric diagenesis. Tucker, ME Bathurst RGC (Eds). *Carbonate diagenesis. Reprint series*, 1, pp.181-183.

- Vajdova, V., Baud, P. and Wong, T. 2004. Compaction, dilatancy, and failure in porous carbonate rocks. *Journal of Geophysical Research: Solid Earth*. **109**(B5).
- Vajdova, V., Zhu, W., Natalie Chen, T.-M. and Wong, T. 2010. Micromechanics of brittle faulting and cataclastic flow in Tavel limestone. *Journal of Structural Geology*. **32**(8), pp.1158–1169.
- Van Noten, K., Claes, H., Soete, J., Foubert, A., Özkul, M. and Swennen, R. 2013. Fracture networks and strike-slip deformation along reactivated normal faults in Quaternary travertine deposits, Denizli Basin, western Turkey. *Tectonophysics*. **588**, pp.154–170.
- Van Noten, K., Topal, S., Baykara, M.O., Özkul, M., Claes, H., Aratman, C. and Swennen, R. 2019. Pleistocene-Holocene tectonic reconstruction of the Ballık travertine (Denizli Graben, SW Turkey): (De)formation of large travertine geobodies at intersecting grabens. *Journal of Structural Geology*. **118**, pp.114–134.
- Verbiest, M., Soete, J., Fay-Gomord, O., Adriaens, R., Aratman, C. and Swennen, R. 2021. Petrographical and mineralogical study of detrital strata near and within the Ballık travertine deposit (SW Turkey): architecture of a mixed clastic–carbonate succession. *International Journal of Earth Sciences*. **110**(3), pp.1049–1071.
- Vignaroli, G., Berardi, G., Billi, A., Kele, S., Rossetti, F., Soligo, M. and Bernasconi, S.M. 2016. Tectonics, hydrothermalism, and paleoclimate recorded by Quaternary travertines and their spatio-temporal distribution in the Albegna basin, central Italy: Insights on Tyrrhenian margin neotectonics. *Lithosphere*. **8**(4), pp.335–358.
- Walton, G., Arzúa, J., Alejano, L.R. and Diederichs, M.S. 2015. A Laboratory-Testing-Based Study on the Strength, Deformability, and Dilatancy of Carbonate Rocks at Low Confinement. *Rock Mechanics and Rock Engineering*. **48**(3), pp.941–958.
- Walton, G., Hedayat, A., Kim, E. and Labrie, D. 2017. Post-yield Strength and Dilatancy Evolution Across the Brittle–Ductile Transition in Indiana Limestone. *Rock Mechanics and Rock Engineering*. **50**(7), pp.1691–1710.
- Walton, G. 2021. A New Perspective on the Brittle–Ductile Transition of Rocks. *Rock Mechanics and Rock Engineering*. **54**(12), pp.5993–6006.
- Wang, S. and Yang, S.-Q. 2022. A new constitutive model capturing brittle–ductile transition for crystalline marble. *Arabian Journal of Geosciences*. **15**(10), p.996.
- Wang, S., Zhao, W., Fu, X., Zhang, Z., Wang, T. and Ge, J. 2020. A universal method for quantitatively evaluating rock brittle-ductile transition behaviors. *Journal of Petroleum Science and Engineering*. **195**, p.107774.
- Warren, L.V., Varejão, F.G., Quaglio, F., Simões, M.G., Fürsich, F.T., Poiré, D.G., Catto, B. and Assine, M.L. 2017. Stromatolites from the Aptian Crato Formation, a hypersaline lake system in the Araripe Basin, northeastern Brazil. *Facies*. **63**(1).
- Weger, R.J., Eberli, G.P., Baechle, G.T., Massaferro, J.L. and Sun, Y.F. 2009. Quantification of pore structure and its effect on sonic velocity and permeability in carbonates. *American Association of Petroleum Geologists Bulletin*. **93**(10), pp.1297–1317.
- Welch, M.J., Souque, C., Davies, R.K. and Knipe, R.J. 2015. Using mechanical models to investigate the controls on fracture geometry and distribution in chalk *In*: S. M. Agar and S. Geiger, eds. *Geological Society Special Publications No. 406. Fundamental Controls on Fluid Flow in Carbonates: Current Workflows to Emerging Technologies*. Geological Society of London, pp.281–309.
- Wennberg, O.P., McQueen, G., de Luca, P.H.V., Hunt, D., Chandler, A.S., Waldum, A. and Lapponi, F. 2019. Open fractures in pre-salt reservoirs in the Campos Basin: examples from silicified

- carbonates in BM-C-33 *In: First EAGE Workshop on Pre-Salt Reservoir: from Exploration to Production*. Rio de Janeiro, Brazil, : European Association of Geoscientists & Engineers, pp.1–5.
- Wong, T.-F. 1990. Mechanical compaction and the brittle–ductile transition in porous sandstones. *Geological Society, London, Special Publications*. **54**(1), pp.111–122.
- Wong, T.F. and Baud, P. 2012. The brittle-ductile transition in porous rock: A review. *Journal of Structural Geology*. **44**, pp.25–53.
- Woodcock, N.H. and Mort, K. 2008. Classification of fault breccias and related fault rocks. *Geological Magazine*. **145**(3), pp.435–440.
- Woodcock, N.H., Miller, A.V.M. and Woodhouse, C.D. 2014. Chaotic breccia zones on the Pembroke Peninsula, south Wales: Evidence for collapse into voids along dilational faults. *Journal of Structural Geology*. **69**, pp.91–107.
- Wright, V.P. and Barnett, A.J. 2015. An abiotic model for the development of textures in some South Atlantic early Cretaceous lacustrine carbonates *In: D. W. Bosence, K. A. Gibbons, D. P. Le Heron, W. A. Morgan, T. Pritchard and B. A. Vining, eds. Geological Society Special Publication No 418. Microbial Carbonates in Space and Time: Implications for Global Exploration and Production*. Geological Society of London, pp.209–219.
- Wright, P. and Rodriguez, K. 2018. Reinterpreting the South Atlantic Pre-Salt ‘Microbialite’ reservoirs: petrographic, isotopic and seismic evidence for a shallow evaporitic lake depositional model. *First Break*. **36**(5), pp.71–77.
- Wright, P. and Tosca, N., 2016. A geochemical model for the formation of the pre-salt reservoirs, Santos Basin, Brazil: implications for understanding reservoir distribution. *AAPG Search and Discovery, article*, 51304.
- Wu, G., Zhao, K., Qu, H., Scarselli, N., Zhang, Y., Han, J. and Xu, Y. 2020. Permeability distribution and scaling in multi-stages carbonate damage zones: Insight from strike-slip fault zones in the Tarim Basin, NW China. *Marine and Petroleum Geology*. **11**. 104208
- Wyllie, M.R.J., Gregory, A.R. and Gardner, L.W. 1956. Elastic wave velocities in heterogeneous and porous media. *Geophysics*. **21**(1), pp.41–70.
- Yielding, G., Freeman, B. and Needham, D.T. 1997. Quantitative fault seal prediction. *AAPG Bulletin*. **81**(6), pp.897–917.
- Yielding, G., Bretan, P. and Freeman, B. 2010. Fault seal calibration: a brief review *In: S. J. Jolley, Q. J. Fisher, R. B. Ainsworth, P. J. Vrolik and S. Delise, eds. Geological Society Special Publication No. 347. Reservoir Compartmentalisation*. Geological Society of London, pp.243–255.
- Yielding, G. 2015. Trapping of buoyant fluids in fault-bound structures *In: F. L. Richards, N. J. Richardson, S. J. Rippington, R. W. Wilson and C. E. Bond, eds. Geological Society of London Special Publication No. 421. Industrial Structural Geology: Principles, Techniques and Integration*. Geological Society of London, pp.29–39.
- Zhang, L., Ba, J., Fu, L., Carcione, J.M. and Cao, C. 2019. Estimation of pore microstructure by using the static and dynamic moduli. *International Journal of Rock Mechanics and Mining Sciences*. **113**, pp.24–30.
- Zhao, J., Feng, X.-T., Zhang, X.-W., Zhang, Y., Zhou, Y.-Y. and Yang, C.-X. 2018. Brittle-ductile transition and failure mechanism of Jinping marble under true triaxial compression. *Engineering Geology*. **232**, pp.160–170.

- Zheng, Z., Sun, W. and Fish, J. 2016. Micropolar effect on the cataclastic flow and brittle-ductile transition in high-porosity rocks: *Journal of Geophysical Research: Solid Earth*. **121**(3), pp.1425–1440.
- Zhu, W., Baud, P. and Wong, T.F. 2010. Micromechanics of cataclastic pore collapse in limestone. *Journal of Geophysical Research: Solid Earth*. **115**(4).

Appendix

Appendix 1: Crato Formation core plug data

The following table provides measured petrophysical (porosity and permeability) data for intact and faulted core plugs sampled from the Crato Formation. k is the Klinkenberg permeability measured at 2500 psi.

Fault zone	Sample name	Fault/host	fault throw (cm)	Weight (g)	Length (mm)	Diameter (mm)	Porosity (%)	Density g/cc	k mD
NO F1	NO-F1-F1	Fault		150.3	58.24	37.45	11.72	2.34	0.0460
	NO-F1-F2	Fault	1.1	135.2	57.60	37.43	12.46	2.13	0.0521
	NO-F1-H1	Host		148.0	51.51	37.76	14.50	2.57	0.0718
NO F2	NO-F6-F1	Fault		101.1	39.64	37.45	17.59	2.32	0.0067
	NO-F6-F2	Fault	3.6	167.6	64.74	37.47	10.78	2.35	0.0072
	NO-F6-H1	Host		97.6	37.85	37.44	18.54	2.34	0.0227
NO F3	NO-F7-F1	Fault	1.6	146.5	53.43	37.48	9.53	2.49	0.0035
	NO-F7-H1	Host		131.5	48.46	37.49	12.82	2.46	0.0064

Appendix 2: Travertine core plug petrophysical data

The following table provides measured petrophysical (porosity and permeability) data for intact travertine core plugs used within this study.

Acronym and symbol definitions used in table:

Φ : Porosity

k: Permeability (Klinkenberg corrected)

PMM: Peloidal micrite/microsparite

LMM: Laminated micrite/microsparite

SS: Steady State

PD: Pulse Decay

Sample name	Formation	Country	Facies	Angle of bedding	Weight	Length	Diameter	ϕ	Density	<i>k</i> method	<i>k</i>	<i>k</i>
				(°)	(g)	(mm)	(mm)	(%)	(g/cc)		<i>Pc = 1500</i> Psi (mD)	<i>Pc = 2500</i> Psi (mD)
AT26 H1	Acquasanta Terme	Italy	PMM	0	149.2	58.3	37.0	4.66	2.49	SS		19.31
AT26 H2	Acquasanta Terme	Italy	PMM	0	144.9	58.8	37.0	8.88	2.51	SS		1143.9
AT26 P1	Acquasanta Terme	Italy	PMM	90	138.2	55.3	37.0	8.52	2.54	PD		0.091
AT26 P2	Acquasanta Terme	Italy	PMM	90	131.7	54.6	37.0	13.15	2.58	PD	0.139	0.072
AT27 H1	Acquasanta Terme	Italy	LMM	0	149.8	65.3	37.0	15.28	2.51	SS		22.8
AT27 H2	Acquasanta Terme	Italy	LMM	0	131.0	53.3	37.0	13.79	2.64	SS		0.608
AT27 P1	Acquasanta Terme	Italy	LMM	90	137.0	56.3	37.0	11.96	2.58	PD	0.197	0.002
AT27 P2	Acquasanta Terme	Italy	LMM	90	131.5	52.0	36.1	6.40	2.65	PD		0.001
MT1 A1	Ballik	Turkey	PMM	45	75.2	59.5	25.5	3.79	2.57	PD	0.200	0.195
MT1 A5	Ballik	Turkey	PMM	45	75.3	59.8	25.5	3.87	2.56	PD	0.036	0.037
MT1 H1	Ballik	Turkey	PMM	0	69.6	55.1	25.6	4.10	2.57	PD	0.002	0.001
MT1 H8	Ballik	Turkey	PMM	0	67.4	53.2	25.5	2.31	2.54	PD		0.001
MT2 A1	Ballik	Turkey	PMM	45	71.4	55.1	25.5	0.023	2.54	PD	<0.001	<0.001
MT2 H3	Ballik	Turkey	PMM	0	70.2	54.7	25.6	0.037	2.50	PD	1.12	1.483
MT2 H6	Ballik	Turkey	PMM	0	73.3	57.0	25.5	1.73	2.55	PD	1.260	2.171
RT1 A1	Rapalona Terme	Italy	Shrubs	45	69.4	60.9	25.4	39.51	2.70	SS	103.67	112.63
RT1 A2	Rapalona Terme	Italy	Shrubs	45	72.9	77.8	25.5	50.34	2.68	PD	8.301	5.7461
RT1 A3	Rapalona Terme	Italy	Shrubs	45	72.4	62.0	25.5	37.59	2.64	PD	0.053	0.030
RT1 A4	Rapalona Terme	Italy	Shrubs	45	72.0	60.7	25.3	36	2.68	PD y	0.038	0.028
RT1 A5	Rapalona Terme	Italy	Shrubs	45	70.5	59.9	25.5	43.19	2.65	PD	0.002	0.002
RT1 A6	Rapalona Terme	Italy	Shrubs	45	72.8	61.4	25.4	40.84	2.66	PD	0.006	0.004
RT1 H1	Rapalona Terme	Italy	Shrubs	0	69.6	57.8	25.5	41.82	2.66	SS	64.8	64.37
RT1 H2	Rapalona Terme	Italy	Shrubs	0	70.0	56.7	25.5	29.51	2.62	SS	1.46	1.18
RT1 H3	Rapalona Terme	Italy	Shrubs	0	74.2	59.3	25.5	37.59	2.65	PD	0.157	0.153
RT1 H4	Rapalona Terme	Italy	Shrubs	0	61.5	59.7	25.3	45.06	2.60	SS	>1000	>1000

RT1 H5	Rapalona Terme	Italy	Shrubs	0	63.7	59.4	25.2	42.27	2.69	SS	>1000	>1000
RT1 P2	Rapalona Terme	Italy	Shrubs	90	68.1	59.5	25.5	39.51	2.68	PD	0.982	1.630
RT1 P5	Rapalona Terme	Italy	Shrubs	90	68.9	58.9	25.5	43.93	2.69	PD	0.024	0.019
RT22 H1	Rapalona Terme	Italy	LMM	0	95.4	44.8	36.8	28.12	2.77	SS		992.6
RT24 P1	Rapalona Terme	Italy	Shrubs	90	67.2	29.2	36.9	19.99	2.68	SS		205.63
RT25 P1	Rapalona Terme	Italy	Shrubs	90	62.5	26.5	36.9	15.79	2.62	S		0.169
RT5 A1	Rapalona Terme	Italy	PMM	45	68.2	54.4	25.5	6.86	2.45	PD	0.073	0.089
RT5 A2	Rapalona Terme	Italy	PMM	45	70.6	54.4	25.6	5.37	2.53	PD	0.036	0.021
RT5 A3	Rapalona Terme	Italy	PMM	45	72.7	56.6	25.5	5.23	2.52	PD	1.076	0.692
RT5 H4	Rapalona Terme	Italy	PMM	0	67.8	51.7	25.6	21.04	2.56	PD	0.116	0.071
RT5 H8	Rapalona Terme	Italy	PMM	0	63.8	49.8	25.6	7.56	2.50	PD	0.068	0.042
RT5 P1	Rapalona Terme	Italy	PMM	90	69.5	54.0	25.6	32.95	2.51	PD	0.223	0.179
RT5 P4	Rapalona Terme	Italy	PMM	90	69.9	53.4	25.5	4.54	2.56	PD	0.008	0.008
RT5 P5	Rapalona Terme	Italy	PMM	90	67.5	52.6	25.5	6.00	2.51	PD	0.019	0.013
RT5 P7	Rapalona Terme	Italy	PMM	90	66.7	51.9	25.6	5.36	2.50	PD	0.019	0.012
RT6 H1	Rapalona Terme	Italy	PMM	0	72.4	56.9	25.6	6.37	2.48	PD	0.695	0.711
RT6 P1	Rapalona Terme	Italy	PMM	90	67.2	54.0	25.5	8.07	2.43	PD	0.026	0.014
RT7 H1	Rapalona Terme	Italy	PMM	0	76.3	59.6	25.5	3.41	2.50	PD	0.167	0.199
RT7 H5	Rapalona Terme	Italy	PMM	0	66.2	51.6	25.6	4.62	2.50	PD	0.034	0.018
RT7 P1	Rapalona Terme	Italy	PMM	90	66.7	53.1	25.6	6.67	2.45	PD	0.053	0.053
RT7 P2	Rapalona Terme	Italy	PMM	90	64.5	51.6	25.6	6.43	2.43	PD	0.016	0.013
RT7 P3	Rapalona Terme	Italy	PMM	90	67.7	53.4	25.6	5.65	2.47	PD	0.013	0.011
RT7 P4	Rapalona Terme	Italy	PMM	90	64.9	52.3	25.6	15.93	2.42	PD	0.004	0.002
RT7 P5	Rapalona Terme	Italy	PMM	90	63.2	51.2	25.6	8.72	2.40	PD	0.010	0.004
RT7 P6	Rapalona Terme	Italy	PMM	90	57.5	46.8	25.5	7.83	2.40	PD	0.028	0.021
SAT1 H7	Saturnia	Italy	Shrubs	0	69.3	54.2	25.5	3.42	2.51	SS	3.829	3.366
SAT1 P7	Saturnia	Italy	Shrubs	90	66.9	53.7	25.6	5.02	2.56	PD	0.004	0.002
TIV1 H1	Tivoli	Italy	Shrubs	0	157.2	63.0	36.9	7.65	2.53	SS		457.9

TIV1 P1	Tivoli	Italy	Shrubs	0	109.6	56.0	36.9	33.37	2.74	SS	1742.37
TIV1 P1	Tivoli	Italy	Shrubs	90	150.2	67.1	36.9	18.89	2.59	SS	3.90
TIV8 H1	Tivoli	Italy	Shrubs	0	152.3	65.1	36.9	14.93	2.57	SS	1320.7
TIV8 P1	Tivoli	Italy	Shrubs	90	148.5	66.5	37.3	21.33	2.59	PD	0.029

Appendix 3: P-Q Critical stresses

The follow tables provide critical stress data for each triaxial test.

P: Mean stress

Q: Differential Stress

C': Onset of inelastic dilatant deformation

C*: Onset of shear enhanced compaction

C*': Switch from shear enhanced compaction to dilatant mechanisms.

Sample RT1 H2

Critical stress	P (MPa)	Q (MPa)
C*	48	76
C*	76	112
C*	92	125
C*'	103	147

Sample RT1 P5

Critical stress	P (MPa)	Q (MPa)
C*	20	20
C*	35	30
C*	56	47

Sample RT8 A1

Critical stress	P (MPa)	Q (MPa)
C'	31	43
C'	43	46
C'	68	76

Sample RT8 A2

Critical stress	P (MPa)	Q (MPa)
C*	38	56
C*	62	85
C*'	75	102

Sample RT8 P1

Critical stress	P (MPa)	Q (MPa)
C*	29	36
C*	38	37
C*	44	30

Sample RT8 P3

Critical stress	P (MPa)	Q (MPa)
C*	34	48
C*	41	42
C*	62	50
C*	93	127

Sample RT8 H2

Critical stress	P (MPa)	Q (MPa)
C'	55	92
C'	77	114
C'	90	122

Sample AT6 P1

Critical stress	P (MPa)	Q (MPa)
C'	33	47
C'	53	65
C'	68	76

Sample AT6 H1

Critical stress	P (MPa)	Q (MPa)
C'	51	83
C'	85	129
C'	101	142

Sample AT6 H2

Critical stress	P (MPa)	Q (MPa)
C'	44	69
C'	66	92
C'	80	100

Sample AT6 H2

Critical stress	P (MPa)	Q (MPa)
C'	44	69
C'	66	92
C'	80	100

Sample AT7 P2

Critical stress	P (MPa)	Q (MPa)
C'	29	39
C'	47	55
C'	69	78

Sample AT7 H2

Critical stress	P (MPa)	Q (MPa)
C'	42	56
C'	67	94
C'	84	108

Sample TIV1 P1

Critical stress	P (MPa)	Q (MPa)
C'	32	44
C'	47	55
C'	56	52

Sample TIV8 P1

Critical stress	P (MPa)	Q (MPa)
C'	30	29
C'	42	41
C'	55	52

Appendix 3: Stress-strain curves

Triaxial mechanical data is presented for each samples as stress-strain curves for both the volumetric strain (%) against mean stress (MPa) and Axial strain (%) against Axial Stress (MPa).

Summary of figures in appendix 3:

Figure 1. Stress-strain curves for sample AT6 P1.

Figure 2. Stress-strain curves for sample AT6 H1.

Figure 3. Stress-strain curves for sample AT6 H2.

Figure 4. Stress-strain curves for sample TIV1 P1.

Figure 5. Stress-strain curves for sample TIV8 P1.

Figure 6. Stress-strain curves for sample RT1 H2.

Figure 7. Stress-strain curves for sample RT1 P5.

Figure 8. Stress-strain curves for sample AT7 P2.

Figure 9. Stress-strain curves for sample RT8 P1.

Figure 10. Stress-strain curves for sample RT8 P3.

Figure 11. Stress-strain curves for sample AT7 H2.

Figure 12. Stress-strain curves for sample RT8 A1.

Figure 13. Stress-strain curves for sample RT8 A2.

Figure 14. Stress-strain curves for sample RT8 H2.

Figure 15. Stress-strain curves for sample SAT1 P7. Note: lateral strain could not be measured for this sample due to failure of the lateral strain gauge recording measurements.

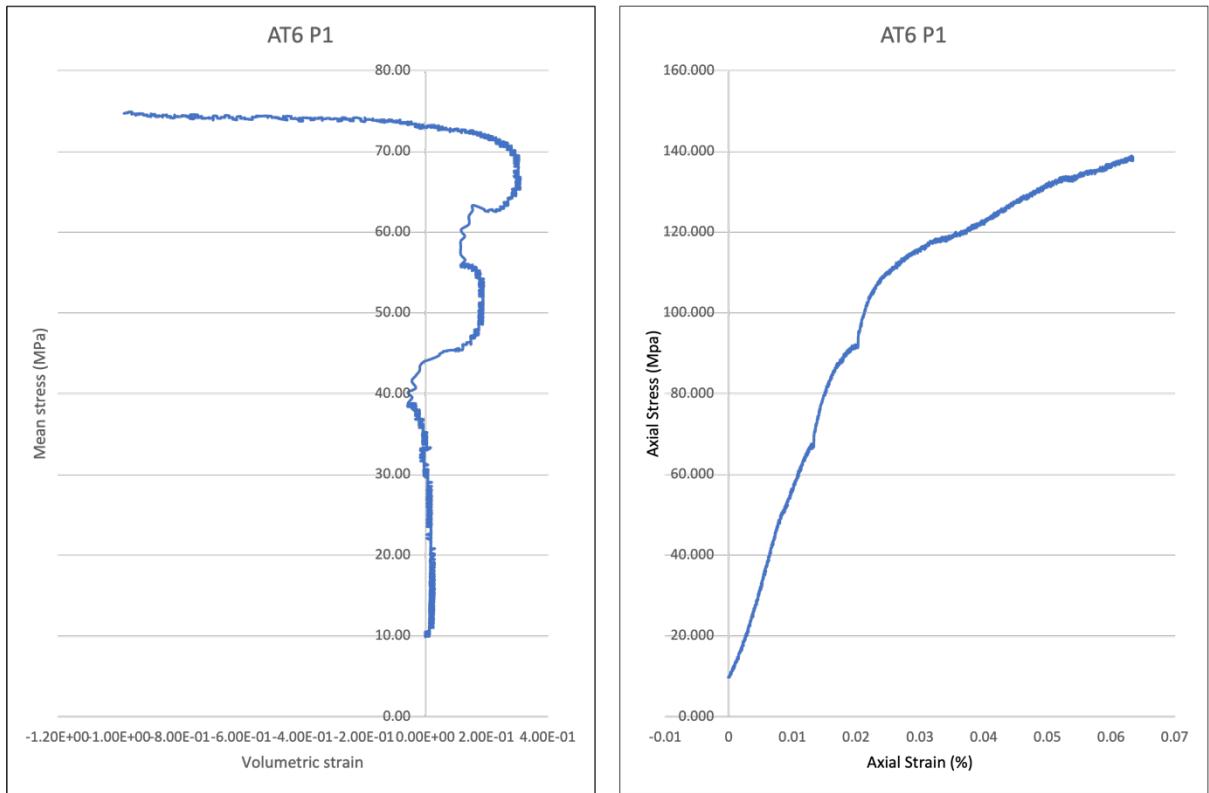


Figure 1. Stress-strain curves for sample AT6 P1.

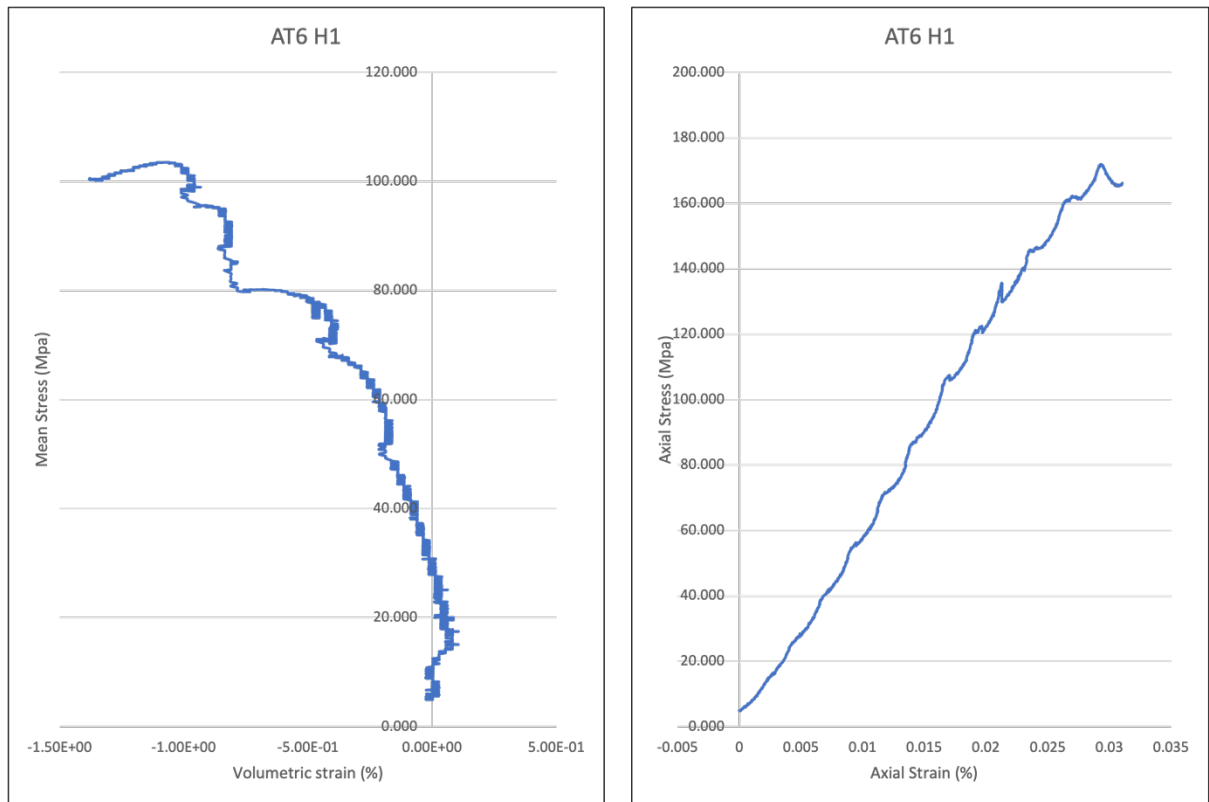


Figure 2. Stress-strain curves for sample AT6 H1.

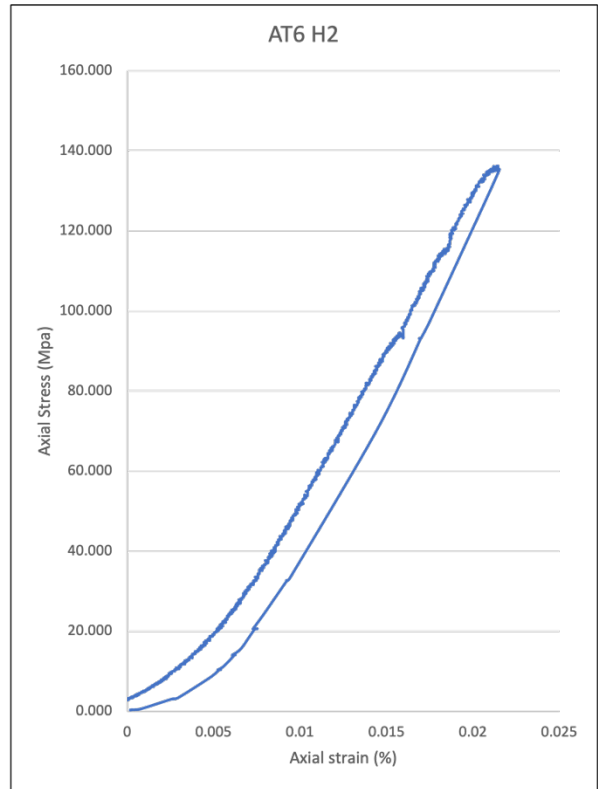
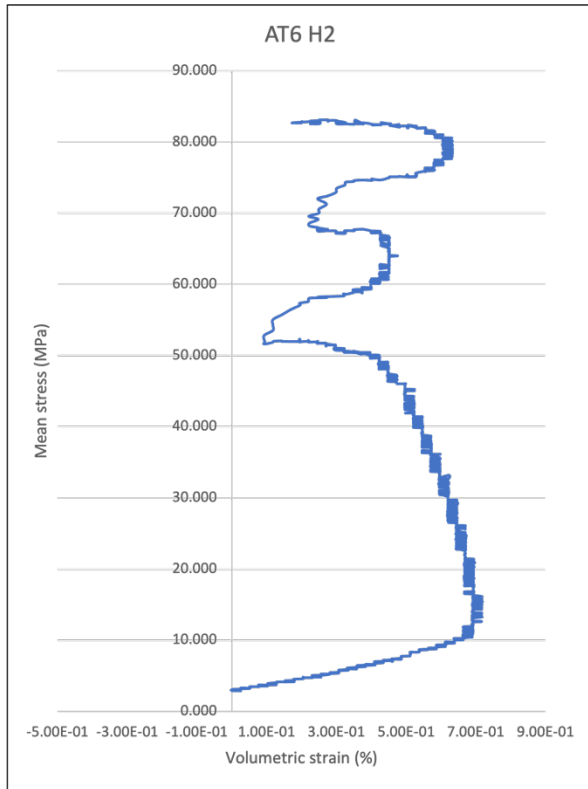


Figure 3. Stress-strain curves for sample AT6 H2.

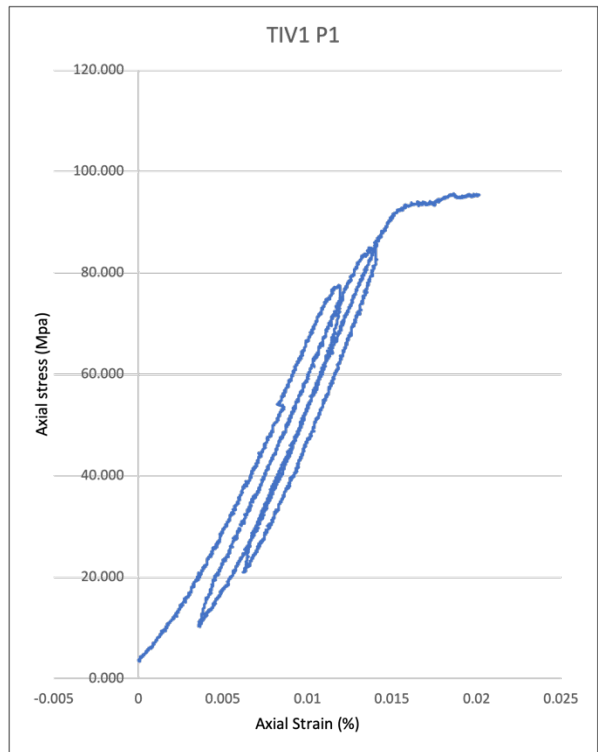
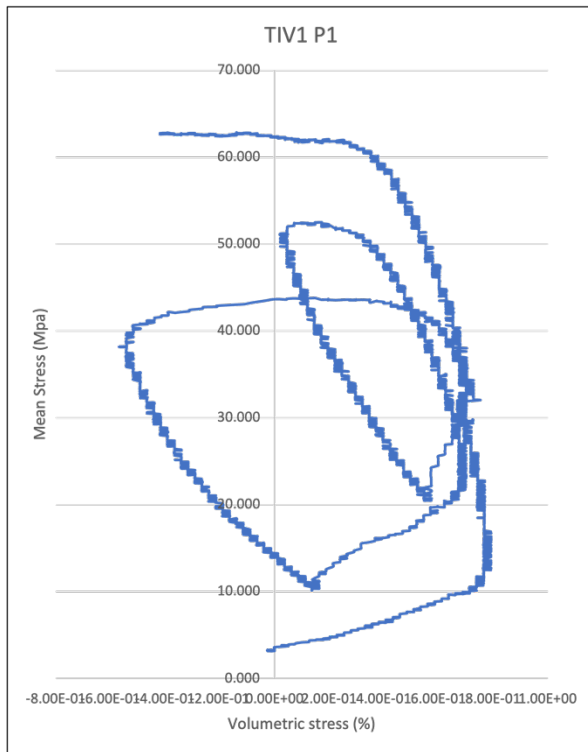


Figure 4. Stress-strain curves for sample TIV1 P1.

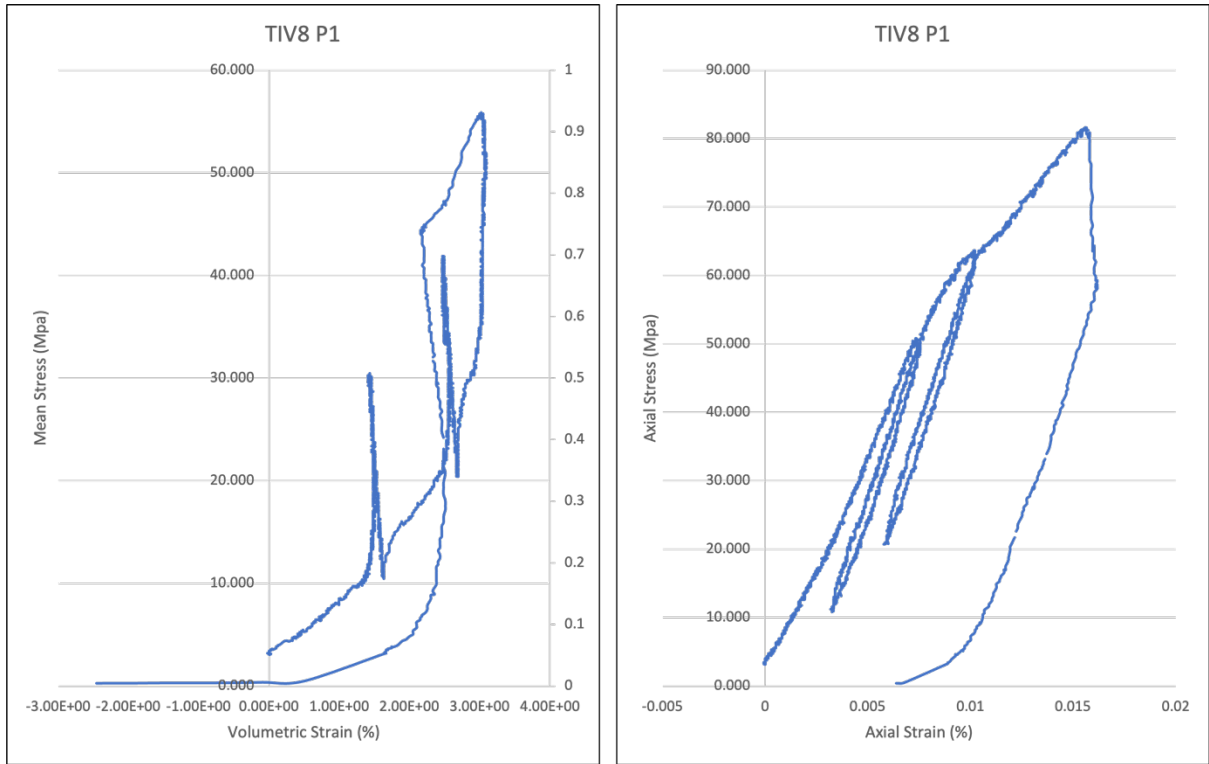


Figure 5. Stress-strain curves for sample TIV8 P1.

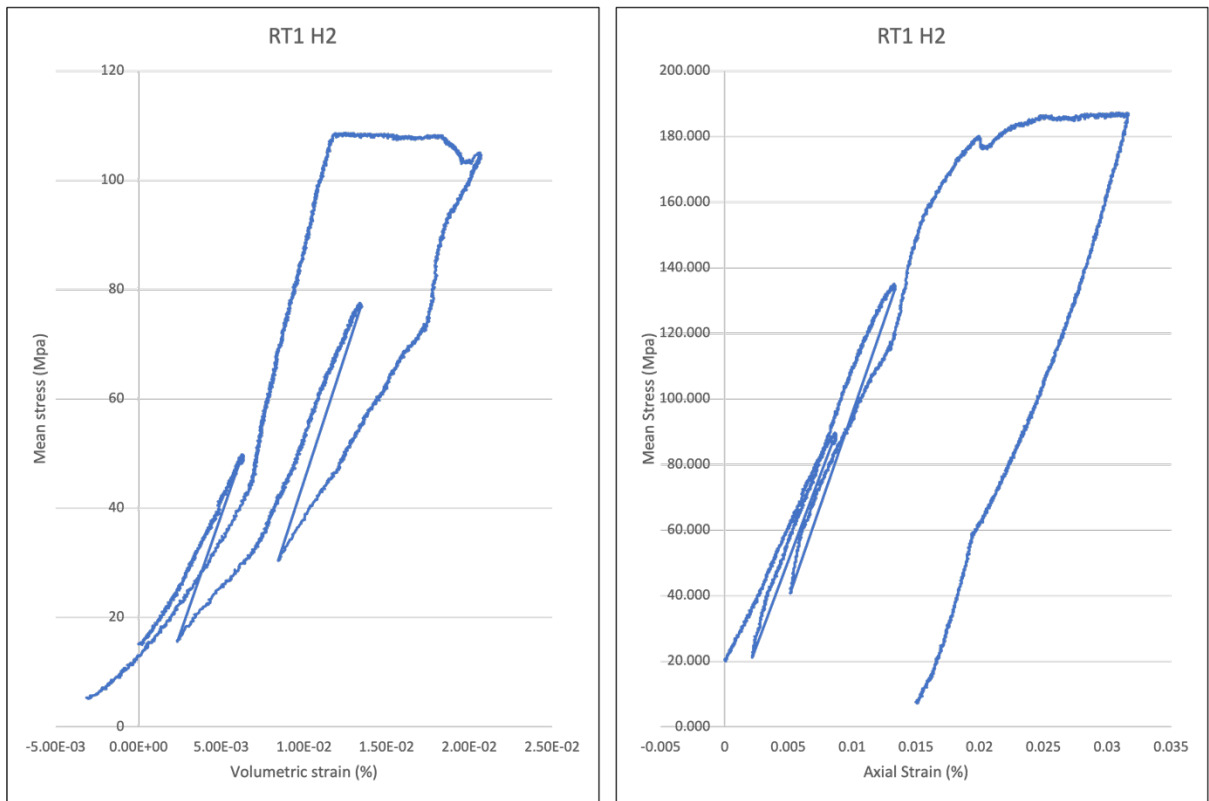


Figure 6. Stress-strain curves for sample RT1 H2.

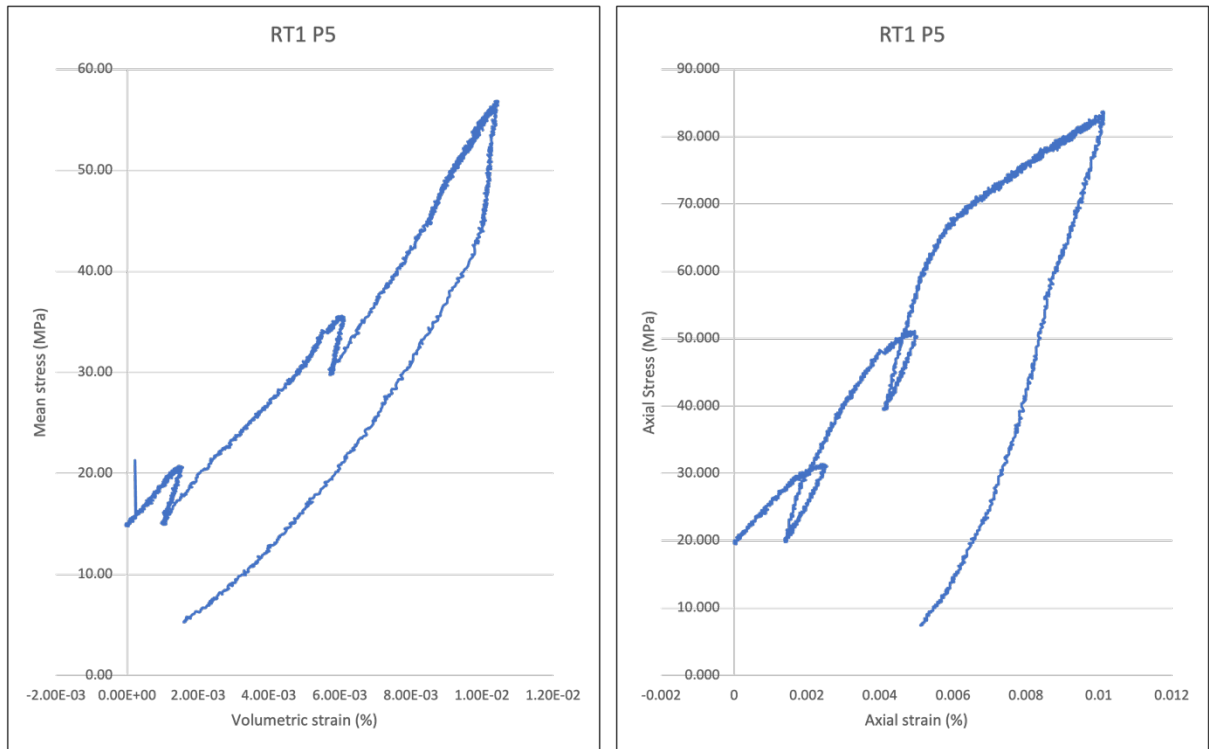


Figure 7. Stress-strain curves for sample RT1 P5.

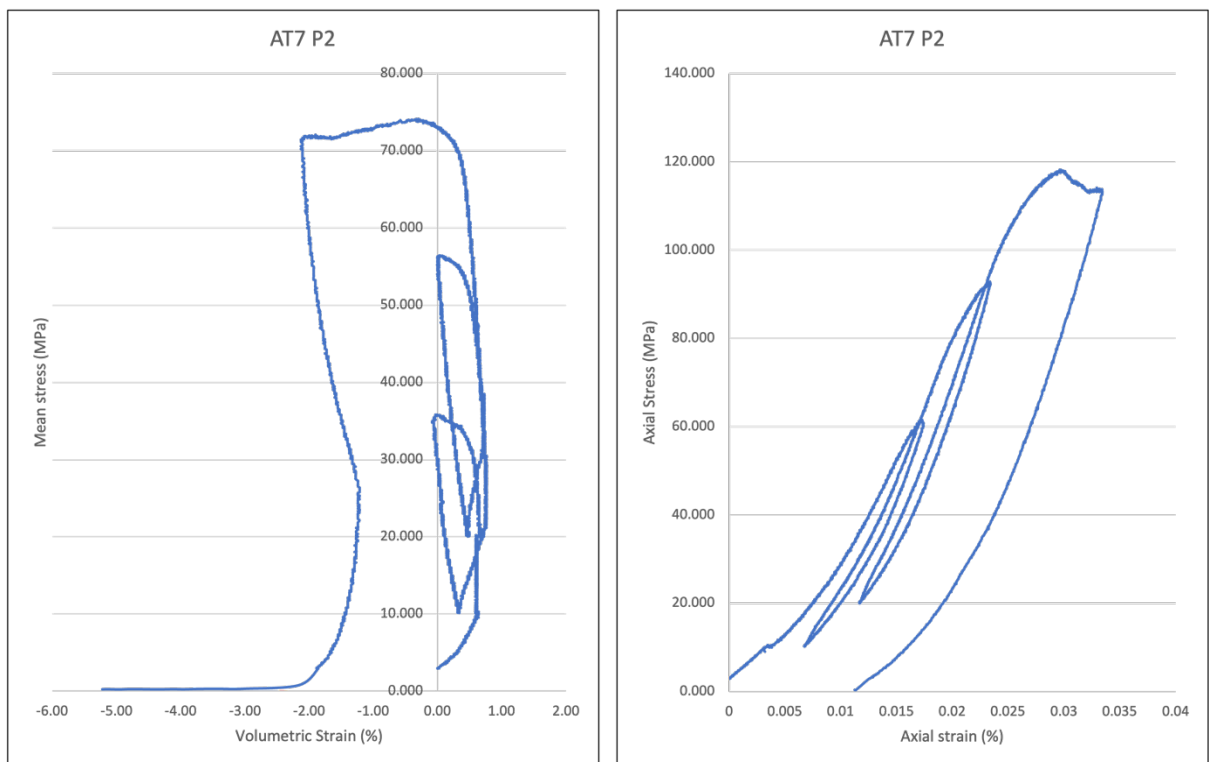


Figure 8. Stress-strain curves for sample AT7 P2.

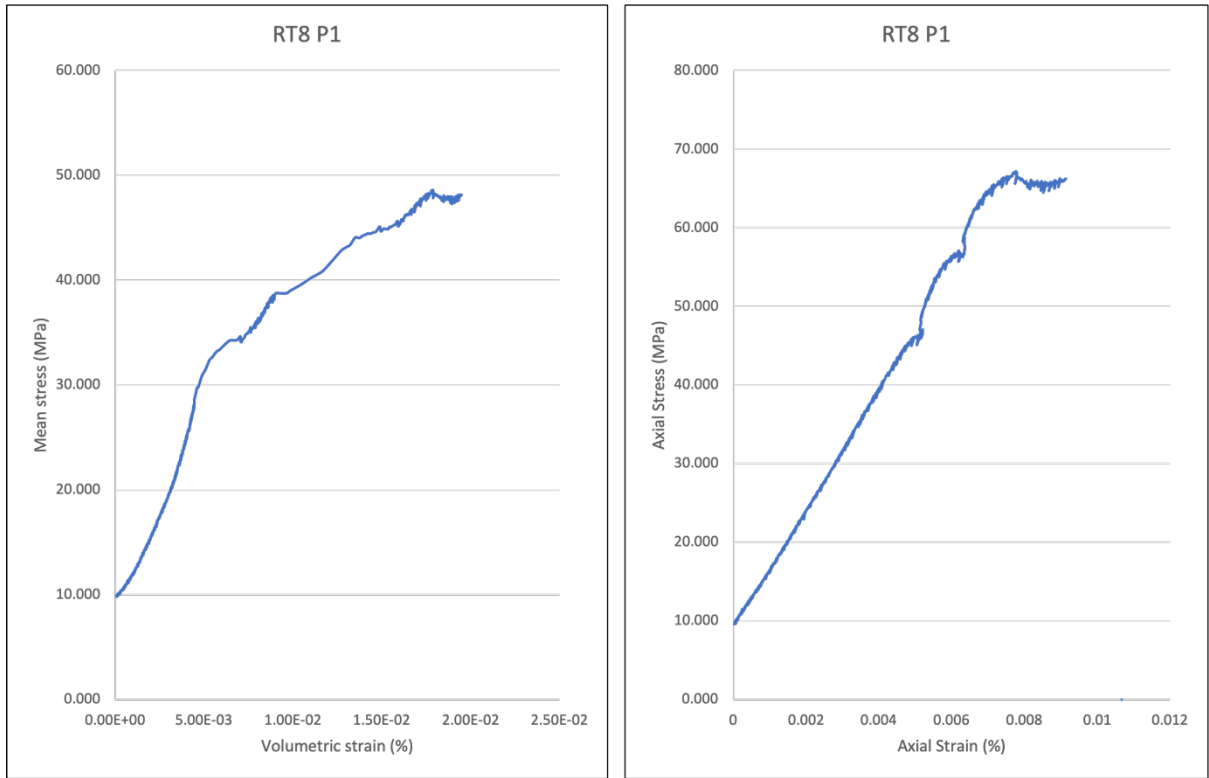


Figure 9. Stress-strain curves for sample RT8 P1.

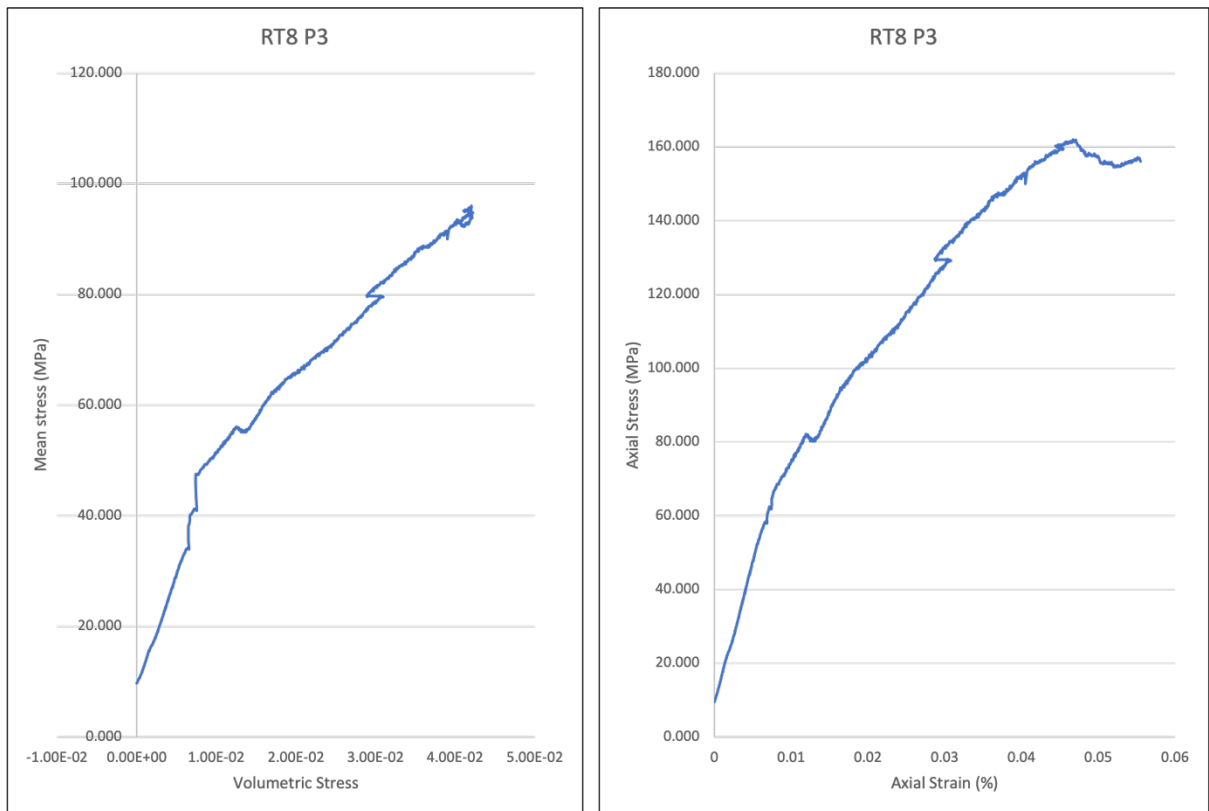


Figure 10. Stress-strain curves for sample RT8 P3.

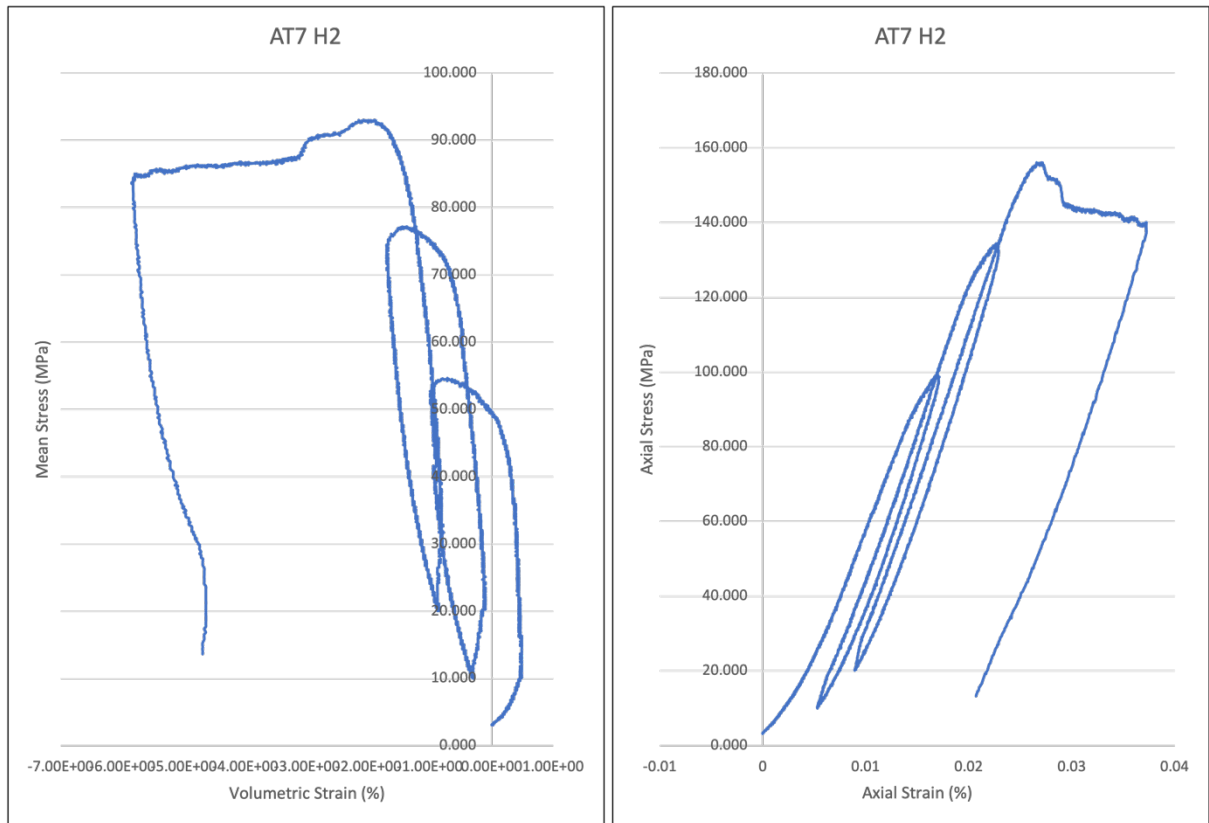


Figure 11. Stress-strain curves for sample AT7 H2.

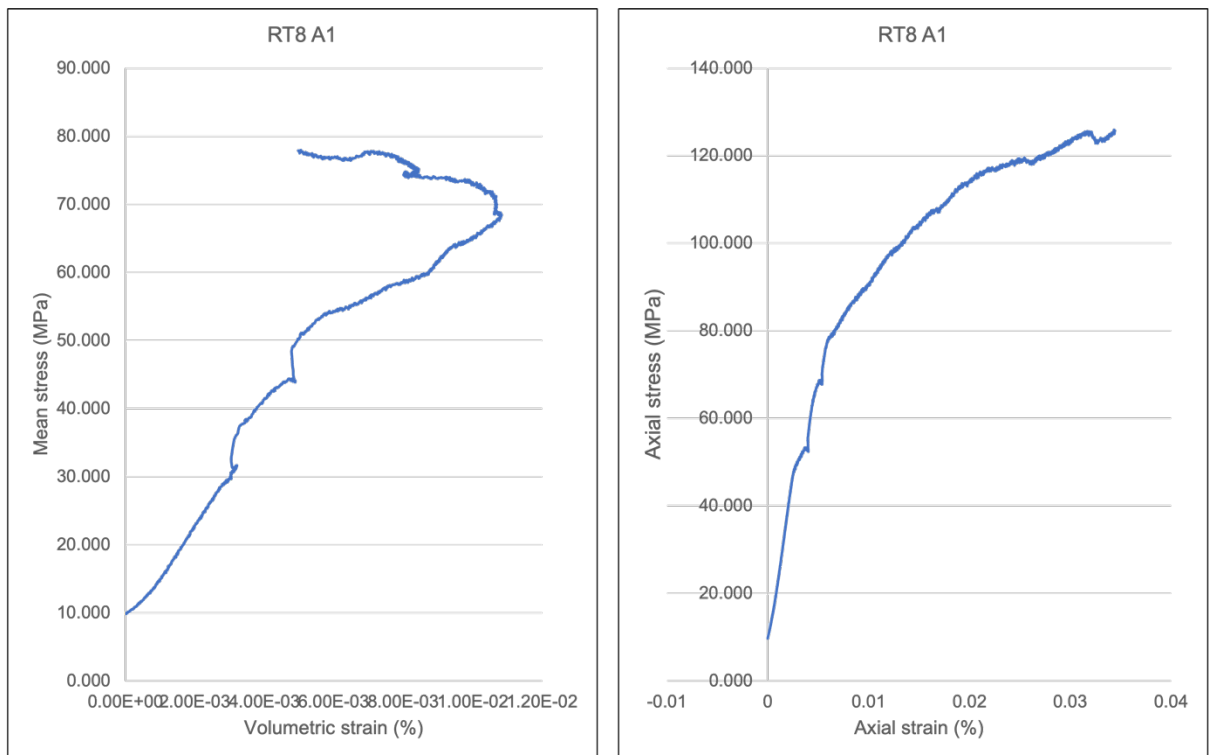


Figure 12. Stress-strain curves for sample RT8 A1.

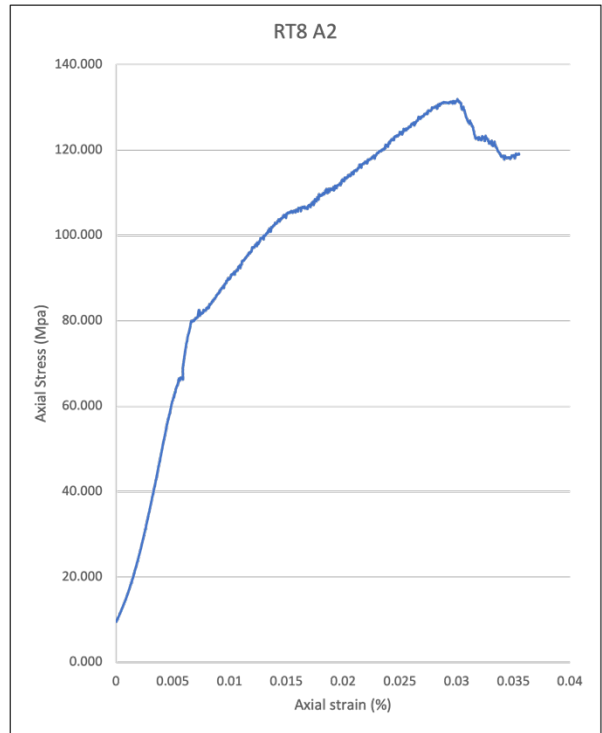
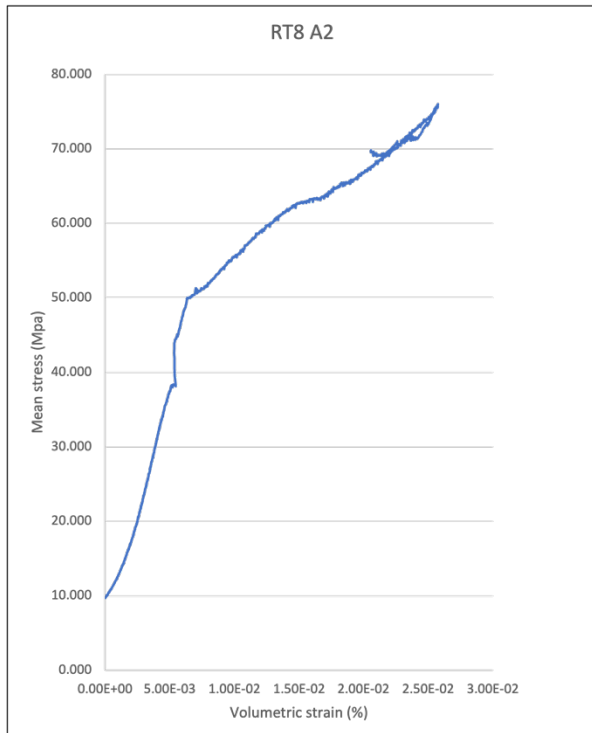


Figure 13. Stress-strain curves for sample RT8 A2.

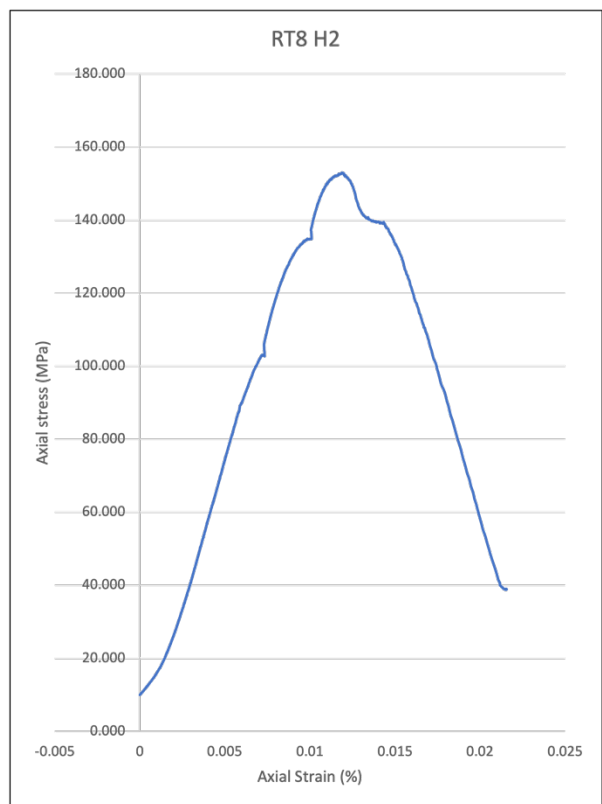
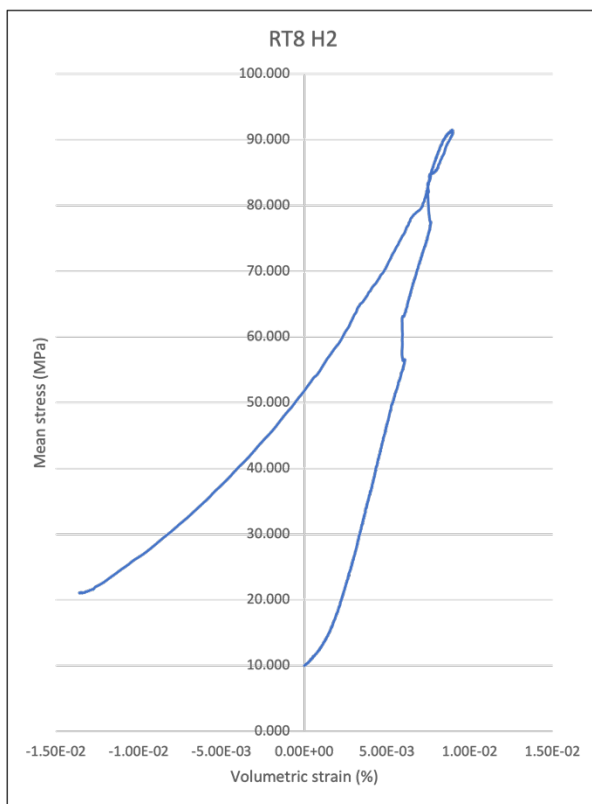


Figure 14. Stress-strain curves for sample RT8 H2.

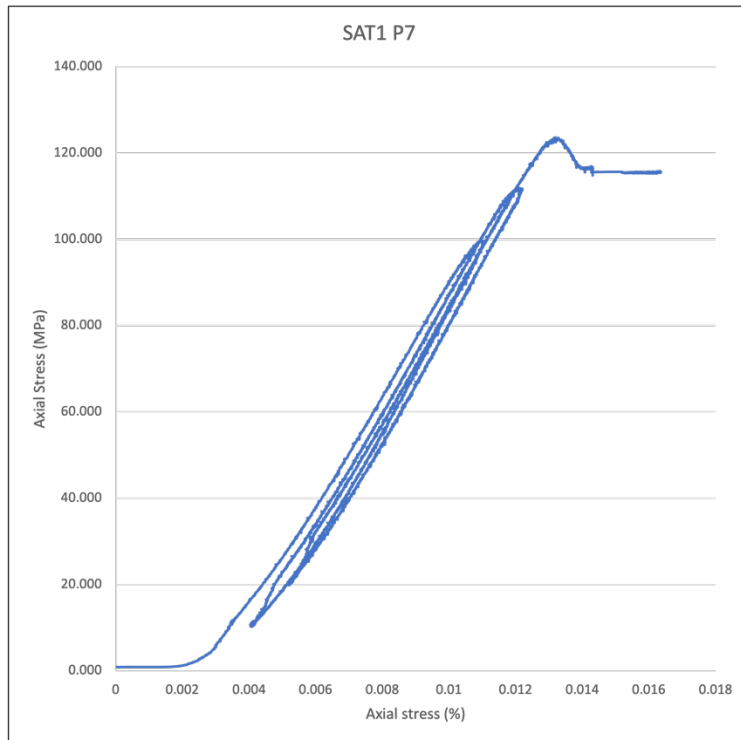


Figure 15. Stress-strain curves for sample SAT1 P7. Note: lateral strain could not be measured for this sample due to failure of the lateral strain gauge recording measurements.